UC San Diego

UC San Diego Electronic Theses and Dissertations

Title

Designing, Testing, and Optimizing the Laser-cut Foil X-pinch and Benchmarking it against Wire and Hybrid X-pinches

Permalink

https://escholarship.org/uc/item/8tz633t3

Author

Collins, Gilbert W

Publication Date

2020

Peer reviewed|Thesis/dissertation

eScholarship.org Powered by the California Digital Library
University of California

UNIVERSITY OF CALIFORNIA SAN DIEGO

Designing, Testing, and Optimizing the Laser-cut Foil X-pinch and Benchmarking it against Wire and Hybrid X-pinches

A dissertation submitted in partial satisfaction of the
requirements for the degree
Doctor of Philosophy

in

Engineering Sciences (Engineering Physics)

by

Gilbert W Collins

Committee in charge:

Professor Farhat Beg, Chair
Professor Alexey Arefiev
Professor Rick Moyer
Professor Clifford Surko
Professor Daniel Tartakovsky

2020

Copyright
Gilbert W Collins, 2020
All rights reserved.

The dissertation of Gilbert W Collins is approved, and it is acceptable in quality and form for publication on microfilm and electronically:

_____

_____

_____

_____

_____

Chair

University of California, San Diego

2020

-

TABLE OF CONTENTS

LIST OF ABBREVIATIONS

Al-My ..... Aluminized-Mylar (a filter used on pinholes and diodes).

CAD ..... Computer Aided Design.

FWHM ..... Full-Width at Half-Maximum.

HEDP ..... High Energy Density Physics.

HOPG ..... Highly-Ordered Pyrolytic Graphite.

HXP ..... Hybrid X-Pinch.

HXR ..... Hard X-Rays ($\geq$ 3 keV in this dissertation).

ICF ..... Inertial Confinement Fusion.

FFT ..... Fast Fourier Transform.

LCXP ..... Laser-Cut foil X-Pinch.

LTD ..... Linear Transformer Driver.

LWS1 ..... Laser WorkStation 1 (cutting platform at General Atomics Inc.).

MCP ..... Micro-Channel Plate.

MHD ..... Magneto-HydroDynamic.

Nd-YAG ..... Neodymium-doped Yttrium Aluminum Garnet (crystal lasing medium).

nLTE ..... non Local Thermodynamic Equilibrium.

PCD ..... Photo Conducting Diode (diamond in this dissertation).

PIN ..... Positive Intrinsic Negative (layers in Si diodes)/

PP ..... Polypropylene.

PTFE ..... Polytetrafluoroethylene (Teflon).

SXR ..... Soft X-Rays ($\sim$ 1 - 3 keV in this dissertation).

WXP ..... Wire X-Pinch.

XUV ..... eXtreme Ultra-Violet.

LIST OF SYMBOLS AND CONSTANTS

a ..... Pinch radius, sometimes denoted r.

A ..... Atomic number (atomic mass units).

Å ..... Angstroms.

$\mathbf{B}$ ..... Magnetic field (Gauss or Tesla).

B_θ ..... Magnetic field - azimuthal component.

$\mathbf{B}_{\text{global}}$ ..... Azimuthal magnetic field surrounding the entire target.

$\mathbf{B}_{\text{local}}$ ..... Azimuthal magnetic field around an individual wire/leg.

c_s ..... Ion sound speed (distance/unit time).

$\mathbf{E}$ ..... Electric Field.

E_D ..... Dreicer electric field, see Eq. 2.40.

I ..... Current (charge/second).

I_{PB} ..... Pease-Braginskii current, see Sec. 2.2.2

$\mathbf{J}$ ..... Current density (current/unit area).

J_r ..... Current density - radial component.

J_z ..... Current density - axial component.

k_B ..... Boltzmann's constant (conversion factor between energy & temperature).

K_α ..... K-alpha, a 2p-1s transition.

K_β ..... K-beta, a 3p-1s transition.

$ln\Lambda$ ..... Coulomb logarithm.

L_α ..... L-alpha, a 3d-2p transition.

m_e ..... Electron mass.

m_i ..... Ion mass.

n_c ..... Critical electron density, see Eq. 3.2.

n_{crit} ..... Critical ion density, see Sec. 5.5.

n_e ..... Electron density (electrons/unit volume)

n_i ..... Ion density (ions/unit volume)

N_i ..... Ion line density, see Eq. 2.18.

N_{crit} ..... Critical ion line density for anomalous resistivity onset, see Eq. 2.38.

$\mathcal{N}_{i-tot}$ ..... Total number of ions in the pinch hot spot, see Sec. 5.5.

p_b ..... Magnetic Pressure, see Eq. 2.14.

p_t ..... Thermal Pressure, see Eq. 2.13.

p_J ..... Power deposited through Joule heating, see Eq. 2.19.

P_J ..... Power deposited through Joule heating per unit length, see Eq. 2.21.

p_b ..... Power radiated by bremsstrahlung, see Sec. 2.2.2.

P_b ..... Power radiated by bremsstrahlung per unit length, see Eq. 2.22.

P_w ..... Net power deposited per unit length for $P_j - P_b$, see Eq. 2.28.

r ..... Pinch radius, sometimes denoted a.

t_c ..... Plasma electrode gap clearing time, see Eq. 2.42.

T_e ..... Electron temperature.

T_i ..... Ion temperature.

v_A ..... Alfvén velocity, see Eq. 2.27.

v_d ..... Electron drift velocity, see Eq. 2.35.

v_{ti} ..... Ion thermal velocity.

Z^* ..... Average ionization level.

γ_{m0} ..... Growth rate of the m=0 instability, see Eq. 2.27.

ε_0 ..... Vacuum permittivity.

η ..... Refractive index, see Eq. 3.4.

η_s ..... Spitzer Resistivity, see Eq. 2.20.

λ_{mfp} ..... Collisional mean free path (units of length).

μ_0 ..... Vacuum permeability.

ω_l ..... Laser frequency, see Sec. 3.3.1.

ω_p ..... Plasma frequency, see Eq. 3.1.

LIST OF FIGURES

LIST OF TABLES

ACKNOWLEDGEMENTS

I feel immensurable gratitude to the oh-so-many who, throughout this process, supported, educated, assisted, played, listened, and commiserated, and will attempt to direct its expression here:

Dr. Beg, it has been a long road to this point. Thank you for the immeasurable time, support, and perhaps most importantly the patience (and the lack thereof when appropriate) you've given along said road.

To my committee, Professors Daniel Tartakovsky, Cliff Surko, Rick Moyer, and Alexey Arefiev, thank you for sitting through multiple long examinations and presentations usually scheduled at woefully last-minute and inconvenient times, and shepherding me through this degree.

Dr. Fabio Conti, this would not happen without you. Period. So 'Thanks' are really insufficient, but know that I appreciate it all beyond measure. Dr. Maria Pia Valdivia Levia, thank you for starting this process with me way back when, and then fittingly, coming back to finish it. Your knowledge, enthusiasm, and donuts were irreplaceable. Dr. Julio Valenzuela, aka Jules, thanks for the science and non-science help along the way, and being so ridiculously good at fixing my many electrical and physics problems.

Drs. Mingsheng Wei and Rich Stephens, the real credit for the success of the laser-cut X-pinch project goes to you. Thank you for placing your project in my clumsy hands, and continuing to give me the tools to continue it.

Dr. Simon Bott, thank you for all of the guidance, advice, and help along the way, and the unfailingly cheerful 'dude!' in passing.

Dr. Chris McGuffey, thank you for your help and support.

Dr. Stephanie Hansen, thank you for responding so graciously and completely when some random graduate student reached out to you for help with a spectroscopy problem.

To Lane, Chris, Hatim, and Paul at GA, thanks for your help making targets, and then

teaching me how to make more.

So many more of you in the lab deserve more credit than I probably gave you, but to Dr. Jeff Narkis, Valdimir, Apsara, Nick, David, Igor, Dr. Pawel Kozlowski, Dr. Christine Krauland, Dr. Derek Mariscal, Dr. Joohwan Kim, Dr. David Reisman, Georges, Dr. Tom Zick, Bob, Dr. Eric Hahn, Dr. Maylis Dozieres, all of you, thank you.

Prof. Dave Hammer, Ahmed Elshafiey, and Dr. Tania Shelkovenko at Cornell, thank you for the conversations about X-pinches along the way. You all are the true sages of the subject.

Tom, Tyler, and Ian in the shops, guys, so many of the physical pieces in these experiments would've never reached their final form without your help. Thank you.

Chris Cassidy and Dr. Steve Roberts, thank you for helping me solve so many computer and electrical component problems.

Cham, thanks for bringing the PUGGs and inviting me to play.

And, finally...

Mom and Dad, I owe you one...make that two...or many.

Rio, thanks for putting up with my terrible work hours, and consistent whinging. Oh, and for agreeing to be the sugar mama, wife, and mother of our child(ren) to that unshaven and gaudily dressed perennial grad student you randomly bumped into seven years ago.

Athena, thanks for letting me color and play with fire trucks, being my walk buddy with EB, and the unfailing daily soul recharges.

This manuscript contains work supported by the Department of Energy, National Nuclear Security Administration under Award Numbers DE-NA0003842, DE-NA0002955, and DE-NA0003882, as well as General Atomics internal R & D funds.

The text contained in Chapter 4 is modified from two publications of which the author of this dissertation was the first author. The first, Ref. [13], is G. W. Collins IV, M. P. Valdivia, T. O. Zick, J. Kim, D. M. Haas, A. C. Forsman, R. B. Stephens, and F. N. Beg, "Investigation into the dynamics of laser-cut foil X-pinches and their potential use for high repetition rate operation,"

Applied Physics Letters, vol. 105, no. 2, pp 024101, 2014. The second, Ref. [14], is G. W. Collins IV, J. C. Valenzuela, S. B. Hansen, M. S. wei, C. T. Reed, A. C. Forsman, and F. N. Beg, "Characterization of laser-cut copper foil X-pinches," *Physics of Plasmas*, vol. 23, no. 10, pp 101212, 2016.

The text from Chapter 5 is modified from a manuscript submitted for publication to the *Journal of Applied Physics* by G. W. Collins IV, M. P. Valdivia, F. Conti, S. B. Hansen, L. Carlson, D. A. Hammer, A. Elshafiey, J. N. Narkis, and F. N. Beg, titled “Direct comparison of wire, foil, and hybrid X-pinches on a 200kA, 150ns current driver."

VITA

2008	B. S. in Physics, University of California, San Diego
2012	M. S. in Physics, San Diego State University
2016	M. S. in Engineering Sciences (Engineering Physics), University of California, San Diego
2020	Ph. D. in Engineering Sciences (Engineering Physics), University of California, San Diego

PUBLICATIONS

F. Conti, J. C. Valenzuela, V. Fadeev, N. Aybar, D. B. Reisman, A. Williams, G. Collins IV, J. Narkis , M. P. Ross, R. B. Spielman, and F. N. Beg "MA-class linear transformer driver for Z-pinch research," *Physical Review Accelerators and Beams*, **23**, 090401 (2020).

G. W. Collins IV, J. C. Valenzuela, P. Tzeferacos and B. Khiar, A. F. A. Bott and G. Gregori, C. A. Speliotopoulos, N. Aybar, F. Conti, and F. N. Beg, "Role of collisionality and radiative cooling in supersonic plasma jet collisions of different materials," *Physical Review E*, **101**, 023205 (2020).

G. W. Collins IV, J. C. Valenzuela, S. B. Hansen, M. S. Wei, C. T. Reed, A. C. Forsman, and F. N. Beg, "Characterization of laser-cut copper foil X-pinches," *Physics of Plasmas*, **23**, 101212 (2016).

D. Mariscal, J. Valenzuela, G. Collins IV, F. Beg, and J. Chittenden, "Investigation of current transport in 2x2 wire array plasmas," *Plasma Science, IEEE Transactions on*, **43**, 8, 2527 - 2531 (2015).

J. C. Valenzuela, G. W. Collins IV, T. Zick, J. Narkis, I. Krasheninnikov, and F. N. Beg, "Counter-propagating plasma jet collision and shock formation on a compact current driver," *High Energy Density Physics*, **17**, 140 - 145, (2015).

J. Valenzuela, G. Collins IV, D. Mariscal, E. Wyndham, and F. Beg, "Study of instability formation and euv emission in thin liners driven with a compact 250 ka, 150 ns linear transformer driver," *Physics of Plasmas*, **21**, 3, 031208 (2014).

G. W. Collins IV, M. P. Valdivia, T. O. Zick, J. Kim, D. M. Haas, A. C. Forsman, R. B. Stephens, and F. N. Beg, "Investigation into the dynamics of laser-cut foil X-pinches and their potential use for high repetition rate operation," *Applied Physics Letters*, **105**, 024101 (2014).

G. W. Collins IV, M. P. Valdivia, T. Zick, R. E. Madden, M. G. Haines, and F. N. Beg, "Study of X-pinch dynamics using a low current (25 kA) and slower current (400 ns) pulse," *Physics of Plasmas*, **20**, 4, 042704 (2013).

G. Collins IV, D. Marsical, D. Haas, R. Madden, K. Gunasekara, J. Kim, M. Abarr, S. Bott, J. Chittenden, and F. Beg, "Effect of the global to local magnetic field ratio on the ablation modulations on x-pinches driven by 80 ka peak current," *New Journal of Physics*, **14**, 4, 043021 (2012).

S. C. Bott, G. Collins, K. Gunasekera, D. Mariscal, F. N. Beg, D. M. Haas, F. Veloso, I. C. Blesener, A. D. Cahill, C. L. Hoyt, B. R. Kusse, and D. A. Hammer, "A collinear self-emission and laser-backlighting imaging diagnostic," *Review of Scientific Instruments*, **83**, 8, 083507 (2012).

S. C. Bott, D. M. Haas, R. E. Madden, U. Ueda, Y. Eshaq, G. Collins, K. Gunasekera, D. Mariscal, J. Peebles, F. N. Beg, M. Mazarakis, K. Struve, and R. Sharpe, "250 ka compact linear transformer driver for wire array z-pinch loads," *Physical Review Special Topics-Accelerators and Beams*, **14**, 5, 050401 (2011).

D. Haas, S. Bott, J. Kim, D. Mariscal, R. Madden, Y. Eshaq, U. Ueda, G. Collins IV, K. Gunasekera, F. Beg, J. Chittenden, N. Niasse, and C. Jennings, "Supersonic jet formation and propagation in x-pinches," *Astrophysics and Space Science*, **336**, 1, 33–40 (2011).

S. C. Bott, D. M. Haas, Y. Eshaq, U. Ueda, R. E. Madden, G. W. Collins IV, and F. N. Beg, "Ablation Studies of Low-Number Wire Arrays at 200 kA Using A Linear Transformer Driver," *IEEE Trans. Plasma Sci.*, **38**, 567 (2010).

R. E. Madden, S. C. Bott, G. Collins IV, and F. N. Beg, "Investigation of Carbon X-Pinches as a Source for Point-Projection Radiography," *IEEE Trans. Plasma. Sci.*, **37**, 433 (2009).

R. E. Madden, S. C. Bott, D. Haas, Y. Eshaq, U. Ueda, G. Collins, and F. N. Beg, "Cross-point coronal plasma dynamics in two- and four-wire x-pinches," *Physics of Plasmas*, **15**, 112701 (2008).

S. C. Bott, D. M. Haas, U. Ueda, Y. Eshaq, R. Madden, G. Collins, and F. N. Beg, "High Resolution Laser Schlieren Imaging of Coronal Plasma Evolution in 80 kA X-pinches," *IEEE Trans. Plasma. Sci*, **36**, 1274 (2008).

ABSTRACT OF THE DISSERTATION

Designing, Testing, and Optimizing the Laser-cut Foil X-pinch and Benchmarking it against Wire and Hybrid X-pinches

by

Gilbert W Collins

Doctor of Philosophy in Engineering Sciences (Engineering Physics)

University of California, San Diego, 2020

Professor Farhat Beg, Chair

Wire X-pinches have been comprehensively studied for nearly four decades as a fast ($\sim$1 ns Full-Width Half-Max: FWHM), small ($\sim$1μm) X-ray source in pulsed-power experiments. Room for improvement to this array remains though, including reducing variability in source timing, size, quantity, and flux, and the presence of strong electron beam emission post-pinch that tends to doubly expose any acquired radiograph. Many of these limitations can be reduced by optimal mass-matching of the target X to the current driver in use and a reliable cross-point geometry. Addressing these two parameters, we developed a new X-pinch, and tested in on the 200kA, 150ns rise-time GenASIS driver at UC San Diego. This new X is cut from thin metallic

foils using a precision laser-cutting facility which can fabricate virtually any cross-sectional mass or crosspoint configuration. The first laser-cut foil X-pinch (LCXP) experiments used Ta, and demonstrated comparable evolution and equal or superior X-ray source parameters to comparably massed W wire X-pinches (WXPs), despite markedly different initial geometry (ie a square or trapezoidal crosspoint cross-section). Subsequent Cu LCXP experiments showed that the X-ray pulse from these targets was confined to a $\sim$2ns period in contrast with the resolvable second pulse of hard X-ray electron beam emission common in WXPs. However, spectroscopic data showed evidence of a beam source co-located with the $\geq$10% solid density, $\sim$1keV hot pinch source. Another promising X-pinch configuration (developed at Cornell University), the hybrid X-pinch (HXP), which consists of two conical electrodes 1-3mm apart bridged by a thin wire or capillary, demonstrated predominantly single source X-pinches and less hard X-ray emission than found in WXPs. To compare all three aforementioned X-pinch configurations — wire, hybrid, and laser-cut foils — we conducted an in-depth performance study of these X's on the GenASIS driver, representing the first time all three configurations were compared on a single platform. All configurations produced short ($\sim$1ns FWHM), small ($\leq$5μm, both diagnostically limited), soft (Cu L-shell, $\sim$1keV) X-ray sources with comparable peak fluxes, while the thermal K-shell flux increased from hybrid to wire to foil X-pinches. Ultimately, each array possesses benefits and drawbacks which are detailed herein.

Chapter 1

Introduction

The Z-pinch is a well-studied plasma progression driven by pulsed electrical power to produce up to megabar pressures, keV temperatures, and megajoules of soft X-rays, with applications in, amongst other topics, fusion energy, astrophysics, shock physics, and fundamental high energy density physics (HEDP) studies [15–21]. This power is most commonly delivered to cylindrically symmetric loads using a pulsed power generator that comprises numerous capacitors and switches, and stores 10^2 - 10^7 Joules of energy over a period of seconds to minutes. Releasing this energy in short amounts of time (10^{-8} - 10^{-6} s) generates currents ranging from tens of kiloamperes to tens of megaamperes and powers ranging from gigawatts to terawatts. The target—carrying current travelling symmetrically about z-axis that gives it the name 'Z'-pinch—rapidly heats (typically through Joule heating) and turns at least partially into a plasma. This plasma possesses an internal thermal pressure proportional to its density and temperature, and experiences compression from a self-generated magnetic pressure (p_B) given by $\mathbf{J}_z \times \mathbf{B}_\theta$, where $\mathbf{J}_z$ is the axial current density, and $\mathbf{B}_\theta$ is the azimuthal magnetic field. This magnetic pressure ranges from a kilobar to tens of megabar, which drives an implosion of the plasma towards the axis, culminating in a hot, dense plasma that is especially pertinent to inertial confinement fusion concepts. The plasma efficiently radiates in the soft X-ray band (up to $\sim$ 15% of stored energy, or $\sim$ 2MJ on

the largest experiments) which is one of the appealing characteristic features/products of the Z-pinch [17, 22]. The large self-generated $\mathbf{B}_\theta$ makes the array prone to a variety of instabilities including the magneto-hydrodynamic m=0 and m=1 (see Sec. 2.3.1), electrothermal, and magneto Rayleigh-Taylor (MRT) instabilities [23], which are detrimental to ICF efforts, but (as we will see) key to other uses. For decades now, following episodic improvements in driver technology and load sophistication, interest in the extreme plasma conditions and efficient X-ray production of Z-pinches continues to grow, supporting a plethora of laboratories, drivers, and experimental motivations.

1.1 A Brief History of Z-pinch Studies

The Z-pinch certainly ranks among the oldest areas of plasma studies, perhaps beginning with the Dutch scientist Martinus van Marum in 1790. At this time, van Marum stored 1 kJ of energy in Leyden jars, which were an early form of capacitor, and discharged it through a wire, vaporizing it—which makes this maybe the first known pulsed-power experiment as well [24, 25], shown in Fig. 1.1a (courtesy of the Teylers Museum, Ref. [1]). In 1905, over one-hundred years later, Pollock and Barraclough described the electromagnetic pinch effect after observing crushed portions of a copper tube that had served its purpose as a lightning rod at a kerosene refinery in New South Wales [26]. The term 'pinch' was first coined by Edwin Northrup two years later in 1907, as he performed experiments to visualize the internal forces on a conductor, including running current through a trough containing a thin stream of mercury [2]. In these experiments, he noted that, with sufficient current, V-shaped depressions would form in the otherwise smooth stream of mercury. If he increased the current enough, the depressions would steepen, reach the bottom of the trough, and rupture the circuit. One of the different configurations Northrup used to view the forces in a conductor (not the trough of mercury) is shown in Fig, 1.1b, which shows a contraption with a depression that had two liquids of different specific gravity placed in it, one of

a) Van Maruum's 'Elektriseermachine'

b) One setup of Northrup's to view forces in a conductor

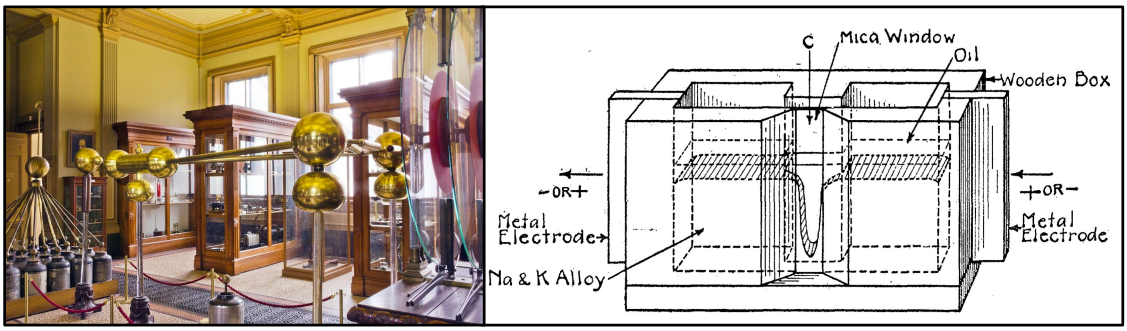

Figure 1.1: a) Martinus van Maurum's 1kJ pulsed power machine, the Large electric generator, or Elektriseermachine, which is on display at Teylers Museum, in Haarlem, Netherlands. The leyden jars are visible to the lower left of the figure, and the current delivery system proceeds towards the right. Image used courtesy of the Teylers Museum, Ref. [1]. b) One configuration used by Northrup to visualize the forces acting inside a conductor, using liquids of two distinct specific gravities, one of which conducted electricity. Image reproduced from Northrup's 1907 paper, Ref. [2].

which conducted; when current was applied, the conductor would depress into the trough. These experiments established the concept and basic physics of the pinch, but more rigorous scientific development would wait another few decades. In 1934, W. H. Bennett derived a relationship between the temperature, ion line density, and current for streams of charged particles (developed formally in Sec. 2.2.1) [27]. Immediately post-World War II, pinch experiments and studies began in earnest, beginning largely at Imperial College in London but expanding elsewhere. [28–31]

Since this time, Z-pinches have enjoyed periodic renaissances typically coupled to excitement regarding their X-ray yield or potential for controlled fusion experiments, and accompanied by improvements in pulsed-power technology. One such rise and fall, circa 1957-1958, included the discovery that deuterium gas Z-pinches produced neutrons and the subsequent disappointment that the neutrons were not evidence of thermonuclear fusion but of accelerated ion interactions with other deuterons [30, 31], perhaps best summed up in the conclusion of Anderson's paper in Ref. [31]: "The denial of the optimistic conclusion of a thermonuclear yield despite so many favorable results was indeed a sobering experience."

The development and improvement of the Marx bank—a chain of capacitors and switches

charged in parallel and discharged in series—coupled with a pulse-forming line to compress the discharge pulse enabled the leap into the more modern area of higher current and significantly higher voltage pulsed-power experiments [32]. From this technology, drivers of increasingly large currents and voltages including XP (450 kA peak current, 50 ns rise-time) [33], Cobra (1 MA, 95 - 230 ns) [34], Zebra (1 MA, 100 ns) [35], MAGPIE (1.4 MA, 250 ns) [36], Saturn (6 MA, 60 ns) [22], and Z (26 MA, 100 ns) [16] have fielded a variety of Z-pinch experiments using various configurations (which we will briefly describe in Sec. 1.2) producing increasingly extreme plasma conditions and larger X-ray yields [17, 21, 22, 37–39].

1.2 Pulsed-Power Z-pinch Configurations

The diverse set of Z-pinch configurations includes gas-filled capillaries [30], single wires [40], wire-arrays [41], foil liners [42], and gas puffs [43], with various sub-configurations to each of these.

A majority of the early Z-pinch experiments involved placing a gas-filled capillary (cylinder) between two electrodes and applying a potential. In such a setup, a current shell forms near the walls of the tube, self-producing the $\mathbf{B}_\theta$ required to radially collapse the plasma. This configuration allows for controlled amounts of mass between the electrodes and does not require synchronization between the current pulse and a target gas release since it is contained (cannot disperse), but this containment leads to interactions with the vessel wall. It was deuterium pinches in this configuration that produced neutrons that were later proven non-thermonuclear in origin [30, 31].

Single wire or fiber Z-pinches, such as that shown and illustrated in Fig. 1.2a, consist of, as the name implies, a single wire or fiber placed between the electrodes of a pulsed-power generator [3, 44]. In these configurations, the intense Ohmic heating from the current pulse forms a warm ($\geq$ 10eV), low-density coronal plasma around a cold (a few eV), dense wire core which

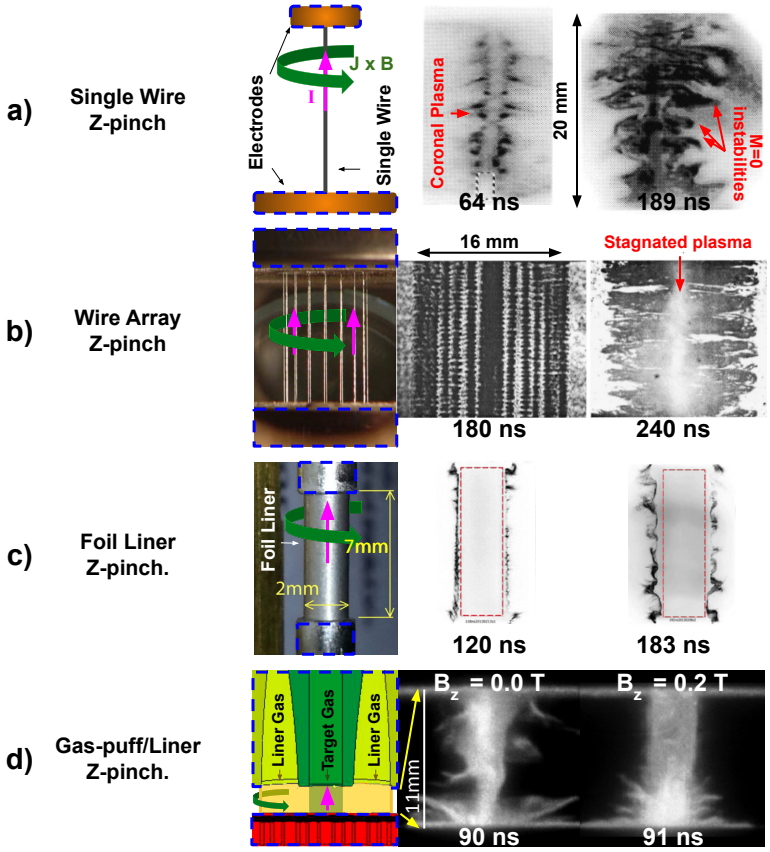

Figure 1.2: Four different configurations of Z-pinches, with examples of the setup and experimental data. Times relative to current start are labelled below each experimental image, and scales are given for each setup. Electrodes in each setup are outlined in blue dashes. a) A drawing of a single-wire Z-pinch setup and schlieren images of a 20mm long, 25 µm Al single-wire Z-pinch from Ref. [3]. b) A 16-wire array Z-pinch on the MAGPIE generator and schlieren images at times relative to current start of an 16 x 15 µm Al Z-pinch array imploding, from Refs. [4] and [5]. c) A 3 µm thick Ni foil liner Z-pinch (non-imploding) on the GenASIS driver, and schlieren images with times relative to current start and outline of original liner position, from Ref. [6]. d) A computer rendering of a two-stage gas-puff Z-pinch setup used on the ZEBRA generator, and gated XUV images at comparable times with two different axial magnetic fields applied (B_z), from Ref. [7] (note that the gas-puff drawing and images are not on the same scale, and that the pinch is significantly compressed from its initial position).

slowly supplies material to the corona over the duration of the discharge until said core is depleted (this process will receive more attention in Sec. 2.4.1) [3, 45–47]. This configuration, like the gas-filled capillary, is extremely prone to m=0 and m=1 MHD instabilities (as is seen in the schlieren images in Fig. 1.2a, via Ref. [3]), since all of the current flows through the corona, with is relatively small radius, creating a sizeable $\mathbf{J}_z$ and $\mathbf{B}_\theta$. Attempts to reduce instability development in single wires included adding a prepulse, changing material, and changing wire size, but none these alterations significantly improved the stability of the single-wire Z-pinch [44].

A wire-array Z-pinch consists of a number of wires—from 4 to ≥ 300 have been used so far —arranged about the z-axis at some radius determined by the designer of the experiment to suit the peak driver current since p_B scales as r^{-2}. Rather than running current directly through a single column of plasma, current flows through the wires, again producing the core-corona structure found in the single wire Z-pinches. In the array though, the $\mathbf{J}_z \times \mathbf{B}_{Global}$—where $\mathbf{B}_{Global}$ here is the $\mathbf{B}_\theta$ around the entire wire array rather than the individual wires—drives the plasma from the wires in towards the axis to stagnate in an axial plasma column. When the wires have ablated sufficient mass an implosion occurs, sweeping much of the remaining wire mass in towards the axis where the kinetic energy of the implosion is converted to thermal energy, heating the plasma, and emitting large amounts of thermal X-rays [5]. This setup and implosion process is shown in Fig. 1.2b, which shows a 16 wire Z-pinch setup and implosion on the 1400 kA MAGPIE driver at Imperial College [4, 5, 48]. Studies showed that increasing the number of wires in the array, and thus increasing symmetry increased X-ray yield [17, 22, 49]. X-ray yields increase further by decreasing the implosion time of the pinch through either reducing wire mass or array radius [50]. The largest X-ray yields from Z-pinches come from nested wire-array Z-pinches, where two coaxial wire arrays were simultaneously discharged [51]. In these, the inner array appeared to significantly mitigate Rayleigh-Taylor instabilities from the implosion of the outer array, appreciably increasing the X-ray yield.

From the aforementioned observations regarding improving X-ray yields, one method to

further improve symmetry is to replace the individual wires with a cylindrical foil or 'liner' at the cost of mass (since even a thin foil will likely outweigh individual wires) [6, 42]. Currently, one of the most concerted fusion efforts in the Z-pinch community is the MagLIF concept, or Magnetic Liner Induced Fusion, in which a thin metallic liner is imploded on a deuterium fuel [21, 52–54]. Experiments using this setup on the 26000 kA Z machine have produced promising data thus far. An image of a small-scale, non-imploding Ni foil Z-pinch and schlieren images of the instabilities on the surface of the liner is shown in Fig. 1.2c (taken from Ref. [6]).

A gas puff Z-pinch is simply a gas-filled capillary Z-pinch sans the capillary tube, where the gas in injected by a valve and nozzle. The main advantage of a gas puff compared to a single wire or wire array Z-pinch is its significantly lower mass, allowing a machine to decrease implosion time and theoretically increase X-ray yields [43, 50]. The discharge of the pulsed power generator must be synchronized with the release of the gas from a pulsed nozzle. On-axis gas puffs can be relatively stable (to m=0 and m=1 MHD instabilities) compared to single-wire Z-pinches due to their larger radius. A hollow gas shell or 'liner' on the other hand, offers improved symmetry over a wire array Z-pinch, and more importantly has a more adjustable mass. This allows a medium-scale driver ($\sim$ 1 MA) to drive a fast gas implosion (high kinetic energy of the collapsing liner) compared to a more massive cylindrical foil or many-wire array at the cost of significant magneto-Rayleigh-Taylor instabilities. Experiments imploding a gas-liner on either another gas-liner, an axial gas puff, or an axial wire showed that current pulse profiles, gas choice, and axial magnetic fields ($\mathbf{B}_z$ play roles in the X-ray yields, final pinch radius, and stability of gas puff implosions [7, 55, 56]. Simulations suggest that a second liner outside the axial target plasma (and first gas liner) could further stabilize the implosion [57].

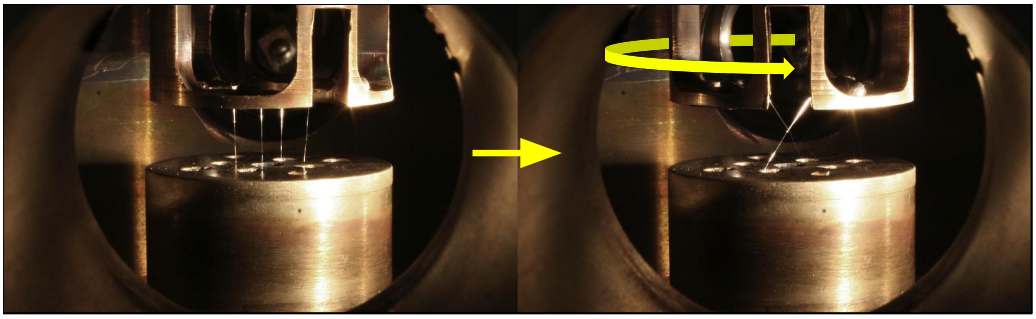

Figure 1.3: A picture of a 4-wire 5μm W X-pinch being set up, first as 4 parallel wires (left) and then after rotation to form an X.

1.3 The X-pinch

Another unique form of wire array Z-pinch is the X-pinch: a thoroughly studied array [58, 59] traditionally assembled by placing two or more parallel wires in the electrodes of a pulsed power driver and rotating one electrode relative to the other so that the wires just touch forming an 'X', shown in Fig 1.3.

The X-pinch is used to create fast ($\sim$ 1 ns), small ($\sim$ 1 μm), and localized X-ray sources (1-10 keV) for use in, amongst other applications, point-projection radiography (see Fig. 1.4a,b) [8, 9, 60], lithography [61, 62], X-ray Thomson scattering [63], Moiré deflectometry via Talbot-Lau interferometry(see Fig. 1.4c) [64, 65], X-ray diffraction (see Fig. 1.4d) [10], and studying other High-Energy Density (HED) plasmas [66, 67].

As with the wire-array Z-pinch configurations, a $\mathbf{B}_{\text{global}}$ surrounds the entire array, driving plasma from the legs of the X to the axis to form counter-propagating axial plasma jets, shown in Fig. 1.5. The X-pinch intentionally localizes the region of maximum $\mathbf{J} \times \mathbf{B}_{\text{global}}$ at the crosspoint, where the private magnetic field in each individual wire ($\mathbf{B}_{\text{local}}$) combines at a minimum radius. At the crosspoint of the X-pinch (and only at the crosspoint), a short (hundreds of μm) 'micro Z-pinch' forms, flanked on either end by large parallel surfaces we will refer to as plasma electrodes. Like longer Z-pinches, the micro Z-pinch eventually develops instabilities and collapses forming one or more hot spots that emit X-rays characteristic of a hot ($T_e \approx 1$ keV), dense ($n_e \geq 10$ % solid

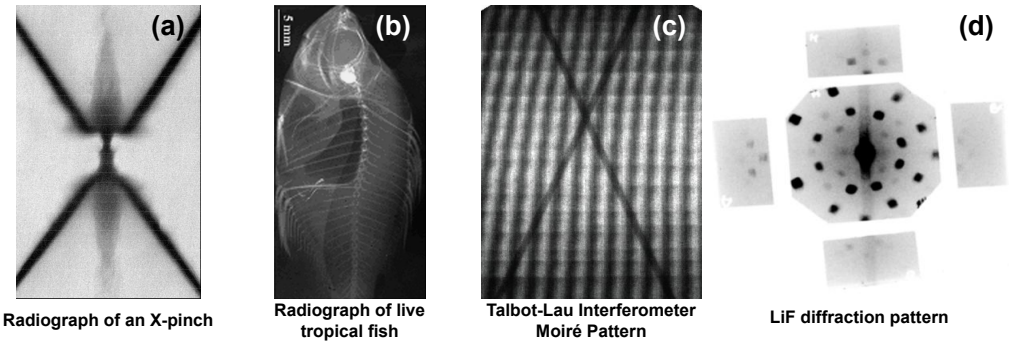

Figure 1.4: An example of four different applications of the X-pinch (all produced using X-pinches). a) Radiograph of a dynamic, dense plasma (another X-pinch) from Ref. [8]. b) Radiograph of a live tropical fish from Ref. [9]. c) A Moiré pattern produced by a Talbot-Lau interferometer of another X-pinch. [65] d) An X-ray diffraction pattern of an LiF crystal from Ref. [10].

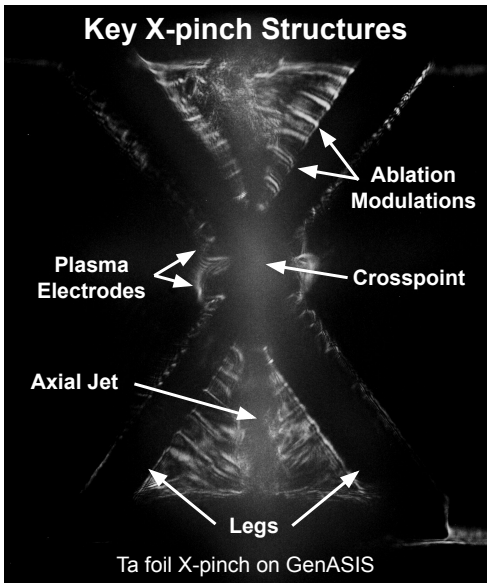

Figure 1.5: A schlieren image of a tantalum foil X-pinch on GenASIS with key macroscopic features labeled.

density) plasma [8, 14, 68–70]. Subsequently, electron beams may form across the gap created in the micro z-pinch immediately post-pinch [71–76]. The basic structures of an X-pinch are labelled in a schleiren image of a tantalum laser-cut foil X-pinch shown in Fig. 1.5

1.3.1 A Review of X-pinch Experiments

The first X-pinch experiments were published in 1982 by Zakharov *et al.* (Ref. [58]), demonstrating their ability to harness the peak plasma parameters of the Z-pinch at a single location (the crosspoint), and in the nearly four decades since their inception X-pinches have been studied on drivers with currents ranging from 25 - 5000 kA and current rise times ranging from 30 - 1200 ns, and at facilities on four different continents.

It is generally accepted that 1 kA/ns is the minimum current rise-rate required to produce micron or sub-micron sized sources [77], and it has been mathematically demonstrated that the magnitude of the current has a strong inverse relation with the minimum source size [70]. Despite this, a number of slow-rising and/or low-current experiments have produced small and fast X-ray sources.

Numerous X-pinch experiments using sub-kA/ns current drivers demonstrated the ability to produce sources with sizes on the order of 10 μm [78–80] and $\sim$ 10 ns pulse widths [81]. The slowest-rising of these, at $\sim$ 0.04 kA/ns were also the lowest current X-pinches the authors are aware of, at 25 kA peak current [81]. Though it was not determined whether the emission emanated from a 'hot' pinch or an electron-beam generated source, these results suggested that even a small capacitive discharge machine can produce sources from an X-pinch, which, given the simplicity of such a driver only increases the versatility of the X-pinch. Slow-rise experiments also include a particularly unique configuration, the 'gas X-pinch,' composed of an annular nozzle driving gas to focus at a point, conducted at 250 kA peak current with a rise of 1000 ns [82].

A handful of faster-rising, low-current drivers have also produced small, bright sources [83–86]. A 40 kA, 30 ns 'Tabletop' generator proved that such a small-scale driver could create

quality x-pinches, with sources measuring $\geq$ 5 μm [83]—a feat previously deemed impossible. X-pinches on this driver also showed that increasing the number of wires in an X-pinch improved source reproducibility [85]. Experiments using an 80 kA peak current, 40 ns rise time generator demonstrated $\geq$ 2 μm sources that produced high-quality radiographs of plastic and foam spheres representing inertial confinement capsules, demonstrating a potential practical application of the X-pinch [84].

Numerous current generators occupy the 'mid-scale' parameter-space between 100 and 300 kA with 100 - 300 ns rise-times, including the GenASIS driver at UC San Diego used for the work in this manuscript (200 kA, 150 ns, described in Sec. 3.1). Experiments on these machines have produced micron-scale X-pinch sources using a variety of materials (most commonly Mo) and wire numbers. The majority of these, especially historically, utilized a Marx-bank type driver (which discharges capacitors in series, creating large voltages but requiring significantly more stored-energy per kA out) coupled with a pulse-forming line and a spark gap, making them fairly high inductance and ideal for driving X-pinches. These experiments typically produced nanosecond (or subnanosecond) and micron-scale pulses [87–91]. Some experiments with sub-nanosecond temporal resolution at 200 kA/ 100 ns showed X-pinches producing two sub-nanosecond pulses within 0.5 ns of one another [92]. A handful of lower-inductance LTD type drivers (including GenASIS)—which though not as suited for driving high inductance, pinching loads are far more efficient in terms of stored energy per kA out—produce X-pinches parametrically similar to those on the Marx-driven machines of the same current and rise-times [10, 93–96]. Carbon fiber X-pinches on GenASIS produced 25 μm, 15 - 20 ns sources, showing the potential for low-Z materials to create small and fast soft X-ray sources [97].

Comparable in peak current and rise time to the mid-scale drivers just described, a number of larger current generators have fielded X-pinches on current returns, meaning an X-pinch is substituted in place of one of the number of solid posts (often 4 to 8 of them) that current flows through after passing through the target load [67, 98–101]. For example, in a 1000 kA/100 ns current

driver, a return current X-pinch could receive 250 - 125 kA (for 4 or 8 return paths respectively), also over a 100 ns rise. This allows concurrent driving of an X-pinch adjacent to another target array driven by the full current, and enables a self-contained dynamic X-ray radiography setup, with no need for an external current driver or laser to produce sources. Radiographs produced from these experiments have illuminated much about the obscured evolution of the dense cores at the center of an exploding wire experiment [47]. In one experiment on the 1000 kA, 100 ns rise-time Cobra driver at Cornell, five current-return Mo X-pinches, each with a different linear mass to control their pinch time, produced a five radiograph time sequence of a collapsing W wire-array Z-pinch [67]. A number of experiments at Cornell university have also driven parallel X-pinches, (both on the main current circuit, rather than a current return X in series) producing highly spatially and temporally resolved radiographs of X-pinch crosspoint dynamics (see Figs. 1.4a and 2.5) [8].

Dedicated X-pinch experiments on larger current drivers, ranging from 400 kA to 6 MA, produced varied quality of X-ray sources, but also excellent electron beam studies, and new and novel configurations. Some of the earliest X-pinch experiments were conducted on the 3000 kA/150 ns BLACKJACK 5 pulser, showing that a 6-wire Ti X-pinch K-shell flux double that of 2-wire Ti X-pinches, and comparable to that from single-wire or cylindrical Ti Z-pinch arrays [102] (though how much of that was due to electron beam remains undetermined). The smallest and shortest X-pinch X-ray pulses the authors are aware of come from experiments using one of the fastest rising, shortest rise-time pulsers: the XP generator (450 kA/ 50 ns, ~ 9 kA/ns) at Cornell [66, 69]. A shunt wire used in parallel to an X-pinch at 800 kA reduced the number of second sources in the X-pinch, providing an alternate path in the circuit for current post-pinching [103]. At such large currents, the linear mass of the X-pinch array needs to be relatively large in order to pinch at or near peak current, requiring larger wires or more wires. This increases the radius and complexity of the structure at or near the crosspoint, typically leading to less reliable micro Z-pinch formation at the crosspoint. Nested wire X-pinches on Cobra, which

involved involved large numbers of carefully arranged wires demonstrated the ability to tailor the wire X-pinch for high-current machines and improve source reliability [104]. A number of X-pinch experiments on the 1000-2000 kA, 100 ns Zebra machine have focused on characterizing the electron-beam driven hard X-ray sources that often follow the hot pinch source in X-pinches [75]. To date, the highest current X-pinch was a solid, machined target (as opposed to fine wires) done at 5000 kA on the Saturn generator [105], which was a predecessor to the hybrid X-pinch discussed in depth later in this work.

Many other works have explored X-pinch properties using various materials, wire numbers, peak currents, and current rise rates. An extensive—but by no means comprehensive—list of pulsed-power facilities used to field X-pinches and their key results is shown in Table 1.1. Another extensive table may be found in Table 1, on page 294 of Ref. [106]).

Table 1.1: An extensive, but by no means comprehensive list of X-pinch experiments at different facilities, and some of their key parameters. Experiments with similar configurations on the same machine are not listed twice, but references are given in the 'Additional Notes' column. The order of the X-pinch experiments is *approximately* chronological, from first publication date found of the listed type of X-pinch experiments at said facility (year of publication in parenthesis).

Facility, Generator	**Peak Current, Rise time**	**X-pinch Type**	**Pulse Width**	**Source Size**	**Additional Notes**
Lebedev Physical Institute, DON	120 kA, 35 ns	Mo Wires	Unk.	$\leq$50 µm	First X-pinch experiments. (1982) [58].
Cornell University, LION	470 kA, 80 ns FWHM	Al wires	Unk.	Unk.	Experiments demonstrating X-pinch applicability to lithography. (1989). [62, 107].
Maxwell Labs, Blackjack 5	3000 kA, 150 ns	Ti wires	7 - 10 ns	Unk.	Showed 6-wire X's produced more flux than 2 wire X's, or single wire Z-pinches. (1990) [102].

Continued on next page

Table 1.1 – List of different X-pinch experiments and key results – continued from previous page

Facility, Generator	Peak Current, Rise time	X-pinch Type	Pulse Width	Source Size	Additional Notes
Naval Research Lab, Gamble II	800 kA, 60 ns FWHM	Al wires	Unk.	Unk.	Developed current vs K-shell yield scaling for X-pinches from LION to GAMBLE II. (1990) [62].
Imperial College, Blacket Laboratory	300 kA, 1200 ns	Al, Const., W wires	$\geq$10 ns	$\sim$50 µm	Early 'slow'-rise (<1kA/ns) X-pinch experiments. (1991) [78, 79]
Lebedev Physical Institute, BIN	200 kA, 100 ns	Mg to W wires (many materials)	>5 ns.	>20 µm	Thorough early characterization of micro Z-pinch and hot-spot development. (1996) [87].
Cornell University: XP	500 kA, 45 ns	Wire, Hybrid X's (many materials)	0.01 ns	1 µm	Among fastest rising currents used for any sort of X. Produced best sources in wire X's. (1997) [68, 72, 77]
Pontificia Universidad Catòlica de Chile, Gepopu	100 kA, 130 ns	Al wires	6 - 8 ns	Unk.	Excellent laser interferometry analysis of Al X-pinches. (2000) [88]
Imperial College, MAGPIE	350 kA, 240 ns	Al, Mo wires	<1 ns	1-5 µm	In current return-1 of four posts, so $\sim$350 kA through X. (2001) [98]
Pontificia Universidad Catòlica de Chile, Llampüdkeñ.	400 kA, 260 ns	Al wires	2.5 ns	<5 µm	(2002) [108, 109]
Nevada Terawatt Facility, Zebra	1000-2000 kA, 100 ns	Wires	$\sim$1 ns	$\leq$30 µm	Many thorough X-pinch electron-beam studies done on Zebra. (2001). [74]
Troitsk Inst. for Innovative and Thermonuclear Research, Angara-5-1	300-400 kA, 90 ns	Mo Wires	$\leq$2 ns	$\leq$2 µm	X-pinches on return posts. Driver operates at up to 5MA. (2002) [99]

Continued on next page

Table 1.1 – List of different X-pinch experiments and key results – continued from previous page

Facility, Generator	Peak Current, Rise time	X-pinch Type	Pulse Width	Source Size	Additional Notes
Imperial College	40 kA, 30 ns	W wires	≤10 ns	≤10 µm	Showed X-pinches can produce µm and ns scale sources at very low currents. (2003) [83]
Ecole Polytechnique	250 kA, 180 ns	Mo wires	1.5 - 2 ns	50 - 100 µm	Compact driver with similar current and rise parameters to GenASIS. (2004) [89]
Imperial College, IMP	160 kA, 80 ns	Al, Mo wires	Unk.	Unk.	Study on the formation of the axial jets. (2006) [110]
Institute of High Current Electronics, Tomsk	220 kA, 145 ns	Ni Wires	<5ns	<5 µm.	Pre-GenASIS driver cavity without power feed. (2006) [93]
UC San Diego X-pinch Pulser	80 kA, 40 ns	Al, Mo, W wires	≤10 ns	≤2 µm	Used to characterize sample ICF capsules. (2006) [84]
Cornell University, COBRA	1000 kA, 100 ns	Multi-wire, Nested, Many materials	≤10 ns	3 µm	Many multiwire X-pinch. Multiwire nested X's showed brighter flux than standard wire X's. (2006) [104]
Cornell University, COBRA	250 kA, 100 ns	Mo wires	<1 ns	7 µm	Multiple return-post X-pinches on a 1000 kA machine of different masses for different timings. (2006) [67, 100]
Florida A&M	320 kA, 1000 ns	Al, Ti, Const., W Wires	≤10 ns	≤10 µm	Smallest slow-rise (<1 kA/ns) sources. (2008) [80]
Russian Research Centre Kurchatov Institute	2300 kA, 150 ns	Mo, W Wires	2 ns	≤20 µm	Fairly high-current, multiwire X-pinch experiments. (2008) [111]
Tsinghua University, PPG-1	200 kA, 100 ns	Mo Wires	≤1.2 ns	≥5 µm	Showed two sub-nanosecond X-ray pulses separated by ∼ 0.5 ns. (2008) [92]

Continued on next page

Table 1.1 – List of different X-pinch experiments and key results – continued from previous page

Facility, Generator	Peak Current, Rise time	X-pinch Type	Pulse Width	Source Size	Additional Notes
UC San Diego: GenASIS	200 kA, 150 ns	C, Cu W wires	15-20 ns 2 ns	$\sim$25 µm $\leq$ 5 µm	Soft X-ray point sources with low-Z C. Nanosecond, micron-scale Cu sources. (2009) [14, 97]
Cornell University: XP	500 kA, 45 ns	Hybrid X's (many materials)	1 ns	1.5 µm	First successful hybrid X-pinch experiments. (2010) [90, 112]
Institute of Fluid Physics, CAEP, YANG	800 kA, 150 ns	Ti, Mo Wires	0.2 ns	19 µm	Use of a shunt seems to increase single-peak X-pinch performance. (2010) [103]
Institute of High Current Electronics, Tomsk	215 kA, 200 ns	W Wires	1-2 ns	$\sim$ µms	Actually called a PZ-pinch. Used electrode configuration to pinch a plasma jet. (2010) [113]
Lebedev Physical Institute, SPAS	300 kA, 200 ns	Mo, W Wires	$\sim$1 ns.	2.5 - 4 µm	First results with SPAS. No beam source observed. (2010) [95].
Tsinghua University QiangGuang-1	350 kA, 60 ns	Mo Wires	2 ns	30 µm	Return-post X-pinches. First LTD X-pinch experiments the authors found. (2011) [101]
Tsinghua University	100 kA, 100 ns	Al, W Wires	3 ns	10 µm	Small LTD data published just after Ref. [101]. (2011) [94]
Tsinghua University, PPG-2	100 kA, 60 ns	Mo, W Wires	Unk.	5 µm	Compact current driver. (2012) [114]
Sandia National Laboratory: Saturn	6000 kA, 60 ns	Solid Hybrid	2 ns	$\sim$5 µm	Highest current X-pinches found. 90 GW, 0.35 kJ peak yields. (2012) [105]
Lebedev Physical Institute, BIN	270 kA, 100 ns	Hybrid Xs	$\leq$1-2 ns	Unk.	Variable brightness in Mo HXPs. (2012) [90]

Continued on next page

Table 1.1 – List of different X-pinch experiments and key results – continued from previous page

Facility, Generator	Peak Current, Rise time	X-pinch Type	Pulse Width	Source Size	Additional Notes
Lebedev Physical Institute, MINI	260 kA, 170 ns	Hybrid Xs	∼1 ns	∼1 µm	4-6 mJ soft X-ray emission. Closest driver parameters used on HXPs to those on GenASIS used in this manuscript. (2012) [90]
Cornell University, COBRA	1000 kA, 100 ns	Mo, W Hybrid	1 ns	1.6 µm	Largest current hybrid X-pinches. Brighter but more variable than nested X's on the same machine. (2012) [90]
Tsinghua University QiangGuang-1	1400 kA, 60 ns	Mo Wires	1 ns	Unk.	Large, multiwire Mo X-pinches with careful spectroscopic analysis. (2013) [115, 116]
Troitsk Institute for Innovation and Fusion Research	250 kA, 1000 ns	Gas-puff	3-5 ns	100 µm	First Gas-puff 'X'-pinch found (2013) [82]
Institute of High Current Electronics, Siberia	140 kA, 110 ns	Mo Wires	2-3.5 ns	≤5 µm	(2013) [91]
UC San Diego: X-pinch Pulser	25 kA, 400 ns	W wires	≥10 ns	Unk.	Slowest rising X-pinch experiments found. Still produce ns-order X-ray pulses (2013) [81]
UC San Diego: GenASIS	200 kA, 150 ns	W, Ta, Cu foil Xs	1-3 ns	≤5 µm	New laser-cut foil X-pinch configuration(2014) [13, 14]
CEA, DAM, GRAMAT, Blackett Laboratory	300 kA, 400 ns	Mo Wires	≤2 ns	30 µm	Generator is based on a single stage of a larger LTD. (2015) [10]
Idaho State University	200 kA, 200 ns	Mo Wires	2-3 ns	12-22 µm	New, compact current driver based on LTD brick design. (2017) [96]

Continued on next page

Table 1.1 – List of different X-pinch experiments and key results – continued from previous page

Facility, Generator	Peak Current, Rise time	X-pinch Type	Pulse Width	Source Size	Additional Notes
Imperial College, Nene	50 kA, 50 ns	Hybrid, Wire Xs	$\leq$1 ns	$\sim$3 μm	Recent Low-current wire and hybrid X-pinch experiments with comparable parameters to similar experiments. (2018) [86]

1.3.2 Limitations of the X-pinch and Potential Improvements

This wealth of experiments clearly demonstrates the capability of the X-pinch as an X-ray source, but room for improving the array remains. One area for improvement involves eliminating the electron beam hard X-ray source, which though potentially desirable for radiographing dense and/or 'wet' biological objects that are $\geq$ 50 - 100 μm in size and temporally static over timescales of $\geq$ 10 - 50 ns, tend to doubly expose or wash out the shorter, smaller (and typically softer) hot-pinch source (see Sec. 2.4.4) [9, 95, 117, 118]. The X-pinch also exhibits a degree of variability in its hot-pinch source, including jitter in the timing ($\geq$ 5 - 10 % of the current rise) [101, 119], source location (along the length of the micro Z-pinch, or $\sim$ a few hundred μm) [8], and number of sources [8, 14, 90, 97, 120]. Some of this variability, especially the timing jitter, is attributable to the variability of the driver current pulse, and some lies in the nature of the emission—that is, a source resulting from the development of an instability (see Secs. 2.3.1, 2.3.2, and 2.4.3) [70, 77, 119, 121]. A few experiments with wire X-pinches have suppressed the aforementioned limitations, including increasing the wire number, carefully nesting multiwire X's, and adding a shunt wire adjacent to the X-pinch, though the latter two references are most appropriate for larger current drivers [85, 103, 104]. Tailoring the linear mass of the X-pinch array to the driver in use lies at the root of the success of these X-pinch modifications, and is likely the key parameter in producing a single, high energy X-ray pulse [77, 118]. In the past decade, studies showed two improvements to the classic wire X-pinch array that enable control of the mass and

shape of the target at the crosspoint, appear to improve reproducibility, minimize the electron beam, and can potentially scale to most current drivers: Hybrid X-pinches (HXP) [90, 112, 122–124] and Laser-Cut Foil X-pinches (LCXP) [13, 14].

Hybrid X-pinches

Hybrid X-pinches (HXPs) consist of a pair of conical electrodes connected by a wire or capillary [90, 112, 122, 123] in place of the longer twisted wires of the traditional wire X-pinch (WXP). An illustrated side by side comparison of the wire and hybrid setups is given in figure 1.6a and b. Current flows through one conical electrode, through the connecting wire, and into the other conical electrode. The conical electrodes are large enough not to experience ablative Ohmic heating, however the 'crosspoint' wire ablates just as a wire in the single wire Z-pinch. A cold plasma forms on the surfaces of the conical electrodes from exposure to intense UV radiation produced by the exploding crosspoint wire, and the rate at which this cold plasma expands from the surfaces of the conical electrodes nearest the crosspoint determines their separation—typically about 1 - 3 mm [112]. If this gap is too small, the electrode plasma from each side will connect and shunt current away from the connecting wire or capillary thus preventing a pinch. If the gap is too large, the likelihood of multiple sources increases dramatically.

The HXP was developed by some of the original X-pinch creators and promoters (including S. A. Pikuz who coauthored the first X-pinch paper found in Ref. [58] and wrote the topical review on X-pinches found in Ref. [106]) bringing a wealth of experience and knowledge to their development. Experiments have tested HXPs on a variety of drivers from low current (50 kA, 50 ns) to high current and extreme rise-rate (500 kA, 45 ns) machines [86, 90]. On all of the platforms tested, HXPs produce ~ 1 μm, ≤ 1 ns sources with a much higher incidence of single sources than WXPs due largely to the cold plasma from the conical electrodes closing the gap post-pinch before an electron beam can form. HXPs on lower-current, longer rise-time (> 100 ns) experiments showed lower soft X-ray (SXR, ~ 1 kev) emission than comparable WXPs [90],

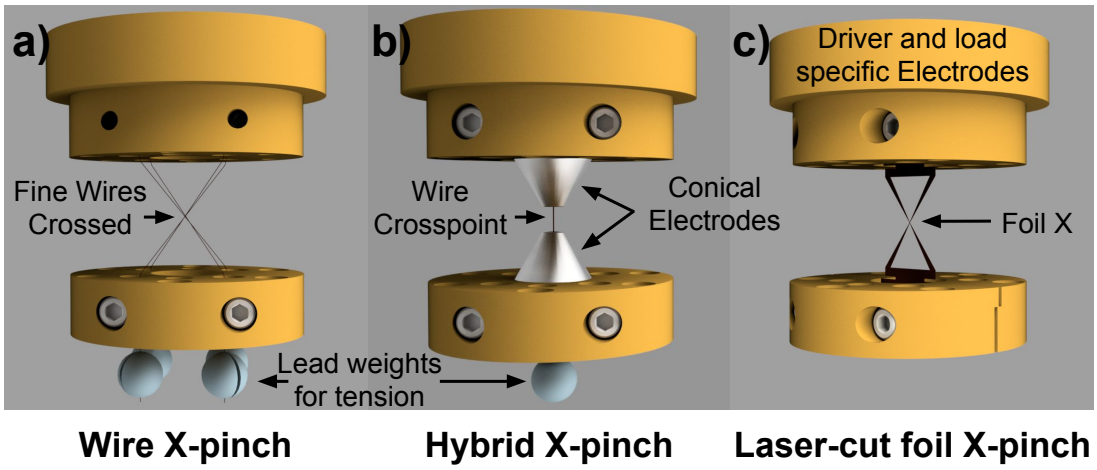

Figure 1.6: Computer aided design (CAD) illustrations of a) four-wire, b) hybrid, and c) laser-cut X-pinch setups with key features labelled. The specific electrodes and configurations here are for the GenASIS pulser at UCSD, but the general setup is similar across most current drivers.

while HXPs on shorter rise-time ($\leq$ 100 ns) generators produced comparable amounts of SXRs to traditional WXPs.

Being made from a single wire (or capillary, etc), the simplicity of the HXP 'crosspoint' makes it significantly easier to load than a wire X-pinch, and as a result, very reproducible from shot to shot (as opposed to twisting wires into contact). The HXP easily facilitates mass-matching by either increasing or decreasing the diameter of the crosspoint wire, which can be further aided by changing the conical electrode spacing. HXPs present the opportunity to pinch virually any material. Along with various metallic wire crosspoints, HXPs using twisted wires, metal tubes containing wires, plastic tubes filled with salts, wires coated in molten sulfur, and even low-density gas in the crosspoint region have all been pinched with varied success regarding source size, quantity, and flux [122]. They have also been tested in series using different materials to produce multiple high resolution sources at different energies. To date, HXPs have demonstrated comparable or superior performance to WXPs, and a noteworthy absence of a second harder X-ray pulse from an electron-beam (especially on the slower rising drivers) also improves their viability as a point source for backlighting.

Laser cut foil X-pinches

Independently, during the nascent stages of HXP studies (circa 2011), development began on the Laser-cut X-pinch, an X cut from thin metal foils using either a marking or cutting laser in collaboration between UC San Diego and General Atomics Inc [13, 125, 126]. This dissertation focuses on the development and testing of the LCXP in detail in later chapters.

As with the HXP, the appeal of the laser-cut foil was initially the ability to specifically tailor the linear mass both at the cross-point to control pinch timing relative to the driver current rise and adjacent to the crosspoint to control post-pinch expansion of the plasma electrodes to close the gap immediately and reduce the likelihood of an e-beam post-pinch, as well as to manufacture a reliable crosspoint configuration from shot to shot. To date, limited experiments characterizing these LCXPs have produced nanosecond pulse-width and micron-order source sizes in the soft ($\sim$ 1 keV) and hard ($\sim$ 8 keV) X-ray range [14]. Different shapes at the cross-point were tested producing mixed results. Ultimately, a simple angle in and out of the cross-point region produced the most reliable results, and the pinch outcome appeared generally insensitive to microscopic ($\sim$ 10 μm) features introduced near the cross-point from the laser cutting process. Spectroscopic analysis of Cu LCXPs showed two sources — one hot ($\sim$ 1 keV) temperature, dense ($n_i = 10^{22}$ cm^{-3}) plasma, and the other from fast electrons hitting a colder, few-hundred eV, lower density plasma, but these two sources were indistinguishable spatially (within 200 μm of one another) and temporally (within $\sim$ 1-3 ns). This indicated that the plasma pinched, and immediately formed an electron beam across the gap formed in the micro Z-pinch. Then the considerable mass of the plasma electrodes (see Fig. 1.5) closed the gap and prohibited any further electron beam formation.

The ability to chose a thin foil and change the cross-point width from one target to the next makes pinch timing optimization quite simple, and plans to electroplate or vapor-deposit more exotic materials to increase the spectral range of the LCXP also exist. Drawbacks include the general fragility of the foil X, which demands a sharp learning curve during loading, and access to

a laser-cutting platform, though these are becoming readily more available.

1.4 Outline of the Thesis

This dissertation covers our efforts to improve the X-pinch and thoroughly characterize the X-ray sources from the different configurations in search of the ideal pinch. This work was done on the 150 ns rise-time, 200 kA GenASIS driver at UC San Diego [127]: a relatively small-scale driver by pulsed-power standards. However, drivers of this scale are growing more common, some built with the express purpose of driving X-pinches as a source for other experiments [10, 96]. Additionally, as 100-200 ns rise-time, 1000 kA linear-transformer drivers (LTDs) grow more common [128–130], GenASIS scales well to the parameters of a return-post X-pinch ($\sim$ 4-8 return posts) on these drivers [67, 98, 99].

The remainder of this dissertation is arranged as follows. Chapter 2 covers X-pinch and Z-pinch physics. Chapter 3 details the GenASIS driver and the diagnostic tools employed during our experiments. In chapter 4 we discuss the development and optimization of LCXPs on GenASIS. We then optimize HXPs on GenASIS in chapter 5 in order to complete a thorough direct comparison between traditional wire, laser-cut, and hybrid X-pinches on a single driver. Chapter 6 summarizes the work and the conclusions drawn from it.

Chapter 2

Z-pinch and X-pinch Theory

A majority of the physics governing the X-pinch are actually identical to, or derived from Z-pinch physics, since the former is merely a modification to the latter. As such, we begin by introducing Z-pinch physics, and then discuss processes more specific to (though certainly not exclusive to) X-pinches. First though, a quick review of the magnetohydrodynamic (MHD) system of equations is warranted.

2.1 The Magnetohydrodynamic (MHD) Equations

Throughout the prior sections of this dissertation, we have superficially named terms, pressures, and forces to describe the behavior of a plasma, which is by no means a simple subject. Plasma involves the movement of large numbers of particles as in a typical statistical mechanics problem and adds in a layer of complexity — the interactions of charged particles and their collective behaviour in electromagnetic fields. Because of this, describing a plasma generally requires making approximations or simplifications.

There are two common approaches to describing a plasma: kinetic, and magnetohydrodynamic (MHD). The former involves using some form of the Boltzmann Equation, which gives the statistical behaviour of a non-equilibrium thermodynamic system. Modified to account only for

electromagnetic forces, the Boltzmann equation is written as (in MKS units)

$$\frac{\partial f}{\partial t} + v \cdot \nabla f + \frac{q}{m}(E + v \times B) \cdot \frac{\partial f}{\partial v} = \left(\frac{\partial f}{\partial t}\right)_c, \tag{2.1}$$

where $f = f(r, v, t)$ is a distribution function of particle position (r), velocity (v), and time (t), F is the sum of forces acting on the particles, m is particle mass, where q is charge, E is the electric field, and B, and the right hand side (RHS) of the equation is a collision operator relating how f changes in time with collisions [131]. This may be simplified by neglecting collisions to arrive at the well known Vlasov equation [132]. While accurate, this approach is complicated (with or without collisions), and as the number of particles in the plasma grows larger, becomes infeasible, even for a computer.

However, given that the integral of f over all velocities v is simply the particle number density n, one can retrieve bulk fluid equations by taking the moments of the Boltzmann equation—that is to say, integrating over dv—in order to get a more macroscopic description of the plasma.

Integrating Eq. 2.1 over dv, one gets the continuity equation:

$$\frac{\partial n}{\partial t} + \nabla \cdot (nu) = 0, \tag{2.2}$$

where u is the fluid velocity. This simply states that mass in the system is conserved, and that the change in mass per unit time relates to the movement of mass into and out of the system.

Mutiplying Eq. 2.1 by mv and integrating over dv, produces the next moment of the Boltzmann Eq:

$$mn\left[\frac{du}{dt} + (u \cdot \nabla)u\right] = qn(E + u \times B) - \nabla \cdot P + \mathscr{P}_{ij}. \tag{2.3}$$

Here, the P in $\nabla \cdot P$ is a pressure stress tensor arising from the thermal velocity component of the velocity, v, and $\mathscr{P}_{ij}$ is a term describing the change of momentum due to collisions between species i and j. To extract pressure from the stress tensor, we know that pressure is a scalar,

p, representing isotropic expansive stress, contained in P as pI where I is the identity tensor. Neglecting other stresses, and using tensor identities, we get that $\nabla \cdot pI$ gives ∇p.

Another moment, by multiplying by $1/2mvv$ and integrating over dv, gives an equation describing the flow of energy, but for our purposes, it lies outside the scope of our descriptions of the plasma.

Equations 2.2, and 2.3 are fluid equations of motion for a plasma. Reasonably, the fluid equations only apply to a plasma if the plasma behaves as a fluid, which is determined using the localization parameter, $\delta_{loc} = \lambda_{mfp}/l$, where λ_{mfp} is the collisional mean free path between particles (which changes dramatically for ion-ion, ion-electron, and electron-electron collisions, the longest λ_{mfp} being between ions, and so is typically the one considered here) and l is the plasma scale length. If $\delta_{loc} \ll 1$, then collisions occur frequently enough for the particles in the plasma to be considered 'localized' and treated as a fluid [133]. Since a plasma has at the very least (when assuming a plasma of only one element and constant ionization) an electron and an ion fluid, this means that any description of the plasma requires two of each fluid equation, which we mark with a subscript e or i, as in n_e or n_i for electron and ion density respectively. Taking each individual fluid and combining them linearly (addition or subtraction), we obtain what are referred to as the single fluid MHD, or magnetohydrodynamic equations [131, 134].

After some algebra, one arrives at the set of MHD equations (all in MKS units):

$$\text{Mass Continuity:} \quad \frac{\partial \rho}{\partial t} + \nabla \cdot (\rho v) = 0, \tag{2.4}$$

$$\text{Charge Continuity:} \quad \frac{\partial \sigma}{\partial t} + \nabla \cdot (J) = 0, \tag{2.5}$$

$$\text{Momentum:} \quad \rho \frac{\partial v}{\partial t} = J \times B - \nabla p, \tag{2.6}$$

$$\text{Ohm's Law:} \quad E + v \times B = \eta J + \frac{J \times B - \nabla p_e}{en}, \tag{2.7}$$

$$\text{No magnetic monopoles:} \quad \nabla \cdot B = 0, \tag{2.8}$$

$$\text{Faraday's Law:} \quad \nabla \times E = -\frac{\partial B}{\partial t}, \tag{2.9}$$

and

$$\text{Ampere's Law:} \quad \nabla \times B = \mu_0 J. \tag{2.10}$$

In these equations, $\boldsymbol{v}$ is the fluid velocity ($\approx \boldsymbol{v}_{\mathbf{ion}}$), ρ is the mass density ($\sim n_i m_i$), σ is the charge density, η is resistivity, and μ_0 is the permeability of free space. The set of equations is usually closed by relatiting pressure to density, $p = nk_bT$. All of the equations here are in MKS units. Note that the momentum equation (Eq. 2.6) often contains a ρg (where g is gravity) term that we have neglected. The $J \times B$ term in Ohm's Law is the Hall term, which, along with ∇p_e is often neglected, shortening Ohm's law to simply ηJ on the right-hand side.

Despite the number of assumptions and simplifications made en route to obtaining the MHD equations, they serve as an effective means for describing many plasmas (generally including those created for this dissertation) — specifically, those fulfilling the requirements that: length scales are much longer than the ion-ion mean free path, ion skin depth, and Larmor radius, and time scales are much longer than the i-i collision time, ion gyration time and the inverse plasma frequency).

2.2 Z-pinch Stability

2.2.1 The Bennett Relation

Perhaps the best place to begin a discussion on Z-pinch stability is the Bennett Relation, derived by W. H. Bennett in 1934 to express the relationship between the thermal and magnetic pressures in a stream of charged particles (which though not directly referring to the magnetic confinement of a plasma, neatly extends to Z-pinches). Bennett's Relation assumes a fairly special case of plasma: one that is in equilibrium ($\partial/\partial t = 0$), and has no viscosity ($\nu = 0$) or gravity. The steady-state form of Eq. 2.6, reads

$$\nabla p = J \times B. \tag{2.11}$$

To satisfy Eq. 2.11, J and B must be orthogonal to the pressure gradient. In the case of a Z-pinch, current lines lie in the axial direction (J_z) enclosed by azimuthally symmetrical magnetic field lines (B_θ), so ∇p is in the radial direction. From this follows a radial pressure balance:

$$\frac{\partial p}{\partial r} = -J_z B_\theta. \tag{2.12}$$

Here, the p is the plasma thermal pressure, p_T,

$$p_T = n_i k_B (Z^* T_e + T_i), \quad (kg \cdot m^{-1} \cdot s^{-2}) \tag{2.13}$$

where k_B is Boltzmann's Constant, Z^* is the average ionic charge, and T_e and T_i are the electron and ion temperatures respectively. $J_z B_\theta$ is the is the derivative of the magnetic pressure,

$$p_B = \frac{B^2}{2\mu_0}, \quad (kg \cdot m^{-1} \cdot s^{-2}) \tag{2.14}$$

which results in

$$-J_z B_\theta = \frac{\mu_0 I^2}{4\pi^2 r^3}. \tag{2.15}$$

One final quantity required to derive Bennett's relation is the ion line density, N_i, given by:

$$N_i = \int_0^a 2\pi r n_i dr, \tag{2.16}$$

where r is the radius variable, a is the radius of the plasma column, and n_i is the ion number density. Substituting N_i into Eq. 2.13 and then taking the partial derivative with respect to r, results in

$$\frac{\partial p}{\partial r} = \frac{2N_i k_b (Z^* T_e + T_i)}{\pi r^3}. \tag{2.17}$$

Plugging 2.15 and 2.17 into 2.12 produces the Bennett Relation,

$$8\pi N_i k_B (Z^* T_e + T_i) = \mu_0 I^2. \quad \text{(mks units)} \tag{2.18}$$

Though a simplistic model, the Bennett Relation establishes a basic description for a plasma in pressure equilibrium, giving the current required to confine a stable plasma with a given N_i and T. It contains no explicit radial dependence, but implies that any temperature changes in a pinch in pressure equilibrium will cause a change in pinch radius to satisfy the relation at that given current.

2.2.2 The Pease-Braginskii Current

Two decades later, in the late 1950's, R. S. Pease [135] and S. I. Braginskii [136] (independently) added a layer of complexity to the Bennett Relation, incorporating the power deposited through Joule heating,

$$p_J \propto I^2 R, \tag{2.19}$$

where R is the resistance in Ω, and the power radiated through bremsstrahlung radiation. A current exists where these two powers balance, aptly named the Pease-Braginskii current, (I_{PB}).

Taking Eq. 2.19, we replace R with the Spitzer resistivity η_s, which is the plasma resistivity transverse to the magnetic field given by:

$$\eta_s \approx \frac{\pi e^2 m_e^{1/2} Z^* ln\Lambda}{(4\pi\varepsilon_0)^2 (k_B T_e)^{3/2}}, \quad (\Omega \cdot m) \tag{2.20}$$

where e is the fundamental charge, m_e is the electron mass (kg), $ln\Lambda$ is the Coulomb logarithm, and T_e is the electron temperature in eV. To determine the power deposited via Joule heating per unit length, we divide by the cross sectional area of the pinch to obtain:

$$P_J = \frac{I^2 \eta_s}{\pi a^2}, \tag{2.21}$$

where P_J is given in W/m, and a is the radius of the pinch.

Bremsstrahlung radiation (literally German for braking radiation) is a form of 'radiative cooling' that occurs when free electrons experience some change in velocity from an interaction with an ion and give off a photon (more on this in Sec. 2.5). This quantity is a bit more complicated. Often, as is developed in references [135] and [137], the power radiated through brehsstrahlung, P_b, is calculated for hydrogen, which is not accurate for the Cu X-pinches presented in this dissertation. However, to develop the concept, we will follow the typically published route.

The power lost through bremsstrahlung radiation per unit length is given by

$$P_b = R_b Z^{*3} n_i^2 (k_B T_e)^{1/2} \left(\pi a^2\right), \quad (W/m) \tag{2.22}$$

where R_b is the brehmsstralung constant, and a is the pinch radius [138,139]. After a bit of algebra, in which we set the ratio of P_b to P_J to one, plug in a modified form of Eq. 2.18 where we assume T_e=T_i such that

$$8\pi N_i k_B T(Z^* + 1) = \mu_0 I^2, \tag{2.23}$$

and solving for I, we get the Pease-Braganskii current, I_{PB}. Using R_b from Ref. [138], I_{PB} for a hydrogen plasma is written

$$I_{PB} \approx 0.499 \frac{(Z^* + 1)}{2Z^*} (ln\Lambda)^{1/2}. \quad (MA) \tag{2.24}$$

At currents greater than I_{PB}, a steady-state Z-pinch collapses, while at lower currents, a pinch expands. Pease's work originally applied to gas cylinder Z-pinches, and though acknowledging the number assumptions made for reasons of mathematical simplicity and "lack of information on the relevant physical phenomena" [135], suggested given a sufficient current to overcome wall effects (recall that this plays a role in gas Z-pinches in a container), that a moderately sized current should be able to achieve conditions appropriate for thermonuclear fusion. In fact, given the plasma conditions taken in to account, Pease suggested that *if* one could bring a plasma to a steady state, then any current beyond 1 MA would exceed equilibrium conditions and cause a collapse.

2.3 Z-Pinch Instabilities and Collapse

While the physics discussed in Section 2.2 describe pressure balances and equilibrium states, actually realizing a true steady state in a plasma proves difficult with the constant and inherent presence of inhomogeneities in the plasma. For Z-pinch inertial confinement fusion efforts, suppressing instabilities is key to increasing X-ray yield and increasing temperature, hence the methods of increasing liner symmetry, decreasing implosion time, or adding axial magnetic fields discussed in section 1.2. Particularly important for Z-pinch experiments are the MHD m=0 'sausage', and m=1 'kink' (and more recently, m=2 'helical' [54, 140]) instabilities, where m refers to the azimuthal order of symmetry.

2.3.1 MHD instabilities

A simple way to introduce these instabilities is to look at an expanded form of the MHD momentum equation (Eq. 2.6). To expand it, we substitute Ampere's Law (Eq. 2.10) into $J \times B$ to get

$$J \times B = \frac{1}{\mu_0}(\nabla \times B) \times B = \frac{1}{\mu_0}\left((B \cdot \nabla)B - \frac{1}{2}\nabla B^2)\right), \tag{2.25}$$

so that the the steady-state version of Eq. 2.6 becomes

$$\nabla p = \frac{1}{\mu_0}\left((B \cdot \nabla)B - \frac{1}{2}\nabla B^2)\right). \tag{2.26}$$

Here, the first term to the right of the equal sign pertains to tension along the magnetic fields lines, and the second is the familiar magnetic pressure, the two of which are in opposition to one another. For the simplest case, in the event that m=0, and $B = (0, B_\theta, 0)$ (there is no axial or radial magnetic field component), vector calculus shows only the magnetic pressure term opposing the thermal pressure in the r direction. The picture grows slightly more complicated when m=1, and/or there is a B_z component, which in many terms act in opposition to B_θ

The m=0 case is illustrated in Fig. 2.1, which shows a time-integrated eXtreme Ultra-Violet pinhole camera image of a single-wire Z-pinch (actually the crosspoint of a Hybrid X-pinch, see Sec. 1.3.2 and Fig. 1.6b). If a region of a Z-pinch is perturbed in the $-r$ direction (towards the axis), that area of the plasma possesses a greater p_B since $B \propto 1/r$. If the plasma is incompressible (as is assumed in Eq. 2.26), this constriction will squeeze the plasma axially into the adjacent regions ($\pm z$), which will then expand outwards where they experience less p_B. If, in the constricted region, the plasma beta is less than 1 ($p_T/p_B < 1$), then the region contracts further, enhancing the instability. Thus, the m=0 instability comprises a set of necks and bulges like a strand of sausages, hence the colloquial name.

The growth rate, γ_{m0}, of the m=0 instability is given by the Alfvén transit time [141], which

is the ratio of the Z-pinch radius r, to the Alfvén velocity v_A,

$$\gamma_{m0} = \frac{r}{v_A}. \tag{2.27}$$

The Alfvén velocity, given by $v_A = B/\sqrt{\mu_0 n_i m_i}$, describes the propagation velocity of a plasma wave caused by the restoring movement of magnetic field lines, which if perturbed in an ideal MHD plasma return to their original positions as if under tension.

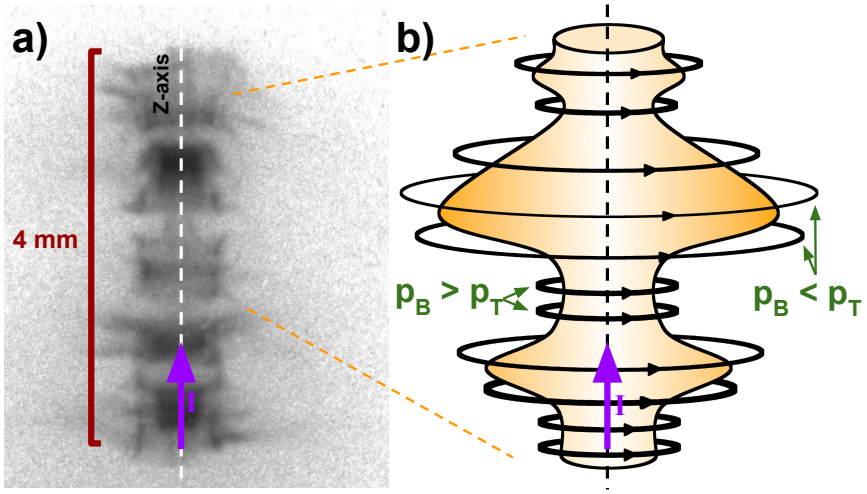

Figure 2.1: a) A time-integrated eXtreme Ultra-Violet pinhole camera image of a single-wire Z-pinch (actually the crosspoint of a Hybrid X-pinch, see Sec. 1.3.2 and Fig. 1.6b) with developed m=0 'sausage' instabilities. b) An illustration of the m=0 instabilities with magnetic field lines superimposed to highlight areas of higher or lower magnetic confinement.

In the case of m=1, where the instability has one order of azimuthal symmetry, the perturbation may drive the plasma column away from the axis of symmetry. This is shown in Fig. 2.2, which shows a gated XUV image of a gas puff Z-pinch with m=1 instabilities (a), and an approximate illustration of the pinch with sample magnetic field lines (b). As is seen in Fig 2.2b, where the plasma is perturbed off of the axis there is an 'inside' and an 'outside' to the displacement. In the inside, the magnetic field lines bunch together, creating a region of higher magnetic pressure, while on the opposite edge of the column, the field lines are more spread out, and here, p_B may again drop below p_T, causing further bulging out. This bunching and bulging

leads to a plasma looking like a kinked hose, thus it is colloquially named the 'kink' instability.

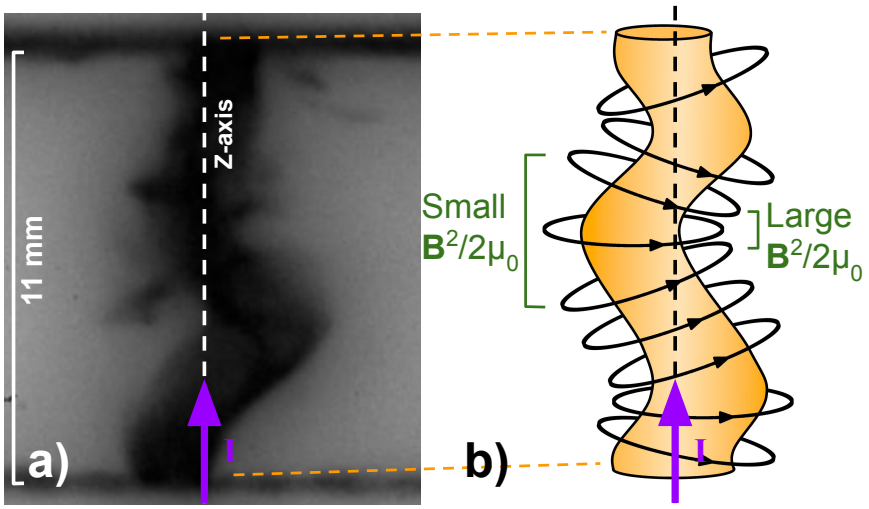

Figure 2.2: a) A gated XUV image of a gas puff Z-pinch showing m=1 kink instabilities. b) An illustration of the m=1 instabilities with magnetic field lines superimposed to highlight areas of higher or lower magnetic confinement.

2.3.2 Radiative Collapse

Recall that when $I > I_{PB}$, a Z-pinch contracts due to the dominance of p_B over p_T as radiation losses begin to cool the plasma faster than joule heating can heat it (see Sec. 2.2.2). Should the appropriate conditions exist, this contraction may result in a radiative 'collapse', which is generally thought to occur at the location of an MHD m=0 necking [70]. Shearer developed this concept of radiative collapse in 1976, equating the PdV work a circuit does per unit length on a pinch, P_w, to $P_J - P_b$, and calculating a radial growth rate using this difference [137]. This starts with with:

$$P_w = \frac{I^2}{2\pi r^2}\frac{d}{dt}\left(\pi r^2\right) = P_J - P_b. \tag{2.28}$$

By rearranging Eq. (2.28), we get the equation of motion for the radius:

$$\frac{1}{r}\frac{dr}{dt} = \frac{1}{I^2}\left(P_J - P_b\right). \tag{2.29}$$

After some rearranging, Eq. (2.29) rewrites as:

$$\frac{1}{r}\frac{dr}{dt} = \frac{P_b}{I^2}\left(\frac{P_J}{P_b} - 1\right), \tag{2.30}$$

which now visibly contains the relationship for the Pease-Braginskii current. Rewriting Equation (2.30) with the Pease-Braginskii current, Shearer defined the radial growth (γ_R), which is positive for increases in radius and negative for decreases in radius:

$$\gamma_R \equiv \frac{1}{r}\frac{dr}{dt} = \frac{3}{4}\frac{1}{\tau_r}\left[\left(\frac{I_{PB}}{I}\right)^2 - 1\right], \tag{2.31}$$

where τ_r gives the characteristic loss time for the bremsstrahlung radiation, given as:

$$\tau_r = \frac{3N_i k_B T_i}{P_b} = \frac{3}{4}\left(\frac{I^2}{P_b}\right). \tag{2.32}$$

The growth rate in Eq. (2.31) is positive when the current begins to increase, depositing energy into the plasma via Joule heating and raising the thermal pressure. When the current surpasses I_{PB}, brehmsstrahlung radiation losses begin to dominate, and the plasma cools. This radiating away of energy decreases the thermal pressure of the plasma, resulting in a reduction in radius due to the magnetic pressure, which increases more as a function of decreasing radius (and as the current continues to rise above I_{PB}, though for the timescales of this collapse, I is effectively constant). In Eq. (2.22), we see that P_b increases with ${n_e}^2$, which will increase as the radius decreases, further accelerating the contraction of the plasma. This collapse must occur on a timescale faster than instability growth times, given by $1/\gamma_R \leq st_a$, where t_a is the acoustic bounce time given by $t_a = a/c_s$ where C_s is the ion sound speed, and s is a stability parameter, relating to the growth of instabilities ($\sim$ 10 - 100 for Z-pinches) [137].

In an ideal case, radiative collapse continues until the plasma reached such a density that electromagnetic radiation released via brehmsstrahlung cannot escape (it has become opaque),

thus decreasing P_b and increasing I_{PB}. Chittenden *et al.* used a similar form of the power balance used by Shearer to find the minimum collapse radius, at which the plasma becomes opaque, and the power emitted from this pinch [70, 142]. For this, the blackbody radiated power per unit length is given by $P_{bb} = \sigma T_R^4 \pi r^2$, where σ is the Stefan-Boltzmann constant, and T_R is the blackbody radiation temperature. To allow further simplification, substitutions were made to simplify the algebra, setting $T_R = \beta T_e$, $Z^* = f T_e^{1/2}$, and simplifying Bennett's relation in Eq. 2.18 to include only T_e, assuming $Z^* \gg 1$. Here β and f establish the proper ratio for their respective quantites. Setting P_{bb} equal to Joule heating from Eq. 2.19, and substituting in both Bennett's relation and the other ratios for T_R and Z^*, one can solve for the minimum collapse radius, occurring when $P_{bb} = P_J$:

$$r = 2.3 \times 10^{-18} \frac{f^{13/9} N_i^{10/9} ln\Lambda^{1/3}}{I^{14/9} \beta^{4/3}}, \quad (m) \tag{2.33}$$

and for the power emitted:

$$P = 6.7 \times 10^{22} \frac{I^{34/9} \beta^{8/3} ln\Lambda^{1/3}}{f^{11/9} N_i^{-14/9}}. \quad (W/m) \tag{2.34}$$

2.3.3 Anomalous Resistivity and Collapse Termination

As the radius in Eq. 2.33 trends towards zero, the density, $n_i = N_i/(\pi r^2)$, approaches infinity. In reality, other processes will interrupt this trend such as the development of instabilities that bring about the onset of significant resistivity, where called anomalous resistivity (a sort of blanket term given to non-Spitzer resistivity), that raises P_J, and increases I_{PB} [70, 138, 143, 144].

Plasmas are prone to the development of micro-instabilities when the electron drift velocity, v_d, reaches or exceeds some critical velocity—typically the ion sound speed, c_s [145]. These micro-instabilities then grow and produce a turbulent electromagnetic—or electrostatic—wave [146, 147]. The scattering of drifting electrons from this wave can exceed the scattering caused by Coulomb collisions with ions, thus generating this so-called 'anomalous' resistivity.

We may write current in terms of the electron drift velocity, v_d, as [148]

$$I = -Z^* N_i e v_d, . \tag{2.35}$$

Still presuming to be in a Bennett Equilibrium, we combine Eq. 2.35 with the Bennett relation, (Eq. 2.18), to get

$$8\pi k_B (Z^* T_e + T_i) = \mu_0 Z^{*2} N_i e^2 v_d^2. \tag{2.36}$$

Setting $v_d = c_s$, written as:

$$v_d^2 = c_s^2 \approx \frac{k_b (Z^* T_e + T_i)}{m_i}, \tag{2.37}$$

we see that a specific $N_i \approx N_{crit}$ satisfies this relation. By combining Equation (2.37) with Equation (2.36) when $T_e \approx T_i$, and solving for N_{crit} we get:

$$N_{crit} = \frac{8\pi m_i}{\mu_o e^2 Z^2} \approx 1.3 \times 10^{18} \frac{A}{Z^{*2}}, (m^{-1}) \tag{2.38}$$

where A is the atomic mass in AMU. Thus, this theoretically limiting ion line density in Z-pinches relates only to the mass and ionization level of the ions.

The lower hybrid drift instability is considered one of the most likely instabilities to create anomalous resistivity in Z-pinches since it arises when electron drift velocities and the current are orthogonal to the magnetic field (as in a Z-pinch), has a rapid growth rate, and is driven by current as well as gradients in density, temperature, and **B**-field. The lower hybrid frequency describes oscillations of a plasma wave that occur when an electrostatic ion wave with wavenumber $\boldsymbol{k}$ is perpendicular to $\boldsymbol{B_0}$ (the current-induced magnetic field, which in our case is $\boldsymbol{B}_\vartheta$). The dispersion relation for this wave is

$$\omega_L^2 = \Omega_c \omega_c, \tag{2.39}$$

where Ω_c is the ion cyclotron frequency and ω_c is the electron cyclotron frequency [131]. The growth timescale of the lower-hybrid-instability is of the order of ω_L, and as such, this instability can arise on the order of picoseconds (dependent, of course, on the plasma conditions) [145]. The electrons gyrate around an elliptical orbit in the r-z plane. In the presence of a density gradient, when the v_d exceeds c_s, the diamagnetic drift can create small charge separations (positive at one end, negative at the other) along the major axis of the elliptical orbit (in the r direction), resulting in an electrostatic wave. When scattering from this exceeds that from Coulomb interactions, this anomalous resistivity replaces the Spitzer component of Eq. 2.21, and increases I_{PB}, terminating collapse. This anomalous resistivity dramatically heats the plasma, causing rapid radial expansion of the plasma and a redirection of the current on a timescale of picoseconds. More thorough development of the effects of the onset of the lower-hybrid drift instability, anomalous resistivity, and their effects on z-pinches may be found in Refs [145–147].

2.4 X-pinch Physics

Having established some of the key physics and processes occurring in Z-pinches (of which the X-pinch is merely a specialized category), we begin examining processes more specific-to (though not exclusive-to) the X-pinch. As mentioned in the beginning of Sec. 1.3, the X-pinch evolves through a number of steps, which are generally invariant to their specific configuration: 1 - explosion and ablation, 2 - micro Z-pinch formation, 3 - pinch collapse and X-ray emission, and 4 - gap closure or electron beam generation and hard X-ray emission. These steps are highlighted in Fig. 2.3, which shows 4 different schlieren images of laser-cut foil X-pinches at the 4 different stages of evolution described with key features labelled. For this reason, we will introduce the X-pinch dynamics in this order.

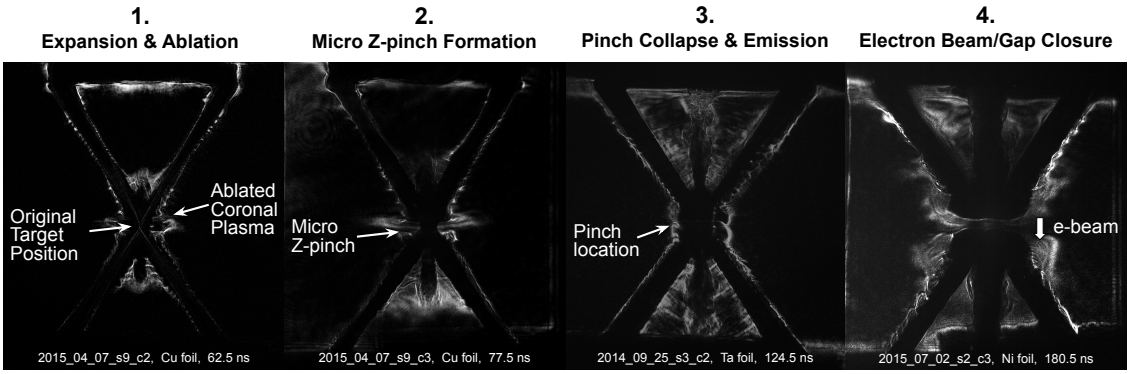

Figure 2.3: Frames a-d show schlieren images of different foil X-pinches from different materials at the four stages discussed at the beginnning of Ch. 2. Key features are labelled in each frame. In frame 1, the position of the original target (from the schlieren background image) is shown. Note the minimal ablation where the target is largest. Frame 2 is from the same shot as frame 1, 15 ns later, and clearly shows the cylindrical micro Z-pinch forming at the crosspoint. Frame 3 is shortly after emission from that particular target, and shows the crosspoint region collapsed and closed. Frame 4 comes from an image much later in time, of an under-massed array with a gap clearly formed where the micro Z-pinch cleared away. The material and time relative to current start (all shots were done on the $\sim$ 150 ns rise-time GenASIS driver) are marked at the bottom.

2.4.1 Initial Target Explosion and Ablation

While the various Z-pinch experiments may employ gas puffs, gas liners, gas capillaries, metallic liners, or fine wires on or around the z-axis (see Sec. 1.2), X-pinch experiments almost exclusively utilize fine wires, (the initial physics of which also applies to the thin metallic foils of the laser-cut X-pinch, see Sec. 1.3.2). When subjected to a fast-rising current a fine wire experiences significant Joule or 'Ohmic' heating (Eq. 2.19) to the point where mass ablates off of the surface of the wire (see Fig 2.3-1) [149, 150]. This results in a distinct coaxial structure comprised of a cold ($\leq$ 10 eV), dense wire core surrounded by a low density, hotter ($\geq$ 10 eV) coronal plasma [3, 45–47]. The exact spatial and temporal characteristics of an exploding wire depend on the wire material, wire diameter, and driver parameters, but radiography of the wire cores showed that they were a boiling liquid, appearing as a foam distinctly filled with bubbles [47]. The core's foam structure is resistant to current flow, so the current shunts over to the lower impedance and lower resistivity coronal plasma when the latter reaches a sufficient

Table 2.1: Order-of-magnitude parameters of the different X-pinch parameters. References for some of the parameters are given. Note that the parameters depend on material and current drive, and so include a larger range in reality, but central ranges are given here. No density or temperature is given for the electron beam, since the beam is composed of fast, non-thermal electrons that strikes a plasma with conditions comparable to either the micro Z-pinch or the corona, and the density could refer to either the micro Z-pinch/corona or beam density.

Component	**Scale** (m)	**Duration** (s)	**Temp.** (eV)	**Density** (ions/m^{-3})	**Refs.**
Core	10^{-5}-10^{-4}	10^{-7}	1-10	10^{28}	[47]
Corona	10^{-4}-10^{-3}	10^{-7}	10	10^{24}-10^{26}	[47, 69]
Micro Z-pinch	10^{-4}-10^{-3}	10^{-7}	10^{1}-10^{2}	10^{25}-10^{27}	[72, 151]
Hot Spot	10^{-6}-10^{-5}	$\leq 10^{-9}$	10^{3}	10^{27}-10^{28}	[14, 68]
Electron Beam	10^{-4}	10^{-8}	NA	NA	[14, 71]

density. This effectively halts the ablation of the core due to Joule heating—radiation and/or compression heating from the coronal plasma are the primary drivers of core ablation past this point. Order-of-magnitude parameters for the core and corona found in X-pinches are given in Table 2.1.

The evolution of the corona is shown in Fig. 2.4, which shows a shadowgram time sequence of a 4 mm long, 25 μm Cu Z-pinch (which is actually the crosspoint of a Cu hybrid X-pinch, see Sec. 1.3.2 and Fig. 1.6b). Figure 2.4a shows a background (pre-shot) image of the array, while Fig. 2.4b-d were taken during the current pulse, with current and times relative to 10% of peak current (which is considered 0 time) given below each frame. The development of MHD M=0 instabilities, covered in section 2.3.1 is visible in 2.4d.

Given sufficient current, the coronal plasma is magnetically confined near the wire by the $\mathbf{J} \times \mathbf{B}_{\text{local}}$, which occurs at the crosspoint of the X, where $\mathbf{B}_{\text{local}}$ and $\mathbf{B}_{\text{global}}$ are synonymous, and often at the ends of the X, where $\mathbf{B}_{\text{global}}$ is smallest. However, in regions where there are multiple wires and sufficient $\mathbf{J} \times \mathbf{B}_{\text{global}}$, some of the coronal plasma is driven inwards towards the axis in quasi-periodic ablation streams, seen in Figs. 2.3-3, and 1.5 [152–156]. The wavelength of these streams (the space between them) decreases with atomic number [5], grows increasingly random as the ratio of $\mathbf{B}_{\text{local}}$ to $\mathbf{B}_{\text{global}}$ increases, and is generally insensitive to features etched into

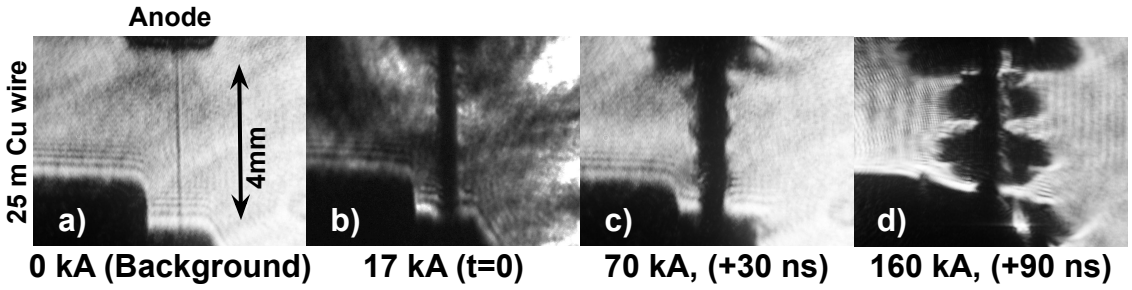

Figure 2.4: Shadowgrams of a 4 mm long 25μm Cu wire Z-pinch (actually the crosspoint of an hybrid X-pinch, see Sec. 1.3.2 and Fig. 1.6b). a) A background image of the array. b) An early current figure at $\sim$ 10% peak current considered t=0). c-d) 30 and 90 ns later of the same array showing the expansion of the corona and the development of characteristic instabilities.

the wire [154, 156]. These streams feed the axial Z-pinch in cylindrical wire arrays, and counter propagating axial jets in X-pinches.

These axial jets, if allowed (if they are not blocked by a driver electrode) can propagate several jet-radii beyond the region where the coronal plasma from the wires feeds them, with a Mach number ($\mathscr{M}$) of 5 - 10 (T $\sim$ 10 eV). Studies indicated that the jets may provide a scalable tool for laboratory-based study of astrophysical jets [133, 157–159]. Perhaps more importantly to the functioning of the X-pinch, these axial jets carry mass away from the thin 'micro' z-pinch that develops at the center of the X.

2.4.2 Pinch formation

The X-pinch was intentionally designed to create a localized maximum $\mathbf{J} \times \mathbf{B}$ at a single location—the crosspoint—where all of the current (regardless of wire-number or configuration) flows through, and the radius is at a minimum. Here, the micro Z-pinch forms (also often referred to as a mini-diode), measuring up to several hundred μm long, and a few hundred μm wide [69], visible in Fig. 2.3-2. It is flanked on either end by comparatively large parallel surfaces (orthogonal to the axis of the micro Z-pinch) we will refer to throughout as plasma electrodes (also visible in Fig. 2.3-2). Parameters for the micro Z-pinch are given in table 2.1.

For a significant portion of the current rise, the micro Z-pinch exists in a state of relative

equilibrium, likely satisfying the Bennett Relation (Eq. 2.18). Using Eq. 2.18 and referring to the parameter values for the micro Z-pinch found in table 2.1, one finds that a $T_e = T_i = 10$ - 100 eV plasma with $n_i = 10^{25}$ ions/m^{-3} and a radius of ~ 0.5 mm (estimated from Fig. 2.3-2), can be confined by a current of 5 - 100 kA, which is easily in the range of most current drivers discussed in Sec. 1.3.1. Using the values specifically from Ref. [14] (X-pinches on UC San Diego's GenASIS driver), we see that the current required to balance a Cu plasma ($Z^* \sim 13$) in this region is ≥ 80 kA, which is about the I_{rms} of GenASIS.

2.4.3 Collapse and Thermal X-ray Emission in an X-pinch

Ultimately, the micro Z-pinch develops strong instabilities, described in section 2.3.1, that lead to localized collapse and X-ray emission. Cursory calculations of the growth rate of an m=0 instability using values of the corona or micro Z-pinch from table 2.1 show that for Cu plasmas at currents around 100 kA (an order-of-magnitude approximation for GenASIS at UC San Diego) $\gamma_{m0} \approx$ 1-10 ns, which easily applies to the experiments presented as the focus of this dissertation. Thus, at the location of the m=0 instability, provided that the driver exceeds I_{PB} (see Sec. 2.2.2), radiative collapse begins (see Sec. 2.3.2), and proceeds until it terminates due to opacity and/or anomalous resistivity.

Recall that in Sec. 2.3.3, we introduced the lower-hybrid-drift instability as a potential mechanism for the development of anomalous resistivity. The growth timescale of this instability is of the order of ω_L (see Eq. 2.39). The ion and electron cylcotron frequencies in a micro Z-pinch on GenASIS exceed 10^9 and 10^{12} Hz respectively, thus one can see how this instability arises adequately quickly [145] — on the order of picoseconds for a micro Z-pinch. The role of anomalous resistivity in X-pinches was simulated using the MHD code GORGON by Chittenden *et al.* in Ref. [70].

Applying the parameters from table 2.1, we find that N_{crit} for a $\sim$ keV Cu plasma (relevant to the work presented in Chs. 4 and 5) is $\sim 10^{17}$ ions/m, which, for a 1 - 10 μm source corresponds

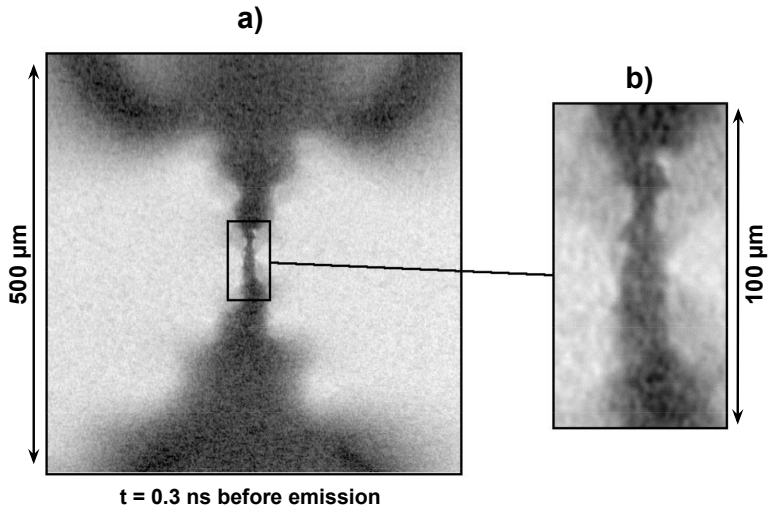

Figure 2.5: Radiographs of a wire X-pinch at two different levels of zoom from Ivanenkov *et al.* in Ref. [8], showing the multi-level collapse at the crosspoint of the X at 0.3 ns before emission time. The radiograph was taken using a parallel X-pinch discharged simultaneously with the one in the image.

to a density of $n_i \approx 10^{26}$ - 10^{28} ions/m^3.

This process of radiative collapse and termination may be seen in X-ray backlighting of X-pinches showing the micro Z-pinch cascading in a series of increasingly smaller micro Z-pinches up to ~ 5 times in less than a nanosecond, with the smallest having been measured as small as 3 µm across. One of these radiographs is reproduced from figure 5 of Ivanenkov *et al* (Ref. [8]) in Fig. 2.5 here, showing an image of the crosspoint of a wire X-pinch at 0.3 ns prior to emission (the radiograph was created using a parallel X-pinch).

2.4.4 Electron beam generated sources

The generation of fast electrons in X-pinches is well documented [71–76], and can feasibly occur at two points in time near the crosspoint: near collapse termination, and post-pinch as the micro Z-pinch clears out. The emission from this fast-electron or electron beam ('e-beam') generated source (or sources) is characteristic of fast electrons interacting with a plasma colder than the thermal, or 'hot' pinch source [106, 160]. E-beam generated sources have been observed

since the early stages of Z-pinch studies (recall Anderson's observations about neutrons from a pinch in Ref. [31]), but is uniquely localized (along with the hot pinch) in the X-pinch, making it easier to isolate and observe, and potentially either useful (see Refs. [9, 117]), or able to be suppressed as is one of the goals for both the hybrid and laser-cut foil X-pinches (see Sec. 1.3.2). The e-beam generated source has been studied in many X-pinch experiments, including but not limited to Refs. [71, 72, 74–76, 117, 161]. Despite all of these studies, considerable uncertainty remains regarding its actual formation in Z and X-pinches [147].

M. G. Haines, in Ref. [147], puts forth a number of potential kinetic mechanisms for generating runaway electrons in Z- (and micro Z-) pinches, and while most of these generally lie outside of the scope of this dissertation one has potential relevance, involving the generation of fast or 'runaway' electrons in the plasma even prior to breakup of the pinch.

Dreicer established a relationship to determine the minimum electric field, E_D, required to create runaway electrons in a plasma given by

$$E_{\mathrm{D}} = \frac{e l n \Lambda}{\lambda_D^{-2}} \propto \frac{Z^* n_i}{T_e}, \tag{2.40}$$

where λ_D is the Debye length [162, 163]. One can estimate the electric field across the hot-spot (or developing gap) as

$$E_{hs} = \frac{I \eta_s}{\pi r^2}, \tag{2.41}$$

where η_s is the Spitzer resistivity, and r is the hot-spot radius. When $E_{hs} \geq E_D$, runaway electrons may occur [147, 164]. Even a small fraction of fast electrons interacting with the micro Z-pinch or hot-spot can significantly change the X-ray spectrum emitted from the X-pinch [73].

More commonly, we focus on the generation of an e-beam after collapse of the micro Z-pinch and the formation of a gap, which opens on a timescale, t_c, of the order

$$t_c = \frac{\ell}{2 c_s} \tag{2.42}$$

where ℓ is the length of the micro Z-pinch and c_s is the ion sound speed. This is approximate, because in reality, experiments show that the material near the crosspoint is shocked post-pinch [8, 81].

The voltage across the micro Z-pinch and across the gap formed post-collapse and termination can be expressed as

$$V(t) = L\frac{dI}{dt} + I\left(\frac{dL}{dt} + R\right) \tag{2.43}$$

where V is voltage, L is inductance, and I is current and R is resistance. Regardless of the voltage applied by the current driver at the time of pinch, one can see how radiative collapse (Sec. 2.3.2) affects the L of the target via a rapid decrease in radius, the onset of anomalous resistivity (Sec. 2.3.3) introduces a significant R, and the increasing R and L and subsequent pinch termination can drive significant dI/dt, all of which can create considerable voltages in very short timescales. As a result, fast electrons accelerate across this newly formed gap and strike the opposing plasma electrode resulting in a source (or sources) composed largely of hard X-rays, ranging from material-specific K-shell emission up to $\sim$ 100 keV continuum [71–76].

Since e-beam photons are generated by fast electrons colliding with some region of the plasma, rather than a thermal source, the average photon energy emitted can be much higher than that found in the hot-pinch emission resulting from the collapse of the micro Z-pinch. In the case of Cu X-pinches (which are most relevant to this dissertation), emission of photons in the Cu K-shell range requires a plasma on the order of 1 keV in order to sufficiently ionize the plasma so that any significant numbers of transitions ending at n=1 may occur. However, the inner shell cross section for ionization due to electron impact for Cu grows exponentially at $\sim$ 8 keV, meaning that fast electrons above this energy can create conditions such that K-shell transitions may occur regardless of the ionization level (and as such, temperature) of the plasma [165]. Furthermore, while the intensity of K-shell emission may reach up to 10 % that of the L-shell emission from a hot pinch (see table 2.1), this drops by orders of magnitude at micro Z-pinch plasma conditions,

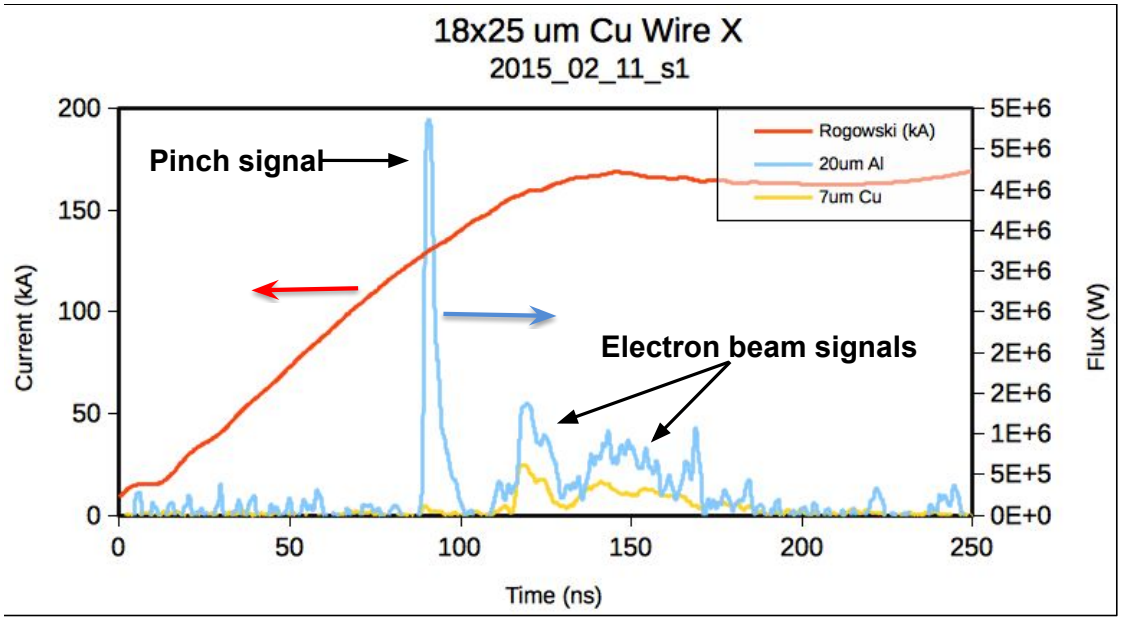

Figure 2.6: A sample set of X-ray diode traces from a 2-wire (18 x 25 µm) Cu X-pinch. The current (red line) is shown with scale on the left axis. The Al-filtered (blue) and Cu-filtered (yellow) diode signals show when X-rays were emitted. The first, narrow pulse is the pinch, comprised of predominantly soft (1-1.5 keV) X-ray emission, while the later, wider electron beam signals have a higher ratio of Cu:Al diode signals, indicating more hard (3 $\sim$ 9 keV) X-rays transmitting through the Cu diode. Note that the Al filter used transmits softer ($\sim$ 1 keV) photons, while the Cu filter blocks them.

and even lower in the coronal plasma. In contrast, at $\sim$ 10 keV electron energy, the ratios of ionization cross sections between K and L-shell in Cu are $\sim$ 0.1, and increase with electron energy [165]. This leads to a much higher ratio of K-shell to L-shell emission from e-beam generated sources than hot pinch sources. This is illustrated in Fig. 2.6, which shows diode signals from a Cu X-pinch (on GenASIS) for the Cu L-shell (light blue line) and the Cu K-shell (yellow line), where the high-flux, temporally narrow hot pinch signal includes a minimal hard X-ray component in contrast with the later e-beam signals labelled.

Since the emission is not localized to a dramatically collapsed Z-pinch, the source size ranges from 10 - >100 µm, and the signal lasts significantly longer, ranging from 2 - 20 ns (as is evident in the signals shown in Fig. 2.6). Even a small fraction of fast electrons can have a significant change on the spectra emitted from the X-pinch [73].

Sources caused by e-beams in X-pinches could serve as a hard X-ray source for low-magnification radiography (or radiography with the target object adjacent to the film) with dynamic spatial and temporal scales exceeding the size and duration of the e-beams, though this is difficult (especially in the typical wire X-pinches) because of their shot-to-shot variability in flux, source location, and number of sources. Hard X-ray (K-shell and up) radiography on the scales of the hot-pinch ($\sim$ μm and 1 ns) has typically been infeasible since though the hot-pinch does emit some hard X-rays, the long duration and large size of an e-beam source creates far more photons that tend to wash out or multiply expose the desired image.

2.5 A Brief Note on Photon Emission

Entire books, dissertations, and courses exist to describe the radiation emitted from plasmas, and the spectroscopic analysis of this radiation. Generally, this lies beyond the scope of this dissertation, but a short introduction to some basics of electromagnetic radiation from a plasma is warranted given that the key use of the X-pinch is its radiation, and we use various tools to observe and analyze said emission.

2.5.1 Three Types of Emission

When a free electron experiences acceleration or a bound electron undergoes a change in its quantum energy level, it emits a photon. The energy spectrum of these photons can provide information about the properties of the plasma, so measuring said spectrum is a useful tool. There are three main types of emission: bound-bound, bound-free, and free-free, the latter of which is the aforementioned bremsstrahlung radiation. Cartoon drawings of these three types of emission are given in Fig. 2.7 to accompany the subsequent text.

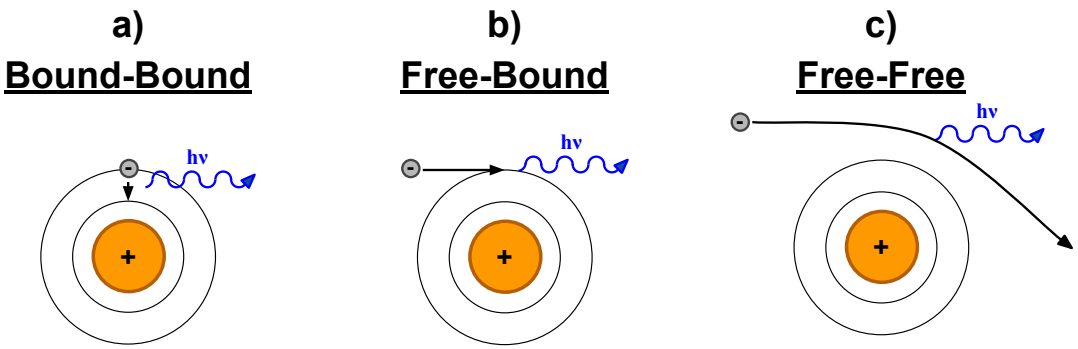

Figure 2.7: Cartoons of the three different types of emission: a) bound-bound, b) free-bound, and c) free-free. The ion is represented by an orange circle with a '+' sign with two orbitals, and the electron is denoted by a grey circle with a '-' sign. The resulting emission is labeled with a blue ν. The electron change in position is denoted by a black line and arrow

Bound-Bound Emission

Bound-bound radiation comes from an electron in an atom or ion moving from a higher to a lower energy level, and emitting a photon, as illustrated in Fig. 2.7a. The electron, being 'bound' to the atom at both ends of the transition, has a limited number of possible steps it can take, from one energy level to another. As such, the photon emitted from the electron is quantized, resulting in what is called 'line' emission, where each transition radiates a specific energy equal to the change in electron energy. When viewed with a spectrometer, which resolves the different photon energies emitted from a source (see Sec. 3.3.4), radiation from bound-bound transitions appears as lines of finite width.

To illustrate what spectra produced by this type of emission look like, simulated emissivities for a T_e = 1000 eV, $n_i = 10^{21} cm^{-3}$ Cu plasma are shown in Fig 2.8a (note that Cu is used for this example due to its later relevance in this dissertation), with the bound-bound emission shown by the purple line. The simulated spectra were created using the FLYCHK code (see sec. 3.3.4) [11]. In Fig. 2.8b, a crude illustration only showing principal quantum number levels approximately aligned with their respective energies in the x-axis of Fig. 2.8a shows key transitions and the relative energy of photons released from each transition.

Transitions to fill a vacancy in the lowest energy level (innermost orbital, principal quantum

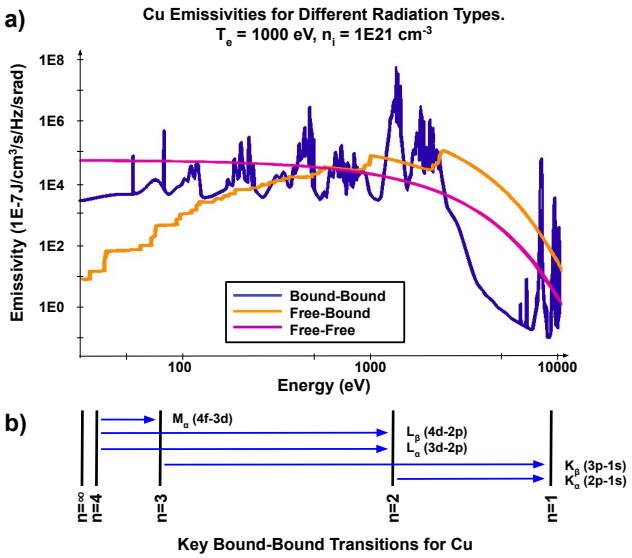

Figure 2.8: a) Simulated emissivities of bb, fb, and ff radiation for a T_e = 1000 eV, $n_i = 10^{21} cm^{-3}$ Cu plasma using the FLYCHK code [11]. b) A rough illustration of key transitions between principal quantum numbers placed approximately to scale with the energy of the plot axis in a) to illustrate the energy of bb line transitions or the locations of jumps in free-bound emission.

number n) are referred to as K-shell emission. The transition between n=2 and n=1 is called K_α (pronounced k-alpha) and the transition between n=3 and n=1 is called K_β. The K_α transition in a neutral atom is a benchmark energy, measuring $\sim$ 8050 eV in un-ionized Cu (note that since the spectroscopy done in this dissertation involves emission from Cu almost exclusively, much of the information given here will specifically refer to Cu). As the ionization level, Z^*, increases, the energy of the bound-bound transitions increases, with, for reference, a hydrogen-like Cu (one electron left) having a $K_\alpha \sim$ 8670 eV. This transition refered to as the Lyman-alpha, or Ly_α.

Free-Bound Emission

Also referred to as electron capture, free-bound emission occurs when a free electron falls into an orbital of an atom or ion, illustrated in Fig. 2.7b. Since the electron has no specified upper energy, this type of emission is a continuum source, meaning rather than radiating in distinct lines, it radiates as a generally smooth and continuous spectrum of radiation energies. However, given

that the final energy state does have a specific value, free-bound continuum experiences jumps where there are jumps in the ionization potential [166]. This is illustrated by the orange line in Fig. 2.8a, and involves electrons beyond the left side of figure 2.8b not in an orbital falling into one of the labelled orbitals.

Free-Free Emission (Bremsstrahlung)

As mentioned in section 2.2.2, bremsstrahlung means 'braking radiation', and refers to the emission from electrons interacting freely with ions. When an interaction occurs, and the electron is deflected, it radiates a photon, as illustrated in Fig. 2.7c. Assuming a smooth distribution of electron energies, this results in a smooth, continuous distribution of photons emitted, hence the term continuum emission. Free-free emission scales with, amongst other factors, the product of n_i and n_e, and Z^{*2} [166]. As the density and temperature of a plasma increase, bremsstrahlung becomes increasingly important, hence its consideration in I_{PB} (Sec. 2.2.2). The smooth profile of the bremsstrahlung radiation is clearly shown in the pink line in Fig. 2.8a.

Chapter 3

Driver and Diagnostics

3.1 The GenASIS Driver

GenASIS at UC San Diego — which stands for **Gen**erator for **A**blation **S**tructure and **I**mplosion **S**tudies — is a compact (1.2 m^2), low inductance pulsed-power generator that delivers 200 - 250 kA over a 150 ns (10-90%) rise time [15, 93, 127]. The bulk of the generator was developed at the Institute for High Current Electronics in Tomsk, Russia. Sandia National Laboratory studied and tested the driver, before loaning it to UC San Diego, where a power feed and vacuum chamber was designed to allow diagnostic access to plasma experiments.

A Linear Transformer Driver (LTD) type machine such as GenASIS represents a number of improvements over the traditionally used Marx bank driven systems (described later in Sec. 3.1.2). The overall footprint of GenASIS is much smaller than other drivers, as it requires no oil-filled capacitor banks, or water-filled pulse-forming lines to compress the current pulse. This is primarily due to the parallel discharge of many capacitors surrounding a central electrode which keeps the overall current path length small, keeping driver inductance, and consequently the driver rise time low. A number of larger (0.5 - 1 MA) LTDs are in development around the world, with data from them beginning to accrue [167–169].

GenASIS consists of a capacitor bank, multigap spark switches, a built-in Marx bank trigger, a coaxial conical power feed, and a vacuum chamber for the load, each portion of which will be discussed. Photographs of the assembled GenASIS driver from the bottom and top, and a side-on cutaway component illustration are given in Figure 3.1a,b and c respectively, and will serve as a reference for the description of the driver throughout Sec. 3.1.

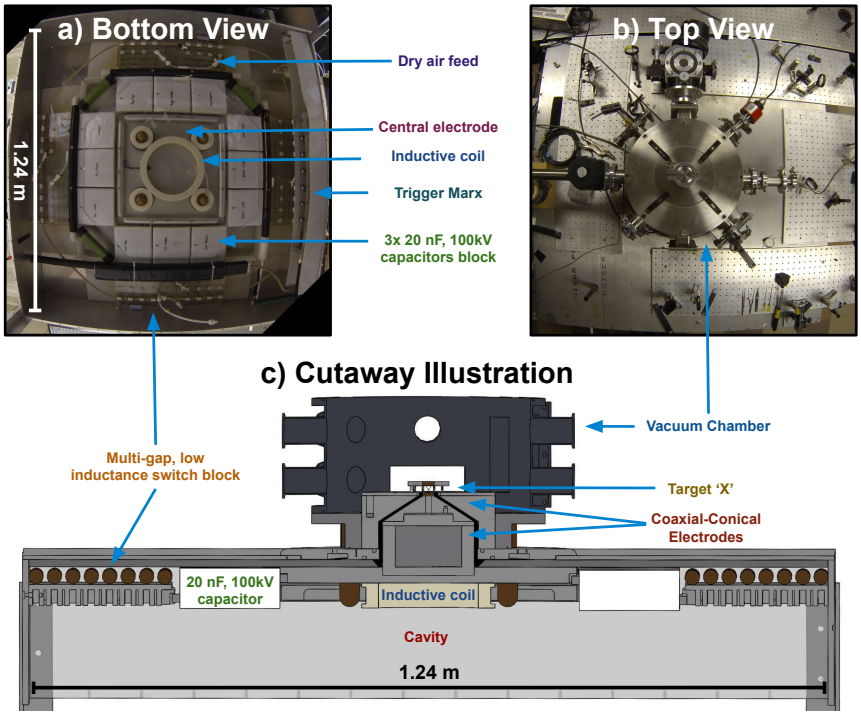

Figure 3.1: a) A photograph of the underside of the GenASIS cavity with many of the components visible and labeled. b) A photograph of the topside of the GenASIS cavity with its vacuum target chamber labeled. c) A side-on cutaway illustration of the GenASIS driver, with key components labeled.

3.1.1 The Capacitor and Switch-block Modules

Charge storage in GenASIS is comprised of 4 blocks of 3 double-ended General Atomics capacitors (model # 35404, 20 nF, 25nH, 0.2 Ω, 100 kV). Each capacitor block sits on a side of the ~ 1.2 m^2 square cavity. Each of the four blocks is coupled to a low-inductance multigap switch block, which consists of 8 rows of 8 x 22mm diameter spherical brass electrodes mounted onto an

acrylic plate. The spherical electrodes in each row are connected via a high-resistance (but still conductive) rubber cord to maintain equal potential. These switches are capacitively triggered by a trigger pulse which arrives at row 3 (from ground) of the electrodes in the switch block, and distorts the previously homogeneous voltage distribution across all of the switch gaps. The switch blocks are open to atmospheric air and during charging may have dry air blown through them which has shown over many shots to decrease the likelihood of self-breaking when nearing full charge. Each switch block/capacitor block comprises a module, which can relatively easily be removed for inspection, repair, or replacement. The modules could also be triggered individually if an appropriate trigger setup was developed.

While the capacitors in GenASIS have a maximum charge rating of 100kV, the configuration of the driver has a maximum charge of $\sim$ 80 kV. Given the open-air nature of these switches, the realistic maximum operating charge for GenASIS is $\sim$ 75 kV, as above this, accidental self-breakdown and subsequent prefires happen at an unacceptably high rate. The pre-fire rate at 75 kV is $\leq$ 5%, but at 72 - 73 kV, this drops to $\leq$ 2%. GenASIS is charged with a Glassman +100 kV power supply at a current of $\sim$ 1.3 - 1.6 mA. From 0 - 55 kV, the charging current is kept low, but slow (but audible) charge leakage at $\geq$ 55 kV requires more current to both reach 70 - 75 kV charge and decrease the liklihood of self-breakdown as the charge leakage in the driver begins to ionize air. The power supply and other connected electronics are protected from any voltage reversal from the driver by a chain of high voltage diodes (Glassman ADC-SNL series, 200 kV-rated) submerged in an oil barrel, which is the only oil used in the entire GenASIS system and is isolated from the rest of the components.

3.1.2 The Trigger System

GenASIS' trigger pulse is supplied by a small, traditional Marx bank built into the inside of the generator cavity. Marx banks are a relatively simple, commonly used system used to create a fast-rising, high voltage pulse, but require significantly more stored energy to achieve comparable

currents to an LTD. A Marx bank consists of a number of capacitors, connected by switches and resistors, charged in parallel to a voltage, V_{MC}, and discharged in series so the voltage adds. The trigger Marx in GenASIS is six stages, composed of TDK UHV-6A, 2.7nF, 30kV capacitors and 68 MΩ charging resistors. In GenASIS, the trigger Marx is charged in parallel with the main driver capactors via a voltage divider to $V_{MC} \leq 20$ kV (20 kV at 80 kV GenASIS charge). Each Marx stage is separated by self-breakdown switches of the same variety as the multigap switches: 22 mm diameter spheres. These spheres are mounted via threaded rod, allowing for simple adjustment of the gap in the event of breakdown troubles—ideally the breakdown voltage is appreciably higher than V_{MC}. The first switch is closed, via a thyratron in the case of GenASIS, which puts the first and second capacitor in series, meaning their voltage sums, and the voltage across the previously open second switch is then approximately double V_{MC}. This process cascades down across all of the gaps, discharging all of the capacitors in series, creating a single high-voltage pulse with a theoretical maximum of V_{MC} times the number of stages. In actuality, as typically used, the Marx delivers ≥ 70 kV in a 25 ns rise time to capacitively break the switches in the switch blocks.

A thyratron switch is used to break the first stage of the trigger marx. A thyratron is a high voltage gas switch (typically using deuterium), with heated grid electrodes allowing the switch to rapidly close and deliver a $\sim$ 20kV pulse to a trigger pin. The thyratron itself is triggered using an external 200V signal from a delay box.

3.1.3 The Coaxial Conical Power Feed

Each capacitor/switch block module is mounted to a large square central electrode with a solid aluminum bar. This square electrode is vacuum sealed to a $\sim$ 1 cm thick insulator, which is in turn sealed against the topside of the cavity with a large ground-side (anode) flange. This plate has a simple coil inductor mounted to it (rather than the ferrite or Metglas® cores used in larger Linear Transformer Driver (LTD) machines) to ensure that current flows through the load during relevant experimental timescales, as opposed to dumping straight to ground since the outside of

the current path is grounded.

A coaxial-conical power feed was developed in order to both best match the generator to a target load, and to raise the electrodes to a height where the target load could be viewed. At the center of the square aluminum plate, the cathode outer diameter (OD) used for the work described in Ref. [93] was $\sim$ 15 cm. Observations and advice indicated that an ideal target array diameter for a driver of GenASIS' parameters was $\sim$ 1.0 cm, so a $\sim$ 2 cm OD cathode would provide adequate space to load such a target array [167]. To reach these diameters, the aforementioned coaxial conical power feed with a constant electrode gap was built, consisting of $\sim$ 15 cm diameter coaxial cylinders to raise the target load, and then a conical section to reduce electrode diameters and raise the target load the final distance to diagnostic height.

The final coaxial conical cathode OD measures 20 mm in diameter, and has 12 x 0-80 threaded holes for mounting different experiment-specific cathodes. The gap between the anode and cathode was set to $\sim$ 4 mm, as this provided the experimentally determined minimum gap to avoid flashover across it. The anode assembly, which serves as the current return structure, includes an annular anode with OD = 7.5cm, and ID $\approx$ 25 mm, held 1 - 5 cm above the cathode by (typically) 4 current return posts that mount into the top of the anode portion of the coaxial conical electrodes. While the coaxial to conical to load setup used here is not the lowest-inductance configuration possible (as compared to a single, large conical feed), the simplicity of the cylindrical first segment much smaller conical segment allowed for in-house machining of the power feed, which reduces cost, and more importantly introduces additional experimental flexibility down the road. The specific load hardware and targets mounted into this hardware are discussed in Sec. 3.2.

3.1.4 The vacuum target chamber

The vacuum chamber of GenASIS is a 15 cm tall cylinder with a radius of 15 cm and two different rows of NW-40 flanges spaced at 90° apart, for a total of 8 ports. Alternating between these (at 90° spacing, and 45° relative to the NW ports) are 3 x 6 inch rectangular ports that can

have either large glass windows or other vacuum adaptors mounted to them. Two of these ports are vertically oriented (tall), and two are horizontally oriented (wide) and centered at the same height as the lower NW-40 ports. Above the large horizontal ports are two more NW-40 ports. This gives a total of 14 ports for diagnostic access. The arrays line up with the lower row of ports, and current monitor cables and vacuum gauges occupy the upper ports.

3.1.5 Current Monitors

While technically a diagnostic, the tools used to measure the current GenASIS produces are machined into the driver itself, and so are discussed here in the GenASIS section. The tools in question are called B-dots (from $\dot{B}$: the derivative of the magnetic field B with respect to time) which are simply grooves which serve as magnetic field pick-up loops. One of these B-dot grooves is machined into the anode flange adjacent to the insulator, and the other into the anode plate the current return posts mount to. These grooves monitor the voltage induced by the changing magnetic field of the driver's fast rising current.

The anode flange mentioned in Sec. 3.1.3 contains a B-dot groove with four outputs — one per capacitor/switch module. This groove, being located adjacent to ground, measures all current on either side of the sandwiched insulator that passes between the cathode and the return structure of the coaxial power feed. Calibration of this 'machine' B-dot was completed and retested in Refs. [93] and [15] respectively. The four signals obtained during each shot (1 per module) are typically quite similar. Raw and integrated signals from the machine B-dot of a pinching and non-pinching load are shown in figure 3.2. These signals are recorded using either a Hewlett Packard (HP) 16500b Logic Analyzer, or a Tektronix TLS-216 Logic Analyzer. The TLS-216 takes 2 Gigasamples per second (GSa/s), and has a bandwidth of 500 MHz, meaning signals faster than this are attenuated to a degree. The Hewlett Packard takes 1 GSa/s, with a 100 - 500 MHz bandwidth.

Because of its location, the machine B-dot does not discern whether current passes through

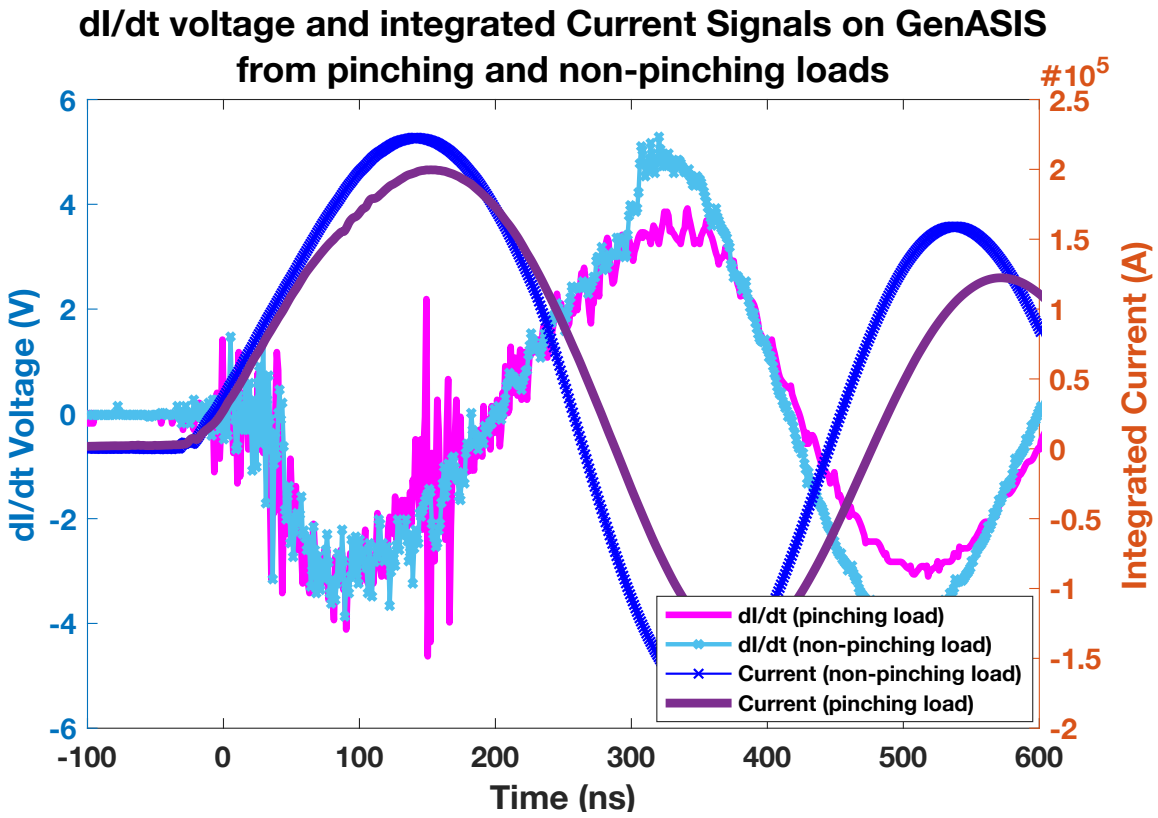

Figure 3.2: Raw voltage and integrated signals from the pre-load 'machine' B-dot probes on GenASIS from a pinching (X-pinch) and non-pinching (a severely over-massed X-pinch). The longer rise caused by the higher overall load inductance as well as inductive dips during pinching are visible in the purple and pink traces respectively.

a target load or shorts the power feed. A smaller groove in the plate where the current return posts mount back to the anode portion of the coaxial cones gives this information. This 'load' B-dot was calibrated against the machine B-dot during short-circuit shots (where a large bolt was placed between the GenASIS electrodes). It is especially useful in experiments such as X-pinches, where the load is initially fairly high inductance, and grows more-so near pinching, as it gives an idea as to how much current GenASIS actually drives through the load versus simply into the power feed (after which some may be lost).

3.2 X-pinch Load Hardware and Targets

Throughout chapters 4 and 5 in this dissertation we present data numerous X-pinches of various configurations. We focus first on the laser-cut foil X-pinch (LCXP, Chap. 4), and then introduce the hybrid X-pinch (HXP, Sec. 5.3). While not the primary focus of this work, wire X-pinch (WXP) experiments accompany every LCXP and HXP experiment as a performance benchmark. Despite the variety of targets presented here, the overall target scale and the basic load hardware, changed very little and as such, we will begin our discussion of target setups with the latter.

3.2.1 Load Hardware

As mentioned in Sec. 3.1.3, the final OD of the cathode in GenASIS is $\sim$ 20 mm, setting the diameter for the load electrodes. Between 10 - 15 mm from the top of the brass load cathode, is the 7.5 cm OD annular anode mentioned earlier, that is mounted on top of four current return posts connecting the target load back to the machine anode. The annular anode has a 25 mm diameter opening at its center to mount smaller 'load' anodes, since handling the larger 7.5 cm plate while loading fragile targets increases the likelihood of damaging said targets.

While new load electrodes often need making for new or modified targets, the same set of electrodes can be used on GenASIS for several experimental campaigns, as the 75 kV and 200 kA of the driver is comparatively gentle on the electrodes relative to larger machines with higher currents and often significantly higher voltages.

All of the load electrodes in these experiments (see Fig. 1.6) were 2 semi-circular pieces that screwed together as a clamp. Each contained four holes for 2 or 4-wire X-pinches, azimuthally separated by 90°, diametrically separated by 1 cm, and big enough to fit a no. 6 (0.11g) or no. 8 (0.07g) split-shot through them (the split shot was used to maintain tension on the wire X-pinch limbs). A 6 - 7 mm opening in both the anode and cathode served to prevent stagnation of the axial

jets from the WXPs and LCXPs on the electrodes, as a window for viewing the crosspoints of WXP and LCXP targets from above during loading, and as a point to clamp or thread the conical elecrodes for the HXP experiments. The laser-cut foil X-pinches would simply be clamped into the electrodes. Throughout the experiments, the anode and cathode were either loaded with an X and placed into GenASIS while connected by a subsequently removed 1-1.5 cm spacer, or, in the case of wire and many laser-cut X-pinches, the components for the X were loaded into the load anode, and lowered into GenASIS, where the load cathode was already mounted.

3.2.2 Wire X-pinch Loads

The wire X-pinches conducted for the experiments described in this dissertation consisted of 2 or 4 wires of a variety of materials and diameters. However, the basic parameters of the WXPs remained constant, with opening angles of $\sim 30^{o}$ - 40^{o} and total heights of 1 - 1.5 cm. As shown in Fig. 3.3, the wires were hung in parallel, gravitationally tensioned using lead weights, and the load anode was then rotated just over 180^{o} until the wires touched at a single point. Wire X-pinches composed of W were used for benchmarking LCXPs made of Ta due to the availability of W wire, and its location laterally adjacent to Ta on the periodic table. Copper LCXPs and HXPs were compared directly to Cu WXPs.

More in-depth details on WXP setup and development are not given here since the functionality and the dynamics of the WXP are already well established, including by the author and PI at the UCSD pulsed power laboratory on GenASIS and other current generators included in (but not limited to) the work in references [13, 14, 81, 84, 97, 156, 159].

3.2.3 Laser-cut X-pinch Setup

The initial goals of the LCXP project were to design a target with the precise controls of a laser-cutting facility rather than hand-rotating wires and then prove that it could create flux comparable to WXPs. Following this, the goal was to modify the crosspoint parameters including

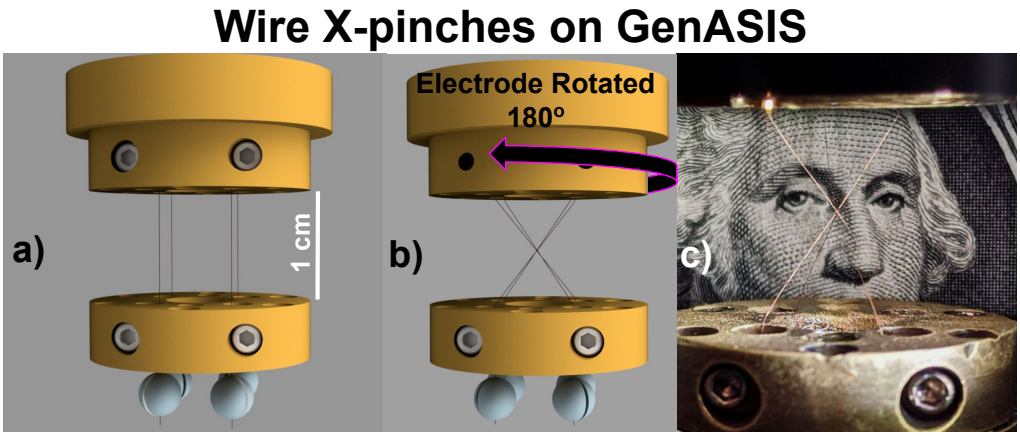

Figure 3.3: a) A CAD drawing of Cu wires placed into the load electrodes of GenASIS prior to rotation to form an X, showing the initial position of the wires with their lead weights. b) A CAD drawing of the setup from frame a) after a 180° rotation of the anode, forming a 4 x 25 μm Cu WXP. c) A photograph of a 4 x 25 μm Cu WXP loaded into GenASIS with a US 1$ bill in the background for scale reference.

linear mass (the product of the cross-sectional area of the X at the crosspoint and the material density: $\sigma_A \rho$) and shape to create a single, reproducible source at the crosspoint, and then to optimize emission flux through a material scan. The hope was ultimately that once optimized, the production of numerous targets could be automated, and even produce spools of targets for rep-rated operation (though this has not been realized yet).

Double-Pulsed Laser Ablation

A process referred to as double-pulsed laser machining enabled the high-precision LCXP target fabrication. When focused to a point, a high intensity ($\geq$ GW/cm^2) laser pulse may ablate a target material, allowing precision mass-removal from targets, and the drilling of high-aspect ratio holes (amongst other shapes). Limitations to this cutting though include the ablated material— a mix of plasma and material ejecta — redepositing on the face of the cut, as well as interactions of the laser pulse with the plasma and ejecta that reduce penetration of the laser into the target.

By using pairs of 3 - 6 ns pulses, with each pulse separated by 40 - 150 ns, and each pair separated by > 100 μs, Forseman *et al.* [125] and Wu *et al.* [126] showed improved material

removal, reduced redeposition of ejecta, and less heat-damage near the cut. The first pulse, as expected, created the plasma/ejecta plume over the target area. By waiting a prescribed amount of time for the plasma to dissipate, the second pulse would interact almost entirely with the ejecta, heating it significantly and driving away the mass, thus preventing if from redepositing back over the original cut or bore. The result of this is a significantly improved aspect ratio, and much higher quality edges to laser-cut targets.

Laser Workstation 1

The initial laser-cut foil X targets were cut using Laser Workstation 1 (LWS1) which uses this double-pulsed ablation method. LWS1 is a green (532 nm) light laser with focal spot sizes of 5 - 25 μm. It is capable of cutting holes $\leq$ 8 μm in diameter through materials up to 75 μm thick, thus achieving a laser-drilling aspect ratio of $\sim$ 10:1. A moving platform passes the target through the fixed-location laser beam, further increasing the stability of the beam, and thus target reproducibility.

The TRUMPF TruMark Station 5000

For later LCXP experiments, most target X's were cut using a commercially available laser-marking platform, the TruMark Station 5000, from TRUMPF [170]. This system is a compact, self-contained unit designed for marking and etching objects, such as barcodes and part numbers onto assemblies, but has adequate power to cut through metals as well. The Trumark system moves the laser beam (rather than the target platform) and can adjust the focal point with an electronically adjustable lens, increasing the speed and versatility of the platform at the expense of accuracy. The focal length of the Trumark is longer than that in LWS1, again allowing a more diverse array of uses, but at the cost of minimum focal spot, which is $\sim$ 30 μm here. The laser has adjustable power and pulse rates, which are easily changed when cutting through different materials or different foil thicknesses. No attempts to replicate the double-pulsed ablation techniques (employed on LWS1)

using the TRUMPF have been tried yet.

The TRUMPF system was used initially due to its availability (as compared to the precision and in-demand LWS1), its speed of target production, and its ease of use. Given this, General Atomics granted the author access to its target fabrication lab and the TRUMPF system, to enable the design, optimization, and production of targets without extortionate time demand on General Atomics' employees.

Nickel foil X-pinches (with a hyperbolic crosspoint, which will be discussed in Sec. 4.2.2) cut on both the LWS1 and TRUMPF systems are shown in Fig. 3.4. The two images from each platform are from the same target, with a) and b) being backlit to show the profile of the rear side of the target, and c) and d) being frontlit to show features on the front surface. The minimum lateral measurement from each target is given at the crosspoint of each frame. Notice that the front surface of each target is smaller than the rear surface, which creates an approximately trapezoidal crosspoint, which is not in agreement with the optimum operating parameters of LWS1. The key difference between the two platforms is the presence of ablated globules redeposited back onto the target cut with the TRUMPF system visible in d), that are not present in frame c) due to the double-pulse method employed on LWS1.

Design of the Foil X-pinch

The overall design of the foil X-pinches is shown in Fig. 3.5, with a total height and width of the X portion of the target measuring 1.0 cm and 0.6 cm respectively, giving an opening angle of approximately 30^{o} from vertical down the center of each leg. A majority of the initial design considerations for the laser-cut foil X-pinches revolved around the strength and stability of the target leading up to loading it into the pulsed-power driver. The legs in the X were tapered from $\sim$ 1 mm at the ends to $\sim$ 20 μm adjacent to the crosspoint in order to reduce the inductance of the array (thus maximizing current through it) and increase the strength and stability of the array during manufacturing.

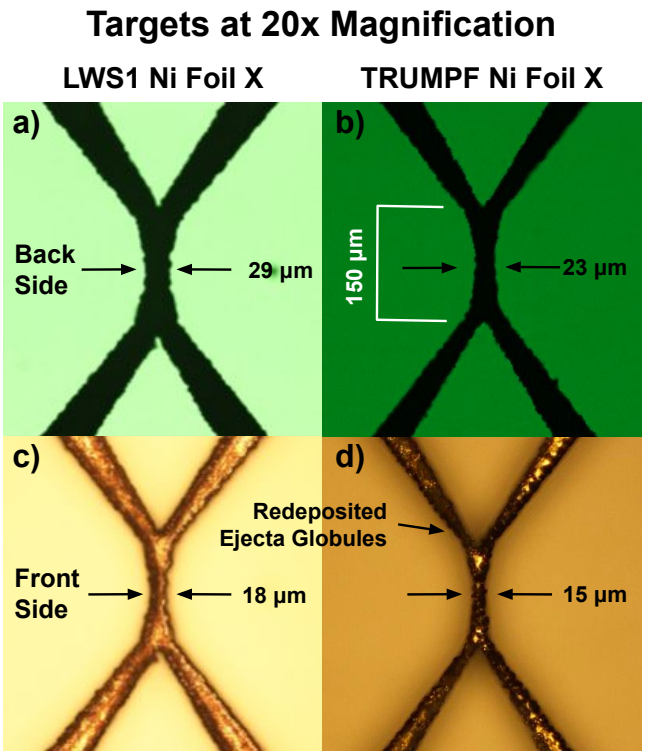

Figure 3.4: 20x magnification images of Ni foil X-pinches cut on both the LWS1 and TRUMPF systems. a) and b) are backlit images showing the profile of the back side of the targets. c) and d) are illuminated from the front to show the front surface of the target. The minimum lateral dimension of each target is labelled near the crosspoint of each frame. The most notable difference between targets is the presence of small spheres in d) representing ablated globules of molten material that settled back onto the target, rather than being removed by the double pulse method used for frame c).

The large tabs at either vertical end of the target were clamped into the target electrodes (see Fig. 3.6) and ranged from 0.15 - 0.5 cm long, though this number proved generally unimportant within this length range. Since the mass at either end of the X can severely strain or break a crosspoint (of say, $\sim$ 20 x 20 µm), lateral support tabs were introduced to add stability during manufacturing, transport, and loading into GenASIS. Once loading was completed, the lateral support tabs could be twisted off. The narrow ($\sim$ 100 µm) slots at either end of the target X provided an additional level of protection for the fragile crosspoint, allowing the target to flex, slightly distorting the entire X rather than severing the crosspoint should longitudinal strain be introduced. Note that the usefulness of this feature proved entirely dependent on the ductility,

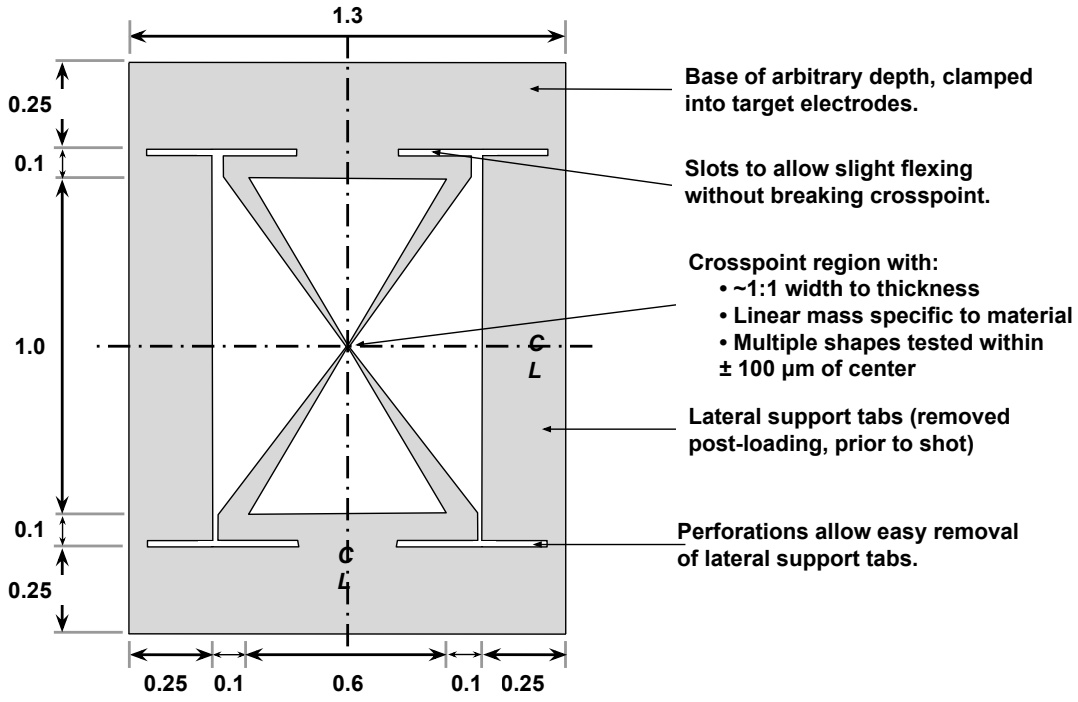

Figure 3.5: A scaled drawing of the initial LCXP designs, with the full target array with all of the engineered support. Key features are labeled. All dimensions are in cm.

malleability, and tensile strength of the target material.

Target linear mass was chosen by extrapolating from the wealth of data about pinch timing of different X's on different drivers (especially those conducted on the driver used in Ref. [84]), and from this, the target foil thickness was chosen to approximate a 1:1 aspect ratio (square cross-section) at the crosspoint, which as Fig. 3.4 shows, was not entirely realizable. The ability to use a $\sim$ 5 μm spot-size laser to cut the crosspoint meant that the transition in-to and out-of the crosspoint is abrupt when compared to the twisted wires of a traditional X —the foil X can neck down to, for example, 20 μm at the crosspoint, and within $\pm$ 10 μm in either axial direction have over twice that width, and a corresponding 4x drop in p_B. This, it was postulated, should confine the emission location. The design, dimensions, and linear mass of the crosspoint region (within

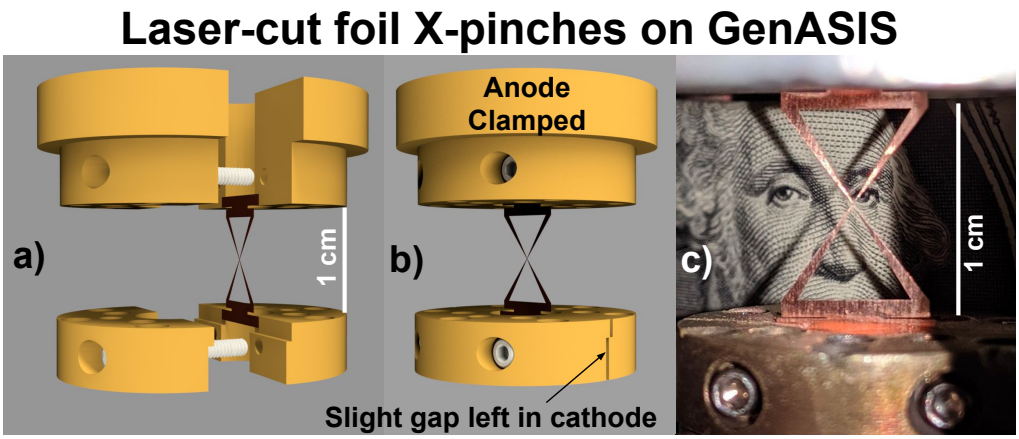

Figure 3.6: a) A CAD drawing of a Cu LCXP with an exploded view of the load hardware. b) A CAD drawing of the LCXP setup in its final loading configuration (see Sec. 4.2.1). c) A photograph of a Cu LCXP loaded into GenASIS with a US 1$ bill in the background for scale reference.

$\pm$ 100 µm of the center of the target) were specific to the material and the experiment, and such details are given when the relevant data is presented in Chaps. 4 and 5.

The loading hardware for the foil X's is described in section 3.2.1, and shown in Fig. 3.6a,b. Initially foil targets were clamped into both the cathode and the anode, and loaded into GenASIS using a brass spacer post which could then be removed when the electrodes were secured inside the chamber.

3.2.4 Hybrid X-pinch Setup

As described in Sec. 1.3.2, the hybrid X-pinch consists of a pair of conical electrodes, separated by some distance relating to ablation of these electrodes (a few mm), connected by a thin wire or capillary. For the experiments in this thesis, two different cone materials and several gap spacings between the cone tips were tested. Initially the conical electrodes were made from hardened stainless steel 1/4-28 threaded rod. The rod was turned on a lathe into a truncated cone with a 30^{o} opening half-angle from the axis, and a 1.5 - 2 mm flat tip. A 1 mm hole was drilled through the vertical axis of the cone to pass the wire through. The cones were connected to the GenASIS driver via 25 mm diameter brass electrodes with 1/4-28 threaded holes at their center.

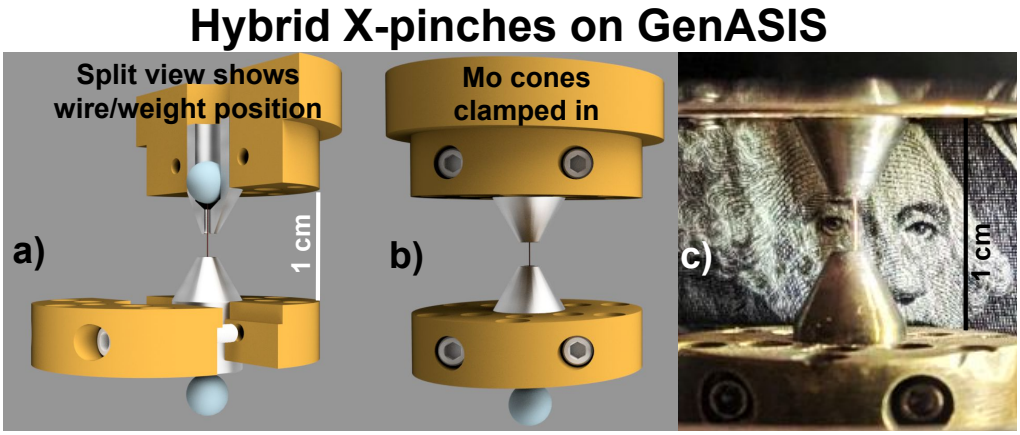

Figure 3.7: a) A CAD drawing of a Cu HXP with a cutaway view of the load hardware, conical electrodes, wire 'crosspoint', and anchoring weights. b) A CAD drawing of the HXP setup ready for discharge. c) A photograph of a Cu HXP loaded into GenASIS with a US 1$ bill in the background for scale reference.

The spacing between the cone tips was set by screwing the conical electrodes back or forth in the larger brass electrodes and measured using feeler gauges. Once the spacing of the cones was established, a wire was passed through the holes, and gravitationally anchored with a suspended split shot. The freely suspended weight at the end allowed the wire to slide without bending during vacuum pump-down, when the GenASIS chamber flexes by a fraction of a mm (see Sec. 4.2.1). Examples of this configuration are given in Fig. 3.7.

After we observed that the stainless steel conical electrodes underwent substantial ablation, resulting in an unpredictable pinch behavior, we switched to using molybdenum cones. Previous HXP experiments used cones made of a Cu-W alloy which is easily machinable and resistant to ablation [112], however Mo was chosen for our experiments to differentiate between emission from the ablated conical electrodes and the pinching center wire. Quarter-inch ($\sim$ 8 mm) Mo rode was used, and the pitch and central hole size of the Mo conical electrodes matched that of the SS electrodes. The Mo cones were clamped into the brass load electrodes (as shown in Figs. 3.7). The Mo conical electrodes were polished using Scotchbrite post-machining and cleaned between shots. While the velocity of the UV ablated plasma from the Mo conical electrodes was similar to that of the SS electrodes, the shape and form of the ablation was much more repeatable, so most

of the data presented here pertains to the HXP's with the Mo conical electrodes.

3.3 Diagnostics

3.3.1 Optical Probing

An Nd-YAG (short for Neodymium-doped Yttrium Aluminum Garnet) laser was used to optically probe the plasmas in these experiments, giving quantitative information on plasma formation scales, velocities, and areal electron density, as well as temporally resolved qualitative information regarding the overall evolution of the target plasma. Nd-YAG lasers emit near infrared (λ = 1064nm) light, which can be passed through a KDP (potassium dihydrogen phosphate) harmonic generating crystal which doubles the frequency to emit λ = 532nm light. The particular laser used for these experiments had a 5ns (FHWM) pulse width, and emitted $\sim$ 200 mJ @ 1064 nm and $\sim$ 20 mJ at 532 nm. Between some of the experiments presented later in this thesis, the optical setup was switched from 532 to 1064 nm, and the (readily apparent) differences between these will be discussed where relevant.

An electromagnetic wave of a given frequency, ω_l, can only probe plasmas up to a certain electron density, n_e, known as the critical density, n_c. Simply put, the probing laser cannot penetrate a plasma when ω_l is lower than the plasma frequency, ω_p. The plasma frequency describes the oscillations in a plasma that occur when the Coulomb force responds to electrons perturbed away from an equilibrium position with respect to ions. In order to solve for n_c, we set ω_l equal to ω_p:

$$\omega_l = \omega_p = \sqrt{\frac{4\pi n_c e^2}{m_e}}, \tag{3.1}$$

where m_e is the electron mass, and e is the fundamental charge, all in cgs units. Since we know that $\omega_l = c/\lambda$ (where c is the speed of light), we can solve for n_c as follows:

$$n_c = \frac{m_e}{4\pi e^2}\left(\frac{c}{\lambda}\right)^2. \tag{3.2}$$

Equation 3.2 shows that the critical density is inversly proportional to the square probing light's wavelength. Plugging in the appropriate values for m_e and e, Eq. (3.2) rewrites simply as:

$$n_c = \frac{1.1 \times 10^{21}}{\lambda^2}, \tag{3.3}$$

where λ is in μm. Thus, for 1064 and 532 nm light respectively, the critical densities are ≈ 1 and 4×10^{21} e^-/cm^3 (though the effects of absorption and refraction will likely limit the maximum probable density lower than this).

Three separate configurations were used over the course of the experiments described in this thesis. We will describe the fundamentals of each here, and make distinctions when necessary at later points.

Shadowgraphy

The simplest setup for laser probing of a plasma is shadowgraphy, which is a type of refraction-based imaging [171]. The refractive index of a plasma is given by

$$\eta = (1 - \frac{n_e}{n_c})^{(1/2)}, \tag{3.4}$$

where n_c is the critical density as determined via Equation 3.2. When $n_e \ll n_c$, η rewrites as:

$$\eta \approx 1 - \frac{n_e}{2n_c}, \tag{3.5}$$

where we see that 1-$\eta \propto n_e$. So, in a shadowgraphy setup, a collimated, expanded laser beam is passed through a plasma, and individual rays of light are refracted, deviating from their

original path proportionally to the density of the plasma they passed through. While there certainly are ways to extricate quantitative data from shadograms, none were used in this work, and so shall not be described. As used, shadowgraphy served as a simple way to view bulk plasma properties, especially in areas of plasma too dense for interferometry to be useful.

The upper detection limit of this setup (and in fact, all of the setups described here) relates to the refractive index of the plasma and the distance of the collection optic outside of the chamber. Light that is scattered to a degree that it avoids the collection optic is not recollimated later to form an image. According to Schmidt and Ruckle in Ref. [172], the maximum deflection angle, θ_{max}, in a plasma of a given n_e is

$$\theta_{max} \approx C_1 \frac{n_e}{n_c}, \tag{3.6}$$

where C_1 is a constant, specific to the density profile of the plasma. For a plasma with a parabolic density profile (which, though not exactly accurate, is adequate for our purposes), C_1 = 1. Rearranging to solve for n_e, we get

$$n_{e-max} = arctan(\frac{f}{r_l}) * n_c, \tag{3.7}$$

where r_l is the radius of the collection optic, and f is the focal length of the collection optic. Depending on the collection optic (which was always a 5 cm diameter lens with f = 400 or 500 mm), and the wavelength in use, the upper limit in the setups used here is between 2×10^{19} e^-/cm^3 for 1064 nm light and $2 \times 10^{20} e^-/cm^3$ for 532 nm light.

Dark-Field Schlieren Imaging

Dark-field schlieren imaging involves placing a small one-dimensional edge (such as a razor) or sphere called a schlieren stop to block the laser beam at a point after the target area where it is focused to a point. When the collimated laser light passes through an empty target area, and

subsequently focused onto the schlieren stop, ideally all of the light is blocked, creating a black or 'dark' image. However, when the beam must instead pass through a refractive medium such as a plasma with a refractive index gradient ($\nabla\eta$) orthogonal to the beam propagation direction, the beam refracts in a direction parallel to the gradient [172]. This is shown as an illustration in Fig. 3.8.

From Eq. 3.5, we recall that 1 - $\eta \propto n_e$, so it follows that $\nabla \cdot \eta$ changes with $\nabla \cdot n_e$ as well. Thus, deflection of the beam occurs where there are electron density gradients. If we refer to the direction of laser propagation as y, and the gradient (deflection) direction as z, then the deflection angle of the light, θ_z, is given by

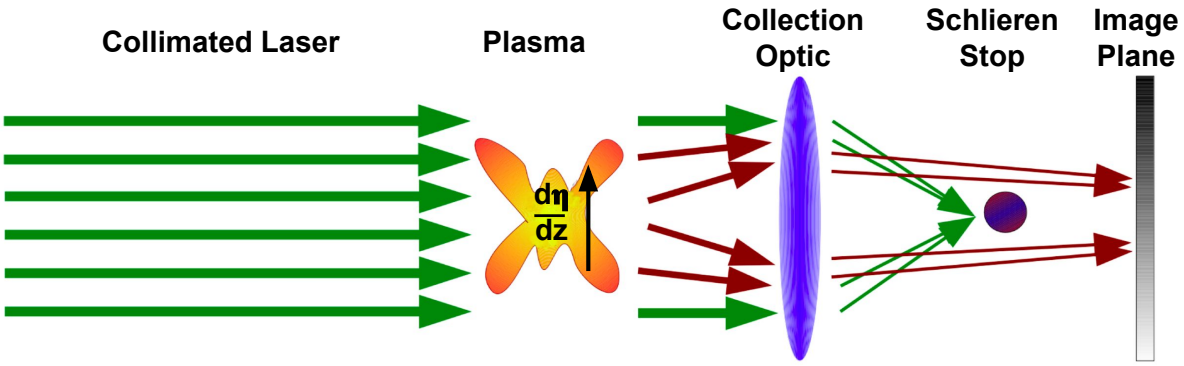

Figure 3.8: A simple cartoon showing the basic setup of a dark-field schlieren system using a spherical stop. Image taken from Ref. [12].

$$\theta_z = \int \nabla\eta\,(y,z)\,dy. \tag{3.8}$$

Plugging in the appropriate values for η and n_c, we get

$$\theta_z \approx \int \frac{d}{dz}\frac{n_e}{8\times 10^{21}}dl, \tag{3.9}$$

for 532 nm light (2×10^{21} in 1064 nm light). If $\nabla \cdot n_e$, integrated over dl creates a sufficiently large θ_z, light will pass beyond the schlieren stop, and create an image at the image plane.

This means there is a relationship between the size of the schlieren stop, d_s, and the θ_z required to avoid blocking. The lower detection limit of a schlieren image is governed by a minimum angle, θ_{min}, d_s, and the focal length of the focusing optic, f, given by

$$\theta_{min} = \frac{d_s}{2f}. \tag{3.10}$$

This is then plugged back in to Eq. 3.6.

For the setups here, the spherical stops measured 0.75 mm, and the collection optic was either an f = 400 or 500 mm lens, creating minimum density cutoffs between $\sim 7\times10^{17}$ - 3×10^{18} e^{-}/cm^3 for 1064 and 532 nm laser light respectvely.

The schleiren setup provides a mix of qualitative and quantitative data. Its high-contrast images create aesthetically desirable, time resolved images with excellent spatial resolution of the plasma for basic observations of plasma dynamics. If the region of the plasma one is observing lies within the proscribed density windows, multi-frame schlieren enables velocity measurements of structures. While not applicable to this work, in some cases schlieren images may also be used for more complicated analysis such as Fourier analysis of plasmas with complex perturbations [173, 174].

Mach-Zehnder Interferometry

Mach-Zehnder interferometry involves splitting a laser beam into two, and recombining the beams to form an interference pattern. One of the beams is passed through a plasma, where the phase velocity of the light is higher than in air or vacuum, and the other beam is not. When the beams are recombined, the interference pattern is altered where sufficient phase-differences occured. The amount of the phase shift tells a user what the areal electron density (n_{eA}, in cm^{-2}) is. An illustration of this setup, taken from Ref. [12] is shown in Fig. 3.9.

From Equation 3.4 we see that an area of high electron density has a lower η than an area

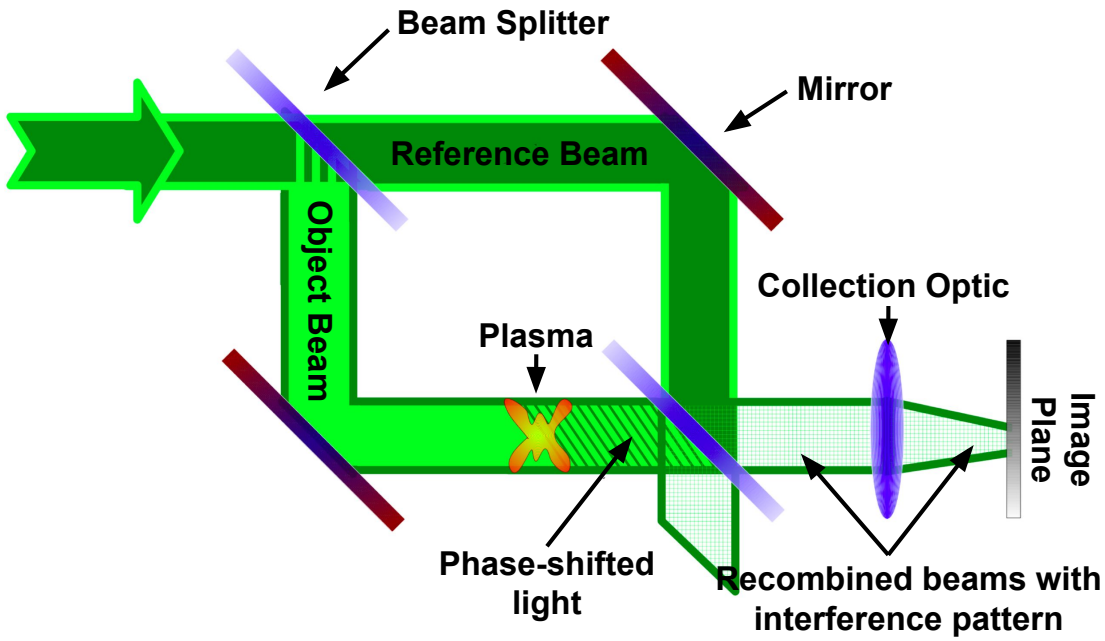

Figure 3.9: A simple cartoon showing the setup of a Mach-Zehnder interferometer. Image taken from Ref. [12].

with little or no electron density. Since phase velocity, $v_\phi = c/\eta$, it is clear that the lower η is, the larger v_ϕ is, so as n_e increases, so does v_ϕ. Provided that the $n_e \ll n_c$, since we know that 1-$\eta \propto n_e$, we can then calculate the phase shift (f_ϕ) of the line integral of the electron density (in cm^{-3}):

$$f_\phi = 4.48 \times 10^{-12} \lambda \int n_e dl. \tag{3.11}$$

λ here is the wavelength, in meters, and the integral along l follows the path of light through the plasma. By integrating Eq. (3.11) along a path of length l and plugging in the Nd-YAG laser's primary or secondary wavelegths, (1064 and 532 nm respectively), $n_e l_{1064} = 2.1 \times 10^{17} f$ and $n_e l_{532} = 4.2 \times 10^{17} f$, where $n_e l = n_{eA}$.

To actually determined the areal electron density of some portion of the interferogram, one historically would draw a 1D line in a background (non-plasma) image and an identical line in an image with plasma, and compare fringe shifts along the lines. By determining the magnitudes of the fringe shifts, and using Equation (3.11), one may calculate n_{eA} along this line. Accuracy

for this process is $\sim$ 1/4 fringe shift, corresponding to minimum quantifiable n_{eA}'s of 0.5 and $1\times 10^{17}\mathrm{e}^{-}/\mathrm{cm}^2$ for 1064 and 532 nm respectively.

However, computer programs make this process significantly more accurate, and offer the ability to gather 2D n_{eA} mappings across whole regions of plasma. The interferometric data presented here was processed using an interferometric data analysis software package called IDEA [175], or a home-brewed script using MATLAB that uses methods similar to IDEA, but handles larger image sizes (thus expanding its capabilities), as IDEA was originally written in the late 1990s. These programs take an interferogram, and perform a fast Fourier transform (FFT) on them to isolate the carrier frequencies. The carrier frequency and a limited range of adjacent frequencies are selected, and the image undergoes an inverse FFT using only the selected frequencies to create a more binary profile of the interference pattern. The phase profile of the interference pattern is mapped out (from 0 to 2π for each fringe), and then smoothed into a continuously counted profile (fringe 1 = 0, 2 = 2π, 3 = 4π etc.) from a selected point. The background and shot image undergo identical processing and are then subtracted from one another, creating a mapping of the phase differences between the two. The minimum value in the difference image is shifted to zero, and then the entire array is multiplied by the value determined from Eg. 3.11 (for example. for 532 nm light, the array is multiplied by $4.2\times 10^{17}/2\pi$). Error for this process is much smaller than the manual measurements, being closer to 1/6 or 1/8 of a fringe shift.

Other forms of interferometer such as the prism based Nomarski setup are significantly easier to set up than a Mach-Zehnder interferometer. However, the ability to utilize the entire beam profile, and change the fringe spacing and orientation in the Mach-Zehnder configuration make it a significantly more versatile tool, especially for X-pinches, with their diverse array of densities, scales, and plasma propagation directions.

The Overall Optical Setup

In order to maximize the number of laser-probing images per shot, the initial laser beam was typically split into multiple beams of different path lengths. Since light travels at roughly 30.5 cm/ns, diverting one of the split beams an extra 15 feet before passing it through the target plasma makes it 15 ns later than the first. In this fashion, a variety of different delay configurations were used for these experiments. Figure 3.10 shows a cartoon of the most complex of these, which includes 4 separate delays in 2 separate polarizations, split again post-target to provide simultaneous 4-frame schleiren and Mach-Zehnder interferometry, for a total of 8 images. In some of the experiments, the beam splitter before the target chamber was removed, omitting the reference beams for the interferometers and creating shadowgraphy.

The four frames were created using a polarizing beam splitter on 45° polarized light to create two orthogonally polarized beams. One was delayed 15 (or 30) ns and the two were recombined and then split 50/50, with one pair proceeding through the target chamber, and the other pair delayed another 30 (or 60) ns (making 0, 15 (30), 30 (60) and 45 (90) ns relative frame delays) before then passing through the target. The beams in each pair overlapped to such a degree that a single schlieren stop could be used to block both, while the two pairs were separated geometrically so they could be 'picked off' with mirrors or beam splitters. The images for the laser diagnostics were captured using Canon DSLR cameras with the IR filter removed from in front of the CCDs. A narrow (3 nm) laser-line filter was mounted on each camera so that their shutters could be left open for a 5 second exposure (during which time GenASIS was triggered) without any significant plasma self-emission or laboratory light reaching the CCDs. Neutral density filters were used to adjust the contrast of the images, especially to change the relative intensities of the reference and object beams in the interferometers. The spatial resolution for these setups measured ~ 50 μm.

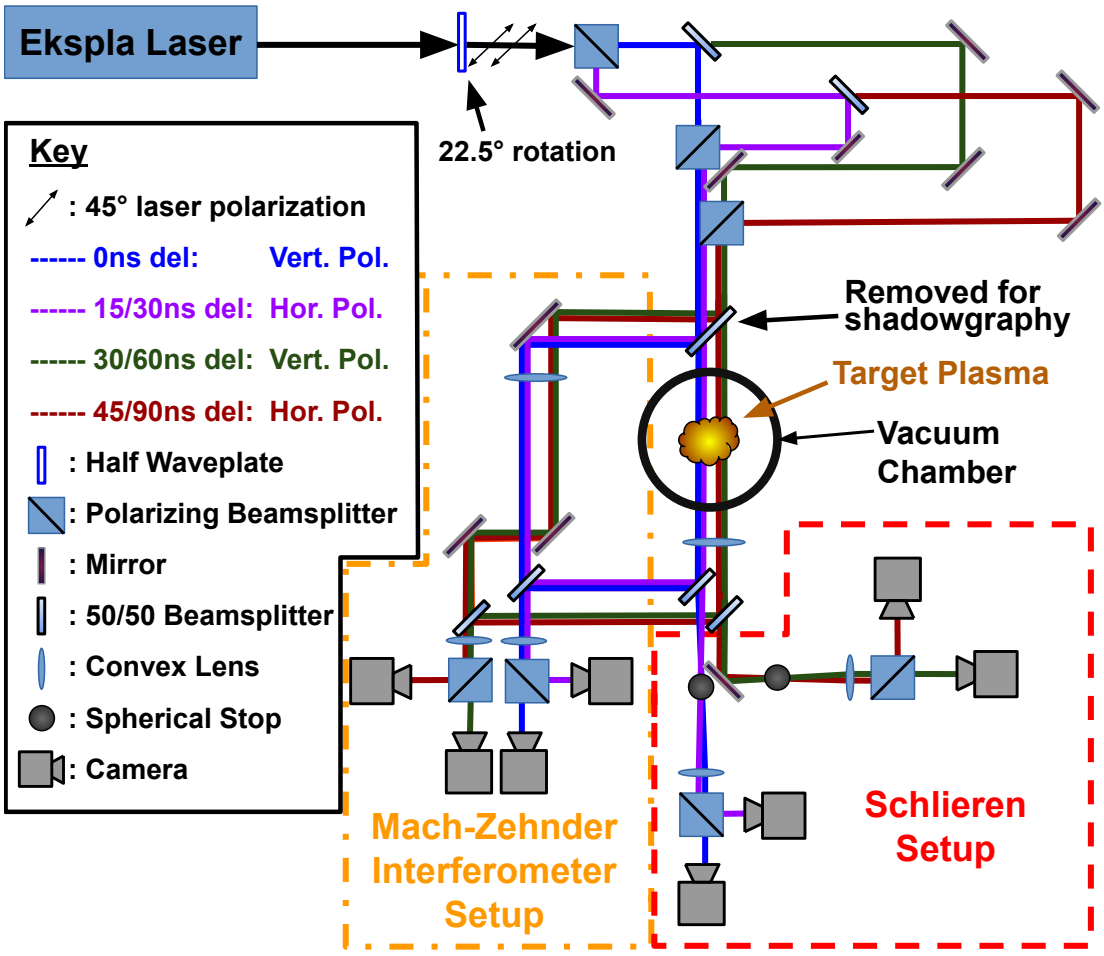

Figure 3.10: A detailed cartoon of the most complex of the optical setups used in this thesis: the 4-framed simultaneous Mach-Zehnder and schlieren. Key components are labeled, and different delay lines are color-coded. The beams in each pair are orthogonally polarized with respect to one another. For some shots, the interferometer was not used, and shadowgraphy was used in its place, which simply required removing the beam splitter prior to the chamber.

3.3.2 X-ray Diodes

X-ray diodes collected temporally resolved, quantitative X-ray data in these experiments. The primary diodes used were Si positive-intrinsic-negative (PIN) diodes covered by filters of various thickness and material. A PIN diode consists of a silicon intrinsic (I) semiconductor sandwiched between p and n-type (P, N) semiconductor regions. A reverse (negative) bias from an external source is applied across the diode causing the I layer to act as an insulator, stopping current and establishing an electric field. When the silicon absorbs photons, it liberates charge

carriers that are accelerated by the bias and produce a current, which passes through a resistor and is recorded by an oscilloscope (as a voltage). The Si diodes used in these experiments had either 0.28 or 1 mm^2 sensitive areas [176]. The rise-time for these diodes is 700 ps. A -50V bias was applied to all of the diodes using a battery-powered bias box.

Diamond photo-conducting detectors (PCDs) were also used in some of the experiments described here. The diamond PCDs are simply a diamond cube placed between an anode and cathode (no P or N layer), that is biased at up to - 500 V (the responsivity increases approximately linearly with bias voltage). The responsivity of the diamond PCD is significantly less than that of the Si PIN diodes, but it is comparably fast-rising, and significantly more robust. The PCDs are not sensitive to visible light, being most useful for photons between 100 and 5000 eV. All diode signals were recorded using the faster Tektronix TLS 216 scope (Sec. 3.1.5).

Ross filter pairs

In order to effectively use the diodes to approximate the relative X-ray flux emitted in specific energy ranges, they were filtered with a variety of materials. Different filters have different transmissivities and cutoffs at different energies, as is shown by the filter transmission curves in Fig. 3.11. By shrewdly choosing which filters to apply to the diodes, the transmission curves from pairs of filters may be subtracted from one another to obtain band-pass windows. These are called Ross pairs [177], and the difference between signals from the two diodes with filters that create one of these windows is a fair approximation of the energy emitted in that energy range. Though Ross pairs are prone error because each material has different scattering properties, or the fact that no transmission curves match up perfectly (especially after their respective L or K-edges) [178], they provide yet another piece of data to cross-reference with the other diagnostics used in these experiments.

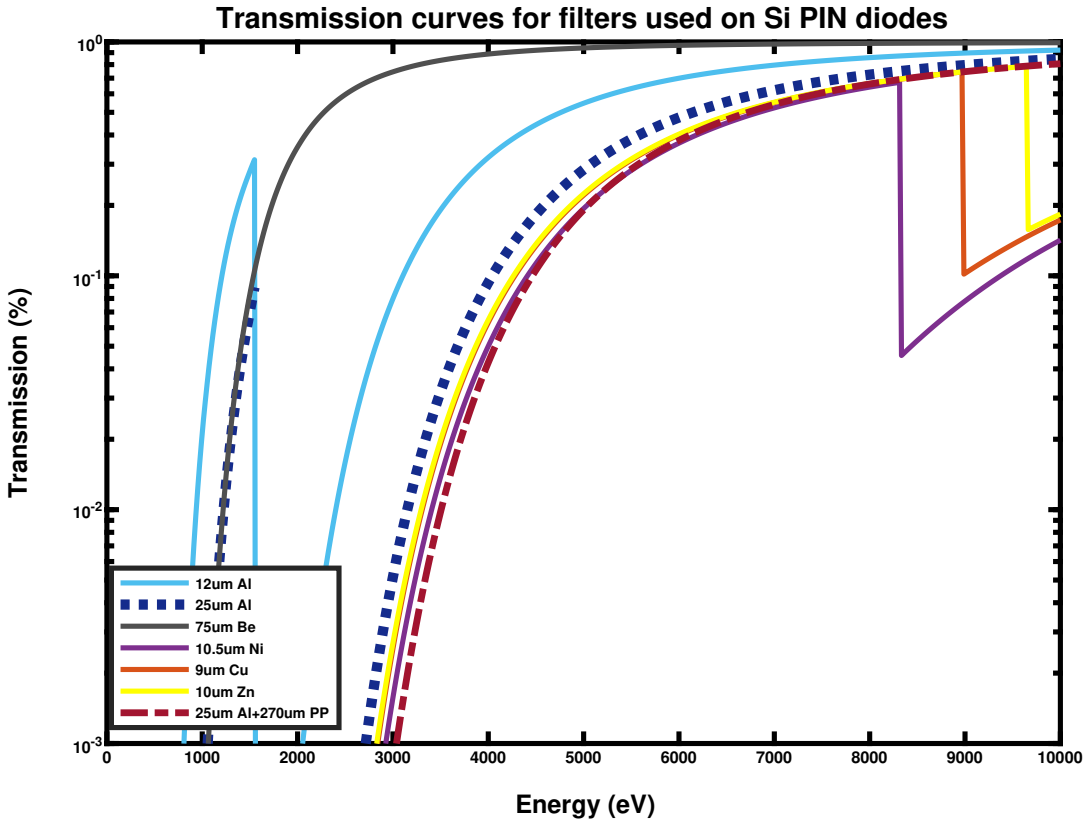

Figure 3.11: Filter transmissions of the filters used for the Si-PIN diodes in these experiments. Some differences in thickness were used at different phases, but in these instances all filters were adjusted to maintain the same general Ross windows.

Calibration of the Diodes

The Si diodes are 'absolutely' calibrated out of the box, meaning that their responsivity, in Amperes per Watt for specific photon energies is known. For example, as much of the work presented in this thesis looks at copper X-pinches, the diode responsivity at the Cu L-shell at $\sim$ 1 - 1.5 keV, which is typically the brightest spectral range in Cu X-pinches is $\sim$ 0.25 A/W. From this, one could theoretically determine the approximate X-ray flux or energy emitted by the pinch in the L-shell range, in conjunction with the Ross windows set up for this range. For example, seeing the transmission curves in Fig. 3.11, 25 μm Al the 25um Al + 270um PP match reasonably well beyond $\sim$ 2.5 keV, while the Al+PP filtered diode sees no flux below this level. Thus, the

difference between these two signals gives the energy seen by the 25 μm Al diode only in the window between 1-1.5 keV, by subtracting any energy from the continuum and Cu K-shell energy ranges.

Since many Si diodes are used at a time (up to eight per shot), they are cross or relatively calibrated to one another upon receipt from purchase, prior to formal experiments. During this cross-calibration, the same filter —usually $\sim$ 25 μm Al in our case —is placed in front of every diode, and signals from 3 - 5 X-pinches are recorded. The relative signals between diodes are determined, and a calibration factor is established relative to the diode performing parametrically in the middle. Variation between diodes tends to be $\leq 15\%$ however, age seems to play a role in decreased responsivity. If in use, the diamond PCD is also calibrated along with the Si diodes.

3.3.3 Pinhole Cameras

The plasma temperatures in an X-pinch range from a few eV to more than 1 keV. Therefore, having the ability to observe a plasma at these different energy ranges is a powerful tool. Pinhole cameras offer one of the simplest ways to do this. This thesis contains a variety of pinhole camera data, coming from both time-integrated and time-resolved pinhole cameras observing different energy ranges.

Time-Integrated Pinhole Cameras

The simplest camera possible is a time-integrated pinhole camera, which involves a small aperture, and a film or other recording medium at some distance back. Time-integrated means that there is no shutter (at least for relevant time scales), so the film captures data over the length of the entire experiment (or the sum of all of the time, hence time-integrated). The magnification, M, is simply the ratio of the distance between the pinhole and the film, d_i, to the distance between the target object and the pinhole, d_o ($M = d_o/d_i$). The geometrical resolution of the pinhole is simply

governed by this magnification and the aperture of the pinhole, A, given as

$$\Delta x_{geo} = A(1 + \frac{1}{M}). \tag{3.12}$$

This makes sense, since one cannot resolve an object smaller than the pinhole, and this limit increases as the image of the pinhole is magnified onto the film.

Diffraction effects may introduce a wavelength limit to the pinhole camera as well [179, 180]. Since light creates a diffraction pattern when passing through an aperture, given as

$$\Delta x_{diff} = 1.22\frac{\lambda d_i}{A}, \tag{3.13}$$

where λ is the wavelength of the photon, information is lost starting at the point where the Airy discs begin to overlap. Plugging in a result for Δx_{geo} to Δx_{diff} and solving Eq. 3.13 for λ one can find the wavelength where diffraction effects begin to dominate over geometric effects, and information from photons with a longer wavelength (lower energy) will be effectively lost.

Pinhole cameras may be filtered to create images within a specific photon energy window (see the tranmission curves in Fig. 3.11). For example, while most X-ray film is sensitive to eXreme Ultra-Violet light (XUV, $\sim$ 10 - 120 eV), one could put a 20 μm Be filter in front of the pinhole and filter out all photons below $\sim$ 675 eV (< 1% transmission). One such pinhole camera is used in these experiments, built into the compact convex mica spectrometer setup describe in Sec. 3.3.4. As described in Ref. [181], the convex mica spectrometer has a pinhole camera that captures a 0.6X magnification time-integrated image on a film or image plate. This 100 μm pinhole is filtered with 20 μm Be which blocks out all XUV emission from the coronal plasma around the X and only lets X-rays above $\sim$ 850 eV through. As such, only emission from the pinch or electron beams will show up on the images. This diagnostic is useful primarily for counting hot spots as the geometric resolution of the image is limited, measuring 270 μm.

Since the filter in the previously described pinhole camera only transmits photons from

the pinch and/or electron beam, it actually creates an effectively time resolved image. When another diagnostic such as a Be-filtered Si-PIN diode records a single, narrow X-ray pulse during the experiment (especially using an array such as an X-pinch), then the resulting image on the Be-filtered pinhole camera is a snapshot of only the temporal window during pinching, and at no other time did the camera image photons. Thus, used in conjunction with other diagnostics, even the simplest of pinhole cameras can provide powerful data.

Other time-integrated pinhole cameras were fielded throughout these experiments, and any data presented from them will include relevant parameters for the particular camera.

Originally, all of the time integrated pinhole camera images (and all subsequently discussed X-ray imaging diagnostics including spectrometers (Sec. 3.3.4) and penumbral slit-wire diagnostics (Sec. 3.3.5) were captured using Kodak Biomax MS film, which has a grain size of 0.12 μm [182]. As space to develop films grew scarce, and developing and fixing chemicals grew harder to find, we began using Fujifilm BAS image plates, which contain photostimulable phosphor crystals that, when exposed to ionizing radiation may leave some electrons suspended in a metastable state. Scanning the image plate with red light will release these electrons, and the resulting phosphorescence is recorded. The maximum resolution of the image plate scanner is 25 μm per pixel, which is significantly poorer resolution than film. However, image plates are not terribly light sensitive, and processing them simply involves a scanner (as opposed to developing), and so shot-to-shot continuity between images is dramatically increased. Additionally, image plates are reusable. Two types were used for these experiments: BAS-SR and BAS-TR. The primary difference between these two is an 8 μm thick layer of Mylar on the former [183], which cuts out some lower energy photons, but makes the -SR image plates much more robust (-TR plates are easily damaged without the plastic layer on top).

The Micro-Channel plate (MCP)

At lower energies, specifically in XUV range, which includes energies from 10 - 124 eV, filtering pinholes is difficult, and many of the standard films or image plates are not particularly sensitive to radiation in this energy range. So temporally resolving pinhole images requires a more rigorous approach. The micro-channel plate is a voltage-gated amplifier that, when used in conjunction with a pinhole camera does just this, adding additional stages to temporally resolve the pinhole image and introduce sufficient photon gain to expose a film or other light-capturing medium.

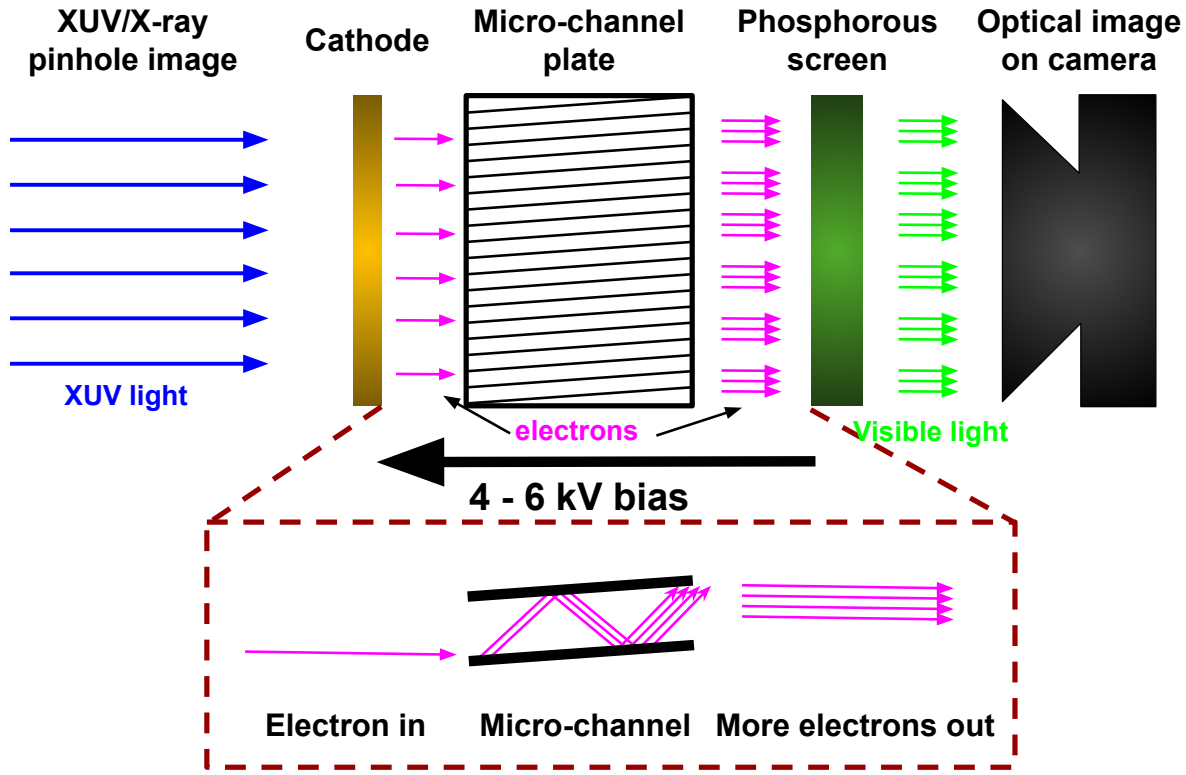

Figure 3.12: An illustration of the basic components and processes that occur in an MCP.

XUV light from the plasma passes through a pinhole, creating an image opposite the plasma. These photons strike a cathode made of gold or some other material that readily frees electrons. Beyond the cathode is the micro-channel plate itself, which is a set of micron-scale

capillaries that serve as electron-multiplier tubes. To drive the electrons out of the cathode, and through the micro-channels, a voltage of 4 - 6 kV is applied. This voltage is pulsed, with a 5 or 10 ns FWHM width, so only during this pulse, does the electron travel and breeding occur. At the other side of the micro-channels, the voltage from this pulse accelerates these electrons into a phosphorous screen that phosphoresces. This visible light is then imaged with a film or camera. A cartoon of this process is shown in figure 3.12, with the different stages labeled, and a zoomed-in inset of the micro-channel plate process.

The MCP used in these experiments is a 5 cm in diameter circle that is broken into quadrants, each of which can be gated independently. The typical magnification was $\sim$ 1.4X, and the pinholes used ranged between 100 and 200 μm in diameter. This created a lower-energy cutoff of 35 eV, and a geometric resolution limit of $\geq$ 180 μm. As mentioned, the FWHM of the voltage pulse was either 5 ns or 10 ns, and in order to create four different time delays, the cables delivering the pulse to each quadarnt are of different lengths (a wave propagates through a coaxial cable at $\sim$ 5 ns/m). While many MCPs apply a DC voltage for the phosphor screen which increases the overall brightness of the images, the MCP used in these experiments uses a single pulse to bias the entire camera. The lack of a DC bias makes this MCP design particularly robust and less prone to accidental damaging.

Kodak T-MAX 120 format optical film with an ISO of 100 or 400 was used with the micro-channel plate during earlier experiments before switching to a Canon DSLR with a short focal length lens. While there is was a slight decrease in sensitivity from film to CCD, there was no other significant experimental change.

3.3.4 X-ray Spectroscopy

X-rays incident upon a crystal are dispersed at angles specific to the photon wavelength and the lattice spacing of the crystal [184]. This was discovered by a father-son duo who noticed unexpected patterns when X-rays reflected off a crystalline structure, and the governing relationship

is known as Bragg's Law [185, 186].

Consider the schematic in Fig. 3.13. In it, X-rays are incident at some angle, θ, upon the layers of the crystal with lattice spacing d. If the X-rays are initially parallel and in phase, then in order to exit together in a fashion that constructively interferes, they must again be parallel and in phase. X-ray '**a**' interacts with point W and diffracts at angle θ. In order for X-ray '**b**' to continue travelling parallel and adjacent to **a**, it must travel the extra distance $\mathbf{XY} + \mathbf{YZ}$. In order for **a** and **b** to remain in phase, then the following relation must be true:

$$\mathbf{XY} + \mathbf{YZ} = n\lambda, \tag{3.14}$$

where n is some integer multiple of the X-ray wavelength λ. Since, from Fig. 3.13, we can see that $sin\theta = \mathbf{XY}/d$, it then follows that

$$\mathbf{XY} = dsin\theta, \tag{3.15}$$

and since $\mathbf{XY} = n\lambda/2$, one can substitute to get Bragg's Law, given by

$$n\lambda = 2dsin\theta. \tag{3.16}$$

The 2d spacing also is the longest wavelength that the crystal can diffract.

Thus, X-rays from a source such as an X-pinch will strike a crystal, and constructively interact at certain incident angles, to sufficiently expose a detector. Ray-tracing from the source location to the crystal to an exposed 'line' on the detector, one can find the angle, θ at which the X-rays hit the crystal, and determine their wavelength or energy. It is therefore clearly obvious that the lattice spacing, which is a material property of the crystal, and the angle of the crystal relative to the plasma govern which X-ray wavelengths, (or energies, as we will from here on out use) can be imaged.

For the majority of the copper X-pinch experiments described in this thesis, two crystal

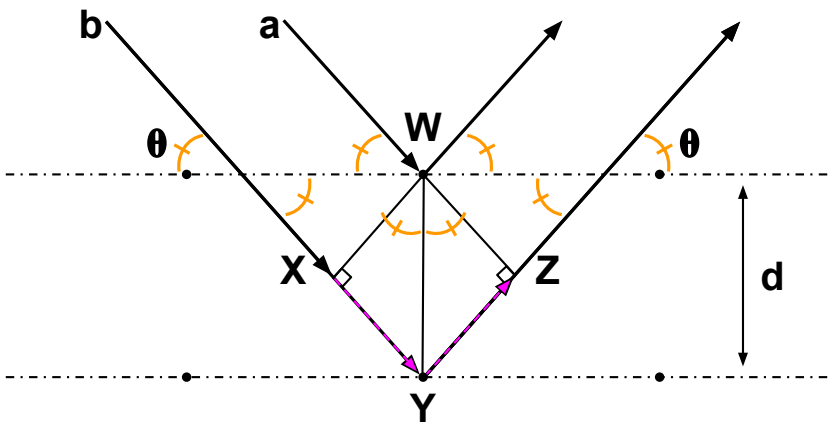

Figure 3.13: A sketch of the Bragg relation for X-ray diffraction in a crystal

spectrometers were fielded: an Highly-Ordered Pyrolytic Graphite (HOPG) crystal spectrometer to observe Cu K-shell lines, and a convex mica crystal spectrometer to observe Cu L-shell lines.

The HOPG Spectrometer

A Highly Ordered (or Oriented) Pyrolytic Graphite, or HOPG, crystal has a high reflectivity, with a 2d lattice spacing of 6.690 Å useful for imaging photon energies from 2 to 10s of keV [187]. The HOPG crystal in these experiments was mounted at a $\sim 13^{\circ}$ incline above horizontal to observe Cu K-shell emission (starting at $\sim$ 8050 eV), in an 6mm thick Al enclosure inside the GenASIS vacuum chamber. A slit roughly 8 cm from the plasma was filtered with 15 μm Kapton to protect the crystal. Above the crystal, also oriented at 13° was the film mount, filtered with 10 μm Al for light-tightness. Throughout the data presented here, both Kodak Biomax MS film, and Fujifilm BAS-SR image plate were used to capture the spectra. The E/ΔE resolving power for the HOPG spectrometer is fairly low, at $\sim$ 30. A cartoon of the HOPG configuration and a sample K-shell spectrum from a Cu laser-cut foil X-pinch are shown in Fig. 3.14

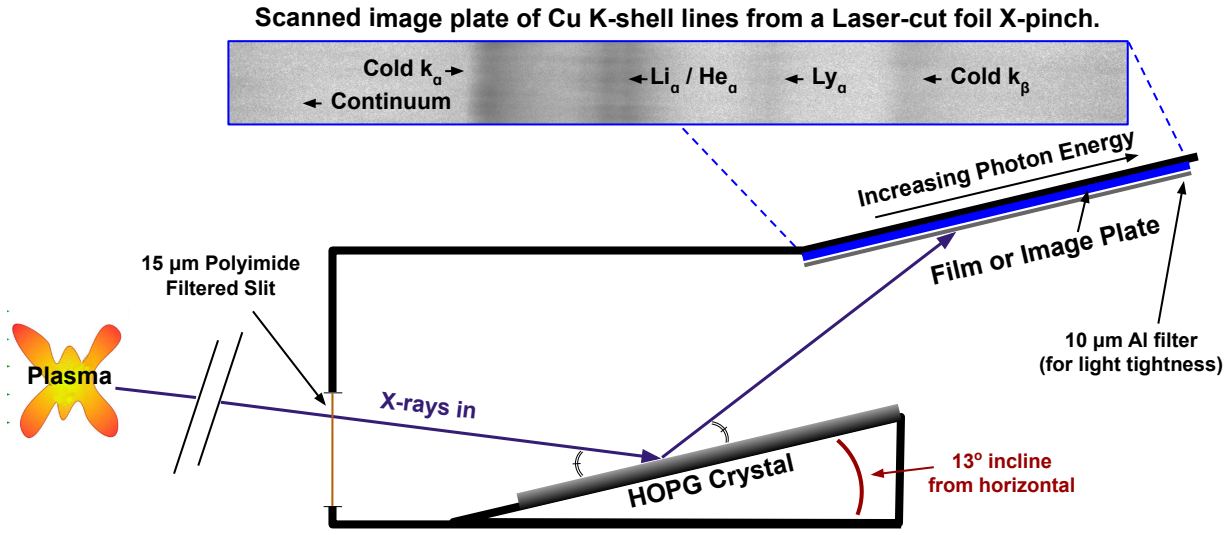

Figure 3.14: A sketch of the HOPG spectrometer setup, with sample X-ray paths, and an image plate scan of actual data from an X-pinch experiment showing Cu K-shell lines.

The Convex Mica Spectrometer

A convex mica crystal spectrometer, with 2d = 1.984 Å, was used to capture Cu L-shell lines at around 1 keV. Detailed specifics about the spectrometer may be found in Ref. [181]. Mica is particularly useful because of the ability to mount thin crystals in a convex fashion, which increases the range of detectable energies for a given setup. Additionally, though its reflectivity is lower than that of the HOPG, many orders of mica have similar reflectivities to one another, which further increases the range of detectable energies for a given setup, though it has the potential to complicate analysis, should a lines across a breadth of energies be present.

The spectrometer used here mounts to an NW-40 flange outside GenASIS. The o-ring where the spectrometer is mounted houses three slits (one per crystal), and a 100 μm pinhole, all of which are filtered with 20 μm Be, which blocks out soft X-rays below $\sim$ 675 eV (< 1% transmission). The first order of the mica crystal in this setup has an upper photon energy limit of $\sim$ 1500 eV. The $E/\Delta E$ resolving power of this spectrometer is $\geq$ 300. Either Kodak Biomax MS

film or Fujifilm BAS-TR image plate was used to record spectra from this device. A brief sketch of the system with some sample data from it are included in Fig. 3.15.

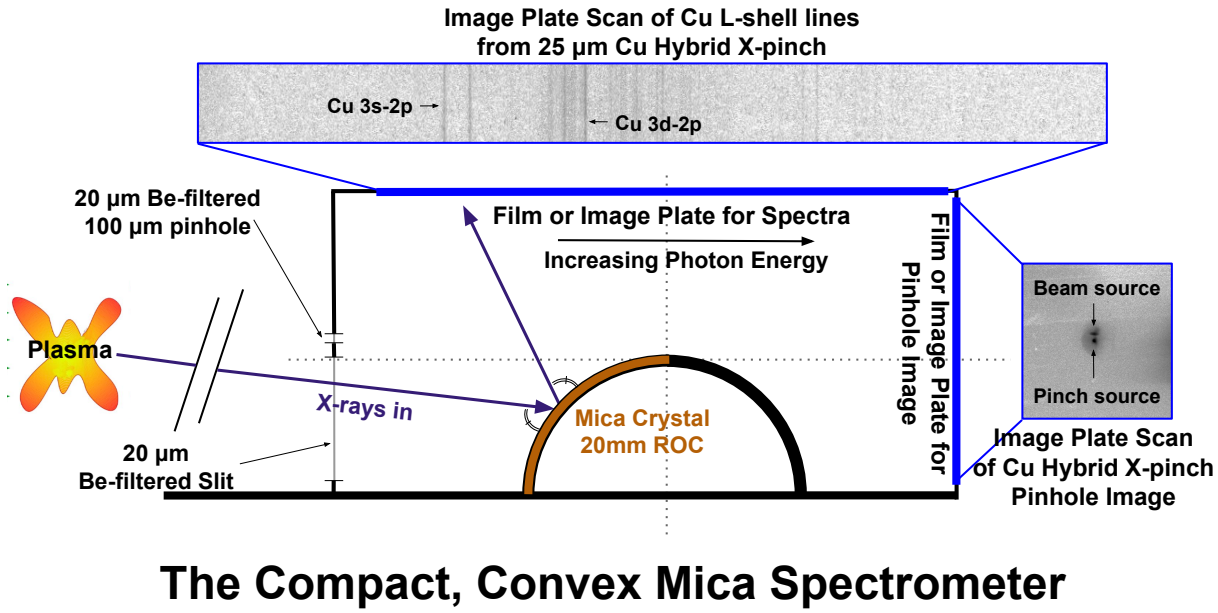

Figure 3.15: A sketch of the convex mica spectrometer setup, with sample X-ray paths, and image plate scans of actual data from X-pinch experiments showing Cu L-shell spectrogram and the filtered time-integrated pinhole camera image that produced the lines.

To determine the energies of specific lines in the recorded spectra, the films or image plates are scanned to a computer and run through a ray-tracing program which matches each pixel of the scan to a diffraction angle on the crystal. For the work here, since the X-rays come from a localized source (even in the event that there are multiple sources), we determine the approximate location of the pinch using the laser probing images. Upon completion, this ray tracing produces an Intensity vs Energy plot. There are many sources for error in this process, mostly with respects to the measurements of the relative crystal, film, and X-pinch positions. The mica spectrometer is generally insensitive to these errors: a 0.2 - 0.3 mm error (the resolution limit of the mica spectrometer pinhole), changes the energies by 1 - 2 eV. However, in the case of the HOPG, this can shift the calculated energies by as much as 50 eV. However, the relative position and intensities of the lines remains unaffected.

Spectroscopic Codes

In order to make estimates about the plasma parameters (temperature, density, ionization level, etc) during pinching, we compare the experimental spectra to synthetic spectra produced using computer codes and atomic tables. For this work, two codes were used: FLYCHK [11], and the hybrid code SCRAM [188–190].

When trying to match synthetic and experimental spectra, one needs to know the appropriate parameters to adjust. Increasing electron or ion density in the plasma typically increases the X-ray flux emitted and the width of the spectral lines (but the latter is generally not a concern here, especially for with the HOPG spectrometer given its low resolving power). Hotter plasmas tend to have higher ionization levels, so characteristic lines increase in energy as temperature increases. Spectroscopic codes give spectral intensities in units of energy per unit time, which can be summed over specific energy band-widths to get the total flux emitted over specific ranges. With the absolutely calibrated diodes and their Ross filter pairs we can estimate the total energy in each Ross pair bin by integrating the flux signal over time (typically FWHM). We can then look for the appropriate temperature and density combination in the simulations to match the line energies, relative intensities, and total fluxes and energies emitted in specific bands. We also attempt to account for the transmission, absorption, and reflectivities of the respective filters, image plates, and crystals.

To simulate a plasma with an electron beam, we set some percentage of the simulated electrons at a separate temperature from the primary plasma. We typically estimated the energy of the beam electrons at between 10 and 30 keV, and ran simulations with various percentages of total electrons from 0 to 15% at this second electron temperature.

3.3.5 Radiography

In order to estimate the size of the X-ray emitting regions in the X-pinches, the most powerful tools were among the simplest. By placing an object between the source and a detector

(again, either Biomax film or BAS-SR or -TR image plate), one can make inferences about the size of the source. Many publications in X-pinches have demonstrated their ability to produce radiographs of insects [77], or small foam spheres [84]. The minimum size of resolvable features on the radiograph corresponds roughly to the size of the source. In some of these experiments, radiographs of small meshes ($\sim$ 10 - 100 μm wires and voids), and insects were created.

A slit-wire array was also constructed, conisisting of several strips of different material filters (including Be, Al, Al+polyimide, Ti, Fe, and Ni) with high-Z wires of various diameters running orthogonal to the filters [191]. This diagnostic was placed at $\sim$ 15 cm from the source, and the image plate was placed at approximately 15 cm from the wires, creating a magnification of $\sim$ 1. The wires in the array were oriented horizontally so that any significant vertical displacement between pinch and beam sources would show multiple images of the same wire on the radiograph. A radiograph of the slit-wire array produced by a Constantan (which is a 45% Ni, 55% Cu high-resistivity alloy discussed more later) hybrid X-pinch is shown in Fig. 3.16, with the filters and wire positions all labeled though not all are the wires are visible due to the size of the source. For the later data, because of the switch from film to image plate, the usefulness of the diagnostic grew limited because of the 25 μm/pixel resolution of the IPs, making it at best useful for giving an idea of which wires can be imaged. At its most powerful, the diagnostic can be used to measure the size of the penumbra at the edge of the shadows the wires cast in the radiograph, allowing for actual source-size calculation.

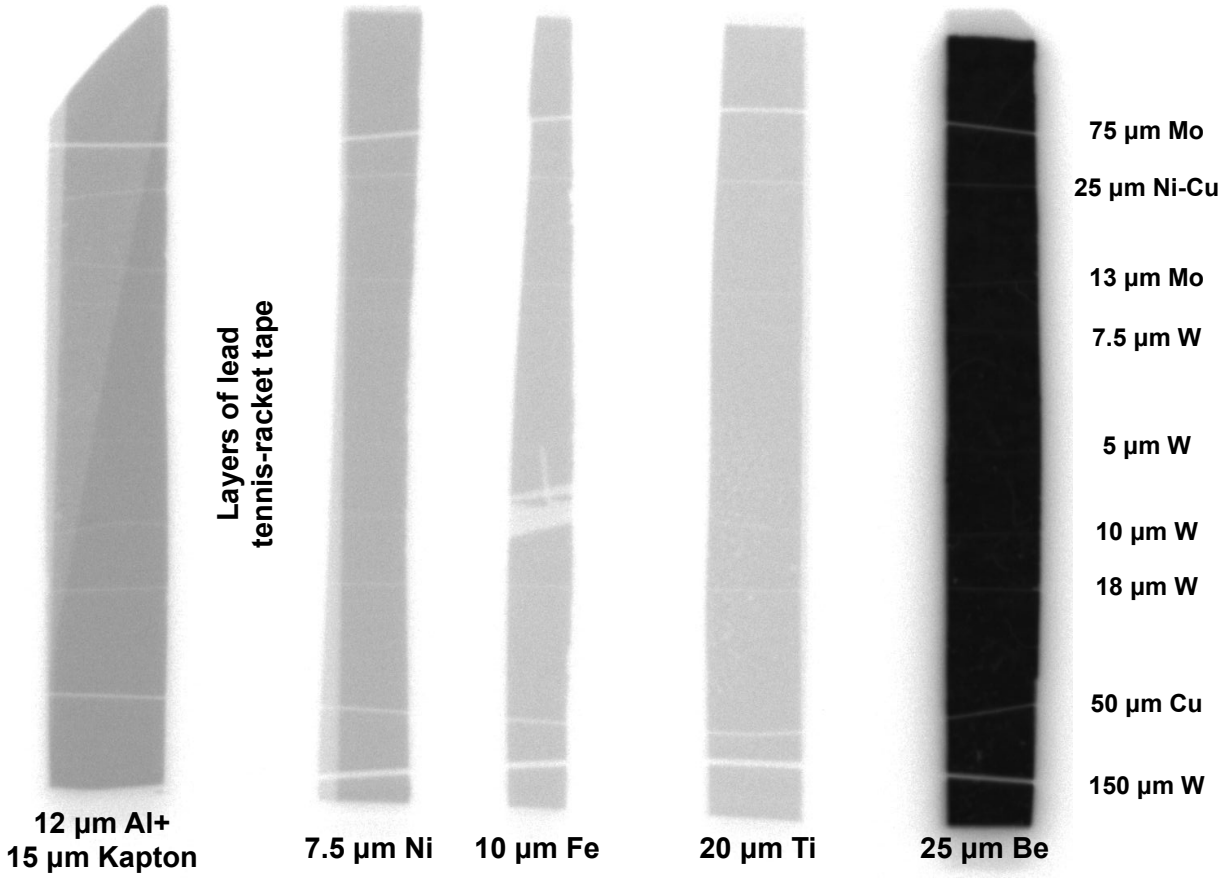

Figure 3.16: A radiograph from the slit-wire penumbral imaging diagnostic from a 25µm Constantan hybrid X-pinch. The different filters and wires used in the array are label, though not all are visible for this particular X-pinch.

Chapter 4

Laser-cut Foil X-pinches

The successful production of X-pinches with nanosecond and micron-scale parameters on a compact, 40 kA peak current, 30 ns rise-time generator by Beg *et al.* demonstrated that quality radiation sources are attainable using space efficient, cost-effective current drivers [83]. Following this, using a compact, 80 kA peak current, 50 ns rise-time current driver, Beg *et al.* used wire X-pinches (WXPs) to characterize small spheres representing inertial confinement fuel (ICF) capsules (with a plastic or low-Z exterior ablator and a frozen DT fuel inside) — the motivation being that even tiny asymmetries in an ICF capsule implosion result in significant performance differences (therefore highlighting the relevance of adequate imaging x-ray diagnostics for ICF and other HEDP experiments) [84]. The experimental capsule was 1 mm in diameter with a 20 μm plastic shell filled with another 80 μm of 10% density plastic foam, and the resulting radiographs clearly showed the boundary layers of the capsules.

The two leading authors on this last work (Ref. [84]), Beg and Stephens, then collaborated to design an improved X-pinch — one that produced single sources, less jitter in emission timing, and could also potentially be developed into a rep-rated X-ray source — using laser-ablation techniques newly developed at General Atomics Inc. to cut a target from a thin foil (see Sec. 3.2.3) [125, 126]. This would become the Laser-Cut foil X-pinch, or LCXP.

4.1 The First Laser-cut Foil X-pinch Experiments

The first foil X-pinch targets produced were made from tantalum and tungsten, cut with LWS1. These materials were deemed safe choices given that W X-pinches routinely produced among the best sources of any material tested on drivers ranging from tens of kA to MA in peak current. While details regarding the overall design and cutting techniques of the laser-cut foil X are given in Sec. 3.2, the cross-sectional dimensions at the crosspoint and the shape of the region within $\pm$ 100 mu m of the crosspoint varied slightly for each experiment described here in Ch. 4 and in Ch. 5. A photograph of a completed Ta foil target (cut on LWS1) is shown in 4.1a. The initial Ta and W foils were 10 or 15 μm thick with a target crosspoint width between 15 and 20 μm across (linear mass of 2.5 - 5.0 $\times$ 10^{-5} g/cm) to make the crosspoint aspect ratio (depth:width) as near to a 1:1 ratio as possible — a benefit of the laser-cut targets over the twisted wires of the traditional WXP. A 10 μm diameter indentation was cut into the crosspoint in an attempt to seed pinching at a specific location. This design and its realization are shown in Figs. 4.1b-c, which show a drawing (with dimensions in cm) and a 50x magnification photograph of the crosspoint — note the $\sim$ 10 μm indentations at the crosspoint in Fig. 4.1c matching the design in Fig. 4.1b, highlighting the precision cutting capability of LWS1. The loaded target is shown in Fig. 4.1d, showing some slight deformation in the base of the target as the manufactured slots shown in Fig. 3.5 serve their purpose, relieving strain from the crosspoint by slight deformation in a non-critical area of the target.

With the laser-cut foil X's designed and manufactured as described in Sec. 3.2.3, and the load hardware completed synchronously (see Sec. 3.2.1), the next step was to load and explode the targets. The former proved a difficult task.

As is evidenced by the distortion of the Ta foil X seen in Fig. 4.1d, loading the targets was an imperfect process. Even $\sim$ 100 μm offsets in the positions of the clamped halves of the load electrodes (about the tolerance of the 0-80 screws holding the two halves together) led to crimping or stretching the foil targets. For the most part, as mentioned earlier, the malleability of the Ta foils

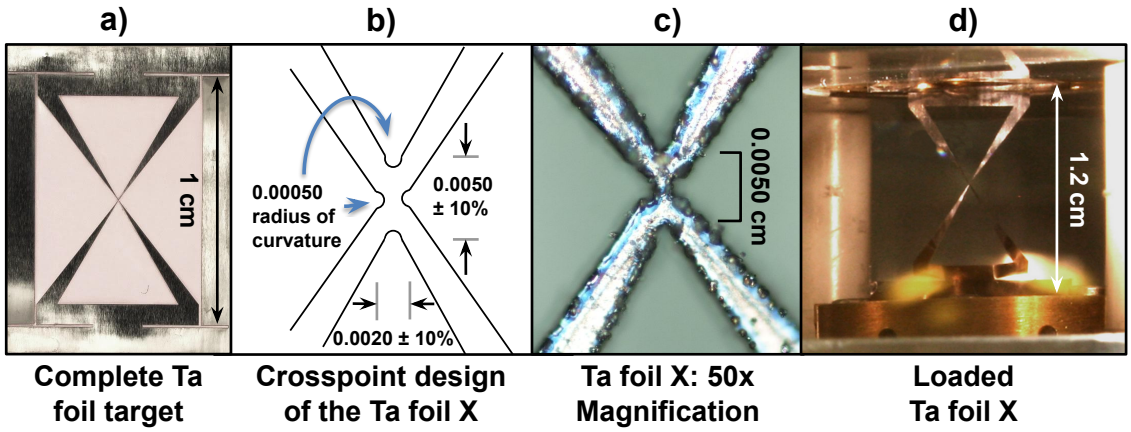

Figure 4.1: a) A photograph of a complete Ta foil X. b) A schematic of the crosspoint with the 10 μm diameters. All dimensions are in cm. c) A 50x magnified photograph of a Ta foil X, showing the final target from the design in frame b, highlighting both the quality of the double-pulse laser-ablation mass removal and the cutting resolution of the LWS1. d) A photograph of the loaded Ta foil X-pinch. Note the deformation at the base of the array introduced during loading.

relieved this introduced strain (if it was tensile) by deforming the base of the target. Removing the spacer post from between the load electrodes and pulling the lateral support tabs of of the clamped and secured target X also introduced slight strains and stresses on the target. All of these factors resulted in a high target casualty rate during loading. As was mentioned at the very beginning of Sec. 3.2.3, both W and Ta foils were cut, with similar crosspoint parameters for the W foils as is shown for the Ta foils. However, with its low deformability and incredibly high tensile strength, W targets did not deform, and simply snapped at the crosspoint, and as such, W targets were deemed infeasible until the engineering problems of loading could be solved (see Sec. 4.2.1).

The few Ta foil X's that were successfully loaded, provided the required information regarding the feasibility of the LCXP as a point source for radiation. Two schlieren images of Ta foil X-pinches from two different shots show the evolution of the coronal plasma, the plasma electrodes, the ablation modulations, and the axial jet of the foil X-pinches. The image in Fig. 4.2a, is from 107 ns after current start, and roughly 70 ns prior to X-ray emission for that particular target, while Fig. 4.2b is at 151 ns after current start (at peak current) and approximately a nanosecond after X-ray emission began (Fig. 4.2 is reproduced from Ref. [13]). One of the initial

questions regarding the LCXP was how the right-angled geometry of the foil X edges (especially at the crosspoint) would alter ablation (and ultimately collapse) when compared to the round, twisted wires in a traditional X. However, observations of the coronal plasma and resulting plasma structures in the LCXPs show no dramatic qualitative differences from traditional WXPs, despite the differences in initial structure (approximately right-angled edges, trapezoidal cross sections, and legs that are considerably wider than they are thick).

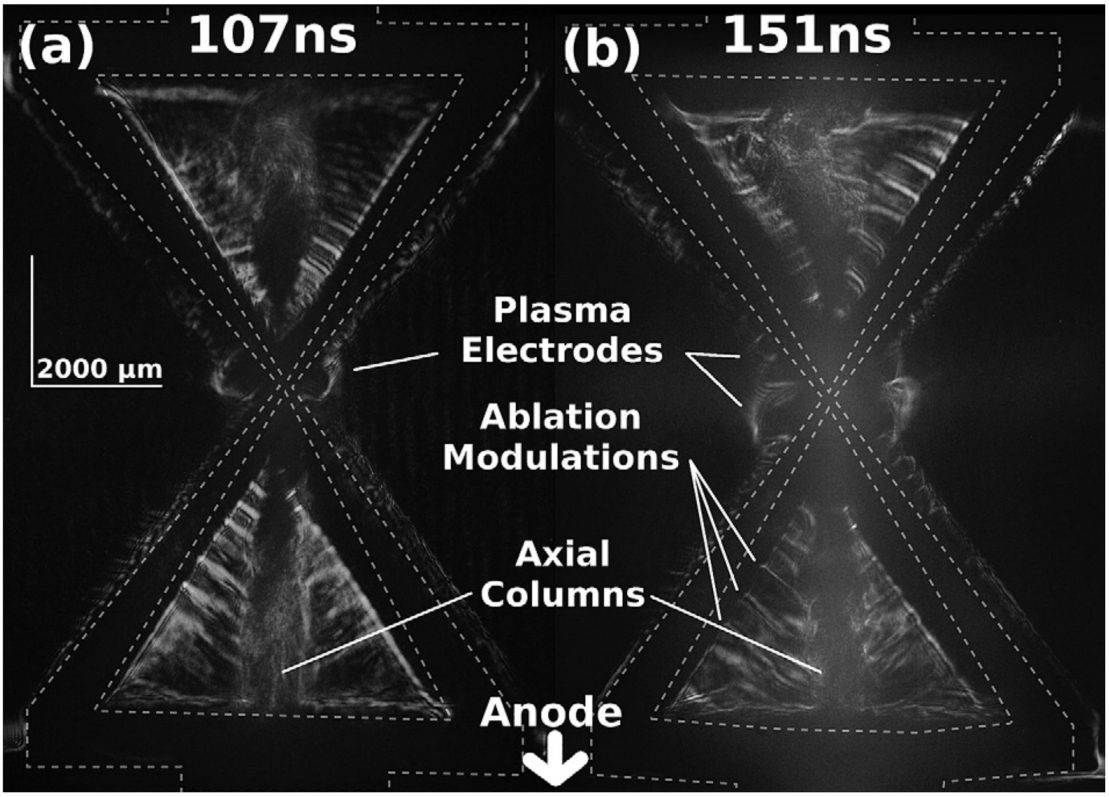

Figure 4.2: Two schleiren images of Ta foil X-pinches at 107 and 151 ns after current start. The original postions of the foil targets are marked with dashed lines. Key features are labelled as well. This figure is reproduced from Ref. [13]

The width of the core-corona structure down the legs of the LCXPs is approximately constant until the crosspoint as is seen in a cylindrical wire, but perhaps was not expected in a tapered leg. Here, the leg regions of lowest mass, and as such the regions subjected to the most significant Joule heating, have the thickest corona (which matches observations of LCXPs at very early times like that seen in Fig. 2.3-1). Whether the changing ratio of core to corona thickness to

maintain a constant total thickness reflects a balance between p_T and p_B, or simply is a product of the reduced ablation in the larger regions is difficult to determine. Concerning the ablation streams towards the axis, prior research showed that the modulation wavelength remains invariant to changes in initial wire diameter, current per leg, and initial surface structures on individual wires, but has a strong inverse relation with atomic mass [152, 153, 192]. The modulation wavelength along the legs of the Ta foil X-pinches averaged 410 μm (σ= 115 μm) —considerably larger than the modulation wavelength measured for tungsten wires in other experiments of $\sim$ 250 μm. The schlieren images in Fig. 4.2 show the modulations wrapping around the outer edge of the foil X legs with a wavelength of $\sim$ 310 μm (σ= 85 μm), which lies closer to the expected range of wavelengths for higher Z materials. Possibly, the large, flat limbs of the foil X-pinch disrupt the typical ablation structure that wraps around the core-corona structure, reducing the number of plasma streams that ultimately propagate towards the axis. Prior to target explosion in these foil X's, as the width of the individual legs increases, calculations of the $\mathbf{B_{Global}}$ to $\mathbf{B_{Local}}$ ratio suggest that the global magnetic field dominates the dynamics all along the individual legs. This potentially explains the relative periodicity of the streams propagating towards the axis all along the legs (especially at later times), in contrast to the observations of more irregular wavelengths along the wires far from the cross-point [156]. As no work has been done to examine the dynamics of tantalum WXPs or cylindrical arrays, there is no data for comparison to the results presented here.

All of this establishes that the LCXP evolves, at least generally, comparably to the traditional WXP. Emission, in pulses of 2 - 14 ns full-width half-max (FWHM) were seen on Al, Sn, Ti, Fe, Ni, and Cu filtered Si PIN diodes. Figure 4.3 shows a plot of GenASIS current (left axis) with five different diode signals in order of hardness — that is to say 2 μm Al transmits the most soft X-rays, followed by 10 μm Al etc. — (right axis) from a Ta LCXP. The broad signal of the 2 μm Al-filtered diode, which transmits up to 6% of photons in the 60-70 eV range, shows the significant amount of extreme ultra-violet (XUV) this X-pinch emits over a long period of time.

The 4-5 ns FWHM pulse seen by the other four diodes shows that there is significant emission between 1-1.5 keV, and the slight ($\sim$ 10%) difference between the Ni and Fe filtered diodes is likely Ta L_α. Total energies, integrated over the pinch time are $\sim$ 50 mJ for the 10 µm Al diode, and 20 - 25 mJ for the harder-filtered diodes, with about 5 mJ of the latter appearing to be Ta L_α, and the remainder likely being continuum. This energy and flux is comparable to W wire X-pinches done on GenASIS.

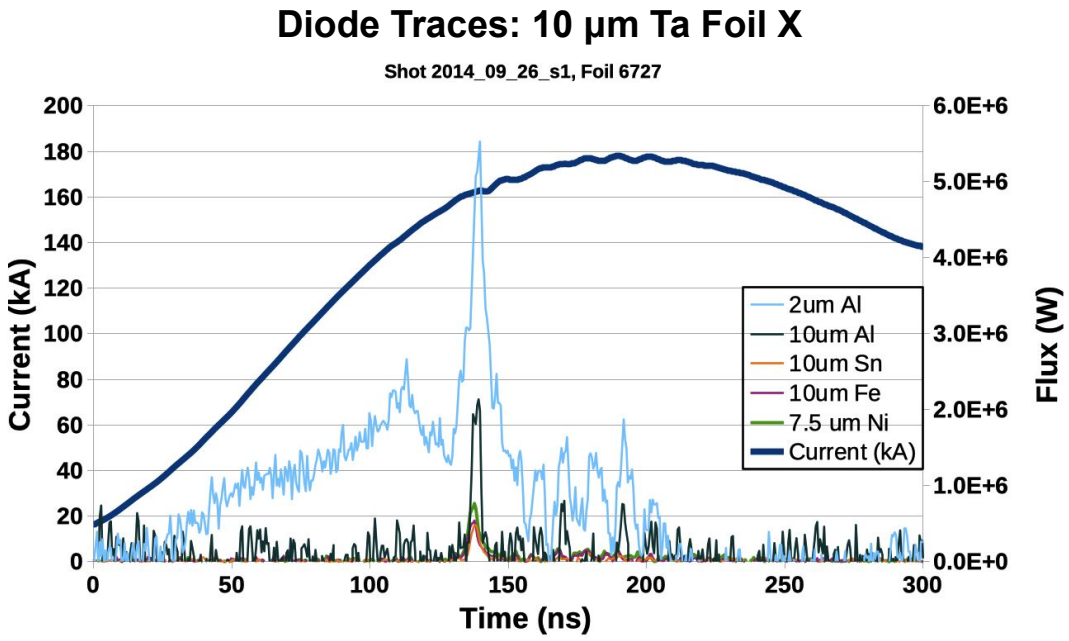

Figure 4.3: A plot showing the GenASIS current trace (left axis) and filtered Si PIN diode signals (right axis) from a Ta foil X. The 2 µm Al-filtered diode shows the large amount of XUV emission coming from the target. The small ($\sim$ 10%) difference between the Ni and Fe filtered diodes is likely Ta L_α, indicating that the comparable emission seen by the Sn, Ti, and Fe diodes is continuum likely below 4 keV.

Radiographs of a honey bee and three different Cu meshes are shown in Fig. 4.4 (reproduced from Ref. [13]), demonstrating the source size of the Ta LCXP and its ability to function as an X-ray source for imaging. The meshes (Fig. 4.4a) were filtered using 3 µm Al foil, while the honey bee (Fig. 4.4c) was filtered using $\sim$ 25 µm heavy-duty household Al foil. The radiographs of the meshes in Fig. 4.4a have been contrast enhanced as the intial film processing was poor, but show the wires and voids in the three different Cu or stainless steel meshes. The mesh wires and

voids are, clockwise from the left: 18.l μm and 7.l μm, 50.l μm (max) and 75.l μm, and 33.l μm (max) and 22 μm (horizontal), respectively. Given the Al filter, this indicates that the size of the source emitting $\geq$ 500 eV photons is $\leq$ 7 μm in size. Cursory calculations of the size of the wires and voids given the magnification and the resolution of the scans agree with this estimate in size. This was determined by taking the difference between the expected and measured width of the wires and dividing by two, to obtain the size of the penumbra, U, and then solving for the source size, S, using

$$U = S * M, \tag{4.1}$$

, where U is the size of the penumbra, S is the source size, and M is the magnification of the image. Note that 3 μm Al does transmit $\leq 2\%$ of photons in the $\sim$ 70 eV range, which may have some effect on source size determination at various energies.

The Ta foil X-pinches established that a flat target with right-angles in the cross-sectional profile, and non-symmetric legs could produce sources with sizes and fluxes on the order of those produced by wire X-pinches. Numerous difficulties also came to light during this initial campaign, two of which would need resolving at the outset of any further experiments.

First, the engineering issues of loading needed resolving, since the rate of damaging or destroying targets reduced the dataset dramatically, and highlighted perhaps the biggest flaw in such a target: the inherent fragility of a target with a few-micron crosspoint. It is worth noting that the meshes shown in Fig. 4.4a and diode signals like that shown in Fig. 4.3 were produced from ideally loaded targets, significantly distorted targets like that seen in Fig. 4.1c and even those where the crosspoint severed during loading. In the later case, the apex of both side of the broken target (where the crosspoint was) were brought into approximate contact, and GenASIS was discharged as usual.

Second, the inductive dips visible in the current trace shown in Fig. 4.3 indicate that even when pinching at peak current, foil X-pinches of this particular design still produce multiple sources — this in spite of the significant mass of the legs adjacent to the crosspoint — though it

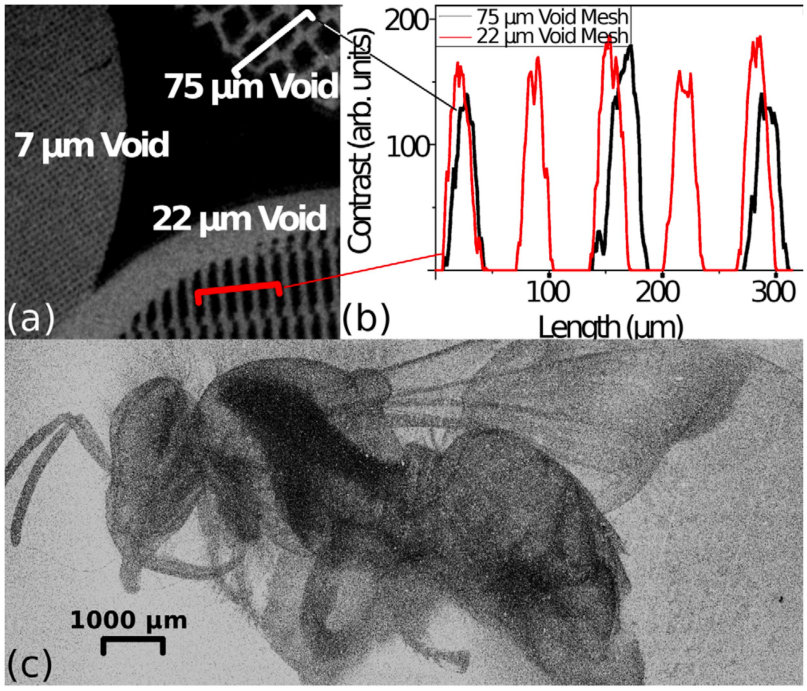

Figure 4.4: (a) Radiograph of Cu and stainless steel meshes, with wires and voids clockwise from the left of 18.1 µm and 7.1 µm, 50.1 µm (max) and 75.1 µm, and 33.1 µm (max) and 22 µm (horizontal), respectively. Meshes were filtered using 3 µm Al. (b) Lineouts of two of the meshes (contrast was enhanced using photo-editing software). (c) Radiograph of a honey bee directly behind a 25 µAl filter (made of heavy-duty household Al foil). Figure is reproduced from Ref. [13]

was not determined whether these were electron beams or hot-pinches. Thus, future experiments would require some degree of target redesign with additional mass or a change in crosspoint shape and an improvement in the diagnostics used.

4.2 Characterization of Cu Laser-Cut Foil X-pinches

A second LCXP campaign using Cu foil X's was conducted to resolve, at least in part, the issues highlighted at the end of Sec. 4.1. Copper was chosen for a variety of reasons including the general robustness of Cu as a material, its generally low cost, the availability of Cu wires to use in WXPs for direct comparison, and a specific interest in 8 keV photon sources (Cu K_α) for, amongst other purposes, flat-fielding X-ray cameras and use in Talbot-Lau deflectometry diagnostics [64].

For these experiments, the Si PIN diodes were cross-calibrated using a consistent 25 μm Al filter across all diodes and following the procedure described in Sec. 3.3.2. Cross-calibration was also completed between the diamond PCDs the Si PIN diodes. Additionally, the Cu LCXP experiments included the HOPG and MICA crystal spectrometers described in Sec. 3.3.4. The meshes were supplemented or replaced with the slit-wire array described in Sec. 3.3.5, which though the latter had lower magnification, allowed source size determination across multiple energy ranges.

However, regardless of diagnostic improvements, before completing any further LCXP experiments the loading process needed significant engineering and operational improvements to sharply reduce the number of targets damaged or destroyed during loading.

4.2.1 Resolving the Target Loading Issues

Improving both the target design and loading procedure represents a continuing process, but since many key observations and improvements were made during the intial Cu LCXP experiments, the majority of the process is described here.

Compared to wire X-pinches, the material clearly plays a role in foil target strength and durability. Copper, compared to the previously tested W and Ta foils, is quite a malleable material, but does not have as high a tensile strength. This makes Cu targets more robust in terms of correcting any accidental damage introduced during loading, but also quite prone to target distortion. The density of Cu is also less than half that of W and Ta, so the Cu target's cross-sectional area can be higher than that of the more dense, higher Z targets in order to produce the same cross-sectional or linear mass at the crosspoint.

Observing the target side-on (simply the flat foil profile) during vacuuming down as the chamber went from atmosphere to $\sim$ tens of microTorr revealed perhaps the key problem in the LCXP target loading process: a small amount of flexing between the anode and cathode of the GenASIS power feed during pumpdown was causing the targets to bow or crimp at the crosspoint.

Such crimping is shown in Fig. 4.5a, which shows schlieren images of the target immediately after loading, after vacuum pumpdown, and during current discharge. The significant amount of bending ocurring between the just-loaded and the vacuumed-down images is clear. This bending was never previously noticed, since when using weights and gravity to maintain tension in a wire X-pinch the wire freely slides against the cathode (as is seen in Fig. 1.6) if any change in electrode spacing occurs. This meant that the cathode (bottom) end of the foil X must be unclamped to allow it the freedom to slide vertically in the cathode when the chamber compressed. The result of leaving the target unclamped at the bottom is evident in Fig. 4.5b, which shows the same sequence of schlieren images (immediately after loading, under vacuum, and during discharge) highlighting the lack of crimping when the bottom of the array can freely slide inside the cathode.

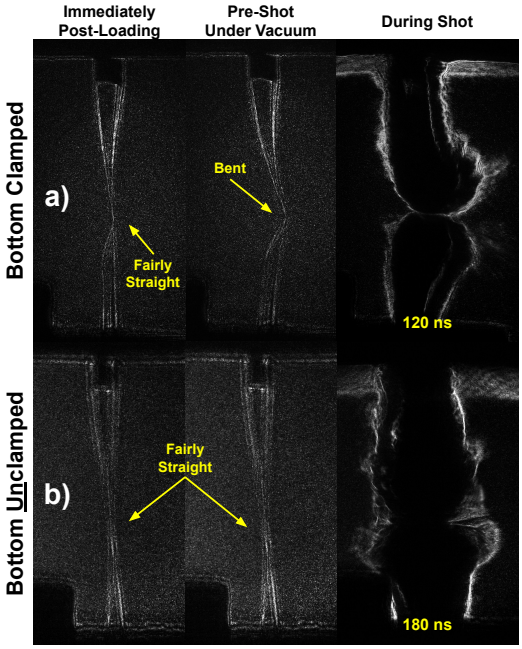

Figure 4.5: Schlieren images of targets with a) clamped and b) unclamped cathodes immediately after loading (ideally straight), after vacuum pump-down (chamber flexes, crimping the clamped target), and during discharge (with times relative to current start given at the bottom of the figures).

For the remainder of the experiments described in this section (Sec. 4.2), the foil X design remained the same, and the targets were loaded into GenASIS fully clamped, then the support

tabs were removed, and then the cathode was loosened (which as mentioned, allowed the foil X to move vertically within the cathode in the event of inter-electrode flexing). For some shots, split-shot lead weights like those used to maintain tension on wires in WXPs (see Fig. 1.6a,b) were attached to the bottom of some foil X's so that the array would remain as straight as possible, but the potential for damaging the target was ultimately too high, and this practice was abandoned after demonstrating only a slight improvement in target reliability over the unweighted, unclamped X's.

Loading and design improvements continued during the work discussed in Chap. 5, but will recieve attention here for the sake of subject continuity. We observed that loosening the cathode after removing the tabs often distorted the target as much as the vacuuming down process in a clamped target. Removing the lateral support tabs altogether from the target design during the laser-machining process allowed the X to be clamped into the load anode and lowered into the slightly open cathode already mounted in GenASIS. This removed both the need for a spacer during loading (and its subsequent removal) and more importantly, the inevitable strains introduced by pulling off the support tabs and loosening the cathode. This decreased target loading time by a factor of 2-3. While some Cu targets would bend slightly during transport from the target cutting facility to GenASIS, and also during loading, this tended to be simple planar bending rather than warping, bowing, or crimping of the crosspoint, and as such, was easily corrected manually. Note that this bending did not happen in more rigid materials such as Mo, Ni, Ti, and Al, though those materials lie outside the scope of this dissertation.

Experiments using this 'floating-cathode' method of loading produced identical peak currents to those when both ends of the X were firmly clamped in. Far more importantly, loading targets without lateral supports and leaving them unclamped reduced the number of targets broken or irreparably damaged during during loading and discharge to zero.

4.2.2 Testing Different Crosspoint Designs

The ability to design the initial structure of the target down to micron scales represents one of the most promising strengths of the LCXP. This was tested to some degree with the Ta foil X's, resulting in little definitive information (see the indentations in Fig. 4.1). However, following observations that many of the Ta LCXPs still produced multiple sources, and could potentially have been under-massed, a variety of modifications to the crosspoint design initially used (see Fig. 3.5) were proposed. These included the 'indented', 'hyperbolic', and 'simple' X crosspoints, as shown in Fig. 4.6. The alterations to the crosspoint that give each design its namesake proceed no further than $\sim$ 150 μm from the crosspoint in either axial direction, and all other features and dimensions of the greater target remained the same.

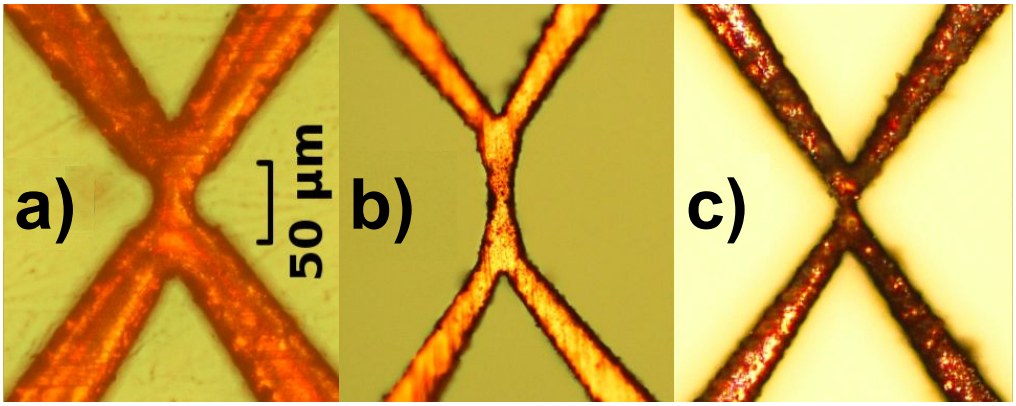

Figure 4.6: Magnified photographs of the three different Cu LCXP crosspoint configurations tested. These were a) The 'indented' X, b) the 'hyperbolic' X, and the 'simple' X.

Laser-Cut Cu Foil X-pinches with an Indented Crosspoint

The first crosspoint design tested was the indented target shown in Fig. 4.6a. The indentations were of the same hemispherical shape as those 10 μm features in the Ta foils, but were instead 50 μm in diameter. The large indentations were intended to serve two purposes: limit the number of sources, since the Ta foils appeared to produce multiple X-ray spots, and to serve as the basis for large plasma electrodes that would limit the pinch location (perhaps as was seen from

the conical electrodes in a hybrid X-pinch), since the significant additional mass at the edges of the indentation would remain longer than the crosspoint.

However, the indented Cu X's did not pinch. A schlieren time sequence of these X-pinches is shown in Fig. 4.7, with times relative to current start given at the top of each frame. Note that the indented LCXPs show no signs of micro Z-pinch formation. In fact, the features designed to inhibit multiple sources appear to project plasma laterally away and axially into the crosspoint region, as denoted by white arrows in Fig. 4.7c and d. These ablation features serve to further widen a crosspoint region already clearly lacking any sort of necking.

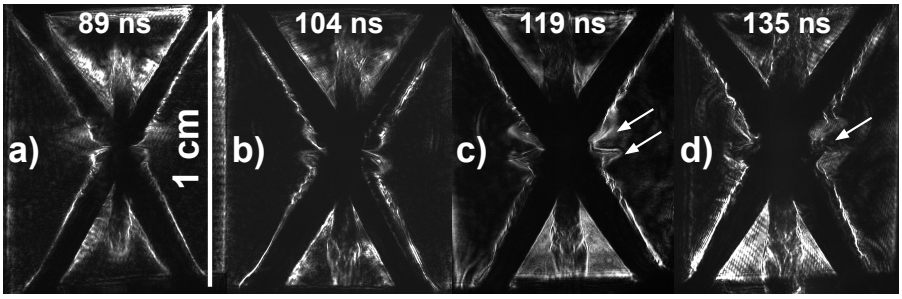

Figure 4.7: A schlieren time sequence of an indented Cu LCXP with times relative to current start given at the top of each frame. The key to the failure of this array type appears to be the ablation features marked with white arrows in frames c and d. Rather than forming larger plasma electrodes that limit the pinch region, the edges of the indentations appear to feed ablation that close the gap prematurely, inhibiting pinching.

To validate this observation, once loaded into GenASIS, the load anode was rotated on a handful of indented foil X's so that the top and bottom of each indentation were orthogonal. The thought was that the ablated plasma from each edge of the indentation would no longer propagate into direct contact with the opposing ablation. About two-thirds of targets discharged in this fashion produed very small ($\leq 3\%$) of the X-ray flux seen in other Cu X-pinches. Clearly, the large horizontal features with their abrupt edges transitioning towards the crosspoint were a hindrance as opposed to a help in terms of pinching.

Laser-cut Cu Foil X-pinches with a Hyperbolic Crosspoint.

Given the clear failure of the targets with large indentations, a crosspoint was designed using a semi-hyperbolic sweep into and out-of the crosspoint, shown in Figs. 4.6b, and 4.8. Figure 4.8a shows a drawing of the planned target with the key target parameters labeled in cm, while Fig. 4.8b shows a magnified photograph of the the laser-cut target at the same scale as the drawing. The plan was to seed pinching in the long crosspoint neck where the array was narrowest, and then shorten the neck in subsequent designs iterations until only one source was reliably produced.

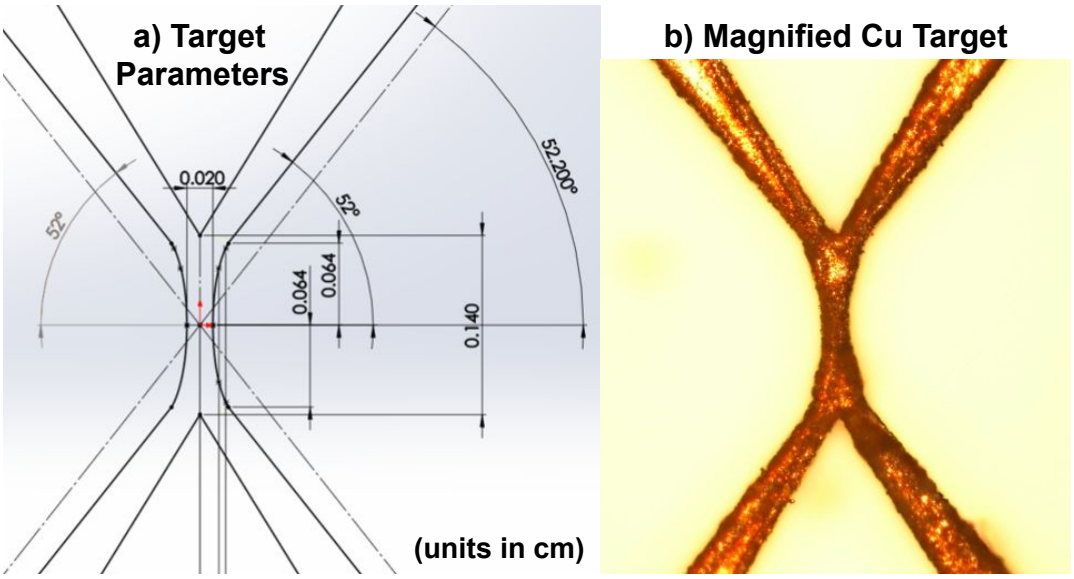

Figure 4.8: (a) A drawing of the hyperbolic crosspoint design with key measurements labeled in cm. (b) A magnified photograph of a 30 μm thick, Cu hyperbolic X at the same relative scale as the drawing.

The hyperbolic X proved a marked improvement over the the indented X's. Pinch outcomes related directly to the quality of target loading. The changes described in Sec. 4.2.1 began during these hyperbolic X-pinch shots, since the long, thin neck of the target amplified the general fragility of the LCXP and the crudeness of the loading process. When successfully loaded, the hyperbolic X-pinches produced (as we will subsequently show) sources with parameters matching or exceeding Cu WXPs also conducted on GenASIS. The remainder of the LCXP results discussed in Sec. 4.2 are split between the hyperbolic X and the subsequently discussed simple X.

Laser-cut Cu Foil X-pinches with a Simple Crosspoint.

The 'simple' crosspoint, as shown in Fig. 4.6c, is — just as the name implies — a simple angled transition in and out of the crosspoint. This change arose out of a desire to strengthen the array, since while the hyperbolic arrays produced good X-pinches, even with improvements to the loading process, the target still proved incredibly easy to deform. The simple X proved far more robust than its hyperbolic cousin.

All of the simple X's were cut using the TRUMPF system, rather than the higher resolution LWS1. This platform produced more varied targets, with coarser features as was described in Sec. 3.2.3, and revealed by microscopic inspection (which produced the images seen in Figs. 3.4b,d and 4.6c). Simple X's pinched reliably, producing smaller and brighter sources than comparable Cu WXPs on GenASIS. Results using this configuration will be differentiated from those using the hyperbolic crosspoint for the remainder of Sec. 4.2.

Figure 4.9 suffices as a concluding remark on the differences between the different foil targets, showing schlieren images of an X, with timings relative to current start (and relative to pinch timing in parenthesis) given at the bottom of each frame. The micro Z-pinch clearly forms in the simple and hyperbolic X's, and never forms in the indented X. The hyperbolic X, despite pinching well, was prone to some degree of distortion, which is clear by the askew angle of the crosspoint and legs.

4.2.3 Comparing the evolution and pinch characteristics of copper laser-cut and wire X-pinches

The remainder of Chap. 4 describes the performance of Cu LCXPs. This is done largely by comparing them to Cu wire X-pinches with comparable linear mass at the crosspoint (to the LCXPs) which provided a performance benchmark for the LCXPs. As such, the remainder of this

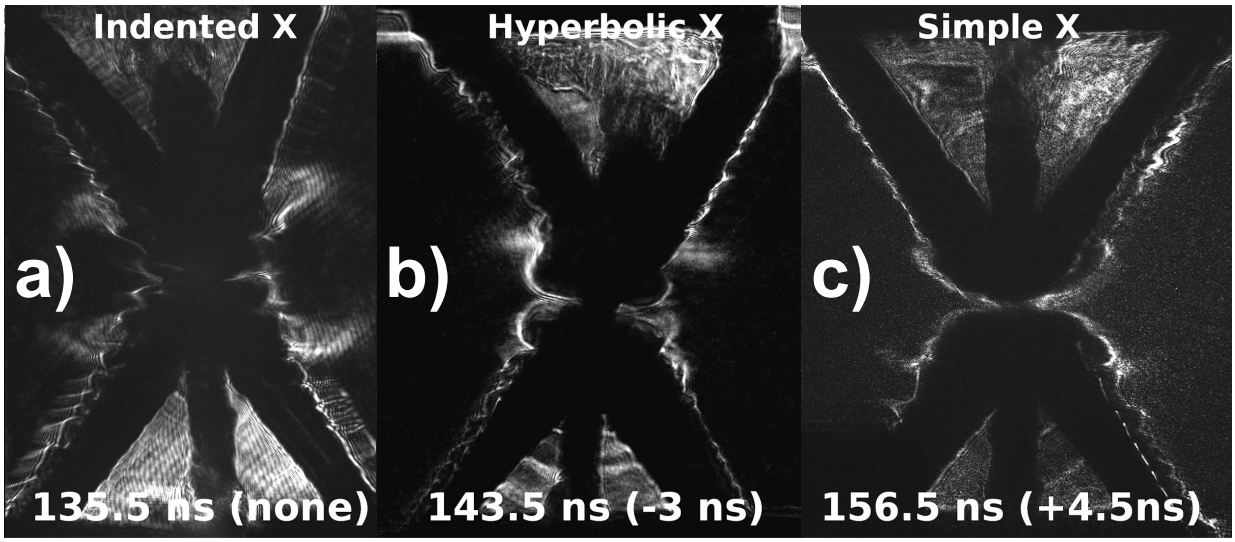

Figure 4.9: Schlieren images of the three variations of Cu foil X-pinch: a) indented, b) hyperbolic, and c) simple X. The timings relative to current start are given (time relative to pinch given in parenthesis). The indented foil did not pinch.

chapter presents the data from both laser-cut and wire in tandem.

The evolution of Cu laser-cut and wire X-pinches is shown in Fig. 4.10b and c respectively, with schlieren images of simple foil X's and 18 μm x 25 μm Cu 2-wire X's at relevant stages of the current drive (reproduced from Ref. [14]). The linear (cross-sectional) mass at the crosspoint of these two arrays is $\sim$ 5-6 $\times$ 10^{-6} and 6.7 $\times$ 10^{-6} kg/m respectively. While the general evolution process (expanding, ablating, and then pinching) of the different targets is comparable, the rate at which they evolve is markedly different. By $\sim$ 50 ns after the current start, the wire X-pinch has expanded and ablated considerably while the larger sections of the legs in the foil pinch at the same time have barely expanded. Similar coronal plasma evolution was seen in the Ta LCXPs described in Sec. 4.1. The disparity in the expansion of the wire and foil targets, and the apparent amount of coronal plasma formed makes sense given that the amount of ablation should relate to both the current skin depth and the total surface area per unit length. The latter quantity is significantly larger in the foil X-pinches away from the crosspoint (than in the wire X-pinches), which understandably reduces the amount of current flowing though each unit-area of the LCXP, and thus spreads the energy deposited by joule-heating over a larger area.

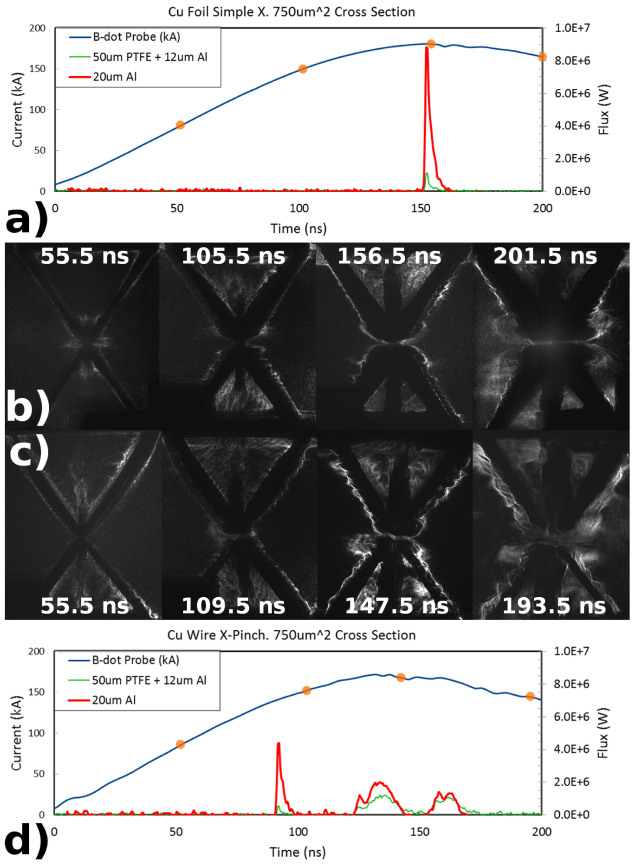

Figure 4.10: a) Current, Al filtered PCD, and Al+PTFE filtered Si diode traces from a simple foil X-pinch. b) Schlieren images showing the time evolution of the foil X-pinches. c) Schlieren images showing the time evolution of 18 x 25 μm Cu wire X-pinches. d) Current and diode traces from a wire pinch. The dots on the current traces approximate the times of the schlieren frames. This figure is reproduced from Ref. [14].

Perhaps less expected is the disparity in pinch timing displayed in figures 4.10a and d, which show the signals from the Al ('soft' X-rays, $\geq \sim 900$ eV) and Al+PTFE ('hard' X-rays, $\geq$ 3 keV) filtered diodes to illustrate the relationship between the evolution of the X-pinches and the emission. The foil X's typically pinched at or near peak current with a single, 2.5-3 ns full width half max (FWHM) X-ray pulse containing both hard and soft X-ray emission (Fig. 4.10a). In the wire pinches, the first emission is generally a ≤ 2 ns FWHM pulse occurring at or before 100 ns, after which the X-pinch breaks apart and the two halves separate. Ranging from 20-60 ns after the first emission, longer (≥ 10 ns FWHM) pulses of X-ray emission comprised of predominantly hard X-rays occur (note the ratio of the flux detected between the Al and Al+PTFE filtered diodes

in the later emission), indicative of emission from electron beams (Fig. 4.10d). The dots placed on the blue GenASIS current trace (left axis in Figs. 4.10a and d) represent the approximate timing of the schlieren frames shown in Figs. 4.10b and c respectively.

The trend in wire X-pinch behaviour shown in Figs. 4.10c and d, with the the early soft emission, array separation, and late electron beam emission was observed in wire pinches with 40 percent less and 30 percent more mass than this configuration as well. The reliability of emission from the heavier wire X's decreased though the percentage of single peaks increased, while the timing and number of sources grew significantly more irregular with the lighter wire pinches.

Time integrated X-ray pinhole images of the X-pinch source from aluminized mylar (Al-My) filtered pinholes (which transmits predominantly the Cu L-shell and above) are presented in Fig. 4.11, with a) a simple LCXP, and b-d) 3 different 18 x 25 μm 2-wire WXPs. The simple LCXP source in Fig. 4.11a is slightly longer in the axial (y) direction, indicative of an elongated source, a moving source, or multiple sources within the geometric resolution limit of the pinhole camera. The geometric resolution of this pinhole camera was $\sim$ 40 μm, so unless the source is $\sim$ 100 μm in size, there is likely a degree of saturation given the amount of transmission the Al-My filter allows. Figures 4.11b-d show how WXP sources vary in both the size and number of sources produced.

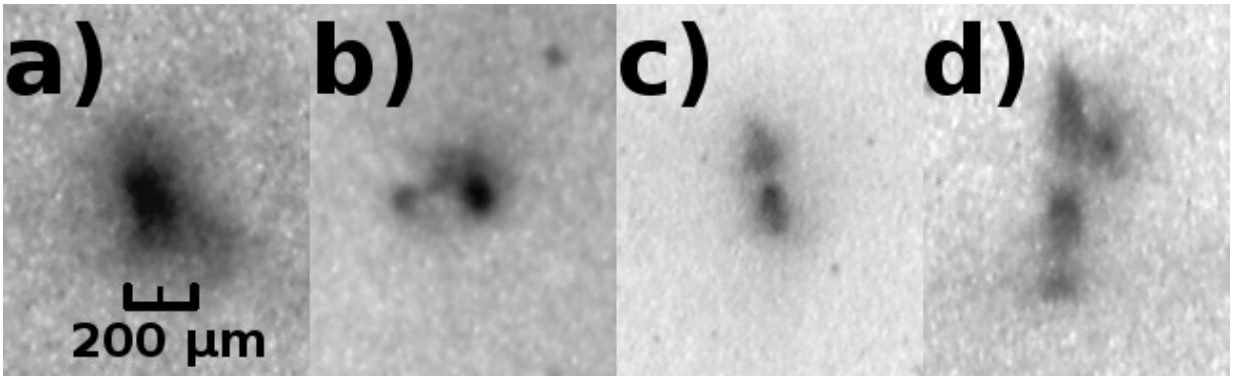

Figure 4.11: Time-integrated images from a 25 μm diameter, aluminized mylar filtered pinhole. A typical foil image is shown in a), while b-d show the range of emission location and sources typical from wire pinches, from a single source in b to many in d. This figure is reproduced from Ref. [14].

Radiographs from the penumbral slit-wire array from foil pinches imaged the smallest wires (either 5 or 7.5 μm W) across all filters transmitting above ∼3 keV (on the Ti, Fe, Ni, and Al+PTFE filtered slits). Below 3 keV, the significant amount of exposure often washed out the smallest wire, imaging only the 7.5 or 10 μm wires. This supports observations of saturation in the Al-My pinhole images. By changing the orientation of the wires in the slitwire array from vertical to horizontal for different shots, we again saw that the sources were slightly larger in the vertical direction, indicating either an elongated source, a moving source, or two sources within tens of microns of one another. In some of the hyperbolic LCXPs, this appeared to clearly be a second, fainter source, as there was a second, overlapping image of a wire, meaning this second source was within ∼ tens of μm of the brighter source. Occasional wire pinches (like that shown in 4.11b) imaged 7.5 or 10 μm wires in the slitwire array, but many more failed to image any but the biggest (∼ 125 to 300 μm) wires or meshes. The limitation of the wire X-pinches as a radiographic tool here is not in their ability to pinch and produce small sources, but in the numerous additional sources that double or triple expose the target. Since the greatest flux of hard X-rays in wire X-pinches comes from the late e-beam generated emission that lasts ∼ 10 ns and because the source produced by the electron beam is moving at the rate of the plasma electrodes, these electron-beam photon sources appear even larger than their actual spot size. Additionally, the actual size of the X-pinch sources is difficult to determine since the transmission of 8 keV photons through the smallest W wires in the slitwire camera is high enough complicate the penumbral imaging.

While the dataset is still limited, the filtered Si PIN diode data from the Al+PTFE filtered diode in figure 4.12a show the extreme reliability of the under-tension hyperbolic X's made with LWS1, with ≤ 5 % variability in timing and ≤ 10 % variability in flux. Hyperbolic and simple X foils from the TRUMPF platform showed more varied X-ray fluxes and pinch timings but the hard emission was still confined to a single pulse per shot (within the 1-2 ns temporal resolution of the diode-scope system). In contrast, a sample of the characteristic signals from 18 x 25 μm wire

X-pinches (again on the same diode) can be seen in figure 4.12b, clearly showing the temporal variablity of the hard X-ray pulses. Note the early peaks at $\sim$ 95 ns which coincide with the dominant soft X-ray peak, and the subsequent higher-flux, longer-duration e-beams later in time.

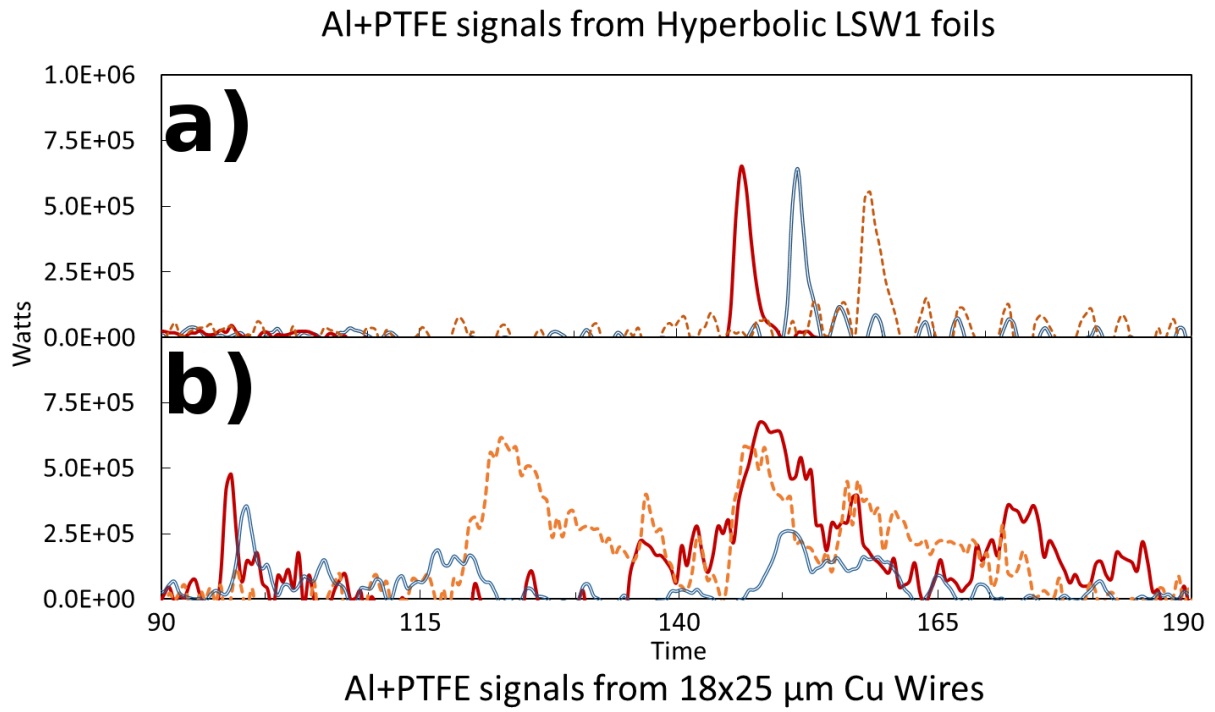

Figure 4.12: Signals from the Al+PTFE filtered Si PN diode which includes all transmission above $\sim$ 3 keV. a) Shows the signals from all pinching hyperbolic LWS1 targets and b) shows typical signals from 18 x 25 µm wire X-pinches. This figure is reproduced from Ref. [14].

Due to the 10% error in diode cross-calibration, the Ross filter-pairs (mentioned in Sec. 3.3.2) yield only order-of-magnitude approximations. As such, we estimate the ratio of L-shell to continuum to K-shell photon flux to be about 100:10:1, representing the differences in energy seen by the Al or Be filtered diodes (flux above $\sim$ 800 eV), the Al+PTFE filtered diode (only photons $\geq$ 3 keV), and between the Al+PTFE and Ni or Fe filtered diodes (assumed to include primarily Cu K-shell line emission). Depending on the actual quantity of L-shell emission through the 1-1.5 keV Al transmission window (a hotter, denser plasma shifts much of the L-shell emission beyond 1.5 keV), the Al-filtered diamond PCD detects about 50 MW peak flux. The Al+PTFE

diode averaged 1-2 MW (max of $\sim$ 6.5 MW), and we estimate about 10 percent of that flux to be solely from K-shell photons (via the consistent difference between the Al+PTFE, Cu, Ni, and Fe-filtered diodes at approximately the error margin of the diode calibration).

4.2.4 Spectroscopic Data from the Cu Laser-cut and Wire X-pinches

We obtained spectra from both the Cu L and K-shell from the convex mica and HOPG spectrometer respectively. When calculating the Bragg angle for both spectrometers, the location of the source is determined using the schlieren images to measure the location of the crosspoint or plasma anode at the time of emission. If the X-ray emission occurred after separation of the X, the plasma anode was used as the source location, and if emission occurred before or at the time of separation the crosspoint was used as the source location. Some wire X-pinch spectra are best described by emission from both locations.

L-shell spectra from both Cu foil and wire X-pinches from the convex mica spectrometer show similar lines and line-ratios (as seen in figure 4.13) indicating that both types of X-pinch share a similar stage of evolution and emission. We have labeled the prominent n=3 to n=2 transitions visible in the spectra. The most noticeable difference between the foil and wire X-pinches is the lower intensity of the 3F line relative to 3G. This ratio is sensitive to opacity and ionization effects, and may indicate that the foil pinches have a slightly lower ionization than the wire pinches.

The K-shell spectra from foil and wire X-pinches differ considerably. Figure 4.14 shows K-shell spectra obtained with the HOPG spectrometer of a typical Cu foil and wire X-pinch. Both spectra show prominent partially ionized Cu K_α, and at the lower detection levels, often weak K_β emission. Additionally, the foil spectrum shows K-shell emission from highly ionized Cu ($\sim$ Cu XXVI-XXVIII) at around 8300 eV. Cu wire X-pinches show no clear end to the cold K_α emission or beginning of the hotter 2p-1s emission. This could be due to the presence of multiple sources with strong spatial and temporal gradients in temperature resulting in emitting regions with parameters between those of the primary sources (such as the two peaks seen in the foil spectrum),

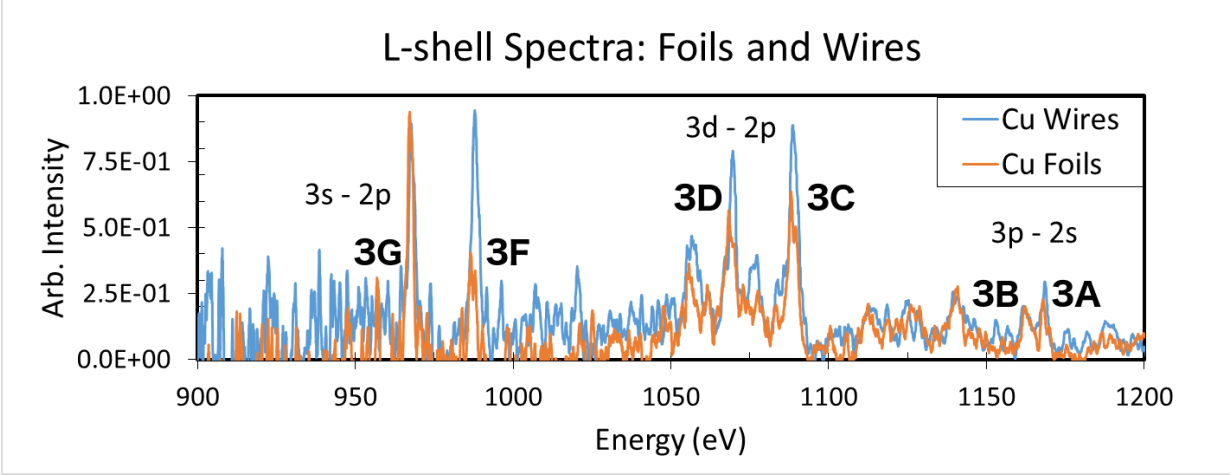

Figure 4.13: Traces of spectra obtained on the convex mica spectrometer from both Cu foils and wire. Labels of the main transitions are included. This figure is reproduced from Ref. [14].

or possibly the blurring that would occur if the source was moving at the rate of the plasma anode measured from this and previous experiments [97] for the duration of the late electron beams.

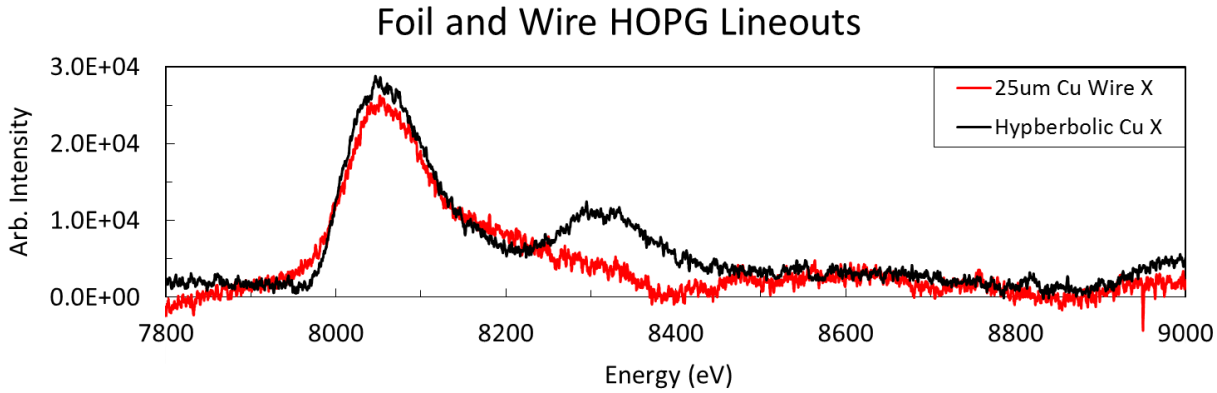

Figure 4.14: Traces from typical HOPG spectra obtained from Cu foils and wires. This figure is reproduced from Ref. [14].

4.2.5 Determining the Plasma Parameters during X-ray Emission for Cu Pinches

At this point, we compared the spectra obtained experimentally to synthetic spectra created by the SCRAM code (Refs [188–190]), to estimate the plasma parameters (ion and/or electron density: n_i and n_e respectively, temperature, and average ionization: Z^*) of the foil X-pinches during X-ray emission. When trying to match synthetic and experimental spectra, one needs to know the appropriate parameters to adjust. Increasing electron or ion density in the plasma typically increases the X-ray flux emitted and the width of the spectral lines (but the latter is generally not a concern here with the HOPG spectrometer given its low resolving power). Hotter plasmas tend to have higher ionization levels, so characteristic lines increase in energy as temperature increases. Spectroscopic codes give spectral intensities in units of energy per unit time, which can be summed over specific energy band-widths to get the total flux emitted over specific ranges. With the absolutely calibrated diodes and their Ross filter pairs we can estimate the total energy in each Ross pair bin by integrating the flux over time (typically FWHM). We can then look for the appropriate temperature and density combination in the simulations to match the line energies, relative intensities, and total fluxes and energies emitted in specific bands. To simulate a plasma with an electron beam, we set some percentage of the simulated electrons at a separate temperature from the primary plasma. We estimated the energy of the beam electrons at between 10 and 30 keV, and ran simulations with various percentages of total electrons from 0 to 15% at this second electron temperature.

Immediately, attempts to characterize the K-shell emission showed that the two distinct K_α lines could not be characterized by a single plasma. The cold K_α (and K_β) emission seen at $\sim$ 8050 - 8100 eV (and $\sim$ 8900 eV) is only produced from a partially ionized ($\sim$ Cu XX or less) Cu atom. As the temperature of the plasma increases, the energy of the lowest K_α lines increases as well, so the second peak seen at 8300 - 8400 eV in the foil spectrum appears to come from a more highly ionized ($\sim$ Cu XXVI-XXVIII) plasma. So, we must find two separate sets of plasma

parameters; one hot, and one cooler.

As mentioned, since the line energy depends primarily on the plasma temperature and we are confident with our spectrometer calibration, estimating the plasma temperature for the synthetic spectra is presumably straightforward. With a general temperature estimate in hand given the energy of the lines, we must make some assumptions based upon the other diagnostics in order to best approximate the conditions in the multiple sources we suspect. The pinhole camera images from foil X-pinches (see Fig. 4.11a) typically show one large emission spot on the order of 100 - 200 μm so the distance between sources must be less than this. Since the slitwire camera clearly shows single wires $\leq$ 7.5 μm in size, one source must be of this order or smaller and the other, if not in the exact same location, must be large enough to not resolve the wires a second time. The pinhole and slitwire data shows that wire pinches producing only cold K and L-shell spectra do not image the smallest wires, instead imaging only the largest wires, suggesting a source that is 100 - 200 μm across. From this, we assume that the highly ionized K_α line which appears concurrently with the smallest sources via the slitwire camera is produced from a 1 μm^3 source, while the colder K_α source will come from a plasma of either 1 or 8 x 10^6 μm^3 (characteristic linear dimensions of 100 and 200 μm respectively).

Data from the filtered diodes further constrain the sources, providing measurements of the total fluxes above $\sim$ 0.9 and $\sim$ 8 keV. The total X-ray emission as mentioned in Sec. 4.2.4, is on the order of 50 MW, while the K-shell emission ($\geq$ 8 keV) is approximately 0.5 MW. Using the source size assumptions, we may sum the synthetic line intensities across all energies to obtain total flux. Since the hard-filtered diodes do not see multiple emission peaks, both sources must occur within a 3 ns window (the average for all hard and soft X-ray pulse widths from the pinching foils was a between 2.5 and 3 ns), which is near the temporal resolution of our system. We will assume that two sources emit for 1 ns each, allowing us to estimate the total X-ray flux and energy produced by the synthetic plasmas and compare this to the experimental diode data.

From these estimates and assumptions we can suggest potential X-ray emission scenarios.

All scenarios involve a hot pinch producing a dense, micron-scale plasma with a temperature near 1 keV, $n_i = 10^{22}$ cm^{-3} (over 10% solid density, $n_e = 2.6 \times 10^{23}$ cm^{-3}), and $Z^* = 26$ (it is worth mentioning that this temperature and density estimate matches the ranges estimated in the X-pinch experiments conducted with a faster rising but similar peak current mentioned in reference [69]). The synthetic spectrum from such a plasma, with instrument broadening applied to match the HOPG spectrometer, is seen in the purple dashed line in figure 4.15. For reference it is plotted against the foil K-shell spectrum shown earlier in figure 4.14. This plasma produces about 8 MW of total (L and K-shell) X-rays, and about 100 kW of K-shell X-rays. After termination of the pinch, the sound speed of this plasma is fast enough to clear the mass out of a 200 μm gap at the center of the X-pinch in $\sim$ 1 ns, providing space for an electron beam to occur.

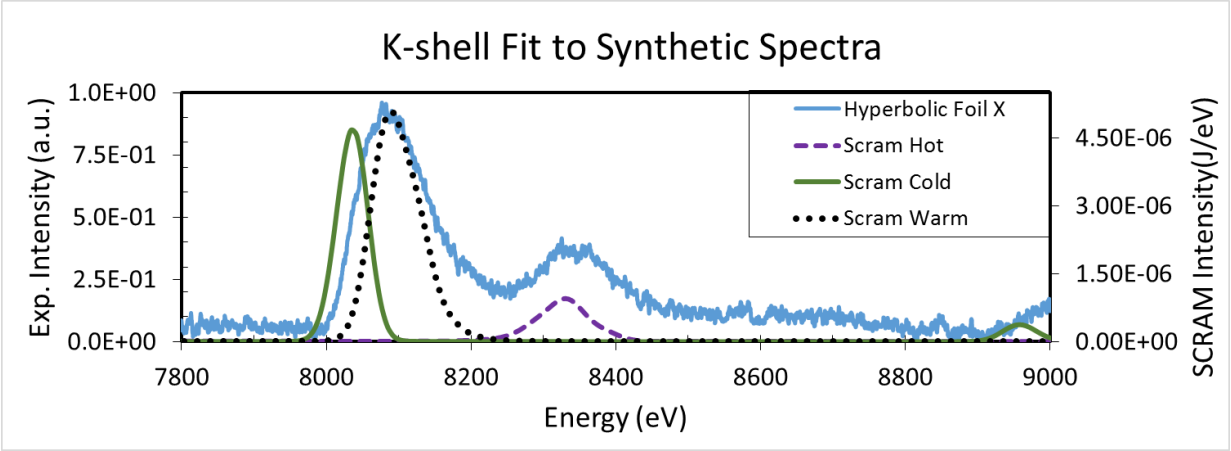

Figure 4.15: A K-shell spectrum from Cu foil X-pinch (blue line) with three different synthetic spectra overlaid: a coronal (30eV, $n_e = 6 \times 10^{19}$ cm^{-3}) plasma with 5 % fast electrons (solid green line), a 200 eV, $n_e = 3 \times 10^{20}$ cm^{-3} plasma with 5 % fast electrons (dotted black line), and a 1000 eV, $n_i = 10^{22}$ plasma (dashed purple line). The experimental spectrum is plotted in arbitrary units of intensity, while the SCRAM spectra are plotted in units of J/eV. This figure is reproduced from Ref. [14].

As mentioned, we simulate an electron beam using a plasma with a fast-electron temperature distribution in addition to the standard Maxwellian distribution. By experimenting with different fractions of fast electrons and electron temperatures we find that the intensity of K-shell emission is more dependent on the number of hot electrons (we tested between 0 and 15% of the

total electrons in this second Maxwellian) than on their energy distribution (we tested between 10 and 30 keV electrons), provided that the electron energy exceeds the transition energy in question (8048 eV for cold Cu K_α). Thus we set the fast electrons to 10 keV.

Depending on the actual location of the source (which changes the location of the lines on the spectrometer film by about 25 eV per 100 μm) the plasma producing the low energy K-shell emission could be a few-tens of eV up to to a few-hundreds of eV. The solid green line in figure 4.15 shows a 8 x 10^6 μm^3, 30 eV, n_e = 6 x 10^{19} cm^{-3} source with 5% fast electrons that produces the K_α and K_β in appropriate ratios. Thirty eV approximates the plasma temperature we expect to see in an X-pinch corona. The noticeable shift in energy from the experimental spectra may be explained by a 100-200 μm shift in source locations relative to the hot, dense source. It produces 9 MW of total X-ray flux, almost 0.3 MW of which are K-shell photons.

Perhaps a better fit for the cold K_α line in terms of line width and location is produced by a simulated plasma from a 1 x 10^6 μm^3, 200 eV, n_e = 3 x 10^{20} cm^{-3} source with 5% fast electrons ($Z^* \sim 20$) shown by the black dotted line in figure 4.15. This synthetic source produces about 55 MW of flux from 900 eV and up, and $\sim$ 0.5 MW of K-shell flux, in excellent agreement with the diode data though it does not appear to produce the amount K_β emission seen experimentally.

Additionally, the L-shell spectra from this plasma matches the experimental L-shell spectra and is shown by the black line in figure 4.16. Excepting the lack of K_β emission, all other fluxes, integrated energies, line locations, and line ratios from this synthetic plasma match the experimental data quite well. It is also possible that the L-shell spectra captured is produced by a similar 200 eV plasma in the micro z-pinch prior to collapse since the presence of fast electrons does not dramatically alter the L-shell lines.

Alone, none of the plasma conditions described here explain the emission detected from the good ($\leq$ 5 μm source width, 3 ns pulse width) foil X-pinches, so some combination of the hot dense source and the cooler plasmas with fast electrons must appear (either co-located or

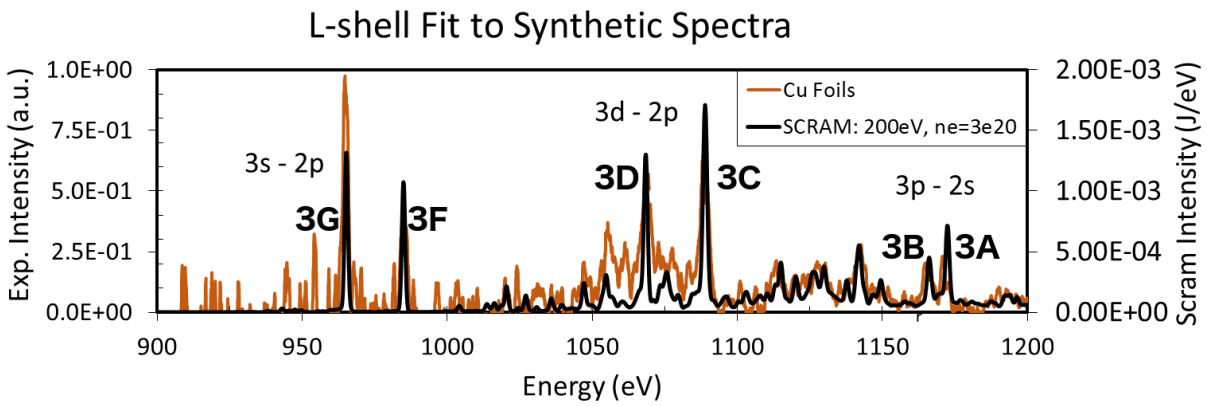

Figure 4.16: The previously shown foil X-pinch L-shell spectrum (orange line) with a SCRAM synthetic spectra overlaid. The black line is a 200eV plasma with n_e = 3 x 10^{20} cm^{-3}, from a 10^6 μm^3 source with 5 % hot (10 keV) electrons. The experimental spectrum is plotted in arbitrary units of intensity, while the SCRAM spectrum is plotted in units of J/eV. This figure is reproduced from Ref. [14].

separated by $\leq$ 200 μm). The hot, dense plasma appears to be the hallmark of the smallest, fastest X-ray sources but does not produce sufficient L-shell emission. The 'coronal' plasma approximation (30 eV, n_e = 6 x 10^{19} cm^{-3}) produces appropriate K-shell lines and fluxes, but the L-shell emission is substantially weaker and does not produce comparable lines. The 200 eV warm plasma produces L-shell spectra and fluxes matching those obtained experimentally and, with a fast electron component added in, nicely matches the cold K_α line but produces no hot K_α and insufficient K_β.

All of this is, of course, subject to further experimentation, and likely only a rough outline of the spatially and temporally dynamic conditions occurring during the emission phase of X-pinches. Again, while we are relatively confident in our temperature estimations, even with the radiographic and diode data to supplement the spectra, the sensitivity of line intensity to plasma density and the time-integrated spectroscopic films' inability to resolve between the actual flux of a source and the time the film was exposed to flux add considerable uncertainty to the data.

4.3 Conclusions from the first two LCXP experiments

From the first two laser-cut foil X-pinch experiments, we showed that the X-ray sources from foil X-pinches matched or outperformed those from similar wire X-pinches in terms of flux, minimum size, and temperature, and reproducibility. The initial geometric differences between the flat foil target with its angular cross-sectional profile, and the three-dimensional twisted WXP crosspoint did not appear to significantly affect the initial ablation and expansion of the X-pinches. Initial Ta LCXPs produced bright sources of similar size and pulse width to comparably matched W WXPs on GenASIS, thus demonstrating proof of concept. These initial experiments were fraught with difficulties revolving primarily around the engineering issues of transporting and loading a target without damaging or breaking it.

Significant improvements to the loading procedure were made while continuing LCXP experiments using Cu foils. Different target designs of these Cu LCXPs were tested, and within the shot-to-shot variability of the sources, we determined that a simple crosspoint angling in and out of the center of the 'X' pinched just as well as any other, more specialized designs — in fact, certain features including sharp angles and excessive mass completely inhibited pinching. The quality and reproducibility of the initial target correlated with the reproducibility of the source timing, as was evidenced when comparing pinch timing between higher quality targets cut on the LWS1 facility compared to the much faster and easier to make (but less similar) targets cut on the TRUMPF platform. The foil X-pinches appear to produce a slightly smaller source ($\leq$ 5 μm) that, according to the HOPG spectroscopy (see Fig. 4.14) is also hotter and/or more dense than the pinch in a WXP. Despite the lack of two resolvable X-ray sources from the diodes, the data also showed that LCXPs produce a hot pinch and an electron beam source, though radiographs of fine wires suggest that this LCXP beam source had a less deleterious effect on the quality of a radiograph than WXP beam source(s).

Thus, while this work represented strides in producing a more reliable, controllable X-ray source from an X-pinch, many questions still remained. Additionally, in light of the increasing

number of publications highlighting the functionality of the hybrid X-pinch, it seemed prudent to directly compare its functionality alongside the WXP and LCXP. As such, the subsequent (and final experimental) chapter represents a further foray into the optimization of the WXP and LCXP on GenASIS, the development of the HXP on GenASIS, and an analysis of the observed differences between the three X-pinch configurations.

4.3.1 Acknowledgements

Chapter 4 contains material that is partially reprinted from two separate publications. The first is G. W. Collins IV, M. P. Valdivia, T. O. Zick, J. Kim, D. M. Haas, A. C. Forsman, R. B. Stephens,and F. N. Beg, "Investigation into the dynamics of laser-cut foil X-pinches and their potential usefor high repetition rate operation," *Applied Physics Letters*, **105**, 024101 (2014). The second is G. W. Collins IV, J. C. Valenzuela, S. B. Hansen, M. S. Wei, C. T. Reed, A. C. Forsman, and F. N.Beg, "Characterization of laser-cut copper foil X-pinches," *Physics of Plasmas*, **23**, 101212 (2016). The dissertation author was a co-investigator and author of the first paper, and the primary investigator and author of the second paper. He thanks all of the co-authors at UC San Diego, General Atomics Inc., and Sandia National Lab who have given their written permission to use this material in this dissertation.

Chapter 5

Characterization of Hybrid X-pinches, and comparison of laser-cut, wire, and hybrid X-pinches.

The data presented in chapter 4 showed the viability of the laser-cut foil X-pinch (LCXP) as an X-ray source, and demonstrated that the reliability and source characteristics of said target represented an improvement over the traditional wire X-pinch (WXP). Hybrid X-pinches (HXPs) also offered an appealing alternative to the WXP, with the first publication of such an array dated a year prior to the first LCXP experiment (see Ref. [112]). Hybrid X-pinches, as described in Sec. 1.3.2, produced a higher rate of single sources with comparable brightness and source size to that found in wire X-pinches, while having significantly less hard X-ray (HXR) radiation. Numerous publications have since demonstrated the versatility of the HXP across various drivers, materials, and configurations [86, 90, 122–124, 193].

Given the inherent usefulness of the X-pinch as an X-ray backlighter for plasma experiments, we set out to determine which of the three aformentioned configurations (HXP, LCXP, WXP) produced the most reliable characteristics including reproducibility, source size, and flux.

To directly compare the HXP performance to that of the LCXP and WXP, we conducted another round of X-pinch experiments on the GenASIS driver. In order to establish a more thorough benchmark of X-pinch performance, Cu wire X-pinches using a variety of wire masses, wire numbers, and arrangements were tested, expanding upon the work shown in Sec. 4.2. A significant number of LCXP's were then tested, facilitated by the final target loading improvements mentioned in Sec. 4.2.1, that further established the baseline for LCXP performance. Then, we began testing and optimizing HXPs on GenASIS to compare, for the first time, the three X-pinch configurations side-by-side.

This chapter presents data from numerous X-pinch configurations, as shown in Table 5.1. The performance of the different X-pinch configurations are presented in Secs. 5.1 through 5.3.3. Section 5.4 contrasts the spectroscopic data obtained and presents estimates for the plasma parameters found in the different X-pinches that are then used to analyze the nature of the emission source(s) in Sec. 5.5.

As before, a number of abbreviations are used to ease the reader through the results. For clarity they are defined again here. WXP refers to a wire X-pinch, an HXP is a hybrid X-pinch, and an LCXP is a Laser-cut foil X-pinch. XUV refers to extreme ultra-violet light, SXR refers to soft X-rays in the $\sim$ 1 keV range, and HXR refers to X-rays beyond the Cu L-shell seen on the harder filtered diodes, which includes all X-rays $\geq$ 3 keV, but are predominantly $\sim$ 8 keV, for the Cu K-shell). With respect to diodes and filters, PP refers to polypropelene, Al-My refers to an aluminized mylar filter, and FWHM refers to the full-width at half-maximum of a signal.

5.1 Wire X-pinches

The primary WXP configuration used in the work published in Ref. [14] and described from Sec. 4.2 and on in Ch. 4 was an 18 μm Cu wire crossed with a 25 μm Cu wire. This particular configuration matched the linear mass (6.7×10^{-5} g/cm) of the LCXPs that pinched nearest to peak

Table 5.1: Tabulation of some of the different X-pinch configurations presented in this manuscript and their linear cross-point masses in g/cm.

X Type	Material and Configuration	Linear Mass of Array (g/cm)
Wire	2 x 25 μm Cu Wire	8.8×10^{-5}
Wire	4 x 18 μm Cu Wire	9.1×10^{-5}
Wire	4 x 25 μm Cu Wire	1.8×10^{-4}
Hybrid	25 μm Cu Wire	4.4×10^{-5}
Hybrid	40 μm Cu Wire	1.1×10^{-4}
Laser-cut foil	30 μm Annealed Cu foil	$5\text{-}7\times 10^{-5}$

current on GenASIS (which was kept the same for the experiments presented here in Ch. 5, and so matches the value given in Table 5.1). This 18 and 25 μm WXP pinched at 100 ns into current rise or earlier —meaning it pinched too early. Just to verify this, 2 x 18 μm WXPs (linear mass = 4.6×10^{-5} g/cm) were tested, and interestingly pinched at about the same time, but produced significantly more signals. Wire X-pinches composed of 2 x 50 μm Cu wires (linear mass = 3.5×10^{-4} g/cm) were significantly overmassed and did not pinch at all. The WXP configurations presented here in Ch. 5 in any sort of depth are those given in table 5.1: 2 x 25, 4 x 18, and 4 x 25 μm Cu WXPs.

5.1.1 2 x 25 μm Cu wire X-pinches

As shown in Table 5.1, the 2 x 25 μm wire X-pinch is the lightest wire X tested in terms of linear mass, measuring 8.8×10^{-5} g/cm. Figures 5.1a-c show a three-frame schlieren time sequence of the 2 x 25 μm WXPs, with the time relative to pinch given at the bottom of each frame. Typical traces of 4 diode signals presented in Fig. 5.1d show that the 2 x 25 μm WXP's generally produced two X-ray pulses. Note that the Be diode trace in Fig. 5.1d is divided by 5 in order to show the Ni, Cu, and Al+PP signals on the same vertical scale. The first X-ray pulse occurs at 122 ± 4 ns after current start with a FWHM of 1.5 ns. This signal, produced by the hot-pinch, is predominantly SXR as indicated by the high maximum flux of the Be-filtered signal relative to the other diode signals. Subsequent pulses that occur 4 - 40 ns after the pinch signal

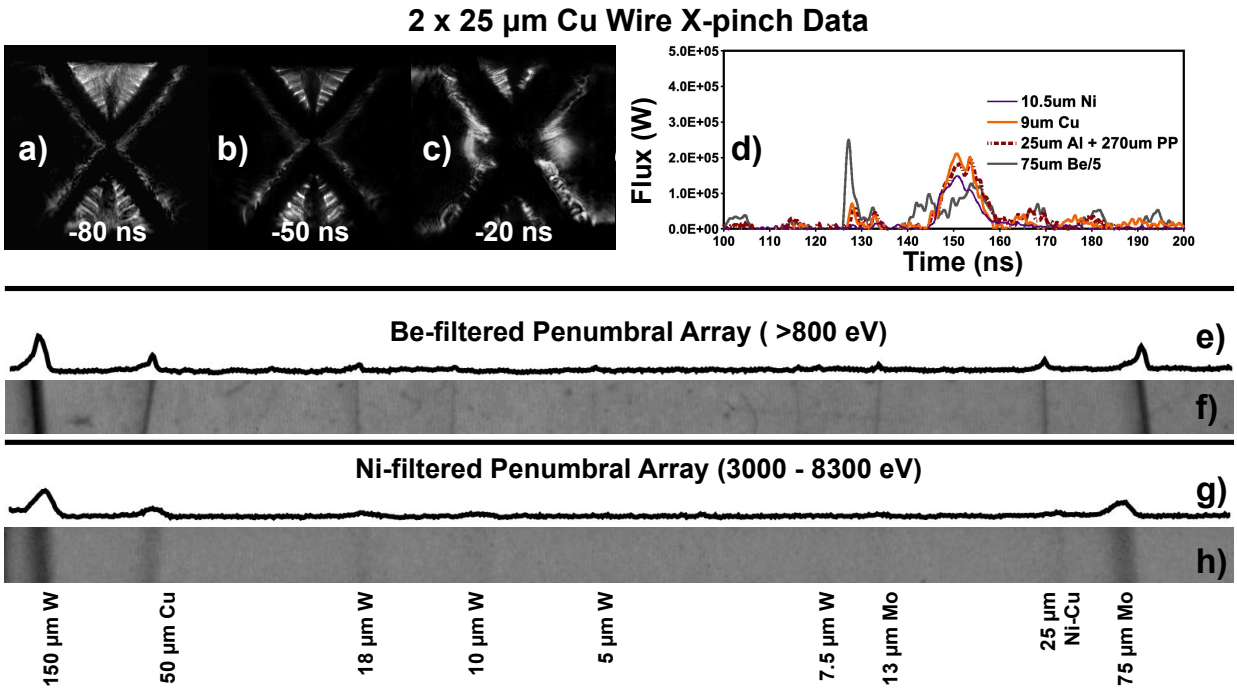

Figure 5.1: Frames a-c show a brief schlieren time sequence of a 2 x 25 µm wire X-pinch (WXP) before pinching (times relative to pinch are given at the bottom of each frame). Frame d shows four Si-PIN diode signals: Ni, Cu, Al+PP, and Be filtered. The softer Be signal is divided by 5 to fit in the plot with the Ni, Cu, and Al+PP signals. X-ray fluxes are integrated over 4π. Data from the Be filtered slit-wire array are shown in e and f. Data from the Ni filtered slit-wire array are shown in g and h giving an idea of the source size. The wires used in the array are labeled at their approximate position at the bottom of the figure. Note that the wires may not be visible in the lineout or the image. Also note that the lineouts in frames e and g were taken from the unprocessed image plate scans and normalized, while the contrast of the radiographs displayed in frames f and h may have been adjusted to better show the wires present.

with FWHM ranging from 2.5 to $\geq$ 10 ns are generated by the electron beam, as evidenced by their larger relative fraction of HXR to SXR emission (seen when comparing fluxes from the Ni, Cu, Zn, and Al+PP-filtered diodes to those from the Al and Be-filtered diodes). It is worth noting that $\sim$ 25% of these X-pinches produced only one resolvable X-ray pulse, and $\sim$ 25% produced 3 or more.

Figures 5.1e-f and g-h show line-outs and image plate scans of the Be and Ni filtered slit-wire arrays, respectively. The wires present in the array are labeled at the bottom of Fig. 5.1. Both slit-wire arrays shown in Fig. 5.1 are from the same shot as the traces shown in Fig. 5.1d.

The Be filtered slit-wire data show that the soft X-ray source resolves the 10 μm W wire, but the smaller 7.5 and 5 μm W wires are just visible as well. The second, e-beam generated source (the hard X-ray peak in Fig. 5.1d) is seen in the more diffuse penumbra adjacent and to the left of the primary wires imaged. Figures 5.1g-h show the size of a typical e-beam generated source through the Ni filtered slit-wire array. The source is typically of the order of 100 - 200 μm. The K-edge for the Ni filter, as shown in Fig. 3.11 is 8.33 keV, which means it images electron-beam sources striking a cooler Cu plasma (up to a few hundred eV) rather than a pinch source. Some 2 x 25 μm WXPs do produce harder X-ray sources down to $\sim$ 10 μm, though this is the exception rather than the norm ($\leq$ 1 in 4 WXPs).

Note that the contrast of the penumbral images (frames f and h) may have been adjusted to better show the wires present. The lineouts (frames e and g) were taken from an unprocessed image and then normalized. Also note that in order to use a penumbral diagnostic to accurately determine the size of a source, the resolution of the recording medium needs to far exceed the spatial scale of the object on the film, which is decidedly not the case for the low-magnification penumbral slit-wire array used here. In the work presented in Ch. 4, Kodak Biomax X-ray film captured all of the radiographic data. Due to changing circumstances regarding darkroom, film, and developer availability, combined with the decreasing cost of reusable, calibratable image plates (IPs), we switched to using IPs for the work presented in Ch. 5. The advantages of a reusable medium with quick and easily reproducible processing (IPs are not very sensitive to visible light exposure, and fairly stable over a processing time of tens of minutes) were balanced by the two-order-of-magnitude decrease in resolution ($\geq$ 25 μm for IPs). This is mentioned because given this, a 5 μm wire is not technically resolvable by the image plate in its present configuration with the slite wire array, and vacuum components weren't available to expand the magnification of the diagnostic further at the time. Thus, shadows cast by the wire can be recorded, but provide only general source size evidence.

From this, the simple 2-wire X-pinch represents a fairly reliable diagnostic for radiograph-

ing micron-scale objects moving on nanosecond timescales in the $\sim$ 1 keV photon range. The small standard deviation of the hot-pinch timing is also remarkable from a pulsed power system. However, the longer, e-beam generated source in the majority of these pinches often creates a photon count incident on the target comparable to that from the hot-pinch, which washes out the radiographs from the latter. Additionally, the lack of reliable timing and source size reproducibility in the e-beam generated Cu K-shell range makes this configuration a poor K-shell radiography source for objects $\leq$ 100 μm-scale and/or dynamically changing on $\leq$ 10 ns timescales.

5.1.2 4 x 18 μm Cu wire X-pinches

Previous studies showed that increasing the number of wires in an X-pinch (from 2 to 4 or 6) increased the peak flux, reproducibility, and the time at which the pinch occurred relative to current start [85]. Since the 2 x 25 μm WXPs pinch 24 - 32 ns prior to peak current, we expected that a slightly heavier array with more wires would produce better sources. However, wire X-pinches composed of 4 x 18 μm Cu wires produce considerably less desirable results that 2 x 25 μm WXPs, despite having more wires and a slightly higher linear mass ($\sim 9.1 \times 10^{-5}$ g/cm). While evolving similarly to its 2 x 25 μm WXP counterpart, the 4 x 18 μm WXP typically pinches multiple times, and eventually creates e-beam generated sources as well, seen as multiple, increasingly large, HXR diode signals in Fig. 5.2d. The Be filtered slit-wire diagnostic (see Figs. 5.2e-f) showed that the pinch size at low energies may be between 10 - 20 μm, though the large number of signals make true source-size determination difficult. The Ni filtered slit-wire diagnostic (see Fig. 5.2g-h) showed multiple shadows (indicating multiple sources) as well. This array still appears under-massed (gauging by the early pinch time), so though previous results, as in Ref. [85], indicate that increasing the number of wires increases the reliability of the X-pinch, the overall mass of the array needs to appreciably increase as well. In this case it is possible that the individual 18 μm wires ablate away exceedingly quickly not only at the cross-point but adjacent to it, creating a larger plasma electrode gap than in other arrays, and subsequently more

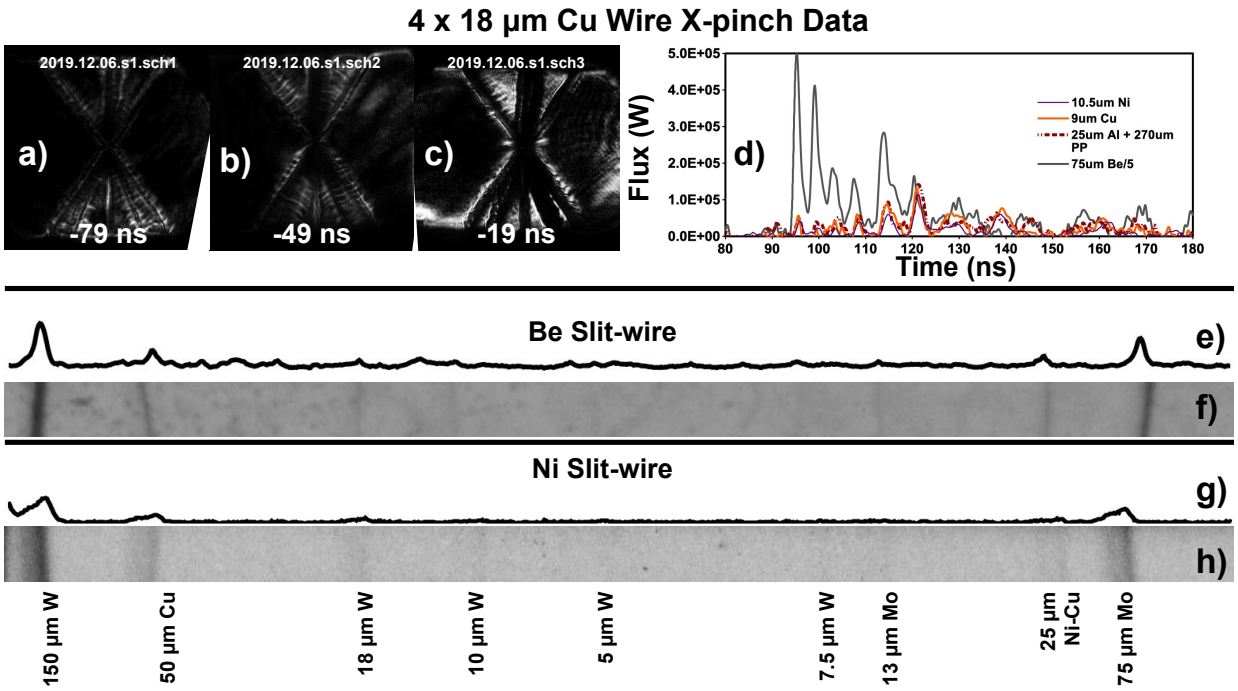

Figure 5.2: Frames a-c show a brief schlieren time sequence of a 4 x 18 µm wire X-pinch (WXP) before pinching (times relative to the first peak are given in parenthesis). Frame d shows four Si-PIN diode signals and a post-load integrated current profile from GenASIS. The softer Be signal is divided by 5 to fit in the plot with the Ni, Cu, and Al+PP signals. X-ray fluxes are integrated over 4π. Data from the Be filtered slit-wire array are shown in e and f. Data from the Ni filtered slit-wire array are shown in g and h giving an idea of the source size. The wires used in the array are labeled at their approximate position at the bottom of the figure.

time and space for pinches to occur.

5.1.3 4 x 25 µm Cu wire X-pinches

Copper wire X-pinches composed of 4 x 25 µm wires have a linear mass of 1.8×10^{-4} g/cm, or double that of the 2 x 25 and 4 x 18 µm WXPs. Data from this configuration is shown in Fig. 5.3, which has the same layout and set of diagnostics as Fig. 5.1. The micro Z-pinch and plasma electrodes structure is visible throughout the schlieren time sequence in Figs. 5.3a-c, and there is considerably less lower-density plasma around the cross-point near pinch time (see Fig. 5.3c) than seen at comparable times in the 2 x 25 µm WXPs (Fig. 5.1c). Similar to the typical 2 x 25 µm WXP, the 4 x 25 µm WXP typically produces a hot-pinch source and then an electron beam

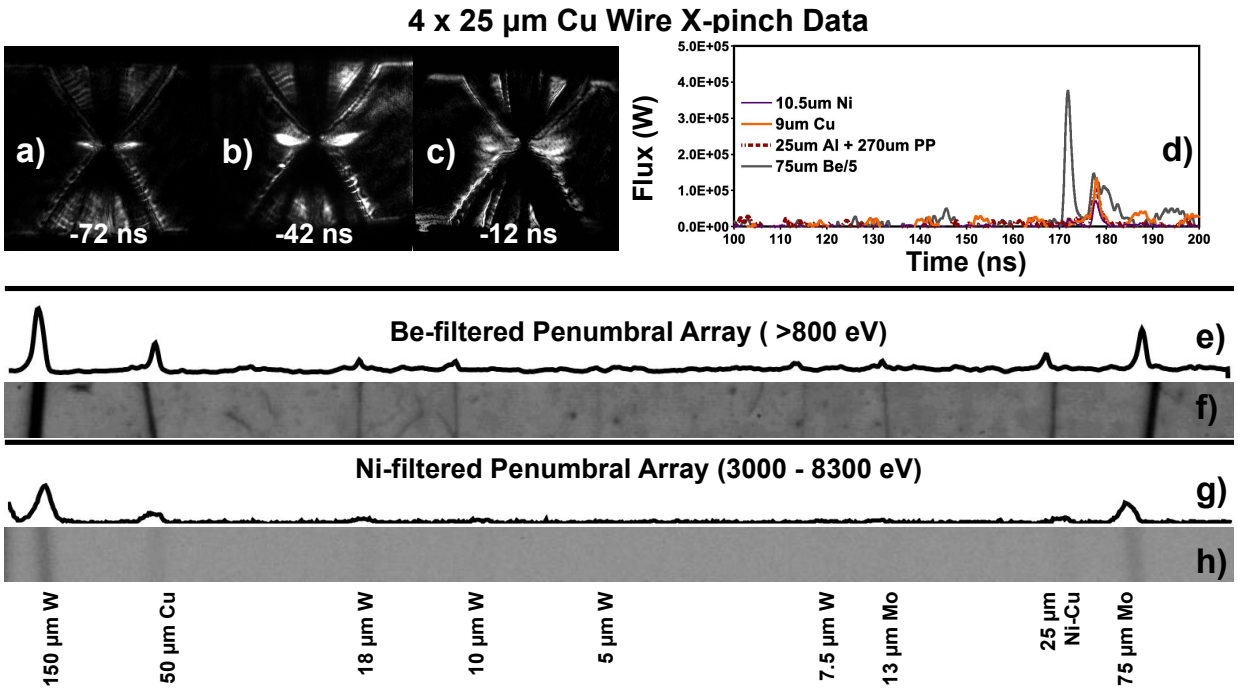

Figure 5.3: Frames a-c show a brief schlieren time sequence of a 4 x 25 µm wire X-pinch (WXP) before pinching (times relative to pinch are given at the bottom of each frame). Frame d shows four Si-PIN diode signals: Ni, Cu, Al+PP, and Be filtered. The softer Be signal is divided by 5 to fit in the plot with the Ni, Cu, and Al+PP signals. X-ray fluxes are integrated over 4π. Data from the Be filtered slit-wire array are shown in e and f. Data from the Ni filtered slit-wire array are shown in g and h giving an idea of the source size. The wires used in the array are labeled at their approximate position at the bottom of the figure.

generated source. The pinches in this configuration occur after peak current, between 160 and 170 ns after current start (peak current is at $\sim$ 150 ns), with the beam following in $<$ 10 ns.

Soft X-ray radiographs from the Be-filtered slit-wire array (see Figs. 5.3e-f) resolve the 7.5 and 10 µm W wires in the lineout, and the 5 µm W wire is visible in the radiograph to the naked eye. The quality of the soft X-ray source is the best of the three WXP configurations tested here. The e-beam generated source in Fig. 5.3d has a narrower FWHM and comparable flux (through the Al+PP and Cu filters) than that from the typical 2 x 25 µm WXP. These parameters together mean e-beam generated sources from 4 x 25 µm WXPs emit fewer total photons than those from 2 x 25 µm WXPs, resulting in less double-exposure and in better radiographs from the hot-pinch source. The e-beam generated source from the 4 x 25 µm WXP resolves comparable wires with

the Ni-filtered slit-wire array (see Figs. 5.3g-h) to that of the 2 x 25 μm WXPs (see Figs. 5.1g-h).

5.2 Laser-cut foil X-pinches

Figure 5.4 shows a dataset from LCXPs similar to those seen in Figs. 5.1 and 5.3 for the WXPs (differences will be subsequently noted). As seen in Fig. 5.4d, the LCXP shots produce — almost exclusively — a single resolvable X-ray peak, supporting previously published observations [14]. Note that there are a handful of changes between Fig. 5.4d, and Figs. 5.1d - 5.3d. First, the 10 μm Zn-filtered diode replaced the Al+PP-filtered diode previously used due to technical difficulties, but these diodes should produce comparable signals since little-to-no line emission is expected above the 9.66 keV Zn transmission edge, and little continuum emission has been seen above this energy in other diagnostics. Second, the 25 μm Al-filtered diode is used in place of the Be-filtered diode due to frequent saturation of the latter in LCXP shots. Additionally, the scale of the y-axis is quadrupled. The Al-filtered diode signal has a 1 - 2 ns FWHM, while the decrease in flux from the Zn to the Cu to the Ni filtered Si-PIN diodes (yellow, orange, purple lines in Fig. 5.4d) was not observed in WXPs, implying that the LCXP emits higher-energy photons than its wire counterpart (this is covered in more depth in Sec. 5.4).

Pinches in the LCXPs occurred at 145 ± 17 ns. This relatively large temporal distribution deviates from that observed in Ref. [14], and is likely due to the use of the Trumpf etching system to cut the targets, rather than the much higher resolution Laser Workstation 1 (LWS1) system that most of the targets in that work were cut with. The range of linear masses of the LCXPs differs by $\leq 20\%$ from the average (see Table. 5.1), which could add to the variability in pinch timing, though the effect or even validity of this is difficult to assess due to the aforementioned error in the cross-point measurement process. Additionally, the edges of the Trumpf-cut foil X's are not as smooth as those from LWS1. Only one of the 18 pinching shots conducted had a second peak, which was entirely soft x-rays. Four X's did not pinch, of which 3 came from the same batch

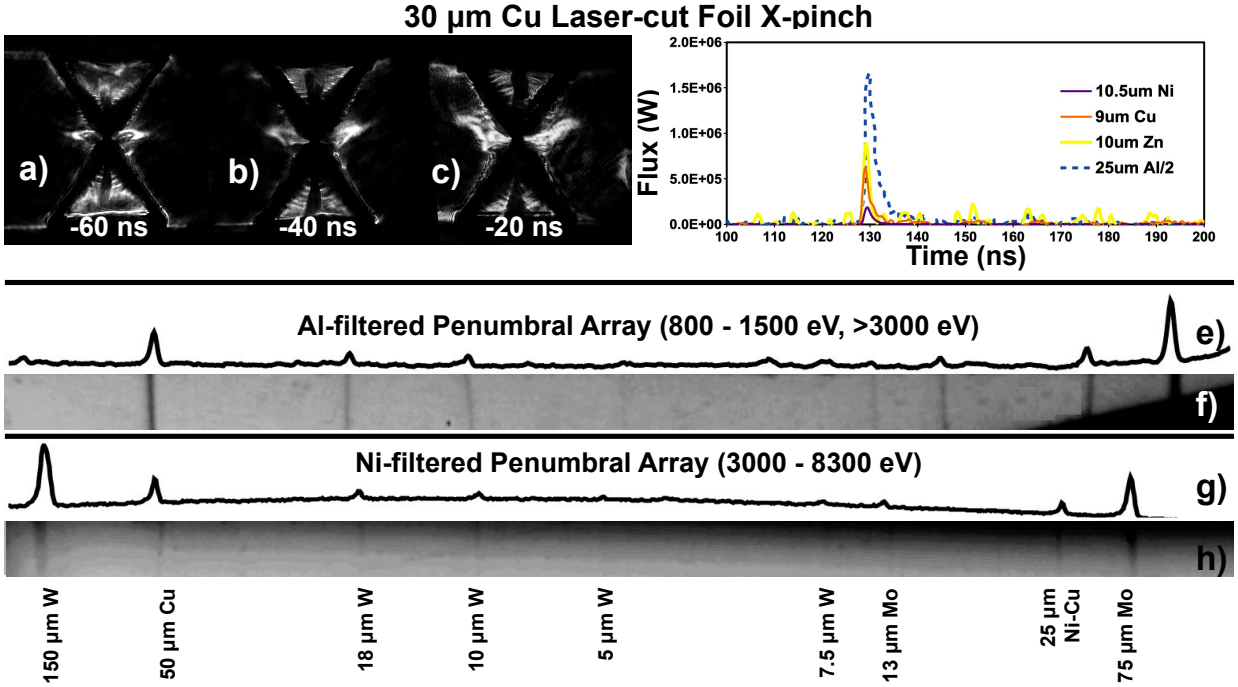

Figure 5.4: Frames a-c show a brief schlieren time sequence of a 30 µm thick laser-cut foil X-pinch (LCXP) before pinching (times relative to pinch are given at the bottom of each frame). Frame d shows four Si-PIN diode signals: Ni, Cu, Zn, and Al filtered. The softer Al signal is divided by 2 to fit in the plot with the Ni, Cu, and Zn signals. X-ray fluxes are integrated over 4π. Also note that the vertical scale of the y-axis is quadruple that of the comparable plots elsewhere in this paper. Data from the Al filtered slit-wire array are shown in e and f. Data from the Ni filtered slit-wire array are shown in g and h giving an idea of the source size. The wires used in the array are labeled at their approximate position at the bottom of the figure.

of targets and in subsequent shots, which likely points to a specific target batch or even a driver problem.

Source size data for the LCXPs shows the smallest wires in both the soft and hard X-ray ranges of the penumbral diagnostic, as shown in the Al and Ni filtered slit-wire arrays shown in Figs. 5.4e-f and g-h respectively. The 25 μm Al-filtered array is used here instead of the Be-filtered array in Figs 5.1g-h and 5.3g-h due to saturation of the Be filtered array in LCXP shots (the cut-off window of the Al filter starting at 1.56 keV is not a limitation since the Cu L-shell emission characteristic of the pinch is almost entirely below this energy range, and the data set aims to show the soft X-ray radiography capabilities of the X-pinch). Also note that the 150 μm W wire is out of frame in the Al filtered slit-wire array. The 5 μm W wire is visible in both arrays (the width of the small peak in the Al filtered array is due to the wire not being completely vertical). Unlike the WXPs, where the e-beam generated source typically imaged only the larger wires with occasional smaller sources, the LCXP hard X-ray sources typically imaged the 5 - 10 μm wires in the Ni-filtered slit-wire array, with occasional sources ($\leq$ 1 in 4) looking more like the large e-beam generated sources in the WXP shots. Potentially more interesting is the strong correlation between the best sources (clearly imaging the smallest 5 μm W wire) and LCXPs that pinched before the average emission timing (145 ns).

Laser-cut foil X's produced single-peak pinches and small ($\leq$ 5 μm) hard and soft X-ray sources as seen in previous experiments [14]. Improvements to the target design and loading process dramatically increased the target success rate. However, the lower-resolution cutting facility correlates to increased pinch timing variability.

5.3 Hybrid X-pinches

The hybrid X-pinches (HXPs) studied here used Cu wire crosspoints with a diameter of 25 - 40 μm (the linear masses of these are given in Table 5.1) to give a firm performance

comparison against the well-established wire and (at this facility) laser-cut X-pinches. The most tested configuration used 25 μm Cu wires as the hybrid 'cross-point'. However, a number of other configurations including 40 μm Cu, 25 μm Ni, 25 μm Constantan (45% Ni - 55% Cu alloy), and a modified 'insulated' 25 μm Cu HXP were tested as well and will be discussed where appropriate.

5.3.1 Determining the spacing of the Conical Electrodes

Before discussing HXP results, we address the establishment of the appropriate separation distance between the conical electrodes, which is governed by the velocity at which low-density plasma ablates off of them [90, 112]. If the electrode plasma closes the gap before the wire ablates enough to pinch, then the pinch will not occur as the low-density electrode plasma completes a more desirable current path than the pinching wire. If the electrode plasma ablates too slowly then the pinch location is not confined, multiple sources can occur, and a large gap remains post-pinch allowing electron beams to form, introducing the same limitations observed in WXPs.

Shadowgraphs in Figs. 5.5a-c show the expansion of plasma off of two Mo conical electrodes spaced at 4 mm. The timings given are relative to pinch timing. At -121 ns, the current is $\leq$ 20 kA, and already it is clear that the Mo electrodes and the wire are ablating. As time progresses, the plasma from the cones moves towards the horizontal mid-plane. The measured velocities as a function of time fit a reverse power law function $v_{cm/s} = 3.3\ t^{-0.754}$ (t in seconds), which when integrated gives the equation $x_{cm} = 13.4\ t^{0.246} + x(0)$. Integrating to t = 95 ns, when HXPs with widely-spaced electrodes pinched, the ablated material will cover about 0.25 cm, indicating that the electrode gap should be set to 5 mm (since the plasma ablates from two directions).

However, as can be seen by the gap (and m=0 instability formation) in Fig 5.5c, even a 4 mm gap is too large. Thus, given the general flattening of the curve around 30 - 40 ns, where a starting gap of $\sim$ 3.5 mm is more appropriate, we started there (at 3.5 mm) and incrementally closed the gap until the pinches grew increasingly unreliable. From this, the ideal conical electrode

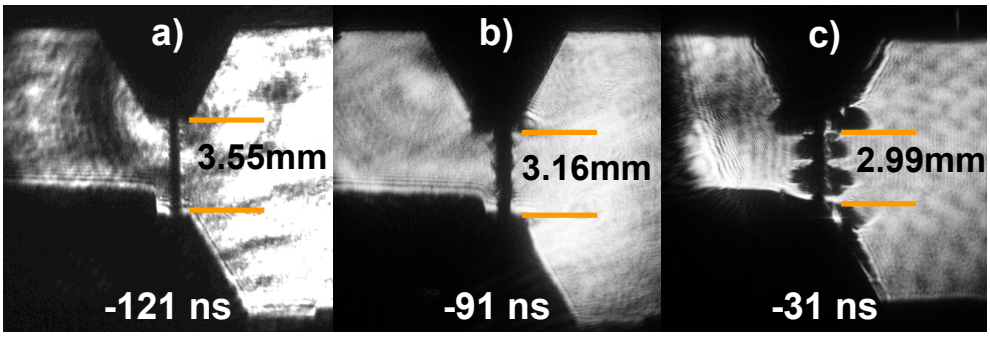

Figure 5.5: Frames a-c show a 25 μm HXP with Mo conical electrodes spaced at 4.0 mm. The timing relative to pinch is given at the bottom of each frame, and the location of the ablated material off of the electrodes is approximately labeled along with the gap between the plasma surfaces.

spacing was determined to be $\sim$ 2.5 mm. Any data presented from HXPs *not* at this spacing will be noted accordingly.

5.3.2 25 μm Cu hybrid X-pinches

The baseline HXP tested on GenASIS used a single 25 μm Cu wire between the conical electrodes. As with the other X-pinch configurations in this paper, Fig. 5.6 shows a comparable set of data to that shown for the WXPs and LCXP from the 2.5 mm spaced, Mo-electrode, 25 μm Cu HXPs. SXR signals from these HXPs resembles that of the LCXPs, with only a single resolvable peak. The peak emission came at 98 ns $\pm$ 13 ns. Worthy of note is that excepting two later pinches, the average pinch time was 91 ns $\pm$ 6 ns, but the two later pinches (at 110 and 120 ns) were among the brightest and had the smallest sources. Also noteworthy is the minimal signal from the harder filtered diodes, consistent with the observations made in Ref. [90] for HXPs on the MINI facility (250 kA, 170 ns). Over 50% of pinching HXPs had a single resolvable signal, while the others had two signals, with the second following the first by $\sim$ 10 ns. This second signal, unlike the e-beam signal in the WXPs, did not contain a higher percentage of harder X-rays.

In the Be-filtered slit-wire array (Figs. 5.6e-f) both the 7.5 μm and the 5 μm W wires are visible (albeit the second one just barely), indicative of a source size on par with the best of the

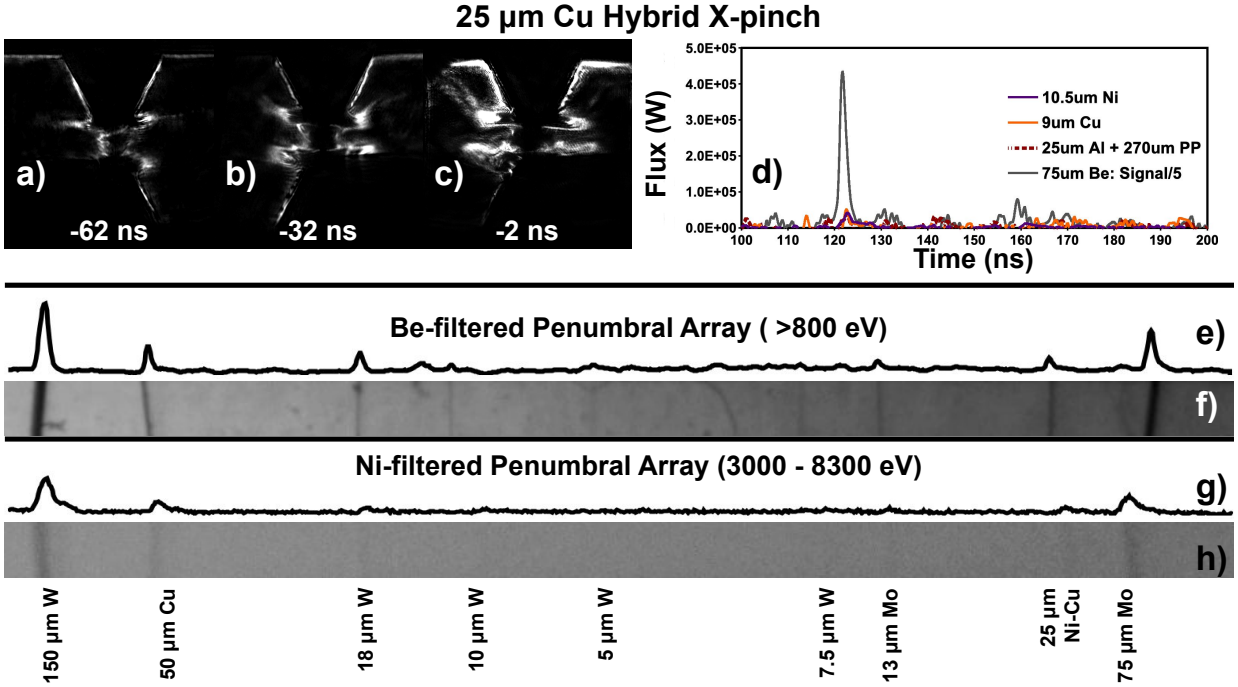

Figure 5.6: Frames a-c show a brief schlieren time sequence of a hybrid X-pinch with Mo conical electrodes spaced at 2.5 mm apart with a 25 µm Cu wire between them (times relative to pinch are given at the bottom of each frame). Frame d shows four Si-PIN diode signals: Ni, Cu, Al+PP, and Be filtered. The softer Be signal is divided by 5 to fit in the plot with the Ni, Cu, and Al+PP signals. X-ray fluxes are integrated over 4π. Data from the Be filtered slit-wire array are shown in e and f. Data from the Ni filtered slit-wire array are shown in g and h giving an idea of the source size. The wires used in the array are labeled at their approximate position at the bottom of the figure.

WXPs and the LCXPs. However, as expected from the lack of hard diode signals, the HXPs here offer little in terms of HXR radiography, as evidenced by the slit-wire data shown in Figs. 5.6g-h.

Given the early pinch timing and the number of HXPs that produced second sources, it appeared that the 25μm Cu array was under-massed, so a larger wire was sought. Curiously, the 25 μm HXP pinches at a similar time to the 4 x 18 μm WXP, despite having roughly half of the linear mass at the cross-point. This disparity in pinch timing vs linear mass is also apparent in the LCXPs, which though only slightly heavier than the 25 μm HXP, pinches relatively near peak current. Thus, choosing the proper linear mass for an HXP to pinch near peak current requires a learning curve independent of those for the WXP or even LCXP linear-mass/pinch-timing relationships.

40 μm Cu hybrid X-pinches

A 40 μm diameter Cu wire was tested in search of HXPs that pinch at or near peak current. In terms of linear mass, a 40 μm HXP weighs 1.1×10^{-4} g/cm, which is more than the 4 x 18 μm WXP but less than the 4 x 25 μm WXP. The flux on the Be-filtered diode was only about 10% of that observed on the same diode from 25 μm HXPs, WXPs, or LCXPs. This considerable drop in flux compared to other arrays was also observed in the comparable-current and rise-time experiments on the MINI generator described in Ref. [90] when comparing HXPs to WXPs. Pinching occured around 140 ns, comparable to LCXP pinch timing, and with a FWHM of 2 ns. Despite the low flux and softness of the X-ray signal, the source size in the low energy (Be filtered slit-wire array) range is comparable to the best of the 25 μm HXPs, LCXPs, and WXPs, while there is too little HXR emission to double expose the SXR filter or create radiographs in the K-shell regime.

5.3.3 HXP reliability issues and solutions

While the HXP results presented so far produced excellent SXR sources with parameters comparable to the LCXPs (which to date are the most reliable and parametrically superior X-

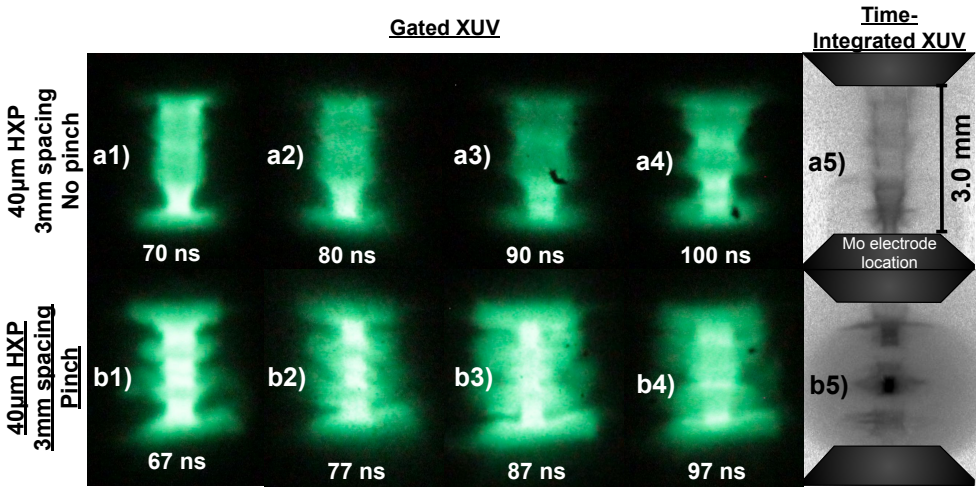

Figure 5.7: Gated XUV time sequences (1-4) and time integrated XUV pinhole images (5) of of two different 40 μm HXPs: a) 3mm electrode spacing, non-pinching, and b) 3 mm electrode spacing, pinching, showing the difference in coronal plasma formation and pinch outcomes in Cu HXPs on GenASIS.

pinches done on GenASIS), HXPs did not pinch consistently, with a success rate of $\sim$ 30-40%. Initially, the lack of reliability was presumed to be an engineering issue, since this problem was not described in the formative works on HXPs [90, 112]. However, a more likely factor is the longer pulse duration (> 100 ns rise time) and slower rate of current rise (closer to the 1 kA/ns threshold vs. the 2-10 kA/ns of most HXP experiments), frequently pointed out as the cause of poor pinching in X-pinches by Shelkovenko *et al.* in numerous publications and detailed in Ref. [77].

Development of the coronal plasma and subsequent expansion and instability growth in the crosspoint region can be driven by relatively low currents. If this occurs early in the current pulse, the $\mathbf{J}\times\mathbf{B}$ force required to confine the coronal plasma and form the micro Z-pinch is insufficient. Small, early-time variability in load current can dictate whether or not this behavior occurs. For example, Fig. 5.7 shows gated and time-integrated XUV images of the same HXP configuration: 40 μm with 3 mm spacing. In Fig. 5.7a, the coronal plasma is highly non-uniform and the pinch fails, whereas in Fig. 5.7b, the coronal plasma is more uniform and at smaller radius, with only the characteristic m=0 flares expanding outward.

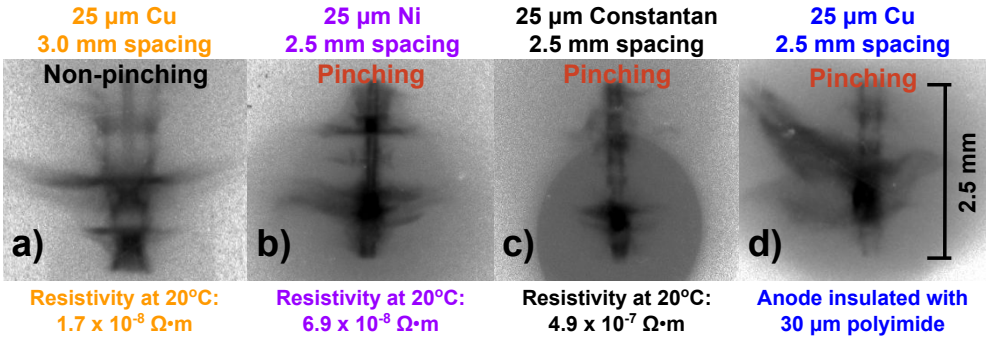

Figure 5.8: Frames a-d) show time integrated XUV pinhole images of hybrid X-pinches from 25 µm Cu, 25 µm Ni, 25 µm Constantan, and 25 µm Cu with a 30 µm polyimide insulator around the conical anode. The decrease in corona radius with the higher resistivity materials and the insulator compared to the uninsulated Cu HXP is clear.

To minimize the shot-to-shot variability in coronal plasma development, two approaches were implemented to reduce the early-time current in the cross-point region. First, noting that Cu is fairly conductive (1.72×10^{-8} Ω·m [194]), similarly-massed materials of higher resistivity were used: Ni (6.9×10^{-8} Ω·m [195]) and Constantan (4.9×10^{-7} Ω·m [194, 196]). Second, the anode was insulated by wrapping 2-3 layers of 15 µm polyimide around it [197, 198]. These approaches were successful, as shown in Fig. 5.8. In these time-integrated XUV pinhole images, the coronal plasma radius is clearly smaller and more uniform in the 25 µm Ni HXP (Fig. 5.8b), the 25 µm Constantan HXP (Fig. 5.8c), and the anode-insulated 25 µm Cu HXP (Fig. 5.8d) relative to the uninsulated 25 µm Cu HXP (Fig. 5.8a).

Additional experimental data confirmed that performance was affected by these changes. Peak fluxes and total SXR energies were generally unaffected by material or insulation. Some degree of pinching occurred in every 25 µm Ni HXP shot, evidenced by small diode signals and/or inductive dips in the B-dot probes. However, less than half showed brightness comparable to WXPs or LCXPs. The 25 µm Constantan HXPs pinched extremely well, with fluxes and scales matching the best-performing HXPs and even producing $\sim$ 7.5 µm HXR sources, similar to the LCXPs. Insulated 25 µm Cu HXPs pinched in every shot, and delayed pinch time from $\sim$ 100 ns to $\sim$ 135 ns, emphasizing how much ablation occurred early in time. Insulated 40 µm Cu HXPs

did not pinch, which was expected assuming a comparable delay in pinch time.

We also observed that the minimum electrode gaps required to adequately pinch the HXPs was affected by these approaches. The 2.5-3.0 mm minimum gap required to pinch uninsulated Cu HXPs was too large for the Constantan and insulated Cu HXPs, as some of the latter produced strong e-beams comparable to those seen in WXPs. This suggests that when the uninsulated Cu HXPs did pinch, the large-radius coronal plasma mitigated e-beam development. Constantan and insulated Cu HXPs required a gap of < 2.0 mm to minimize e-beam formation.

As a final note, wire and laser-cut X-pinches appear insensitive to the effects of the low-current portion of the current rise. While initial electrical contact is not guaranteed for LCXPs as they are left unclamped, HXP pinch outcomes did not change with wires in direct contact to the Mo electrode or not (the hole in the center of the conical electrodes is 40 times bigger than the 25 μm wires passed through them). Thus, clearly the long Z-pinch at the center of the HXP makes this array more sensitive than the WXP or LCXP to the behavior of the initial explosion of the wire and formation of the coronal plasma, and steps must be taken to minimize any small ($\leq$ 10% peak current), early-time current flow through the target to ensure reliable pinching using this configuration.

5.3.4 A brief summary of the data presented thus far

The results presented in Secs. 5.1-5.3 are summarized in Table II, which shows the frequency with which each configuration produced a single source, the average pinch time, and peak fluxes, total energies, and source sizes for both SXRs (>0.8 keV) and HXRs ($\gtrsim$ 3 keV).

Regarding the number of sources, 2 and 4 x 25 μm Cu WXPs typically produced a bright SXR pulse followed at some interval ($\sim$ 10 ns) by a temporally longer, spatially larger, electron beam HXR source, while 4 x 18 μm Cu WXPs produced multiple X-ray flashes. Laser-cut foil X-pinches produced single peaks. Most 25 and all 40 μm Cu HXPs produced single peaks of predominantly soft X-rays, though higher resistivity and some insulated HXPs produced HXR

Table 5.2: Tabulated values of pinch parameters of the different X's tested here. A range of values is given where data did not converge. The 25 μm HXP HXR values are for HXPs where little or no electron beam was present, while the WXP HXR values include beam characteristics.

Type	% Single Source	Pinch Time (ns)	SXR (≥0.8 keV) Flux (MW)	SXR (≥0.8 keV) Energy (mJ)	SXR (≥0.8 keV) Size (μm)	HXR (≥3.5 keV) Flux (MW)	HXR (≥3.5 keV) Energy (mJ)	HXR (≥3.5 keV) Size (μm)
2x25 μm Cu WXP	25	120	1 - 2	1-10	≤ 5	0.2	0.5	10 - 100
4x18 μm Cu WXP	0	100	2-3	3.5	Unk.	0.2	0.1	50 - 100
4x25 μm Cu WXP	NA	170	2	3	≤ 5	0.2	0.1	20 - 100
30 μm Cu LCXP	95	145	3-8	30	≤ 5	0.2-1.2	0.7	5 - 20
25 μm Cu HXP	50	100	2-10	30	≤ 5	0.1-0.5	0.3	≥ 20
25 μm Cu HXP (ins.)	70	135	2-6	30	≤ 5	0.2-0.3	0.5	5 - 20
40 μm Cu HXP	100	140	0.3	0.5	≤ 5	NA	NA	NA
25 μm Const. HXP	50	80	4	10	≤ 5	0.2	0.2	≥ 7.5

signals comparable to the WXP and some LCXP pinches.

SXR source size was $\sim$ 5 μm for all but the 4 x 18 μm WXPs, which may have had small sources masked by multiple exposures. Only the LCXPs reliably produced a small ($\sim$ 5 μm) HXR source, while occasionally 2 x 25 μm WXPs and Constantan HXPs produced a $\leq$ 10 μm HXR source. 25 μm HXPs and 4 x 18/25 μm WXPs produced larger (50-100 μm) e-beam generated sources, and 40 μm HXPs produced very few hard X-rays.

As discussed in Sec. 5.3.3, HXPs did not initially pinch consistently. This is likely due to inconsistent coronal plasma development at the crosspoint, a more significant problem for HXPs than WXPs or LCXPs due to the relative length of this region. Two approaches to improve HXP reproducibility were successful: switching from Cu HXPs to more-resistive Ni and Constantan HXPs and insulating the anode of Cu HXPs with $\sim$30-45 μm polyimide, suggesting that minimizing low, early-time current through the HXP significantly improves its reliability, especially for high-conductivity materials.

5.4 Spectroscopic Analysis of the Different Pinches

As mentioned in Sec. 3.3.4, two different crystal spectrometers were fielded for these experiments: a flat HOPG to measure Cu K-shell lines, and a convex MICA to observe Cu L-shell lines. With these spectra, in combination with the calibrated diode signals, we estimate the

plasma conditions in each pinch using synthetic spectra created using both the hydrogenic code FLYCHK [11], and the hybrid code SCRAM [188–190].

When trying to match synthetic and experimental spectra, one needs to know the appropriate parameters to adjust. Increasing electron or ion density in the plasma typically increases the X-ray flux emitted and the width of the spectral lines. The modelled plasma size and duration also directly affects the intensity. Increasing the temperature increases the charge state of the Cu plasma, determining the energies and relative intensities of line emission. Above temperatures of about 100 eV, Ne-like and nearby ions give rise to complex L-shell emission spectra between 0.9 and 1.6 keV. Temperatures above $\sim$ 1 keV ionize the Cu plasma to He-like and nearby ions, giving rise to He-alpha emission near 8400 eV, and temperatures above about 2 keV can support H-like emission near 8700 eV. Adding hot electrons with energies above the $\sim$ 8 keV cold K-edge can give rise to K_α emission from whatever charge states are supported by the thermal plasma conditions: cold plasmas and solids emit K_α near 8050 eV while plasmas with temperatures of several hundred eV emit K_α satellites between the cold K_α lines and the He_α line. Here, we model hot electrons with 10 – 30 keV Maxwellian distributions and impose fractions up to 15% of the total electron density.

The subsequent results show four sets of plasma conditions which match different aspects of the experimental spectra. These include:

- A 'Cold' plasma, with T_e = 30 eV, $n_i = 5.6\times10^{18}$ cm^{-3}, and 5% fast electrons at 10 keV,
- A 'Warm' plasma, with T_e = 200 eV, $n_i = 1.5 \times 10^{19}$ cm^{-3}, and 5% fast electrons at 10 keV,
- A 'Hot' plasma, with T_e = 1000 eV, $n_i = 1\times10^{22}$ cm^{-3} plasma, and no fast electrons,
- An 'XHot' plasma, with T_e = 3000 eV, $n_i = 1\times10^{22}$ cm^{-3} plasma, and no fast electrons.

Source size and pulse duration for yield calculations from the simulated spectra are given where appropriate.

Characteristic experimental Cu L-shell spectra from the mica spectrometer are shown in Fig. 5.9a, showing lines from a 4 x 25 μm WXP (green line), an LCXP (blue line), and a 25 μm noninsulated HXP (orange line). The intensities are normalized between the peak intensity and unexposed background. The characteristic lines and their energies are all comparable. The considerable similarity between the WXP and HXP spectra suggests either a nearly identical beam source or very comparable warm plasma temperatures in the micro Z-pinch in the lead-up to collapse. Significantly more background emission appears in most LCXP spectra, which was also observed in the outlier insulated HXPs with a hot K_α line. This extra background indicates additional emission from a hotter source with no lines in this energy range ($\sim$ 900 - 1600 eV, including, perhaps, continuum from higher orders of the mica), matching diode measurements (see Fig. 5.4d).

As was determined using the SCRAM code in Ref. [14], the best simulated fit for the Cu L-shell spectra from X-pinches on GenASIS is a 'Warm' plasma, plotted in Fig. 5.9b. Applying the appropriate transmission of the 25 μm Al filters and their respective Si diodes to the simulated spectrum, the total SXR and HXR flux from a 1-2 ns FWHM, 50 - 100 μm diameter source (as determined from the penumbral arrays, see Figs. 5.1g-h and 5.3g-h) at these parameters matches well with the experimentally determined flux ($\sim$ 2 MW for the 25 μm Al filtered diode) and energy ($\sim$ 3 mJ on the same diode) for all of the strongly pinching X-pinch configurations tested (which excludes the 40 μm Cu HXP). Thus, this emission probably originates from an electron beam that forms across the recently broken neck of the micro Z-pinch (though it is worth noting that a 200 eV plasma sans fast electrons will produce similar lines on the mica but will not match the diode measurements terribly well, or produce the cold K_α line discussed subsequently). A 200 eV plasma is hotter than the coronal plasma in the rest of the X, and likely only forms during the collapse and termination process (this is, of course, evidenced by the lack of diode signals from any filter at any time other than pinch timing) [69, 70, 199].

Figure 5.10a shows typical lineouts from HOPG spectra from the same three X-pinch types

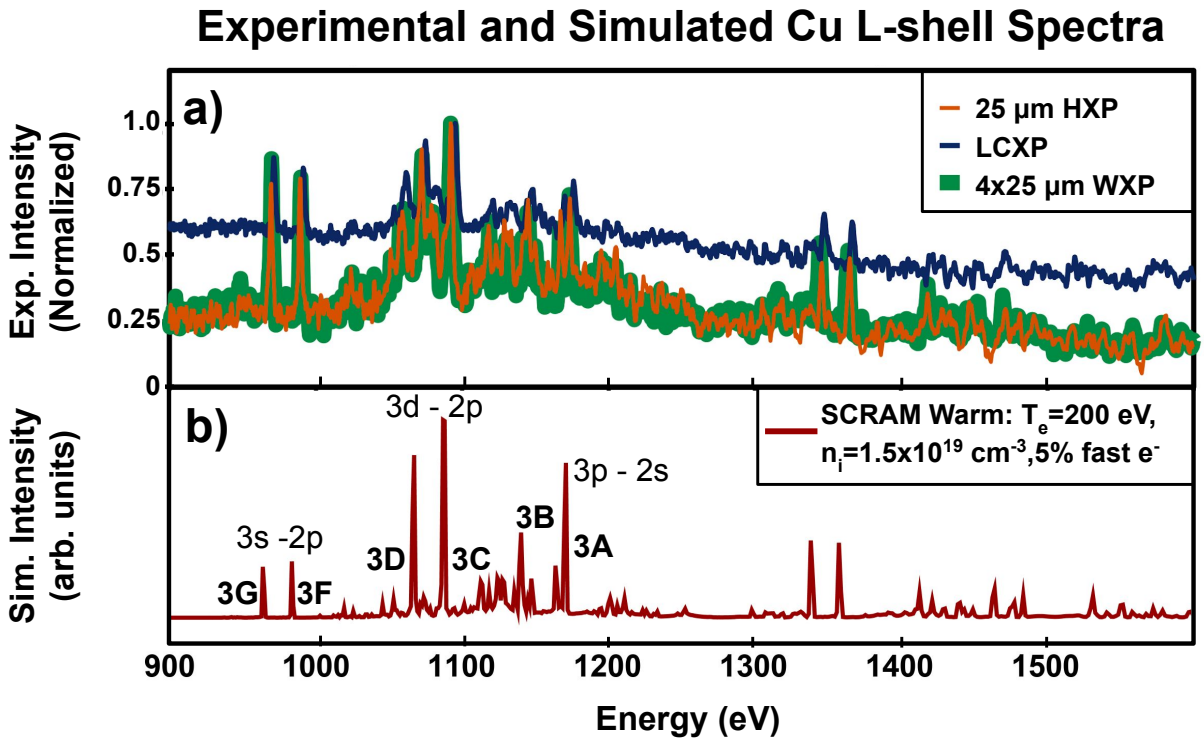

Figure 5.9: a) Experimentally obtained spectra from a 25 μm HXP, an LCXP, and a 4 x 25 μm WXP from the convex mica spectrometer. Intensties were normalized. b) A simulated 'Warm' SCRAM spectrum from a 200 eV, $n_i = 1.54 \times 10^{19}$ cm^{-3} plasma with 5% of its electrons at 10 keV. The intensities for the simulated spectrum are adjusted for the transmission, absorption, and reflectivities of the Be filters, image plate, and mica crystal, respectively. Key transitions are labelled in frame b) as well.

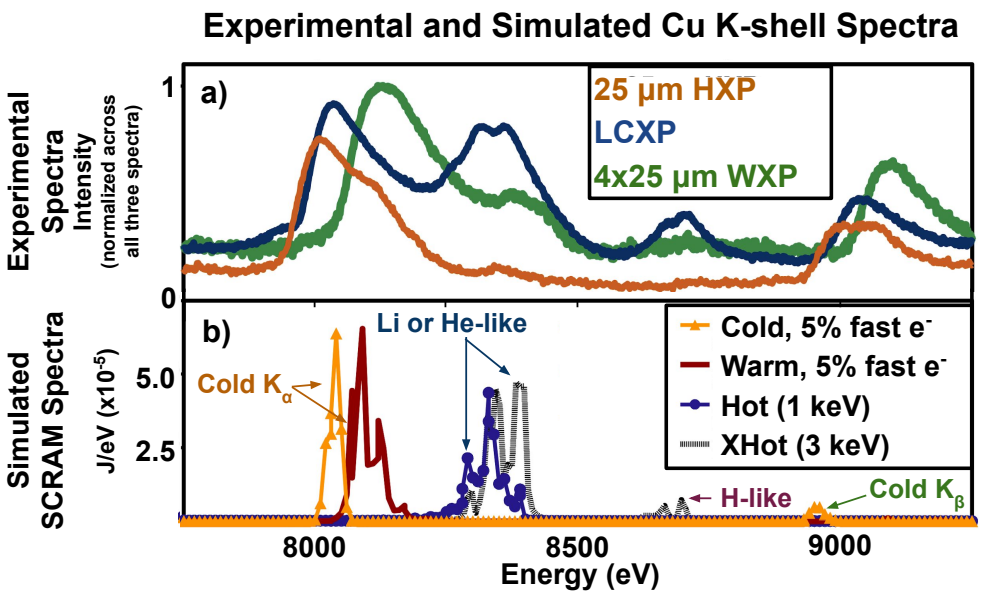

Figure 5.10: a) Lineouts of Cu K-shell spectra from a 25 µm HXP, LCXP, and 4 x 25 µm WXP using the HOPG spectrometer. The intensity of the lineouts is shifted by the minimum (an unexposed region) from each respective image plate, and normalized across all three spectra (to preserve relative intensity). b) Four different simulated spectra from the SCRAM code to match the different spectra captured experimentally. The y-axis is in J/eV, which takes into account the estimated source size and pulse duration to match the integrated experimental diode signals. The 'Cold' plasma is calculated with a 50 µm radius and 4 ns pulse duration, 'Warm' with a 50 µm radius, and a 1 ns pulse duration, 'Hot' with a 1 µm radius and a 1 ns pulse duration, and 'XHot' with a 0.5 µm radius and a 0.5 ns pulse duration. Key lines are labelled in frame b).

shown in Fig. 5.9a. The intensity of the lineouts is shifted by the minimum (an unexposed region) from each respective image plate, and normalized across all three spectra to show the relative amounts of total emission and continuum. Potentially matching synthetic spectra created using the SCRAM code are presented in Fig. 5.10b. Here, the vertical axis of the simulated spectra is in J/eV, meaning that the output spectra have been multiplied by an estimated source size and pulse duration to recreate both the line ratios from the experimental spectra, and the fluxes and energies measured with the diodes.

The 4 x 25 µm Cu WXP K-shell spectrum (green line, Fig. 5.10a) is characteristic of that seen in all of the WXP configurations, containing two K_α features at $\sim$ 8100 and 8400 eV respectively. The simulated 'Warm' spectrum that fit the mica spectra matches reasonably well

with the cold K_α line. Similar parameters estimated for the source creating the L-shell spectra (50 μm in radius and 1 ns pulse width) recreate an appropriate relative cold K_α line intensity in J/eV, and as determined for the L-shell case, match the diode data. However, the 'Warm' spectrum conspicuously lacks the K_β ($\sim$ 9000 eV) line. A 'Cold', 30 eV plasma at $n_i = 5.6 \times 10^{18}$ cm^{-3} with 5% fast electrons at 10 keV, with a 50 μm radius and 4 ns pulse width, would produce K_α and K_β lines that reasonably match the HOPG spectra and diode measurements as well, but not the lines seen in the L-shell spectra. These plasmas are not mutually exclusive though, since no significantly intense L-shell lines are produced by the 'Cold' plasma (they would not be detected above the noise level even if present). A simulated 'Hot' plasma with a 1 μm radius and a 1 ns pulse duration recreates the $\sim$ 8400 eV peak, and the total flux and energy of this synthetic plasma compares well with the diode data (this 'Hot' plasma also matches X-pinch conditions measured on other drivers as well [69]). These findings match previous Cu X-pinch data obtained on GenASIS [14].

The e-beam generated cold K_α line in the WXPs appears to have a higher relative energy than the comparable cold K_α lines seen in LCXPs and HXPs. This could be a real observation, with the e-beam in the WXPs striking a warmer plasma than that in the LCXPs or HXPs. Alternatively, any few-hundred micron separation between pinch and beam sources (plausible given the length of the micro Z-pinch seen in Fig. 5.3c and subsequent gap observed in WXPs) would alter the ray-tracing results, and either lower the beam line energy or raise the hot-pinch line energy by $\sim$ 50 - 100 eV.

The LCXP spectra (blue line, Fig. 5.10a) has three K_α lines and a K_β line. The first, cold K_α line ($\sim$ 8050 eV), and the K_β line again match the 'Cold' and/or 'Warm' synthetic spectra (see Fig. 5.10b). The next two lines at $\sim$ 8400 and 8700 eV come from a much hotter plasma. Note that the $\sim$ 8700 eV line is seen in at least 50% of the LCXPs, while in the remainder, as in the WXP results (green line), it is not. Since the Zn filtered diode captures all the lines in Fig. 5.10a, while the Cu filter transmission cutoff is at $\sim$ 8980 eV and the Ni filter cutoff is lower, at $\sim$

8330 eV (see Fig. 3.11), the decrease in peak flux from the Zn to the Cu to the Ni filtered diodes observed in Fig. 5.4d is expected given the energy of the lines seen in Fig. 5.10a. The dashed black 'XHot' line in Fig. 5.10b is from a simulated 3 keV, $n_i = 10^{22}$ cm^{-3} plasma, emitting for 0.1 ns from a 1 μm radius source (this pulse duration is plausible, matching highly temporally resolved X-pinch emission measurements at other facilities [8]), and both recreates the hot LCXP K_α line ratios and fits the diode data. Simulations show that simultaneous 8400 eV and H-like 8700 eV lines are attainable from alternative plasma conditions with either a $T_e \geq 2000$ eV and $n_i \geq 10\%$ solid density, or a ≥ 1 keV, solid density plasma with a fast electron component (i.e. an electron beam), though perhaps not with as ideal a fit to the data.

The continuum (and in most shots, line) emission intensity from the majority of insulated and noninsulated Cu HXPs (orange line, Fig. 5.10a) is significantly lower than the other configurations shown, consistent with the diode data shown in Fig. 5.6d. The beam source emits at a comparable energy to the cold source from the LCXPs, but the K_α line is wider than expected (relative to, say, the cold K_α line produced by the LCXPs). It is plausible that the HXP hot-pinch source potentially reaches only $\sim$ 200 eV, and the width of the HXP K_α line is a combination of the 'Cold' and 'Warm' plasmas, which would generally fit the mica, HOPG, and diode data.

However a very minor peak at $\sim$ 8300-8400 eV is just visible (note that a small number of the insulated Cu HXPs produced a hot K_α line resembling that in the WXP spectra). If there truly is a hot 8300 - 8400 eV line near the noise threshold in the typical HXP spectra, then the pinch either reaches only $T_e \approx 800$ eV, $n_i = 1\times10^{22}$ cm^{-3}, or, alteratively, $\sim$ 1000 eV, $n_i = 1\times10^{21}$ cm^{-3}. This is to say that in order to achieve a line of comparable intensity, the source is either the same temperature but an order of magnitude lower density than the WXPs, or a few hundred eV cooler but of comparable density. The generally consistent total emission from the HXPs in contrast with their weak but variable HXR emission requires further study.

Spectra from WXPs, LCXPs, and potentially HXPs cannot be explained by a single set of plasma parameters, mirroring the observations made in Ref. [14]. Instead, targets producing

these spectra require multiple (≥ 2) sources with distinct parameters that are co-located or under-resolved by the geometric resolution limits of the pinhole diagnostics.

5.5 Discussion

Optimized wire, hybrid, and laser-cut X-pinches produce hot-pinch sources with comparable peak X-ray power and total integrated energy, and all of these sources approach or exceed our experimental temporal and spatial resolution limits ($\sim$ 1 ns FWHM, $\sim$5 μm sources). The most striking difference between these sources is the increasing intensity and energy of the K-shell lines from HXP to WXP to LCXP, observed in the K-shell spectra (Fig. 4.14a), and corroborated by a corresponding increase in flux from the hard-filtered diodes (Figs. 5.1d-5.6d), that likely indicates an increasing source temperature from HXP to WXP to LCXP. In this section we will apply and compare our data to established X-pinch theory, postulate reasons for the potential differences in hot-spot temperature, and address the differences in the electron beam generated sources.

In Chap.2, we discussed the basic physics of pinch formation and radiative collapse in an X-pinch, and suggested it occurs above an effective current, analogous to the Pease-Braginskii current, I_{PB}. As mentioned in Sec. 2.2.2, the derivation of I_{PB} assumes bremsstrahlung is the dominant radiation loss mechanism, which is accurate for H and ^{2}D fusion plasmas, but not for higher-Z materials like Cu. An analytic formulation to account for additional radiation losses from bound-bound and bound-free transitions is unfeasible [166], so instead we turn to FLYCHK simulations [11], where we find for the Cu plasma conditions we expect in the X-pinches that the total radiative losses far exceed (3x or more) the amount of free-free radiation losses. This is plotted in Fig. 5.11a, showing total and free-free radiative losses for different n_i as a function of T_e. If we leave — in an admittedly crude assumption — the formulae as they are, and instead incorporate a multiplier reflecting total losses due to radiation, we find that collapse should begin in our Cu plasma between 100 and 200 kA, and we can (under this approximation) assume that all

of the pinches undergo radiative collapse on GenASIS.

Let us assume, based upon the comparable L-shell emission observed in each X-pinch configuration, that radiative collapse begins with a 'Warm' micro Z-pinch (see Sec. 5.4) without fast electrons. Referring to Fig. 5.11b, which shows Z^* as a function of n_i (in cm^{-3}) for different temperatures of an nLTE Cu plasma via the FLYCHK code, we see that Z^* generally changes little along an isotherm — in fact, we find that $Z^* \approx 3.6 \ln(T_e/1.52)$, where T_e is in eV, reasonably approximates the average ionization as a function of temperature (via a logarithmic fit), which will assist in later calculations. Then, solving Eq. 2.18 for the equilibrium radius, r, of the micro Z-pinch estimating both $N_i \approx n_i \pi r^2$, and $T_e \approx T_i$, we find that for the 'Warm' plasma, $r \approx 200$ μm, which is in agreement with laser-probing and XUV pinhole camera observations. Additionally, should the final hot-pinch also be in approximate pressure equilibrium (not necessarily meaning the collapse proceeds as such), for the 'Hot' and 'XHot' plasma, we find that $r \approx$ 2-4 μm, which agrees with the measurements from the penumbral slit-wire diagnostic.

Following the observations by Ivanenkov *et al.* (see Ref. [8]) revealing a cascade of micro Z-pinches, the Alfvén crossing times, τ_A, for increasingly small and dense micro Z-pinches (after the initial m = 0 instability forms in the $r \approx 200$ μm micro Z-pinch), range from tens to hundreds of picoseconds, so multiple stages of instability formation and subsequent collapse can feasibly happen in a sub-nanosecond timescale. Upon reaching the minimum collapse radius, if we assume that the total number of ions in the compressed region is $\mathcal{N}_{i-tot} \approx 1.33\pi r^3 n_i \approx 10^{12}$, and again assuming $T_e \approx T_i$ (likely valid since the ion-electron equilibration time at 200 eV and 10^{22} ions/cm^3 is of the order of 10 ps, via Ref. [134], Eq. 11.47), we find that raising the temperature of this plasma to 1000 eV requires about 10 - 20 mJ ($\sim$ 50 mJ to reach 2500 eV), neglecting radiative losses and assuming constant volume.

Precisely which collapse termination and source heating mechanisms discussed in Sec. 2.4.2 may supply these 10 - 50 mJ cannot be determined with the data collected here. However, we can compare the conditions required for the occurrence of such mechanisms to those observed

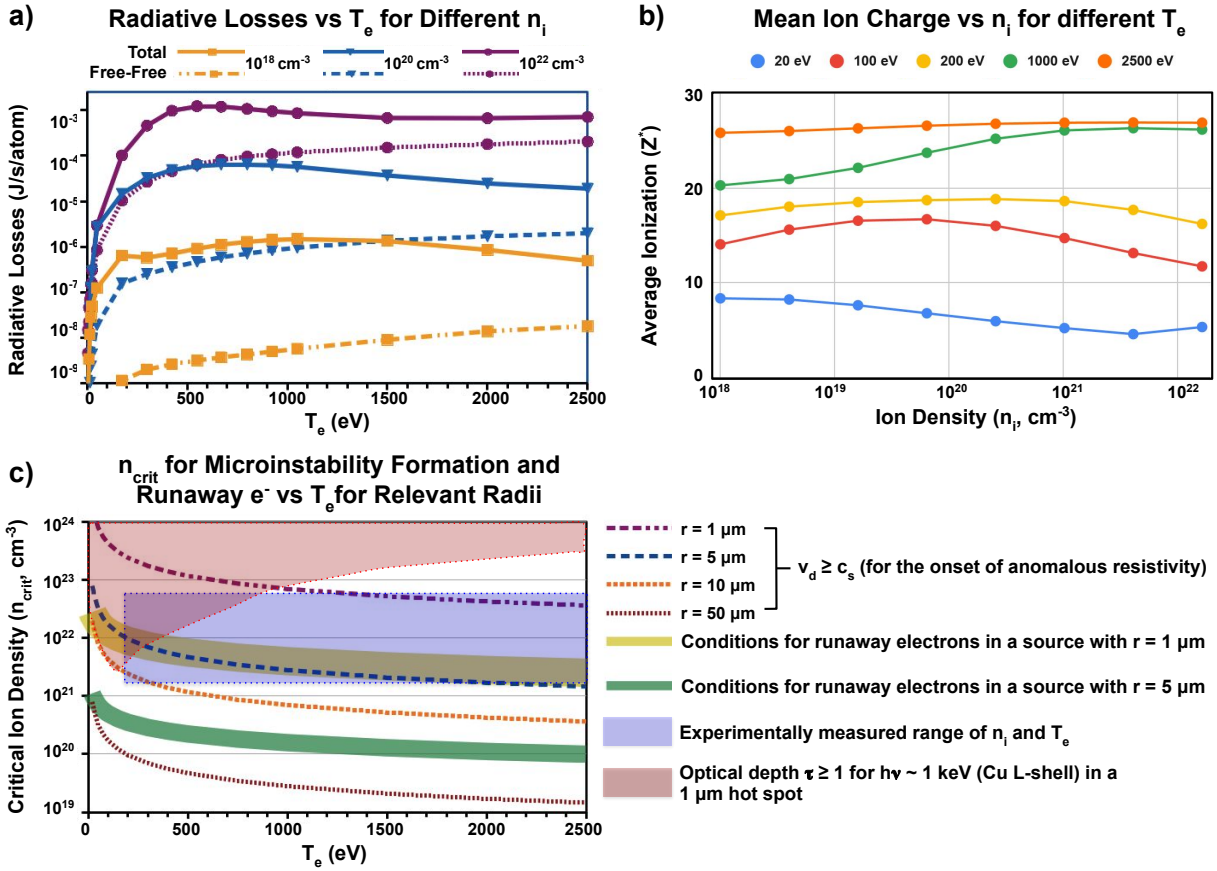

Figure 5.11: a) Total and Free-Free Radiative losses vs T_e for Cu plasmas of different n_i from the FLYCHK tables. The significant differences between total and free-free losses across all energies highlights the need to extrapolate for line and free-bound losses when calculating I_{PB} for higher Z materials. b) A plot of average ionization level, Z^*, as a function of ion density, n_i (cm^{-3}) for a Cu nLTE plasma via the FLYCHK tables, showing that Z^* is generally stable along an isotherm. c) A plot of the critical ion densities, $n_{crit} \approx N_i/(\pi r^2)$, required for the development of microinstabilities (thin dashed lines) and runaway electrons (thick green and yellow lines) at different pinch radii. Below these curves, conditions are analytically appropriate for the different processes to occur. The shaded red region represents the parameter space where the plasma becomes optically thick ($\tau \geq 1$) to the dominant Cu L-shell transitions ($h\nu \approx 1$ keV). The shaded blue area is the estimated range of source densities and temperatures (via flux and energy from the diodes, and spectroscopic analysis). Note that microinstability development conditions are shown for $v_d \geq c_s$, but for $v_d \geq v_{Ti}$ (see Sec. 2.4.2), n_{crit} is bigger by a factor of $\sqrt{\gamma Z^*}$, where γ is the adiabatic index.

in our experiments to determine their potential relevance. This is expressed in Fig. 5.11c, which shows the key thresholds for the onset of anomalous resistivity (plotted dashed lines), runaway electrons (plotted thick lines), and opacity (shaded red region) across relevant n_i and T_e. The range of potential densities and temperatures in the micro Z-pinch and hot-spot determined via the diode and spectroscopy measurements are encompassed by a blue rectangle.

As n_i increases during collapse, the opacity of the plasma trends upwards, meaning fewer photons escape the plasma to cool it. A useful tool for expressing the opacity of a plasma is the optical depth, τ which is a dimensionless quantity relating the photon mean free path to the plasma scale: a plasma is considered optically thick when $\tau \geq 1$ and optically thin in the opposite case. The percentage of photons transmitted at a given wavelength is given by $T_\nu = e^{-\tau}$. While opacity depends strongly on photon wavelength — the plasma does not absorb radiation across a broad spectrum equally — we know from the diode data and L-shell spectroscopy that the majority of the X-ray emission is in the Cu L-shell range. With this in mind, the red-shaded area in Fig. 5.11 denotes the parameter space where a 1 μm plasma grows optically thick to one or more key Cu L-shell transitions ($\sim$ 980 - 1200 eV), determined using the FLYCHK code. Using the emissivity values in Fig. 5.11a, we find that a 1-5 μm (via the penumbral diagnostic), 200 eV, 10^{22} ions/cm^{-3} plasma emitting for 1 ns, radiates enough that even 10% absorption ($\tau \geq 0.1$) could retain tens or more of mJ that would otherwise escape the collapsing hot-spot. In this case, the magnetic compression of the pinch is increasingly adiabatic, potentially resulting in rapid heating of the pinch/hot-spot within the collapse timescale.

Other processes may interrupt the collapse before the pinch grows opaque, or arise just during the explosion phase (following the rapid heating). Recall from Sec. 2.4.2 that microinstabilities are thought to arise when v_d exceeds either c_s or v_{Ti}. Setting $v_d = c_s$, we can solve for $n_i = n_{crit}$, for different radii (again we assume $n_i \approx N_i/(\pi r^2)$). Four such lines are shown in Fig. 5.11c. Below these contours, conditions are analytically appropriate for the development of microinstabilities. The shaded blue region in Fig. 5.11c (our experimental pinch parameter-space) overlaps with the

instability thresholds for final collapse radii in the r = 1-5 μm range. Note that n_{crit} for $v_d \geq v_{Ti}$ is not plotted in Fig. 5.11c for reasons of space, but these contours are simply a factor of $\sqrt{\gamma Z^*}$ larger (where γ is the adiabatic index, leading to $\sqrt{\gamma Z^*} \approx$ 4-7) than the corresponding n_{crit} for c_s. Actually observing the onset of microinstability growth and anomalous requires experiments observing the X-pinch crosspoint using voltage probes with picosecond time resolution, and could be an interesting future project.

Having demonstrated that, at least mathematically, the different X-pinches are all subject to similar processes, we return to focus on the apparent increase in temperature from the HXP to WXP to LCXP sources observed in the K-shell specra, and conclude that it likely relates to decreasing values of either N_i (the ion line density, see Eq. 2.18) or $\mathscr{N}_{i-tot}$. While perhaps oversimplified, if a generally comparable amount of energy, $\mathscr{E}$ is introduced to the hot-spot in each configuration (regardless or origin whether via magnetic compression, anomalous resistivity or another process), temperature increases with decreasing $\mathscr{N}_{i-tot}$, with $\mathscr{E} \propto \mathscr{N}_{i-tot}$ T (Z^*+1), where again $T \approx T_e \approx T_i$ and Z^* increases as a function of T.

Differences in N_i and $\mathscr{N}_{i-tot}$ could be a result of initial target linear mass and geometry. Adjacent to the pinching region in all of the X-pinches is an area where the plasma bulges out, such as an expanded region of an m = 0 instability, the plasma electrodes, or the legs of the X themselves. This increase in radius leads to an $\hat{r}$ component in the current density **J**, or J_r. $J_r B_\vartheta$ is in the axial direction, and thus facilitates mass removal away from the cross-point. Analytical models and simulations by Chittenden *et. al* (Ref. [70]) showed that this mass removal is critical to the evolution of the collapse region.

Hybrid X-pinches, with their long axial wire would seemingly not support the same rate of mass removal as WXPs and LCXPs. Even in areas where significant $J_r B_\vartheta$ exists in an HXP — at the plasma electrodes formed by the low-density ablation from the conical electrodes — the axial wire likely inhibits mass flow away from the cross-point. Considered cumulatively over the course of the entire current pulse, a reduced rate of mass removal from the pinching region likely explains

why pinch time, for the same cross-sectional mass, is so much later in HXPs than in WXPs (as seen in Tables 5.1 and 5.2, the 25 μm HXP has half the linear mass of the 2 x 25 or 4 x 18 μm WXPs, and yet pinches at comparable times).

How mass removal may lead to higher temperature LCXP (than WXP) sources is less clear. The foil target has geometry that facilitates mass removal and a lower initial linear mass than the WXPs, which combined should result in a lower N_i at pinch time than is found in the heavier WXP or the slower-flowing HXP crosspoints. Why the LCXP does not then simply pinch earlier during the current rise (like the comparably initially massed non-insulated HXPs) conceivably relates to the extra mass of the tapered legs (compared to WXPs) adjacent to the cross-point, but how this affects mass flow, target ablation, and collapse timing is unclear as of yet. In the near future we plan to conduct simulations to study the differences in evolution between the different cross-point geometries.

One final possibility is that the sources are not as significantly different in temperature as estimated, but that there are varying degrees of fast electrons in the pinch, which can significantly alter the spectrum of a plasma [73]. As discussed in Sec. 2.4.4, runaway electrons may be generated if E_{hs} exceeds E_D (Eqs. 2.41 and 2.40 respectively) [162–164]. One can solve for the n_{crit} below which E_{hs} exceeds E_D, and this threshold is plotted in Fig. 5.11c, as thick light yellow and green lines for hot-spot radii of 1 and 5 μm respectively. This threshold could actually be significantly higher since the onset of anomalous resistivity (see the plots for n_{crit} where $v_d \geq c_s$ at 1μm) would significantly raise η in E_{hs} (Eq. 2.41), leading E_{hs} to overtake E_D at a larger n_i. Additionally, since we are concerned only with electrons in excess of $\sim$ 10 keV, as is required to ionize the Cu K-shell, the electron-electron mean free path of such fast electrons in the hot-spot exceeds the r used to calculate n_{crit} (meaning the electrons will travel the requisite distance) [200]. Should such electrons occur, a small fraction ($\sim$ 5 %) of fast electrons could significantly alter the emission profile, producing a spectrum equivalent to that characteristic of a hotter plasma (as mentioned near the end of Sec. 5.4).

Finally, the presence of fast electrons interacting with a colder (T_e = 30 - 200 eV), lower density ($n_i = 10^{18}$ - 10^{19} cm^{-3}) plasma was observed in every configuration (see the lowest energy K_α (and K_β) lines in Fig 4.14a). This source most likely correlates with the opening of a gap where the hot-pinch had just radiated and broken up. Here we are not concerned about any limiting E_D in the extremely low density plasma in the gap. Instead, we treat this space like a spark gap, with a V(t) across it given by Eq. 2.43.

The gap clears out in a time given by $t_c = \ell/(2c_s)$, where ℓ is the length of the micro Z-pinch. For WXPs, the measured plasma electrode gap is up to $\sim$ 500 μm. Since we usually observe very narrow plasma electrode gaps in the LCXP and HXP shots at or just-after pinch time, we will assume the lower limit for the gap is around the limit of the schlieren resolution, or $\sim$ 50 μm. For the final temperatures determined in Sec. 5.4, t_c = 0.2 - 1 ns for LCXPs, 0.4 - 4 ns for WXPs, and 0.4 - 4 ns for HXPs.

With the inevitable closure of the gap by the low-density electrode plasma in the HXPs, there is likely little time between cross-point clearing and closure (regardless of clearing time), possibly resulting in less significant beam formation, observed spectrally in Fig. 4.14a, and explaining the lack of a separately resolved HXR X-ray spots via the pinhole camera ($\sim$ 200 μm geometric resolution limit) or diode signal peaks ($\sim$ 1 ns scope resolution limit, see Fig. 5.6d). In an LCXP, t_c is likely less than half that of the HXP, so a gap could form, but the large adjacent plasma electrodes expanding at their local sound speeds (assuming from the spectral simulations with fast electrons to have $T_e \sim$ 30 - 200 eV) would close this gap within the $\sim$ 1 ns time resolution of the diode-scope setup, creating similar conditions for e-beam formation as in the HXP (short time to form, small gap, etc). In the WXPs, for a plasma electrode gap such as that seen in Fig. 5.3c, $t_c \leq 4$ ns. From this we expect beam formation to take longer in WXP than either the shorter-gapped HXP or LCXP, which potentially explains the measurable delay (on the diodes) between the hot-pinch and e-beam generated sources seen in WXPs.

The buildup of voltage across this gap (as well as the current through the pinch during the

collapse phase) likely relates, at least some degree, to the driver parameters. This includes the driver's 'stiffness' or overall inductance and impedance, as well as the voltage it places across the electrodes which is vastly different in the traditional Marx bank and the newer LTD drivers. Hopefully in the near future, circuit simulations can help model the driver dynamics during such a collapse to help improve MHD simulations and analytical modelling of the collapse phase.

5.6 Summarizing the benefits and drawbacks of each X-pinch target.

Copper wire, laser-cut foil, and hybrid X-pinches (WXP, LCXP, and HXP) have been tested, characterized, and optimized on a compact, university-scale driver, to compare the performance of these configurations as soft X-ray ($\sim$ 1 keV) and hard X-ray ($\sim$ 8 keV) sources in terms of reproducibility, flux, and source size. The primary results of this work are summarized in Table 5.2.

WXPs produced small SXR sources of size $\leq$ 5 μm, but significant HXR emission from e-beams frequently double-exposed or washed out radiographs from these small sources. Increasing the wire-count and linear mass of the target effectively reduced HXR emission. LCXPs produced the highest-flux (by up to 2x) and smallest HXR sources, comparable to the $\sim$ 5 μm SXR sources also produced. A decrease in target-to-target similarity caused by using a faster, simpler laser-cutting platform compared to previous work [14] increased source timing error, but had no negative effects on source flux or quantity, with single-source reproducibility (within 200-300 μm) at nearly 100%. Though HXPs initially pinched inconsistently ($\sim$30-40% of the time), when they did, they were shown to produce small ($\leq$ 5 μm) SXR sources more reliably than WXPs, with few HXRs. Two proposed solutions improved shot-to-shot consistency: switching from Cu to higher-resistivity, comparably massed Ni and Constantan, and insulating the anode with polyimide. Implementing these changes increased pinch reliability to 100% and to varying degrees also altered electron

beam formation, pinch timing, and the required conical electrode spacing.

Spectral analysis shows that the X-ray emission from these configurations arises from ≥ 2 different sources or sets of plasma conditions. The spectral data, supported by flux and integrated energy measurements from filtered Si-PIN diodes, also suggests that the hot-pinch temperature increased from HXPs, to WXPs, to LCXPs. This difference is potentially due to differences in both the initial linear mass of the targets, and MHD mass removal processes during the current drive relating to the different X-pinch geometries.

Each X-pinch configuration has its own benefits and drawbacks, and a potential user should choose according to their driver, material, and available facilities.

- WXPs remain a simple, fairly reproducible configuration that work across nearly any viable current and current rise-rate when attention is paid to the linear mass and wire-count of the X. Variable e-beam driven sources are always present, but can be limited with adjustments to the target linear mass and wire count. For low-cost experiments with a high total shot number, WXPs present the simplest option for a high-resolution SXR source with little-to-no optimization time required.

- LCXPs present a higher-performance option than WXPs for lower-rep and higher cost experiments, producing single or co-located sources at a repeatable location $\pm$ 100 μm. They also are the best option for high-resolution HXR backlighting and experiments where higher localized hard X-ray flux is desired, such as for the Talbot-Lau diagnostic described in Ref. [64]. Their primary drawbacks are the need for access to a laser-cutting facility, making them expensive, and the steep initial learning curve in terms of electrode design and target loading. The laser-cutting process allows the user to match the cross-sectional mass at the cross-point to the driver far better than the other configurations, but produces a slightly more variable linear mass at the cross-point, which appears to increase variability in pinch timing.

- The reproducibility of the small, single or co-located sources in HXPs make them a good source for lower-rep, higher cost experiments as well. Their ease of loading and ability to pinch virtually any material exemplify their versatility. Given the need to time pinching with the XUV-ablated cold plasma from the conical electrodes, the HXP does appear to work better on shorter-rise (< 100 ns) drivers, where the variability of this cold electrode plasma is negligible. Determining the ideal conical electrode gap requires a learning curve akin to LCXP loading. The HXP has less flexibility in mass-matching the load to the driver, exhibits a slightly variable source location due to the 1 - 3 mm cross-point region, and is the most sensitive to initial conditions with respect to the early-time current profile of the driver, though we presented two remedies to the latter.

5.6.1 Acknowledgements

Chapter 5 contains material that has been submitted for publication in October of 2020 to the *Journal of Applied Physics*, entitled "Direct comparison of wire, foil, and hybrid X-pinches on a 200kA, 150ns current driver", by G. W. Collins IV, M. P. Valdivia, S. B. Hansen, F. Conti, L. C. Carlson, D. A. Hammer, A. Elshafiey, J. Narkis, and F. N. Beg. The dissertation author was the primary investigator and author, and is indebted to all of the co-authors from UC San Diego, General Atomics Inc., Sandia National Lab, and Cornell University who have given their written permission to use this material in this dissertation.

Chapter 6

Summary and Future Work

The work contained in this dissertation took a tortuous route to its present state, involving equal parts physics and engineering to improve upon the well-known X-pinch X-ray source in part by creating a new type of X-pinch, the laser-cut foil X-pinch or LCXP, and in part by benchmarking the performance of other well-known X-pinch configurations including wire and hybrid X-pinches (WXPs and HXPs respectively). In reality, it represents a superficial scratch on the surface of the capabilities and physics driving the X-pinch, and the realms for future study are broad and abundant.

6.1 Development of the Laser-cut Foil X-pinch

Since its inception, the wire array X-pinch has represented a beautifully simple, and fairly cost-effective means of creating a micron and nanosecond scale X-ray pulse. While the wire X-pinch reliably produces X-rays, the pulse characteristics, including the source size, duration, flux, and quantity are inherently variable, and the presence of strong electron beams which, though potentially usable for lower-resolution radiography (hundreds of microns, tens of nanoseconds) tends to doubly expose the faster pinch radiograph. Thus, the X-pinch is not quite ideal for low-rep, high-cost experiments.

Much of the variability of the X-pinch ties to the need to specifically tailor the mass of the target X to the peak current and current rise-time of the specific pulsed-power driver. With this in mind, we set out to precisely tailor the target by using laser-ablation/cutting techniques developed at General Atomics Inc to cut the targets from a single thin foil.

The first LCXPs were made from Ta foils, and mass-matched to ideally massed W WXPs on the $\sim$ 200 kA peark current, 150 ns rise-time GenASIS driver. When successfully loaded, these Ta LCXPs produced sources on the order of 10 μm, with peak X-ray flux comparable to that produced from traditional W WXPs. These Ta LCXPs represented a proof of concept: the foil X, cut with a laser, with its (approximately) right-angle edges and tapered legs, pinched, and pinched well.

However, loading the foil X's presented a challenge, given the inherent fragility of a 100-500 μm^2 crosspoint. Targets were broken at a higher rate than they were successfully loaded, so engineering a better loading process, or perhaps even a better design was required.

Iteratively, the design and loading processes were gradually improved while conducting Cu LCXP experiments, until the loading success rate reached 100%. Once targets could be loaded consistently (and thus not introduce pinch variability due to loading problems) the Cu LCXPs were compared to Cu WXPS, and eventually HXPs.

6.2 Comparing Different X-pinches

All three configurations: laser-cut, hybrid, and wire X-pinches produced comparable soft X-ray flux (Cu L-shell at $\sim$ 1 keV) from hot pinch sources measuring $\leq$ 5 μm. The LCXPs produced higher hard X-ray (Cu K-shell) flux than the WXPs, but less total energy, since the LCXPs produced no separately resolvable electron beam source (within $\sim$ 200 μm and 1-2 ns of the hot pinch), while the WXPs produced long lasting electron beam sources ($\geq$ 5 ns) that measured 50 - 100 μm across and occured $\geq$ 5 ns after the pinch. Optimized HXPs produced single

peaks, with significantly less total K-shell emission, and, like the LCXPs, no separately resolvable electron beam source. In the case of the LCXP and HXP, the significant amount of low density plasma from the legs of the target and the ablation of the conical electrodes respectively, appeared to close the gap formed post-pinch before significant e-beam sources could occur. Undermassed LCXPs and over-spaced (too much distance between the conical electrodes) HXPs did produce resolvable e-beams.

K-shell spectroscopy showed cold K_α and K_β lines for all configurations, showing that some degree of electron beam occured in all of the X-pinches. The intensity of these cold K-shell lines was significantly lower in the majority of the HXPs, matching the diode data. Matching simulated spectra from the SCRAM code to the spectrographs and the diode data, we estimated the pinch parameters. All of the wire and laser-cut X-pinches, and occasional hybrid X-pinches produced hotter ($\sim$ 8400 eV) K_α lines indicating a hot pinch source at $\geq$ 10% solid density and $T_e \approx$ 1keV. The lack of significant highly ionized K_α lines in the HXP spectra indicates either a colder or lower density source: the former would produce less of this $\sim$ 8400 eV, while the latter would be less bright, leading to less intense lines recorded in the spectra. A majority of LCXPs showed H-like lines ($\sim$ 8700 eV) as well, suggesting that the laser-cut X-pinches reached up to $T_e \approx$ 2500 eV, or had a fast electron component that struck the 1 keV plasma source.

L-shell spectroscopy indicated a T_e = 200 eV, $n_i = 1.5 \times 10^{19}$ cm^{-3} source in all configurations, that may have contained a 5 - 10 % fast-electron ($\geq$ 10 keV) component. This suggests that all of the micro Z-pinches reach this temperature adjacent to the collapse region where the higher-temperature pinch occurs. Whether the electron beam seen in all of the K-shell spectra strikes this 200 eV plasma, or a colder, $T_e \approx$ 30 eV plasma, which better reproduces the experimentally measured cold K_β line remains undetermined.

Calculations of the Pease-Braginskii current, I_{PB}, using measured parameters, indicate that all of the X-pinches driven on GenASIS undergo radiative collapse. During this collapse, an instability (likely m=0) in the micro Z-pinch seeds a rapid contraction of the pinch in the

unstable region to a smaller radius until interrupted by the effects of opacity or the onset of particle scattering that outpaces the typical Coulomb collisions called anomalous resistivity. This anomalous resistivity occurs when the electron drift velocity, v_d exceeds the ion sound speed, c_s, which happens at a critical ion line density, N_{crit} which scales as Z^{*-2}. How this relates to the differences in observed final pinch temperature, which increases from HXP to WXP, to LCXP, is difficult to say. However, the key difference in these X-pinches relates to their geometry and their initial masses. Previous work showed that mass removal from the crosspoint was key to pinching, and that this mass removal occured in part to to a geometrically introduced $\mathbf{J}_r\mathbf{B}_\vartheta$ which accelerates material in the axial direction. A combination of the linear geometry in the HXP (no significant $\mathbf{J}_r$) and the lower initial mass in the LCXP likely contribute to the temperature and density differences seen, but this remains a subject for further investigation.

6.3 Areas for Future Study

6.3.1 Target Improvements

As an X-pinch, the laser-cut foil X proved, over three separate experimental campaigns, that it pinches as-well-as or better than other X-pinch configurations. That said, it has only been tested by one group (the author of this dissertation and a rotating supporting cast), on a single machine (GenASIS). X-pinches notoriously produce more electron beams on higher current, higher voltage drivers, so the foil target needs testing on larger machines and at different rise-times — both slower and faster.

Moving to larger machines will allow for larger linear masses in the targets' crosspoint, which inherently makes them easier to load, while a lower-current driver will require additional engineering improvements, or the use of more rigid materials such as W or Ni.

The cutting process itself offers an interesting problem. While high-resolution cutting centers like LWS1 can cut ideal targets, using double-pulse techniques and a ≤ 10 μm laser spot

size, these are economically out-of-reach for a university pulsed-power facility. An off-the-shelf cutting platform such as the TRUMPF Trumark laser marking station cannot yet cut as reproducible of a target as the LWS1, but there are many adjustable parameters including laser pulse rate, laser power, and laser-head speed that have only been superficially investigated here, and could prove important in producing more consistent X's.

Exploring the relationship between K-shell yield and material for a given current could also provide insights into the nature of the pinch itself, and the versatility of the target.

Finally, as was mentioned at the end of Ref. [13], a long-term goal of the X-pinch is to rep-rate it, meaning the source could be driven at the rate the machine could feasibly be fired, without the need to break vacuum. Designing a spool or reel of X's that can be moved into place between the driver electrodes via a mechanical process represents a time-consuming but doable and desirable engineering project

6.3.2 X-pinch Physics

Simulations are an increasingly powerful tool to help understand difficult to diagnose processes in plasmas physics. Investigating the mechanisms and rates of mass removal from the different crosspoint configurations tested in Ch. 5 using MHD codes could provide insight into the final differences in temperature and/or density observed between the different pinches. Furthermore, better understanding this could lead to fundamental improvements in the overall target design.

The relationship between the current driver and target during the final stages of pinch collapse also provide fertile ground for study, requiring both experiments and simulations. Circuit simulations accompanied by resistivity and spatial (pinch geometry for inductance calculations) data from the MHD simulations mentioned in the previous paragraph could could highlight the currents and voltages expected through a rapidly collapsing plasma. The current through the pinch ties to the balance between joule heating and radiative losses, while the potential

relates to the consistent presence of fast electrons observed in X-pinches across all configurations. Voltage and current probes always prove difficult to field in the electromagnetically noisy pulsed-power environment, complicated further by the picosecond timescales required to observe these parameters during radiative collapse, but are vital for verifying any circuit-type simulations.

A final point of interest lies in the relationship between the radiative properties of the materials in the micro Z-pinch, and the final flux and size of the hot pinch. Given the established theory, mostly laid out by Chittenden *et al.*, higher Z materials (which radiate more than low Z materials) collapse more efficiently and have a smaller final radius. By testing targets with identical linear masses but different elemental compositions, say taking an Al foil X and incrementally cutting it smaller but electroplating or vapor-depositing incrementally more and more Cu onto it, one may carefully track the total flux emitted (especially in the Cu L-shell/Al K-shell region) and the source size (this would require a penumbral diagnostic with $\geq$ 10x magnification using film (not image plate) as a function of expected total radiated power for the combined materials.

The X-pinch remains an enticing and simple configuration for pulsed-power plasma physics. Its capacity to serve as both a unique and accessible diagnostic, and an easily creatable extreme plasma environment should provide ample grounds for future use and study in years to come.

Bibliography

[1] Teylers Museum. De'ongemeen groote' elektriseermachine. https://www.teylersmuseum.nl/nl/collectie/gebouw-en-geschiedenis/verhalen/de-ongemeen-groote-elektriseermachine, 2020.

[2] Edwin F. Northrup. Some newly observed manifestations of forces in the interior of an electric conductor. *Phys. Rev. (Series I)*, 24:474–497, Jun 1907.

[3] F N Beg, A E Dangor, P Lee, M Tatarakis, S L Niffikeer, and M G Haines. Optical and x-ray observations of carbon and aluminium fibre z-pinch plasmas. *Plasma Physics and Controlled Fusion*, 39(1):1–25, jan 1997.

[4] Magpie gallery: Experiments. https://www.imperial.ac.uk/plasma-physics/magpie/gallery/.

[5] S. V. Lebedev, F. N. Beg, S. N. Bland, J. P. Chittenden, A. E. Dangor, M. G. Haines, K. H. Kwek, S. A. Pikuz, and T. A. Shelkovenko. Effect of discrete wires on the implosion dynamics of wire array z pinches. *Physics of Plasmas*, 8(8):3734–3747, 2001.

[6] J. C. Valenzuela, G. W. Collins, D. Mariscal, E. S. Wyndham, and F. N. Beg. Study of instability formation and euv emission in thin liners driven with a compact 250 ka, 150 ns linear transformer driver. *Physics of Plasmas*, 21(3):031208, 2014.

[7] F. Conti, N. Aybar, J. Narkis, J. C. Valenzuela, H. U. Rahman, E. Ruskov, E. Dutra, S. Haque, A. Covington, and F. N. Beg. Study of stability in a liner-on-target gas puff z-pinch as a function of pre-embedded axial magnetic field. *Physics of Plasmas*, 27(1):012702, 2020.

[8] G. V. Ivanenkov, S. A. Pikuz, T. A. Shelkovenko, J. Greenly, D. B. Sinars, and D. A. Hammer. Formation, cascade development, and rupture of the x-pinch neck. *Journal of Experimental and Theoretical Physics*, 91(3):469 – 478, 2000.

[9] Byung Moo Song, T. A. Shelkovenko, S. A. Pikuz, M. A. Mitchell, K. M. Chandler, and D. A. Hammer. X pinch x-ray radiation above 8 kev for application to high-resolution radiography of biological specimens. *IEEE Transactions on Nuclear Science*, 51(5):2514–2519, 2004.

[10] F. Zucchini, S. N. Bland, C. Chauvin, P. Combes, D. Sol, A. Loyen, B. Roques, and J. Grunenwald. Characteristics of a molybdenum x-pinch x-ray source as a probe source for x-ray diffraction studies. *Review of Scientific Instruments*, 86(3):033507, 2015.

[11] H.-K. Chung, M. H. Chen, W. L. Morgan, Yu-Ralchenko, and R. W. Lee. Flychk: Generalized population kinetics and spectral model for rapid spectroscopic analysis for all elements. *High Energy Density Physics*, 1:3, 2005.

[12] Gilbert W Collins IV. Study of x-pinch dynamics using a low current (25ka) and long-rising (400ns) pulse. Master's thesis, San Diego State University, 5500 Campanile Dr, San Diego, CA 92182, 2013.

[13] G. W. Collins IV, M. P. Valdivia, T. O. Zick, J. Kim, D. M. Haas, A. C. Forsman, R. B. Stephens, and F. N. Beg. Investigation into the dynamics of laser-cut foil x-pinches and their potential use for high repetition rate operation. *Applied Physics Letters*, 105(2):024101, 2014.

[14] G. W. Collins IV, J. C. Valenzuela, S. B. Hansen, M. S. Wei, C. T. Reed, A. C. Forsman, and F. N. Beg. Characterization of laser-cut copper foil x-pinches. *Physics of Plasmas*, 23(10):101212, 2016.

[15] S. C. Bott, D. M. Haas, Y. Eshaq, U. Ueda, R. E. Madden, G. W. Collins, and F. N. Beg. Ablation studies of low-number wire arrays at 200 ka using a linear transformer driver. *IEEE Transactions on Plasma Science*, 38(4):567–573, April 2010.

[16] Joel S. Lash. The sandia z machine: an overview of the world's most powerful pulsed power facility. https://www.osti.gov/servlets/purl/1429410, 2017. Accessed: 2020-04-10.

[17] R. B. Spielman, C. Deeney, G. A. Chandler, M. R. Douglas, D. L. Fehl, M. K. Matzen, D. H. McDaniel, T. J. Nash, J. L. Porter, T. W. L. Sanford, J. F. Seamen, W. A. Stygar, K. W. Struve, S. P. Breeze, J. S. McGurn, J. A. Torres, D. M. Zagar, T. L. Gilliland, D. O. Jobe, J. L. McKenney, R. C. Mock, M. Vargas, T. Wagoner, and D. L. Peterson. Tungsten wire-array z-pinch experiments at 200 tw and 2 mj. *Physics of Plasmas*, 5(5):2105–2111, 1998.

[18] M G Haines, T W L Sanford, and V P Smirnov. Wire-array z-pinch: a powerful x-ray source for ICF. *Plasma Physics and Controlled Fusion*, 47(12B):B1–B11, nov 2005.

[19] J. E. Bailey, G. A. Rochau, C. A. Iglesias, J. Abdallah, J. J. MacFarlane, I. Golovkin, P. Wang, R. C. Mancini, P. W. Lake, T. C. Moore, M. Bump, O. Garcia, and S. Mazevet. Iron-plasma transmission measurements at temperatures above 150 ev. *Phys. Rev. Lett.*, 99:265002, Dec 2007.

[20] G. C. Burdiak. *An Investigation of Cylindrical Liner Z-pinches as Drivers for Converging Strong Shock Experiments.* PhD dissertation, Imperial College, Imperial College London, January 2013.

[21] M. E. Cuneo, M. C. Herrmann, D. B. Sinars, S. A. Slutz, W. A. Stygar, R. A. Vesey, A. B. Sefkow, G. A. Rochau, G. A. Chandler, J. E. Bailey, J. L. Porter, R. D. McBride, D. C. Rovang, M. G. Mazarakis, E. P. Yu, D. C. Lamppa, K. J. Peterson, C. Nakhleh, S. B. Hansen, A. J. Lopez, M. E. Savage, C. A. Jennings, M. R. Martin, R. W. Lemke, B. W. Atherton, I. C. Smith, P. K. Rambo, M. Jones, M. R. Lopez, P. J. Christenson, M. A. Sweeney, B. Jones, L. A. McPherson, E. Harding, M. R. Gomez, P. F. Knapp, T. J. Awe, R. J. Leeper, C. L. Ruiz, G. W. Cooper, K. D. Hahn, J. McKenney, A. C. Owen, G. R. McKee, G. T. Leifeste, D. J. Ampleford, E. M. Waisman, A. Harvey-Thompson, R. J. Kaye, M. H. Hess, S. E. Rosenthal, and M. K. Matzen. Magnetically driven implosions for inertial confinement fusion at sandia national laboratories. *IEEE Transactions on Plasma Science*, 40(12):3222–3245, 2012.

[22] C. Deeney, T. J. Nash, R. B. Spielman, J. F. Seaman, G. C. Chandler, K. W. Struve, J. L. Porter, W. A. Stygar, J. S. McGurn, D. O. Jobe, T. L. Gilliland, J. A. Torres, M. F. Vargas, L. E. Ruggles, S. Breeze, R. C. Mock, M. R. Douglas, D. L. Fehl, D. H. McDaniel, M. K. Matzen, D. L. Peterson, W. Matuska, N. F. Roderick, and J. J. MacFarlane. Power enhancement by increasing the initial array radius and wire number of tungsten z pinches. *Phys. Rev. E*, 56:5945–5958, Nov 1997.

[23] M. Kruskal and M. Schwarzschild. Some instabilities of a completely ionized plasma. *Proceedings of the Royal Society of London. Series A, Mathematical and Physical Sciences*, 223(1154):348–360, 1954.

[24] W. D. Hackmann. The researches of dr. martinus van marum (1750–1837) on the influence of electricity on animals and plants. *Medical History*, 16(1):11–26, 1972.

[25] M G Haines. A review of the denseZ-pinch. *Plasma Physics and Controlled Fusion*, 53(9):093001, jun 2011.

[26] J. A. Pollock and S.H. Barraclough. Note on a hollow lightning conductor crushed by the discharge. *Procession of the Royal Society NSW*, 39:131, 1905.

[27] Willard H. Bennett. Magnetically self-focussing streams. *Phys. Rev.*, 45:890–897, Jun 1934.

[28] M Blackman. Self-magnetic field in high current discharges. *Proceedings of the Physical Society. Section B*, 64(12):1039–1045, dec 1951.

[29] S W Cousins and A A Ware. Pinch effect oscillations in a high current toroidal ring discharge. *Proceedings of the Physical Society. Section B*, 64(2):159–166, feb 1951.

[30] L. A. Artsimovich, A. M. Andrianov, E. I. Dobrokhotov, S. Yu. Lukyanov, I. M. Podgornyi, V. I. Sinitsyn, and N. V. Filippov. High-energy radiation from pulsed discharges. *J. Nuclear Energy II*, 4:213–215, 1957.

[31] Oscar A. Anderson, William R. Baker, Stirling A. Colgate, Harold P. Furth, John Ise, Robert V. Pyle, and Robert E. Wright. Neutron production in linear deuterium pinches. *Phys. Rev.*, 109:612–613, Jan 1958.

[32] J. C. Martin. Nanosecond pulse techniques. *Circuit and Electromagnetic System Design Notes*, 1970.

[33] D. H. Kalantar. *An experimental study of the dynamics of X-pinch and Z-pinch plasmas.* PhD dissertation, Cornell University, Ithaca, NY, 1993.

[34] J. B. Greenly, J. D. Douglas, D. A. Hammer, B. R. Kusse, S. C. Glidden, and H. D. Sanders. A 1ma, variable risetime pulse generator for high energy density plasma research. *Review of Scientific Instruments*, 79(7):073501, 2008.

[35] J S Shlachter. Solid d2fiber experiments on HDZP-II. *Plasma Physics and Controlled Fusion*, 32(11):1073–1081, nov 1990.

[36] I. H. Mitchell, J. M. Bayley, J. P. Chittenden, P. Choi, J. F. Worley, A. E. Dangor, and M. G. Haines. The magpie generator. *AIP Conference Proceedings*, 299(1):486–494, 1994.

[37] B. S. Bauer, V. L. Kantsyrev, N. Le Galloudec, R. Presura, G. S. Sarkisov, A. S. Shlyaptseva, S. Batie, W. Brinsmead, H. Faretto, B. Le Galloudec, A. Oxner, M. Al-Shorman, D. A. Fedin, S. Hansen, I. Paraschiv, H. Zheng, D. McCrorey, J. W. Farley, J. Glassman, and J. S. De Groot. Two-terawatt zebra z-pinch at the nevada terawatt facility. In *Digest of Technical Papers. 12th IEEE International Pulsed Power Conference. (Cat. No.99CH36358)*, volume 2, pages 1045–1047 vol.2, 1999.

[38] S. V. Lebedev, I. H. Mitchell, R. Aliaga-Rossel, S. N. Bland, J. P. Chittenden, A. E. Dangor, and M. G. Haines. Azimuthal structure and global instability in the implosion phase of wire array *Z*-pinch experiments. *Phys. Rev. Lett.*, 81:4152–4155, Nov 1998.

[39] M. R. Gomez, S. A. Slutz, A. B. Sefkow, D. B. Sinars, K. D. Hahn, S. B. Hansen, E. C. Harding, P. F. Knapp, P. F. Schmit, C. A. Jennings, T. J. Awe, M. Geissel, D. C. Rovang, G. A. Chandler, G. W. Cooper, M. E. Cuneo, A. J. Harvey-Thompson, M. C. Herrmann, M. H. Hess, O. Johns, D. C. Lamppa, M. R. Martin, R. D. McBride, K. J. Peterson, J. L. Porter, G. K. Robertson, G. A. Rochau, C. L. Ruiz, M. E. Savage, I. C. Smith, W. A. Stygar, and R. A. Vesey. Experimental demonstration of fusion-relevant conditions in magnetized liner inertial fusion. *Phys. Rev. Lett.*, 113:155003, Oct 2014.

[40] C M Dozier, P G Burkhalter, D J Nagel, S J Stephanakis, and D Mosher. High ionization states in exploded-wire plasmas. *Journal of Physics B: Atomic and Molecular Physics*, 10(3):L73–L77, feb 1977.

[41] C. Stallings, K. Nielsen, and R. Schneider. Multiple-wire array load for high-power pulsed generators. *Applied Physics Letters*, 29(7):404–406, 1976.

[42] T. J. Nash, C. Deeney, G. A Chandler, D. B. Sinars, M. E. Cuneo, E. M. Waisman, W. A. Stygar, D. Wenger, S. Speas, R. J. Leeper, J. F. Seaman, J. McGurn, J. Torres, D. Jobe, T. Gilliland, D. Nielsen, R. Hawn, H. Seaman, K. Keller, T. Moore, T. C. Wagoner, P. D. LePell, J. Lucas, D. Schroen, C. Russell, and M. Kernaghan. Comparison of a copper foil to a copper wire-array z pinch at 18 ma. *Physics of Plasmas*, 11(10):L65–L68, 2004.

[43] J. Shiloh, A. Fisher, and N. Rostoker. z pinch of a gas jet. *Phys. Rev. Lett.*, 40:515–518, Feb 1978.

[44] S. V. Lebedev, R. Aliaga-Rossel, J. P. Chittenden, I. H. Mitchell, A. E. Dangor, M. G. Haines, and J. F. Worley. Coronal plasma behavior of the z pinch produced from carbon and cryogenic deuterium fibers. *Physics of Plasmas*, 5(9):3366–3372, 1998.

[45] IK Aivazov, VD Vikharev, GS Volkov, LB Nikandrov, VP Smirnov, and V Ya Tsarfin. Formation of axial foreplasma channel in the initial stage of the compression of a multiwire system by megampere currents (experimental). *Sov. J. Plasma Phys*, 14(2):110–113, 1988.

[46] D. H. Kalantar and D. A. Hammer. Observation of a stable dense core within an unstable coronal plasma in wire-initiated dense z-pinch experiments. *Phys. Rev. Lett.*, 71:3806–3809, Dec 1993.

[47] S. A. Pikuz, G. V. Ivanenkov, T. A. Shelkovenko, and D. Hammer. On the phase state of the core matter in a high-power discharge through a wire. *Journal of Experimental and Theoretical Physics Letters*, 69(5):377 – 382, 1999.

[48] S. V. Lebedev, R. Aliaga-Rossel, S. N. Bland, J. P. Chittenden, A. E. Dangor, M. G. Haines, and I. H. Mitchell. The dynamics of wire array z-pinch implosions. *Physics of Plasmas*, 6(5):2016–2022, 1999.

[49] T. W. L. Sanford, G. O. Allshouse, B. M. Marder, T. J. Nash, R. C. Mock, R. B. Spielman, J. F. Seamen, J. S. McGurn, D. Jobe, T. L. Gilliland, M. Vargas, K. W. Struve, W. A. Stygar, M. R. Douglas, M. K. Matzen, J. H. Hammer, J. S. De Groot, J. L. Eddleman, D. L. Peterson, D. Mosher, K. G. Whitney, J. W. Thornhill, P. E. Pulsifer, J. P. Apruzese, and Y. Maron. Improved symmetry greatly increases x-ray power from wire-array Z-pinches. *Phys. Rev. Lett.*, 77:5063–5066, Dec 1996.

[50] T. W. L. Sanford, R. C. Mock, R. B. Spielman, M. G. Haines, J. P. Chittenden, K. G. Whitney, J. P. Apruzese, D. L. Peterson, J. B. Greenly, D. B. Sinars, D. B. Reisman, and D. Mosher. Wire array z-pinch insights for enhanced x-ray production. *Physics of Plasmas*, 6(5):2030–2040, 1999.

[51] C. Deeney, M. R. Douglas, R. B. Spielman, T. J. Nash, D. L. Peterson, P. L'Eplattenier, G. A. Chandler, J. F. Seamen, and K. W. Struve. Enhancement of x-ray power from a Z pinch using nested-wire arrays. *Phys. Rev. Lett.*, 81:4883–4886, Nov 1998.

[52] S. A. Slutz, M. C. Herrmann, R. A. Vesey, A. B. Sefkow, D. B. Sinars, D. C. Rovang, K. J. Peterson, and M. E. Cuneo. Pulsed-power-driven cylindrical liner implosions of laser preheated fuel magnetized with an axial field. *Physics of Plasmas*, 17(5):056303, 2010.

[53] Stephen A. Slutz and Roger A. Vesey. High-gain magnetized inertial fusion. *Phys. Rev. Lett.*, 108:025003, Jan 2012.

[54] D. A. Yager-Elorriaga, Y. Y. Lau, P. Zhang, P. C. Campbell, A. M. Steiner, N. M. Jordan, R. D. McBride, and R. M. Gilgenbach. Evolution of sausage and helical modes in magnetized thin-foil cylindrical liners driven by a z-pinch. *Physics of Plasmas*, 25(5):056307, 2018.

[55] H. U. Rahman, F. J. Wessel, and N. Rostoker. Staged z pinch. *Phys. Rev. Lett.*, 74:714–717, Jan 1995.

[56] N. Qi, E. W. Rosenberg, P. A. Gourdain, P. W. L. de Grouchy, B. R. Kusse, D. A. Hammer, K. S. Bell, T. A. Shelkovenko, W. M. Potter, L. Atoyan, A. D. Cahill, M. Evans, J. B. Greenly, C. L. Hoyt, S. A. Pikuz, P. C. Schrafel, E. Kroupp, A. Fisher, and Y. Maron. Study of gas-puff z-pinches on cobra. *Physics of Plasmas*, 21(11):112702, 2014.

[57] J Narkis. *Modeling of implosion dynamics and the magneto-Rayleigh-Taylor instability in single and double liner-on-target, gas-puff Z-pinches.* PhD dissertation, University of California, San Diego, San Diego, CA, 2019.

[58] SM Zakharov, GV Ivanenkov, AA Kolomenskii, SA Pikuz, AI Samokhin, and I Ulshmid. Wire x-pinch in a high-current diode. *Soviet Technical Physics Letters*, 8(9):456–457, 1982.

[59] SM Zakharov, GV Ivanenkov, AA Kolomenskii, SA Pikuz, and AI Samokhin. Plasma of an exploding multiwire load in the diode of a high-current accelerator. *Soviet Technical Physics Letters*, 13(2):115–121, 1987.

[60] D. H. Kalantar and D. A. Hammer. The x-pinch as a point source of x rays for backlighting. *Review of Scientific Instruments*, 66(1):779–781, 1995.

[61] D. A. Hammer, D. H. Kalantar, K. C. Mittal, and N. Qi. X-pinch soft x-ray source for microlithography. *Applied Physics Letters*, 57(20):2083–2085, 1990.

[62] D. H. Kalantar, D. A. Hammer, K. C. Mittal, N. Qi, J. R. Maldonado, and Y. Vladimirsky. Intense pulsed plasma x-ray source for lithography. *Journal of Vacuum Science & Technology B: Microelectronics and Nanometer Structures Processing, Measurement, and Phenomena*, 9(6):3245–3249, 1991.

[63] C. L. Hoyt, S. A. Pikuz, T. A. Shelkovenko, and D. A. Hammer. Preliminary investigations into utilizing standard/hybrid x-pinch line radiation as a probe for x-ray thomson scattering experiments. In *2012 Abstracts IEEE International Conference on Plasma Science*, pages 3P–136–3P–136, July 2012.

[64] M. P. Valdivia, F. Veloso, D. Stutman, C. Stoeckl, C. Mileham, I. A. Begishev, W. Theobald, M. Vescovi, W. Useche, S. P. Regan, B. Albertazzi, G. Rigon, P. Mabey, T. Michel, S. A. Pikuz, M. Koenig, and A. Casner. X-ray backlighter requirements for refraction-based electron density diagnostics through talbot-lau deflectometry. *Review of Scientific Instruments*, 89(10):10G127, 2018.

[65] M. P. Valdivia, D. Stutman, and M. Finkenthal. Moiré deflectometry using the talbot-lau interferometer as refraction diagnostic for high energy density plasmas at energies below 10 kev. *Review of Scientific Instruments*, 85(7):073702, 2014.

[66] S. A. Pikuz, D. B. Sinars, T. A. Shelkovenko, K. M. Chandler, D. A. Hammer, G. V. Ivanenkov, W. Stepniewski, and I. Yu. Skobelev. High energy density *Z*-pinch plasma conditions with picosecond time resolution. *Phys. Rev. Lett.*, 89:035003, Jun 2002.

[67] J. D. Douglass and D. A. Hammer. Cobra-star, a five frame point-projection x-ray imaging system for 1ma scale wire-array z pinches. *Review of Scientific Instruments*, 79(3):033503, 2008.

[68] T. A. Shelkovenko, S. A. Pikuz, D. A. Hammer, Y. S. Dimant, and A. R. Mingaleev. Evolution of the structure of the dense plasma near the cross point in exploding wire x pinches. *Physics of Plasmas*, 6(7):2840–2846, 1999.

[69] T. A. Shelkovenko, D. B. Sinars, S. A. Pikuz, and D. A. Hammer. Radiographic and spectroscopic studies of x-pinch plasma implosion dynamics and x-ray burst emission characteristics. *Physics of Plasmas*, 8(4):1305–1318, 2001.

[70] J. P. Chittenden, A. Ciardi, C. A. Jennings, S. V. Lebedev, D. A Hammer, S. A. Pikuz, and T. A. Shelkovenko. Structural evolution and formation of high-pressure plasmas in *x* pinches. *Phys. Rev. Lett.*, 98:025003, Jan 2007.

[71] S A Pikuz, V M Romanova, T A Shelkovenko, D A Hammer, and A Ya Faenov. Spectroscopic investigations of the short wavelength x-ray spectra from x-pinch plasmas. *Physica Scripta*, 51(4):517–521, apr 1995.

[72] S.A. Pikuz, T.A. Shelkovenko, V.M. Ramanova, J. Abdallah, G. Csanak, R. E. H. Clark, A. Ya. Faenov, I. Yu. Skobelev, and D. A. Hammer. Effect of an electron beam generated in an x-pinch plasma on the structure of the k spectra of multiply charged ions. *Journal of Experimental and Theoretical Physics*, 85(3):484–491, September 1997.

[73] J Abdallah, A Ya Faenov, D Hammer, S A Pikuz, G Csanak, and R E H Clark. Electron beam effects on the spectroscopy of satellite lines in aluminum x-pinch experiments. *Physica Scripta*, 53(6):705–711, jun 1996.

[74] V. L. Kantsyrev, A. S. Shlyaptseva, B. S. Bauer, D. A. Fedin, R. Presura, S. Fuelling, S. Hansen, S. Batie, A. Oxner, H. Faretto, N. Ouart, S. Keely, H. LeBeau, and D. Chamberlain. X-ray temporal, spatial and spectral study of 0.9 ma x-pinch ti, fe, mo, w and pt radiation sources. energetic electron beam and hard x-ray generation. In *PPPS-2001 Pulsed Power Plasma Science 2001. 28th IEEE International Conference on Plasma Science and 13th IEEE International Pulsed Power Conference. Digest of Papers (Cat. No.01CH37251)*, volume 1, pages 346–349 vol.1, June 2001.

[75] V. L. Kantsyrev, D. A. Fedin, A. S. Shlyaptseva, S. Hansen, D. Chamberlain, and N. Ouart. Energetic electron beam generation and anisotropy of hard x-ray emission from 0.9 to 1.0 ma high-z x pinches. *Physics of Plasmas*, 10(6):2519–2526, 2003.

[76] T. A. Shelkovenko, S. A. Pikuz, B. M. Song, K. M. Chandler, M. D. Mitchell, D. A. Hammer, G. V. Ivanenkov, A. R. Mingaleev, and V. M. Romanova. Electron-beam-generated x rays from x pinches. *Physics of Plasmas*, 12(3):033102, 2005.

[77] T. A. Shelkovenko, S. A. Pikuz, J. D. Douglass, R. D. Mcbride, J. B. Greenly, and D. A. Hammer. Multiwire*x*-pinches at 1-ma current on the cobra pulsed-power generator. *IEEE Transactions on Plasma Science*, 34(5):2336–2341, Oct 2006.

[78] Christos Christou and Peter Choi. Characterization of the radiation from a low-energy X-pinch source. *Proceedings of the Society for Optics and Photonics: Short-Wavelength Radiation Sources*, 1552:278 – 287, 1991.

[79] C. Christou, A. E. Dangor, and D. A. Hammer. Characterization of wire x pinches driven by a microsecond-long capacitive discharge. *Journal of Applied Physics*, 87(12):8295–8303, 2000.

[80] R. K. Appartaim and B. T. Maakuu. X-pinch x-ray sources driven by a 1μs capacitor discharge. *Physics of Plasmas*, 15(7):072703, 2008.

[81] G. W. Collins, M. P. Valdivia, T. Zick, R. E. Madden, M. G. Haines, and F. N. Beg. Study of x-pinch dynamics using a low current (25 ka) and slower current (400 ns) pulse. *Physics of Plasmas*, 20(4):042704, 2013.

[82] Zaitsev, V.I., Barykov, I.A., Boldarev, A.S., and Olkhovskaya, O.G. Gas x-pinch: The progress, technology and results. *EPJ Web of Conferences*, 59:10001, 2013.

[83] F. N. Beg, K. Krushelnick, P. Lichtsteiner, A. Meakins, A. Kennedy, N. Kajumba, G. Burt, and A. E. Dangor. Table-top x-pinch for x-ray radiography. *Applied Physics Letters*, 82(25):4602–4604, 2003.

[84] F. N. Beg, R. B. Stephens, H.-W. Xu, D. Haas, S. Eddinger, G. Tynan, E. Shipton, B. DeBono, and K. Wagshal. Compact x-pinch based point x-ray source for phase contrast imaging of inertial confinement fusion capsules. *Applied Physics Letters*, 89(10):101502, 2006.

[85] J. S. Green, S. N. Bland, M. Collett, A. E. Dangor, K. Krushelnick, F. N. Beg, and I. Ross. Effect of wire number on x-pinch discharges. *Applied Physics Letters*, 88(26):261501, 2006.

[86] T. A. Shelkovenko, S. A. Pikuz, I. N. Tilikin, S. N. Bland, D. Lall, N. Chaturvedi, and A. Georgakis. X-pinch x-ray emission on a portable low-current, fast rise-time generator. *Journal of Applied Physics*, 124(8):083303, 2018.

[87] G. V. Ivanenkov, A. R. Mingaleev, S. A. Pikuz, V. M Romanova, and T. A. Shelkovenko. Experimental study of x-pinch dynamics. *Plasma Physics Reports*, 22(5):363–378, Aug 1996.

[88] I. H. Mitchell, R. Aliaga-Rossel, R. Saavedra, H. Chuaqui, M. Favre, and E. S. Wyndham. Investigation of the plasma jet formation in x-pinch plasmas using laser interferometry. *Physics of Plasmas*, 7(12):5140–5147, 2000.

[89] L. E. Aranchuk, A. S. Chuvatin, and J. Larour. Compact submicrosecond, high current generator for wire explosion experiments. *Review of Scientific Instruments*, 75(1):69–74, 2004.

[90] T. A. Shelkovenko, S. A. Pikuz, S. A. Mishin, A. R. Mingaleev, I. N. Tilikin, P. F. Knapp, A. D. Cahill, C. L. Hoyt, and D. A. Hammer. Hybrid x-pinches. *Plasma Physics Reports*, 38(5):359–381, May 2012.

[91] I. V. Lavrinovich, A. P. Artyomov, N. V. Zharova, V. F. Fedushchak, A. V. Fedyunin, and A. A. Erfort. A compact nanosecond pulse generator. *Instruments and Experimental Techniques*, 56(1):55–58, 2013.

[92] R. Liu, X. Zou, X. Wang, L. He, and N. Zeng. X-pinch experiments with pulsed power generator (ppg-1) at tsinghua university. *Laser and Particle Beams*, 26(1):33–36, 2008.

[93] A. V. Kharlov, B. M. Kovalchuk, and V. B. Zorin. Compact high current generator for x-ray radiography. *Review of Scientific Instruments*, 77(12):123501, 2006.

[94] Jian Wu, Tie-Ping Sun, Gang Wu, Liang-Ping Wang, Juan-Juan Han, Mo Li, Pei-Tian Cong, Ai-Ci Qiu, and Min Lv. Aluminum and tungsten x-pinch experiments on 100 ka, 100 ns linear transformer driver stage. *Physics of Plasmas*, 18(5):052702, 2011.

[95] G. A. AU Mesyats, T. A. Shelkovenko, G. V. Ivanenkov, A. V. Agafonov, S. Yu. Savinov, S. A. Pikuz, I. N. Tilikin, S. I. Tkachenko, S. A. Chaikovskii, N. A. Ratakhin, V. F. Fedushchak, V. I. Oreshkin, A. V. Fedyunin, A. G. Russkikh, N. A. Labetskaya, A. P. Artemov, D. A. Hammer, and D. B. Sinars. X-pinch source of subnanosecond soft x-ray pulses based on smallsized lowinductance current generator. *Journal of Experimental and Theoretical Physics*, 111(3):363 – 370, 2010.

[96] Roman V. Shapovalov, Rick B. Spielman, and George R. Imel. An oil-free compact x-pinch plasma radiation source: Design and radiation performance. *Review of Scientific Instruments*, 88(6):063504, 2017.

[97] R. E. Madden, S. C. Bott, G. Collins, and F N Beg. Investigation of carbon x-pinches as a source for point-projection radiography. *IEEE Transactions on Plasma Science*, 37:433–437, 2009.

[98] S. V. Lebedev, F. N. Beg, S. N. Bland, J. P. Chittenden, A. E. Dangor, M. G. Haines, M. Zakaullah, S. A. Pikuz, T. A. Shelkovenko, and D. A. Hammer. X-ray backlighting of wire array z-pinch implosions using x pinch. *Review of Scientific Instruments*, 72(1):671–673, 2001.

[99] V. V. Alexandrov, I. N. Frolov, M. V. Fedulov, E. V. Grabovsky, K. N. Mitrofanov, S. L. Nedoseev, G. M. Oleinik, I. Yu. Porofeev, A. A. Samokhin, P. V. Sasorov, V. P. Smirnov, G. S. Volkov, M. M. Zurin, , and G. G. Zukakischvili. Prolonged plasma production at current-driven implosion of wire arrays on angara-5-1 facility. *IEEE TRANSACTIONS ON PLASMA SCIENCE*, 30(12):559–566, 2002.

[100] J. D. Douglass, J. B. Greenly, D. A. Hammer, R. D. McBride, S. A. Pikuz, and T. A. Shelkovenko. The imaging of z-pinches using x-pinch backlighting. *AIP Conference Proceedings*, 808(1):129–132, 2006.

[101] J. Wu, L. Wang, A. Qiu, J. Han, M. Li, T. Lei, P. Cong, M. Qiu, H. Yang, M. Lv, and et al. Experimental investigations of x-pinch backlighters on qiangguang-1 generator. *Laser and Particle Beams*, 29(2):155–160, 2011.

[102] N. Loter, M. Gersten, R. Grandey, J. Rauch, K. Ware, M. Coulter, J. Davis, and K. Whitney. X-pinch wire load experiments on blackjack 5. *Journal of Quantitative Spectroscopy and Radiative Transfer*, 44(5):509 – 518, 1990. Special Issue Radiation and Spectroscopy of Pulse-Power-Driven Plasmas.

[103] Jing Li, Jian-Jun Deng, Wei-Ping Xie, Xian-Bin Huang, Li-Bing Yang, Shao-Tong Zhou, Xiao-Li Zhu, Shu-Chao Duan, Si-Qun Zhang, and Jia-Kun Dan. Study of kev radiation properties of mo and ti x-pinch plasma sources using a pinhole transmission grating spectrometer. *Physics of Plasmas*, 17(7):073104, 2010.

[104] T. A. Shelkovenko, S. A. Pikuz, R. D. McBride, P. F. Knapp, H. Wilhelm, D. A. Hammer, and D. B. Sinars. Nested multilayered x pinches for generators with mega-ampere current level. *Physics of Plasmas*, 16(5):050702, 2009.

[105] D. B. Sinars, R. D. McBride, S. A. Pikuz, T. A. Shelkovenko, D. F. Wenger, M. E. Cuneo, E. P. Yu, J. P. Chittenden, E. C. Harding, S. B. Hansen, B. P. Peyton, D. J. Ampleford, and C. A. Jennings. Investigation of high-temperature bright plasma x-ray sources produced in 5-ma x-pinch experiments. *Phys. Rev. Lett.*, 109:155002, Oct 2012.

[106] S. A. Pikuz, T. A. Shelkovenko, and D. A. Hammer. X-pinch. part i. *Plasma Physics Reports*, 41(4):291–342, Apr 2015.

[107] N. Qi, D. A. Hammer, D. H. Kalantar, G. D. Rondeau, J. B. Workman, M. C. Richardson, and Hong Chen. X-ray source characterization of aluminum x-pinch plasmas driven by the 0.5 tw lion accelerator. *AIP Conference Proceedings*, 195(1):71–78, 1989.

[108] I. H. Mitchell, R. Aliaga-Rossel, J. A. Gómez, H. Chuaqui, M. Favre, and E. S. Wyndham. X ray emission from x pinch experiments on the llampüdkeñ generator. In *2002 14th International Conference on High-Power Particle Beams (BEAMS)*, volume 2, pages 145–148, 2002.

[109] I H Mitchell, J A Gomez, F A Suzuki, R Aliaga-Rossel, H Chuaqui, M Favre, and E Wyndham. X-ray emission from 125 μm diameter aluminium wire x-pinches at currents of 400 kA. *Plasma Sources Science and Technology*, 14(3):501–508, may 2005.

[110] F. N. Beg, A. Ciardi, I. Ross, Y. Zhu, A. E. Dangor, and K. Krushelnick. Jet formation and current transfer in*x*-pinches. *IEEE Transactions on Plasma Science*, 34(5):2325–2329, 2006.

[111] S. S. AU Anan'ev, Yu. L. Bakshaev, P. I. Blinov, V. A. Bryzgunov, S. A. Dan'ko, A. I. Zhuzhunashvili, A. A. Zelenin, E. D. Kazakov, Yu. G. Kalinin, A. S. Kingsep, V. D. Korolev, V. I. Mizhiritskiĭ, S. A. Pikuz, V. M. Romanova, V. P. Smirnov, S. I. Tkachenko, G. I. Ustroev, A. S. Chernenko, T. A. Shelkovenko, and V. A. Shchagin. Investigations of the mega-ampere multiwire x pinch. *Journal of Experimental and Theoretical Physics Letters*, 87(7):364 – 370, 2008.

[112] T. A. Shelkovenko, S. A. Pikuz, A. D. Cahill, P. F. Knapp, D. A. Hammer, D. B. Sinars, I. N. Tilikin, and S. N. Mishin. Hybrid x-pinch with conical electrodes. *Physics of Plasmas*, 17(112707):112707–1 – 112707–5, November 2010.

[113] A. G. Rousskikh, V. I. Oreshkin, S. A. Chaikovsky, N. A. Labetskaya, A. V. Shishlov, I. I. Beilis, and R. B. Baksht. Study of the strata formation during the explosion of a wire in vacuum. *Physics of Plasmas*, 15(10):102706, 2008.

[114] R. Zhang, X. Zou, X. Zhu, S. Zhao, H. Luo, and X. Wang. X-ray emission from a table-top x-pinch device. In *2012 IEEE International Power Modulator and High Voltage Conference (IPMHVC)*, pages 144–147, 2012.

[115] J. Wu, L. P. Wang, J. J. Han, M. Li, L. Sheng, Y. Li, M. Zhang, N. Guo, T. S. Lei, A. C. Qiu, and M. Lv. X-pinch radiography for the radiation suppressed tungsten and aluminum planar wire array. *Physics of Plasmas*, 19(2):022702, 2012.

[116] Jian Wu, Mo Li, Xingwen Li, Liangping Wang, Gang Wu, Guo Ning, Mengtong Qiu, and Aici Qiu. Estimations of mo x-pinch plasma parameters on qiangguang-1 facility by l-shell spectral analyses. *Physics of Plasmas*, 20(8):082706, 2013.

[117] T. A. Shelkovenko, S. A. Pikuz, C. L. Hoyt, A. D. Cahill, L. Atoyan, D. A. Hammer, I. N. Tilikin, A. R. Mingaleev, V. M. Romanova, and A. V. Agafonov. A source of hard x-ray radiation based on hybrid x pinches. *Physics of Plasmas*, 23(10):103303, 2016.

[118] T.A. Shelkovenko, S.A. Pikuz, I.N. Tilikin, M.D. Mitchell, S.N. Bland, and D.A. Hammer. Evolution of x-pinch loads for pulsed power generators with current from 50 to 5000 ka. *Matter and Radiation at Extremes*, 3(6):267 – 277, 2018.

[119] T. A. Shelkovenko, S. A. Pikuz, D. B. Sinars, K. M. Chandler, and D. A. Hammer. X pinch plasma development as a function of wire material and current pulse parameters. *IEEE Transactions on Plasma Science*, 30(2):567–576, 2002.

[120] Byung Moo Song, Sergei A. Pikuz, Tatiania A. Shelkovenko, and David A. Hammer. Determination of the size and structure of an x-pinch x-ray source from the diffraction pattern produced by microfabricated slits. *Appl. Opt.*, 44(12):2349–2358, Apr 2005.

[121] L. E. Aranchuk, J. Larour, and A. S. Chuvatin. Experimental study of x-pinch in a submicrosecond regime. *IEEE Transactions on Plasma Science*, 33(2):990–996, 2005.

[122] T. A. Shelkovenko, S. A. Pikuz, C. L. Hoyt, A. D. Cahill, and D. A. Hammer. Study of new configurations of hybrid *x* pinches. *IEEE Transactions on Plasma Science*, 42(3):748–752, March 2014.

[123] T. A. Shelkovenko, I. N. Tilikin, G. V. Ivanenkov, W. Stepniewski, A. R. Mingaleev, V. M. Romanova, A. V. Agafonov, A. D. Cahill, C. L. Hoyt, P. A. Gourdain, D. A. Hammer, and S. A. Pikuz. Dynamics of hybrid x-pinches. *Plasma Physics Reports*, 41(1):52–70, Jan 2015.

[124] V. M. Romanova, I. N. Tilikin, T. A. Shelkovenko, A. R. Mingaleev, E. A. Bolkhovitinov, A. A. Rupasov, A. E. Ter-Oganesyan, and S. A. Pikuz. The hybrid x-pinch as a source of xuv radiation. *IEEE Transactions on Plasma Science*, 46(11):3837–3841, Nov 2018.

[125] A. C. Forsman, P. S. Banks, M. D. Perry, E. M. Campbell, A. L. Dodell, and M. S. Armas. Double-pulse machining as a technique for the enhancement of material removal rates in laser machining of metals. *Journal of Applied Physics*, 98(3):033302, 2005.

[126] Benxin Wu, Yun Zhou, and Andrew Forsman. Study of laser-plasma interaction using a physics-based model for understanding the physical mechanism of double-pulse effect in nanosecond laser ablation. *Applied Physics Letters*, 95(25):251109, 2009.

[127] S. C. Bott, D. M. Haas, R. E. Madden, U. Ueda, Y. Eshaq, G. Collins, K. Gunasekera, D. Mariscal, J. Peebles, F. N. Beg, M. Mazarakis, K. Struve, and R. Sharpe. 250 ka compact linear transformer driver for wire array z-pinch loads. *Phys. Rev. Spec. Top. - Accel. Beams*, 14(5):050401, 2011.

[128] R. M. Gilgenbach, M. R. Gomez, J. C. Zier, W. W. Tang, D. M. French, Y. Y. Lau, M. G. Mazarakis, M. E. Cuneo, M. D. Johnston, B. V. Oliver, T. A. Mehlhorn, A. A. Kim, and V. A. Sinebryukhov. Maize: a 1 ma ltd-driven z-pinch at the university of michigan. *AIP Conference Proceedings*, 1088(1):259–262, 2009.

[129] P.-A. Gourdain, M. B. Adams, M. Evans, H. R. Hasson, R. V. Shapovalov, R. B. Spielman, J. R. Young, and I. West-Abdallah. Current adding transmission lines for compact ma-class linear transformer drivers. *Phys. Rev. Accel. Beams*, 23:030401, Mar 2020.

[130] F. Conti, J. C. Valenzuela, V. Fadeev, N. Aybar, D. B. Reisman, A. Williams, G. Collins, J. Narkis, M. P. Ross, F. N. Beg, and R. B. Spielman. Ma-class linear transformer driver for z-pinch research. *Phys. Rev. Accel. Beams*, 23:090401, Sep 2020.

[131] F. F. Chen. *Introduction to Plasma Physics and Controlled Fusion*, volume 1. Springer Science, 2006.

[132] A A Vlasov. The vibrational properties of and electron gas. *Soviet Physics Uspekhi*, 10(6):721–733, jun 1968.

[133] D. Ryutov, R. P. Drake, J. Kane, E. Liang, B. A. Remington, and W. M. Wood-Vasey. Similarity criteria for the laboratory simulation of supernova hydrodynamics. *The Astrophysical Journal*, 518:821–832, June 1999.

[134] R. J. Goldston. *Introduction to Plasma Physics*. Inst. of Physics Publishing, Philadelphia, PA, 1995.

[135] R S Pease. Equilibrium characteristics of a pinched gas discharge cooled by bremsstrahlung radiation. *Proceedings of the Physical Society. Section B*, 70(1):11–23, jan 1957.

[136] S I Braginskii. The behavior of a completely ionized plasma in a strong magnetic field. *Soviet Journal of Experimental and Theoretical Physics*, 6(3):645–654, Mar 1958.

[137] J. W. Shearer. Contraction of z pinches actuated by radiation losses. *The Physics of Fluids*, 19(9):1426–1428, 1976.

[138] A. E. Robson. Radiative collapse of a z pinch in hydrogen and helium. *Physics of Fluids B: Plasma Physics*, 1(9):1834–1842, 1989.

[139] S. Glasstone and R. H. Loverberg. *Controlled Thermonuclear Reactions*, chapter 2. Van Nostrand, New York, 1960.

[140] C. E. Seyler, M. R. Martin, and N. D. Hamlin. Helical instability in maglif due to axial flux compression by low-density plasma. *Physics of Plasmas*, 25(6):062711, 2018.

[141] M Coppins. Ideal magnetohydrodynamic linear instabilities in the z-pinch. *Plasma Physics and Controlled Fusion*, 30(3):201–216, mar 1988.

[142] J P Chittenden, S V Lebedev, C A Jennings, S N Bland, and A Ciardi. X-ray generation mechanisms in three-dimensional simulations of wire array z-pinches. *Plasma Physics and Controlled Fusion*, 46(12B):B457–B476, nov 2004.

[143] M G Haines. An analytic model of radiative collapse of a z-pinch. *Plasma Physics and Controlled Fusion*, 31(5):759–778, may 1989.

[144] J. P. Chittenden and M. G. Haines. Processes terminating radiative collapse in a hydrogen fiber z pinch. *Physics of Fluids B: Plasma Physics*, 2(8):1889–1897, 1990.

[145] J. P. Chittenden. The effect of lower hybrid instabilities on plasma confinement in fiber z pinches. *Physics of Plasmas*, 2(4):1242–1249, 1995.

[146] A. E. Robson. Anomalous resistivity and the pease-braginskii current in a z pinch. *Phys. Rev. Lett.*, 63:2816–2818, Dec 1989.

[147] M.G. Haines. Kinetic effects in z pinches. *Laser and Particle Beams*, 19(3):345–353, 2001.

[148] Michael A. Liberman, John S. De Groot, Arthur Toor, and Rick B. Spielman. *Dynamics of Z-Pinch Plasmas*, pages 44–95. Springer New York, New York, NY, 1999.

[149] James P Joule. On the production of heat by voltaic electricity. *Proceedings of the Royal Society*, Dec 1840.

[150] James Prescott Joule. *The Scientific Papers of James Prescott Joule*, volume 1 of *Cambridge Library Collection - Physical Sciences*. Cambridge University Press, 1884.

[151] V. I. Oreshkin, S. A. Chaikovsky, A. P. Artyomov, N. A. Labetskaya, A. V. Fedunin, A. G. Rousskikh, and A. S. Zhigalin. X-pinch dynamics: Neck formation and implosion. *Physics of Plasmas*, 21(10):102711, 2014.

[152] J. Ruiz-Camacho, F. N. Beg, A. E. Dangor, M. G. Haines, E. L. Clark, and I. Ross. Z-pinch discharges in aluminum and tungsten wires. *Physics of Plasmas*, 6(6):2579–2587, 1999.

[153] B. Jones, C. Deeney, J. L. McKenney, C. J. Garasi, T. A. Mehlhorn, A. C. Robinson, S. E. Wunsch, S. N. Bland, S. V. Lebedev, J. P. Chittenden, S. C. Bott, D. J. Ampleford, J. B. A. Palmer, J. Rapley, G. N. Hall, and B. V. Oliver. Study of three-dimensional structure in wire-array *z* pinches by controlled seeding of axial modulations in wire radius. *Phys. Rev. Lett.*, 95:225001, Nov 2005.

[154] D. J. Ampleford. *Experimental study of plasma jets produced by conical wire array z-pinches*. PhD dissertation, Imperial College London, London, UK, March 2005.

[155] A. J. Harvey-Thompson, S. V. Lebedev, S. N. Bland, J. P. Chittenden, G. N. Hall, A. Marocchino, F. Suzuki-Vidal, S. C. Bott, J. B. A. Palmer, and C. Ning. Quantitative analysis of plasma ablation using inverse wire array Z pinches. *Physics of Plasmas*, 16(2):022701, Feb 2009.

[156] G W Collins, D Marsical, D M Haas, R E Madden, K Gunasekara, J Kim, M L L Abarr, S C Bott, J P Chittenden, and F N Beg. Effect of the global to local magnetic field ratio on the ablation modulations on x-pinches driven by 80 kA peak current. *New Journal of Physics*, 14(4):043021, apr 2012.

[157] D. D. Ryutov, B. A. Remington, H. F. Robey, and R. P. Drake. Magnetohydrodynamic scaling: From astrophysics to the laboratory. *Physics of Plasmas*, 8(5):1804–1816, May 2001.

[158] F. N. Beg, A. Ciardi, I. Ross, Y. Zhu, A. E. Dangor, and K. Krushelnick. Jet formation and current transfer in*x*-pinches. *IEEE Transactions on Plasma Science*, 34(5):2325–2329, Oct 2006.

[159] D. M. Haas, S. C. Bott, J. Kim, D. A. Mariscal, R. E. Madden, Y. Eshaq, U. Ueda, G. Collins IV, K. Gunasekera, F. N. Beg, J. P. Chittenden, N. Niasse, and C. A. Jennings. Supersonic jet formation and propagation in x-pinches. *Astrophysics and Space Science*, 336(1):33–40, 2011.

[160] Bruce A. Hammel and Larry A. Jones. Effects of the internally produced nonthermal electrons on the temperature diagnostics of a hollow gas shell z pinch. *Applied Physics Letters*, 44(7):667–669, 1984.

[161] T. A. Shelkovenko, S. A. Pikuz, A. R. Mingaleev, V. M. Agafonov, A. V. andRomanova, A. E. Ter-Oganes'yan, S. I. Tkachenko, I. C. Blesener, M. D. Mitchell, K. M. Chandler, B. R. Kusse, and D. A. Hammer. Accelerated electrons and hard x-ray emission from x-pinches. *Plasma Physics Reports*, 34(9):754–770, 2008.

[162] H. Dreicer. Electron and ion runaway in a fully ionized gas. ii. *Phys. Rev.*, 117:329–342, Jan 1960.

[163] L. Hesslow, L. Unnerfelt, O. Vallhagen, O. Embreus, M. Hoppe, G. Papp, and T. Fülöp. Evaluation of the dreicer runaway generation rate in the presence of high- z impurities using a neural network. *Journal of Plasma Physics*, 85(6):475850601, 2019.

[164] V. I. Oreshkin, E. V. Oreshkin, S. A. Chaikovsky, and A. P. Artyomov. Coulomb explosion of "hot spot". *Physics of Plasmas*, 23(9):092701, 2016.

[165] Xavier Llovet, Cedric J. Powell, Francesc Salvat, and Aleksander Jablonski. Cross sections for inner-shell ionization by electron impact. *Journal of Physical and Chemical Reference Data*, 43(1):013102, 2014.

[166] Hans R. Griem. *Principles of Plasma Spectroscopy*. Cambridge Monographs on Plasma Physics. Cambridge University Press, 1997.

[167] R. M. Gilgenbach, M. R. Gomez, J. C. Zier, W. W. Tang, D. M. French, Y. Y. Lau, M. G. Mazarakis, M. E. Cuneo, M. D. Johnston, B. V. Oliver, T. A. Mehlhorn, A. A. Kim, and V. A. Sinebryukhov. Maize: A 1 ma ltd-driven z-pinch at the university of michigan. In *AIP Conference Proceedings*, volume 1088, pages 259–262, 2009. 7th International Conference on Dense Z-Pinches ; Conference date: 12-08-2008 Through 21-08-2008.

[168] Michael G. Mazarakis, William E. Fowler, Alexander A. Kim, Vadim A. Sinebryukhov, Sonrisa T. Rogowski, Robin A. Sharpe, Dillon H. McDaniel, Craig L. Olson, John L. Porter, Kenneth W. Struve, William A. Stygar, and Joseph R. Woodworth. High current, 0.5-ma, fast, 100-ns, linear transformer driver experiments. *Phys. Rev. ST Accel. Beams*, 12:050401, May 2009.

[169] Chuan Liang, Lin Zhou, Fengju Sun, Jiangtao Zeng, Mingjia Li, Zhen Wang, Zhenghong Li, and Xianjue Peng. A repetitive 800 ka linear transformer drivers stage for z-pinch driven fusion-fission hybrid reactor. *Laser and Particle Beams*, 33(3):535–540, 2015.

[170] TRUMPF. Laser marking systems: Trumark station 5000. https://www.trumpf.com/en_US/products/machines-systems/marking-systems/trumark-station-5000/, 2020.

[171] Pradipta Kumar Panigrahi and Krishnamurthy Muralidhar. *Laser Schlieren and Shadowgraph*, pages 23–46. Springer New York, New York, NY, 2012.

[172] H. Schmidt and B. Rückle. Beam deviation method as a diagnostic tool for the plasma focus. *Appl. Opt.*, 17(8):1275–1279, Apr 1978.

[173] T. G. White, M. T. Oliver, P. Mabey, M. Kühn-Kauffeldt, A. F. A. Bott, L. N. K. Döhl, A. R. Bell, R. Bingham, R. Clarke, J.Foster, G. Giacinti, P. Graham, R Heathcote, M. Koenig, Y. Kuramitsu, D. Q. Lamba, J Meinecke, F. Miniati, M. Notley, B. Reville, D. Ryu, S. Sarkat, Y. Sakawa, M. P Selwood, J. Squire, R. H. H. Scott, P. Tzeferacos, N. Woolsey, A. A. Schekochihin, and G. Gregori. Supersonic plasma turbulence in the laboratory. *Nature Communications*, 10(1758), 2019.

[174] G. W. Collins, J. C. Valenzuela, C. A. Speliotopoulos, N. Aybar, F. Conti, F. N. Beg, P. Tzeferacos, B. Khiar, A. F. A. Bott, and G. Gregori. Role of collisionality and radiative cooling in supersonic plasma jet collisions of different materials. *Phys. Rev. E*, 101:023205, Feb 2020.

[175] M. Hipp, J.Woisetschlaeger, P.Reiterer, and T.Neger. Digital evaluation of interferograms. *Measurement*, 36:53–66, 2004.

[176] Opto diode corporation. http://optodiode.com/pdf/AXUVHS5.pdf, 2019.

[177] P. A. Ross. A new method of spectroscopy for faint x-radiations. *J. Opt. Soc. Am.*, 16(6):433–437, Jun 1928.

[178] Paul Kirkpatrick. On the theory and use of ross filters. *Review of Scientific Instruments*, 10(6):186–191, 1939.

[179] G. R. Fowles. *Introduction to Modern Optics*, chapter 11. Dover Publications, Inc., New York, NY, 1989.

[180] K. U. Ingard. *Fundamentals of Waves and Oscillations*, chapter 11. Cambridge University Press, New York, NY, 1988.

[181] E. Baronova, B. Bucher, D. Haas, D. Fedin, A. Stepanenko, and F. N. Beg. Three-channel x-ray crystal spectrometer for diagnosing high energy density plasmas. *Review of Scientific Instruments*, 77(10):103104, 2006.

[182] J. P. Knauer, F. J. Marshall, B. Yaakobi, D. Anderson, B. A. Schmitt, K. M. Chandler, S. A. Pikuz, T. A. Shelkovenko, M. D. Mitchell, and D. A. Hammer. Response model for kodak biomax-ms film to x rays. *Review of Scientific Instruments*, 77(10):10F331, 2006.

[183] A. L. Meadowcroft, C. D. Bentley, and E. N. Stott. Evaluation of the sensitivity and fading characteristics of an image plate system for x-ray diagnostics. *Review of Scientific Instruments*, 79(11):113102, 2008.

[184] Albert Thompson, Ingolf Lindau, David Attwood, Yanwei Liu, Eric Gullikson, Piero Pianetta, Malcolm Howells, Arthur Robinson, Kwang-Je Kim, James Scofield, Janos Kirz, James Underwood, Jeffrey Kortright, Gwyn Williams, and Herman Winick. *X-ray Data Booklet*, chapter 4. Lawrence Berkeley National Laboratory, Berkeley, CA, 2009.

[185] William Henry Bragg and William Lawrence Bragg. The reflection of x-rays by crystals. *Proc. R. Soc. Lond.*, 88(605):428– 438, 1913.

[186] William Henry Bragg and William Lawrence Bragg. The structure of some crystals as indicated by their diffraction of x-rays. *Proc. R. Soc. Lond.*, 89(610):248– 276, 1913.

[187] H. Legall, H. Stiel, V. Arkadiev, and A.A. Bjeoumikhov. High spectral resolution x-ray optics with highly oriented pyrolytic graphite. *Opt. Express*, 14(10):4570–4576, May 2006.

[188] S.B. Hansen, J. Bauche, C. Bauche-Arnoult, and M.F. Gu. Hybrid atomic models for spectroscopic plasma diagnostics. *High Energy Density Physics*, 3(1):109 – 114, 2007. Radiative Properties of Hot Dense Matter.

[189] S.B. Hansen. Configuration interaction in statistically complete hybrid-structure atomic models1this article is part of a special issue on the 10th international colloquium on atomic spectra and oscillator strengths for astrophysical and laboratory plasmas. *Canadian Journal of Physics*, 89(5):633–638, 2011.

[190] Stephanie Hansen, G.S.J. Armstrong, S. Bastiani-Ceccotti, C. Bowen, H.-K. Chung, J.P. Colgan, F. [de Dortan], C.J. Fontes, F. Gilleron, J.-R. Marquès, R. Piron, O. Peyrusse, M. Poirier, Yu. Ralchenko, A. Sasaki, E. Stambulchik, and F. Thais. Testing the reliability of non-lte spectroscopic models for complex ions. *High Energy Density Physics*, 9(3):523 – 527, 2013.

[191] P. Choi, C. Dumitrescu-Zoita, B. Etlicher, and A. V. Shislov. A hard x-ray slit-wire camera. In *Digest of Technical Papers. Tenth IEEE International Pulsed Power Conference*, volume 2, pages 886–891 vol.2, July 1995.

[192] S. V. Lebedev, F. N. Beg, S. N. Bland, J. P. Chittenden, A. E. Dangor, M. G. Haines, S. A. Pikuz, and T. A. Shelkovenko. Effect of core-corona plasma structure on seeding of instabilities in wire array *Z* pinches. *Phys. Rev. Lett.*, 85:98–101, Jul 2000.

[193] I. N. Tilikin, T. A. Shelkovenko, S. A. Pikuz, S. N. Mishin, A. R. Mingaleev, and D. A. Hammer. Studying the dynamics of hybrid x-pinches. *Bulletin of the Russian Academy of Sciences: Physics*, 82(4):386–389, Apr 2018.

[194] Francis W. Sears, Mark W. Zemansky, and Hugh D. Young. *University Physics, 6th ed.* Addison-Wesley Publishing Company, 1981.

[195] Technical information: Nickel. http://www.goodfellowusa.com/PDF/TAB003A.pdf, 2020. Accessed: 2020.01.31.

[196] J. R. Davis. *Copper and copper alloys*. ASM International, 2001.

[197] D. A Hammer. private communication, 2020.

[198] A. Elshafiey. private communication, 2020.

[199] R. E. Madden, S. C. Bott, D. Haas, Y. Eshaq, U. Ueda, G. Collins, and F. N. Beg. Cross-point coronal plasma dynamics in two- and four-wire x-pinches. *Physics of Plasmas*, 15(11):112701, 2008.

[200] P. W. Rambo and R. J. Procassini. A comparison of kinetic and multifluid simulations of laser-produced colliding plasmas. *Physics of Plasmas*, 2:3130–3145, 1995.